Cassini RADAR Users Guide

E.R. Stofan
S.D. Wall
B.W. Stiles
R.L. Kirk
R.D. West
P.S. Callahan

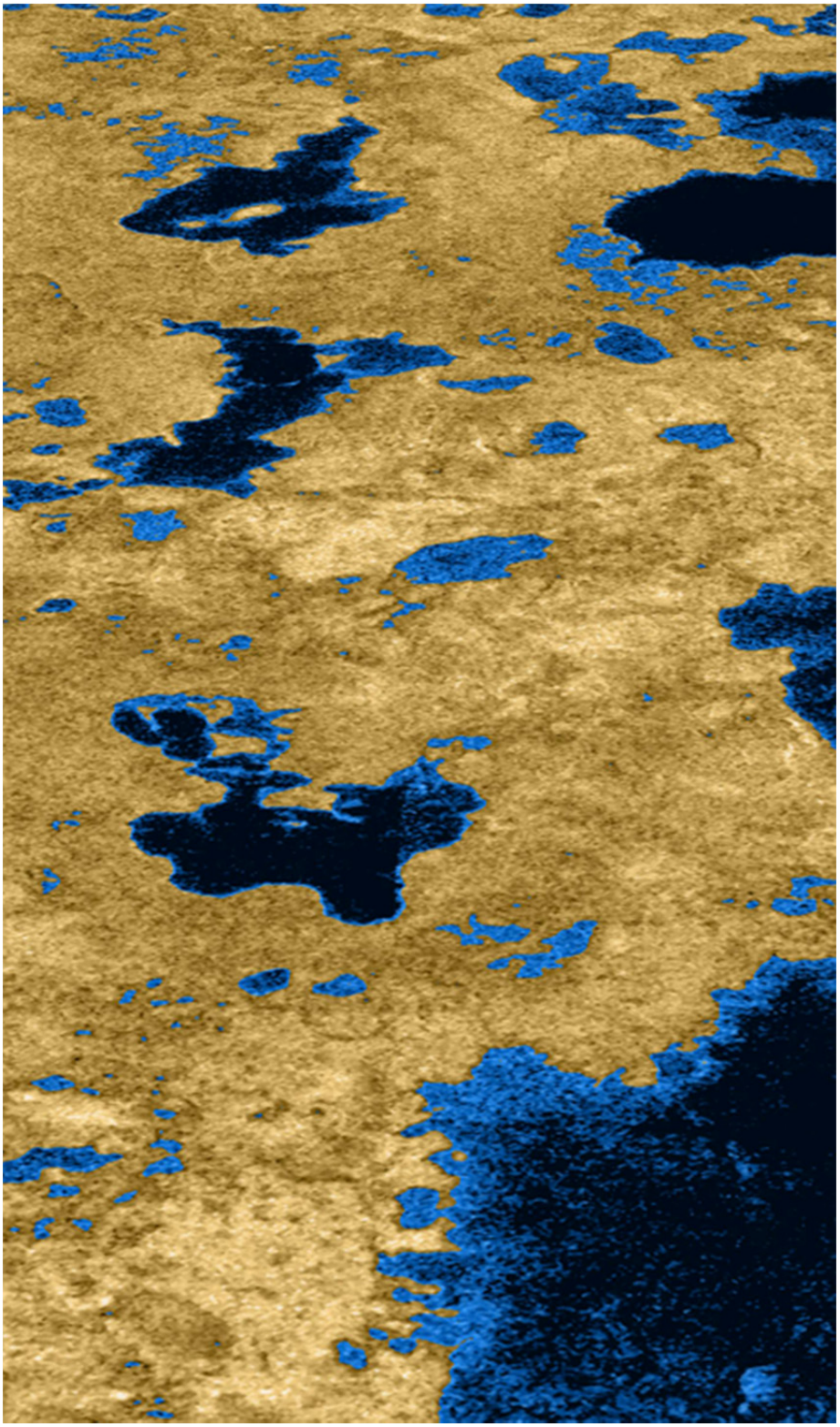

The authors wish to thank Yanhua Anderson, Reta Bebe, Terri Formico, Ralph Lorenz, Claire Marie-Peterson, and Curt Niebur for their assistance in producing this document.

This publication was prepared for the Jet Propulsion Laboratory, California Institute of Technology, under a contract with the National Aeronautics and Space Administration.

Reference herein to any specific commercial product, process, or service by trade name, trademark, manufacturer, or otherwise, does not constitute or imply its endorsement by the United States Government or the Jet Propulsion Laboratory, California Institute of Technology.

This document has been reviewed and determined not to contain export-controlled technical data.

This guide is dedicated to the memory of Bill Johnson and Steve Ostro.
They were fundamental to the success of the Cassini RADAR,
and we miss them not only as colleagues, but as friends.

Contents

1 Introduction 1
2 The Cassini Spacecraft and Mission 3
2.1 The Cassini Orbiter 4
2.2 Mission Operations 7
2.3 Mission Phases 8
3 The Cassini RADAR Experiment 9
3.1 Cassini RADAR Overview 9
3.2 Experiment Description 10
3.2.1 RADAR Modes 10
3.2.2 Secondary RADAR Data Types 11
3.3 Typical RADAR Observation of Titan 12
3.4 Titan Coverage 12
3.5 Other RADAR Coverage 25
3.5.1 Rings 25
3.5.2 Icy Satellites 25
3.5.3 Saturn 27
4 RADAR Data Product Overview 29
4.1 Burst Ordered Data Products (BODPs) 29
4.1.1 Product Overview 30
4.1.2 Short Burst Data Record (SBDR) 30
4.1.3 Long Burst Data Record (LBDR) 32
4.1.4 Altimeter Burst Data Record (ABDR) 33
4.1.5 Data Validation and Archiving 33
4.2 Basic Image Data Products (BIDRs) 33
4.2.1 Data Format and Description 34
4.2.2 Data Validation and Archiving 35
4.3 Digital Map Products (DMPs) 35
4.3.1 Pass Radiometry Data Records (PRDRs) 36
4.3.2 Pass Scatterometry Data Records (PSDRs) 37
4.3.3 Global Radiometry Data Records (GRDRs) 38
4.3.4 Global Scatterometry Data Records (GSDRs) 40
4.3.5 Global Topography Data Records (GTDRs) 40
4.3.6 Mosaicked Image Data Records (MIDRs) 41
4.3.7 Repeat Image Data Records (RIDRs) 41
4.3.8 Digital Topographic Models (DTMs) 43
4.3.9 PDS Label Format for DMPs 44
4.3.10 Validation and Archiving of DMPs 47
5 Calibration 48
6 Titan SAR Swath Summary 52
6.1 Swath Descriptions 55
6.2 Ontario Lacus: A Case Study 60

7 Data Outages, Anomalies, and Related Data Issues 62
7.1 Major Data Outages and Corruption 62
7.1.1 Dione/Mimas 00b (Total Loss) 62
7.1.2 The T7 Anomaly 63
7.1.3 The T60 Anomaly 64
7.1.4 Iapetus 49 64
7.1.5 The T64 Anomaly 64
7.2 Other Experiment Anomalies 65
7.3 Complexities to Consider When Interpreting SAR Images 65
8 Case Studies in Quantitative Use of Cassini RADAR Data 67
8.1 Case 1: Topography from SAR Data 67
8.2 Case 2: Titan Pole and Spin Rate Estimation 71
8.3 Case 3: SAR Stereo 73
8.4 Case 4: Altimetry Refinement 75
9 Obtaining Cassini RADAR Data Products 77
10 Information for Educators 80
11 Appendix 1: References and Bibliography 82
12 Appendix 2: Acronyms 103
13 Appendix 3: Links to SAR Swaths on Photojournal Site 106
14 Appendix 4: Cassini RADAR Uplink/Downlink Spreadsheet 108
15 Appendix 5: BIDR PDS Label, Primary Data Set, 32-Bit Data 123

1 Introduction

The surface of Saturn's moon Titan, shrouded in haze, has been revealed by data returned from the Cassini Orbiter, as well as from descent and surface images from the Huygens probe. The revealed surface is far more complex than hypothesized prior to Cassini, with very few impact craters, but with abundant channels, dunes, and polar lakes (Figure 1-1). The Cassini Radio Detection and Ranging instrument (RADAR) data set,[1] covering approximately 30% of Titan in the Prime Mission and approximately an additional 30% in the extended missions, should have appeal to a wide range of researchers, from planetary scientists who study how surface processes vary from body to body across the solar system, to possibly more terrestrially-oriented scientists who now have the opportunity to study the only other body in the solar system besides Earth with an active liquid cycle, and active lacustrine and riverine processes.

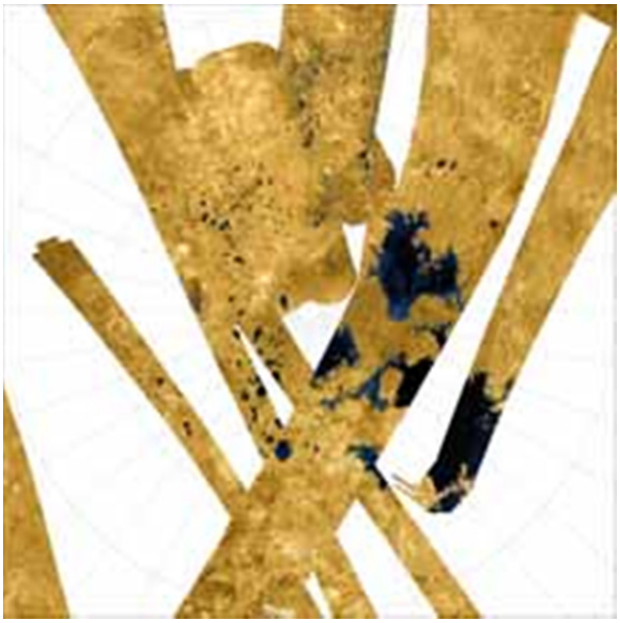

Figure 1-1. PIA10008. Cassini RADAR images of lakes near the North Pole of Titan.

In order to fully exploit the scientific information within the Cassini RADAR data, the user must understand how the data were collected, including the peculiarities of the instrument and events that might have occurred during data collection or processing. As with any NASA mission, these descriptions exist across a range of documents and locations. In sections 2 and 3, this guide draws together the most pertinent information for future users of the Cassini RADAR data, facilitating the data access and manipulation that necessarily precede interpretation. A similar guide was put together for the Magellan mission to Venus (Wall et al. 1995) by one of the authors of this report, and it has proven to be a useful document for users of that data set. We aim similarly to aid future users of Cassini RADAR data.

Most scientific analyses of Cassini RADAR data performed to date have used synthetic aperture radar (SAR) imagery, altimeter surface heights, scatterometer backscatter values (sigma-0), or radiometer temperatures. These are the primary scientific measurements in the data set. The SAR imagery is contained in the Basic Image Data Record (BIDR) files. The other values are in the Short Burst Data Record (SBDR) files. Both of these data sets are archived by NASA's Planetary Data System (PDS). Other data, including high-altitude imaging (HiSAR), SARTopo, and SARStereo, are described in Section 4 of this guide, an overview of RADAR data products.

[1] In this guide we distinguish between radar, a microwave sensing technique, and RADAR, an instrument aboard the Cassini spacecraft.

This guide specifically addresses data acquired from Cassini's Saturn Orbit Insertion (SOI) on July 1, 2004, through Titan pass 69, although at this writing we expect both spacecraft and instrument to continue operation through the end of Cassini's Solstice Mission (the XXM or second extended mission) in 2017.

The Cassini RADAR operates in four modes: SAR or imaging, altimetry, scatterometry, and radiometry. While most users will likely be familiar with the imaging data, the other three RADAR data sets greatly enhance interpretation of the SAR data where they are coincident. Scatterometer and radiometer data, which cover the entire surface at widely varying resolutions, provide a background for understanding the other data as well as providing specific information about surface properties. In Section 6.2 we provide an illustration of their combined use.

This guide is a compilation of previous Cassini Project reports, some of which are internal to the project and some of which have been published and/or presented in popular, scientific, or engineering journals and conferences. We have tried to attribute this work accurately; any errors or omissions are the responsibility of the authors of this data guide.

The true credit for the information in this report, however, goes to the hundreds of scientists and engineers from NASA, ASI, ESA, and numerous other organizations who have made the Cassini mission a resounding success, and who are allowing it to continue extended operations through the Solstice Mission until 2017.

This document has been reviewed and determined not to contain export-controlled technical data.

2 The Cassini Spacecraft and Mission

The Cassini-Huygens mission to the Saturn system was launched in October of 1997, arriving at Saturn on July 1, 2004, with the Huygens probe landing on Titan on January 14, 2005 (Figure 2-1). In this section, we briefly describe the mission and how it operates, in order to provide a framework for the more detailed descriptions of the RADAR experiment in Section 3.

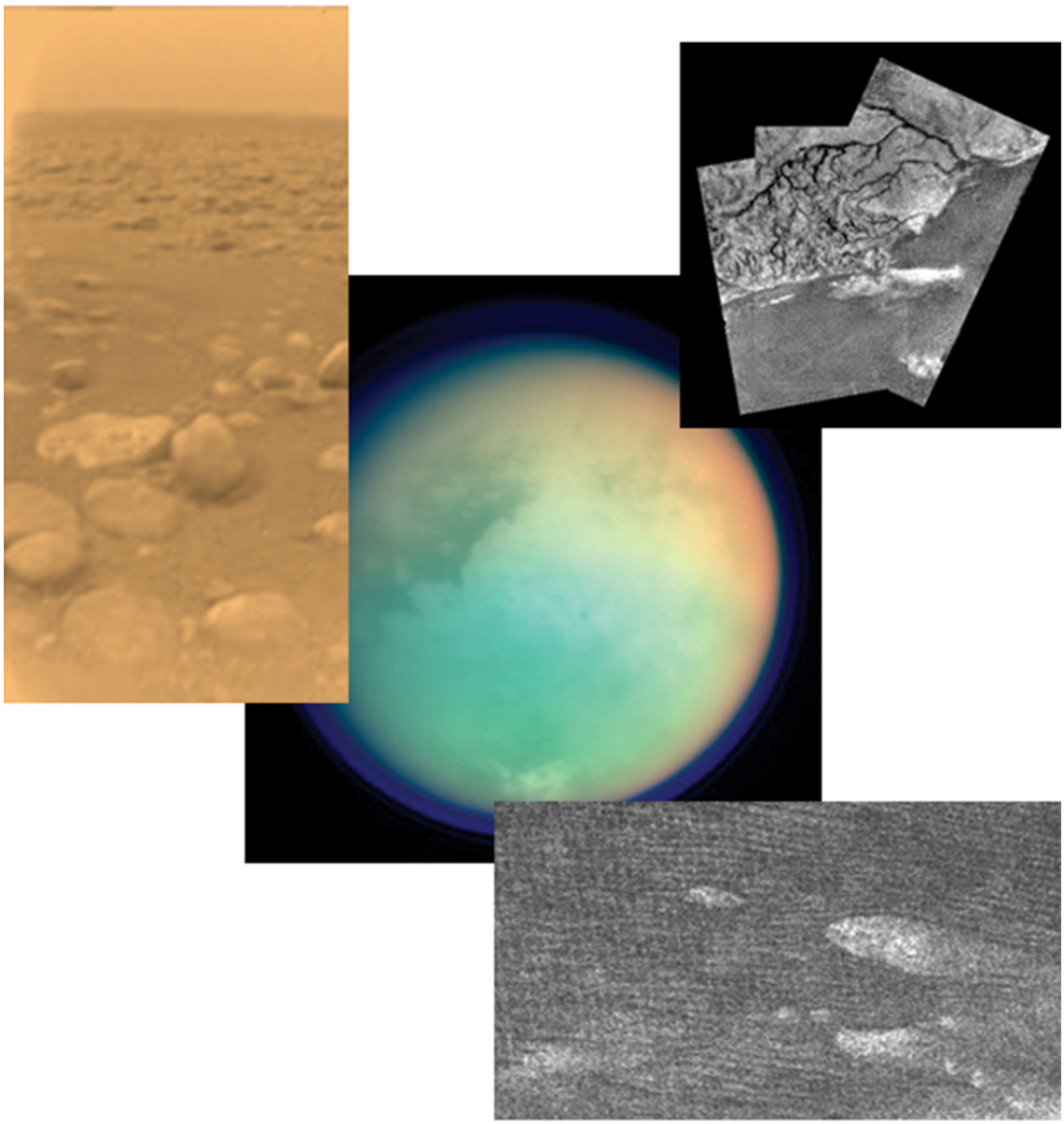

Figure 2-1. Montage of Cassini at Titan results. Clockwise from upper left: PIA07232, the surface of Titan from Huygens; PIA06139, imaging science subsystem (ISS) false-color image of Titan; PIA07236, surface channels in Huygens descent image; and PIA03567, Cassini RADAR image of dunes.

2.1 The Cassini Orbiter

The Cassini Orbiter has 12 science instruments to study the Saturn system, in addition to the Huygens probe. It stores science data and relays data back to Earth. The design of the Orbiter was driven by a number of factors, including the great distances from Saturn to the Sun and Earth, the length of the mission, the complexity and volume of the science observations, and the spacecraft's path to Saturn.

The Orbiter consists of a four-part stack: the high-gain antenna (HGA), provided by the Italian Space Agency (ISA); the upper and lower equipment modules; and the propulsion module (Figure 2-2). Attached to this stack are the remote-sensing and fields and particles instruments. The magnetometer is mounted on an 11-m boom. The height of the spacecraft is 6.8 m; it is the largest planetary spacecraft ever launched.

The Cassini Orbiter is powered by three radioisotope thermoelectric generators (RTGs), which use heat from the decay of plutonium to produce direct-current electricity. The Cassini RTGs are similar to those used on the Galileo and Ulysses missions, and are mounted on the lower equipment module. Saturn's distance from the Sun precludes the use of solar panels. Cassini's distance from Earth, between 8.2 and 10.2 astronomical units (AU), also makes communication with the spacecraft a challenge. Signals between Earth and the spacecraft have a travel time of 68–84 minutes, meaning that the spacecraft team cannot give the spacecraft "real-time" commands. This necessitates robust spacecraft system fault protection to ensure that, in the event of onboard problems, spacecraft health can be maintained long enough to permit engineers back on Earth to analyze and correct the problems.

Communications on the spacecraft are handled by the radio frequency subsystem (RFS) and the antenna subsystem. The antenna subsystem is made up of the 4-m-diameter HGA and two low-gain antennas (LGA1 and LGA2). The HGA also houses redundant X-band receivers and transmitters; feeds for a Ka-band receiver, a Ka-band transmitter, and an S-band transmitter, all for radio science; and feeds for the RADAR instrument's Ku-band transmitters and receivers. The RFS produces an X-band carrier (frequency 8.4 GHz), modulates it with data received from the command and data subsystem (CDS), amplifies the carrier, and delivers the signal stream to the antenna subsystem for transmission to Earth. The RFS receives X-band (frequency 7.2 GHz) ground commands and data signals from the antenna subsystem, demodulates them, and sends the telemetry to the CDS for storage and/or execution. For the first two and a half years, the spacecraft used the HGA for sun-shading and communicated via the LGAs. When it was no longer needed for shading, the HGA became (and remains) the primary communications antenna. Commands and data from Earth are received at 1000 bps by the HGA, and transmitted to Earth at rates from 14,220 to 165,900 bps. During operations, data are recorded on the solid-state recorders for about 15 hours each day, while the HGA is not pointed at Earth. The data from the solid-state recorders are then played back for nine hours each day (generally during Goldstone, California, tracking station coverage), while data collection from the fields and particles investigations continues. About one gigabit of data can be returned each day via a 34-m Deep Space Network (DSN) antenna; approximately 4 gigabits of data can be returned in 9 hours via a 70-m ground antenna.

Figure 2-2. The Cassini spacecraft, including the Huygens (Titan) probe.

The CDS on the spacecraft handles command, control, fault protection, and data handling. The CDS executes sequences of stored commands to conduct normal preplanned flight activities, processes and issues real-time commands from Earth,

controls and selects data modes, and collects and formats science and engineering data for transmission to Earth. Bus interface units (BIUs) in each instrument control data flow and allowable power states for the instrument, handle commands and data from the CDS to the instrument, and convey data from the instrument to the solid-state recorders. The CDS can handle combined data rates in excess of 430,000 bps from the instruments while still carrying on its command and control functions.

Cassini uses solid-state recorders to store data. Two redundant solid-state recorders have a capacity guaranteed to be at least 1.8 gigabits 15 years after launch. The recorders can record and read out data simultaneously, record the same data simultaneously in two different locations on the same recorder, and record simultaneously on both recorders. So that Cassini is not restricted to instantaneous data collection rates, the recorders buffer essentially all data that are collected, permitting data transmission to Earth to occur at the highest available rates. They can be partitioned by command from the CDS, store backup versions of memory loads for almost all computers on the spacecraft, and store a running record of recent engineering activities to assist in fault analysis.

The attitude and articulation control subsystem (AACS) is primarily responsible for maintaining the orientation of Cassini in space. The AACS consists of redundant Sun sensors mounted to the HGA, redundant stellar reference units on the remote-sensing platform, three mutually perpendicular reaction wheels on the lower equipment module, and a fourth reaction wheel on the upper equipment module, as a backup that can be rotated to be parallel to any one of the three other reaction wheels. Redundant inertial reference units are located on the upper equipment module, along with an accelerometer, to measure changes in the spacecraft's velocity. The AACS points the antenna (either the HGA or LGAs) toward Earth when required, points the HGA at appropriate radar or radio science targets, points the instruments on the remote sensing pallet toward targets that are themselves in motion relative to the spacecraft, turns the spacecraft at a constant rate around the HGA axis for fields and particles measurements during transmission of data to Earth or receipt of commands from Earth, points one of the two redundant main propulsion engines in the desired direction during main engine burns, performs trajectory correction maneuvers of smaller magnitude using the onboard thrusters, and provides sufficient data in the transmitted engineering data to support science data interpretation and mission operations. The AACS uses a pointing system known as inertial vector propagation that keeps track of spacecraft orientation; the direction and distance of the Sun, Earth, Saturn, and other possible remote-sensing targets in the Saturn system; and the spacecraft-relative pointing directions of all the science instruments, pointing any instrument at its selected target.

The propulsion module subsystem (PMS) is the largest and most massive subsystem on Cassini, consisting of a bipropellant element for trajectory and orbit changes and a hydrazine element for attitude control, small maneuvers, and reaction wheel desaturation or unloading. The RTGs are a part of the power and pyrotechnics subsystem (PPS). The power conditioning equipment converts the RTG power output to provide a regulated 30-V direct-current power bus and provides the capability to turn power on and off to the various spacecraft power users in response to commands from the CDS. The power conditioning equipment can detect overcurrrent conditions. If overcurrent exceeds a predetermined level, the power to the affected user is switched

off. The pyro switching unit also provides redundant power conditioning and energy storage, and controls the firing of pyro devices on 32 commandable circuits, most of which open or shut valves to control the pressures and flows within the propulsion module plumbing.

The temperature control subsystem (TCS) keeps spacecraft units within their specified temperature limits. It monitors temperatures using electrical temperature sensors on all critical parts of the spacecraft. The TCS controls the temperature of the various units by several means: turning electrical heaters on or off, opening or shutting thermal louvers in one of the bays of the upper equipment module, using small radioisotope heater units to raise the temperatures of selected portions of the spacecraft that would otherwise cool to unacceptably low temperatures, and the use of thermal blankets and shields. Several instruments also have radiator plates to cool their detectors. Even at the distance of Saturn from the Sun, spacecraft orientations that point those radiator plates in the same half of the sky as the Sun can severely degrade the data collected by some of the science instruments. In at least one case, it is even necessary to avoid having Saturn illuminate the radiator plate(s) simultaneously.

New technology incorporated into Cassini-Huygens includes the solid-state data recorder, the main onboard computer that incorporates new families of electronic chips, including very-high-speed integrated circuit (VHSIC) chips, and new application-specific integrated circuit (ASIC) parts. The Orbiter power system utilizes an innovative solid-state power switch that eliminates the rapid fluctuations or “transients” that can occur with conventional power switches. In addition, Cassini uses hemispherical resonator gyroscopes that have no moving parts.

2.2 Mission Operations

Several teams carry out mission planning for Cassini, including the Titan Orbiter Science Team (TOST), Satellites Orbiter Science Team (SOST), and the Rings, Saturn, and Cross-Disciplinary Target Working Teams (TWTs). These teams are responsible for integrating segments of Saturnian orbits (referred to as “revs”). RADAR observations have been included in the integration done by all these teams. The Orbiter Science Teams (OSTs) and TWTs deliver an integrated, conflict-free timeline based on science agreements. Project science working groups on surfaces, atmospheres, rings, and magnetospheres also help resolve conflicts that cannot be resolved in the OSTs and TWTs.

The science planning process consists of two steps: first, production of a Science Operation Plan (SOP), and then development of a process to allow changes in the plan, called the “Aftermarket” process. The SOP is an integrated, conflict-free plan that includes all science and engineering events. The Aftermarket process allows limited reintegration and/or renegotiations of Tour segments in the Tour SOP (including trades among tour sequences) prior to final sequence command generation. The scope of the Aftermarket process is to allow changes due to 1) liens resulting from the SOP implementation, 2) changed instrument or spacecraft performance, 3) new science discoveries, and 4) rebalance of the science plan to include required observations that were not integrated. The top priority is solving liens. The renegotiations and reintegration are made through the TWT and OST. Changes that involve multiple tour segments are treated in a joint meeting of all the TWTs and OSTs involved.

This document has been reviewed and determined not to contain export-controlled technical data.

The SOP is then updated to reflect changes and trades made in the Aftermarket process. The SOP is updated using the actual DSN station allocations, new ephemeris files, and the latest version of the MSS. The final process before uplink is called the Science and Sequence Update Process (SSUP).

Changes to pointing (e.g., to observe new targets identified due to ongoing discoveries) have to be made prior to the start of the SSUP for a particular sequence. The SSUP is started approximately 10 weeks before the sequence start date. Instrument commands, ephemeris changes, and changes due to revised DSN allocations are done during the SSUP.

2.3 Mission Phases

The Cassini-Huygens mission consists of three phases: the Prime Mission (2004–2008), the Equinox mission (2008–2010, also known informally as the Extended Mission, XM), and the Solstice mission (2010–2017, also known as XXM) (Figure 2-3). The Solstice mission, which ends in September 2017, is named for the Saturnian summer solstice that occurs in May 2017. The northern summer solstice marks the beginning of summer in the northern hemisphere and winter in the southern hemisphere. As Cassini arrived at Saturn just after the planet's northern winter solstice, the Solstice phase of the mission permits the first study of a complete seasonal period.

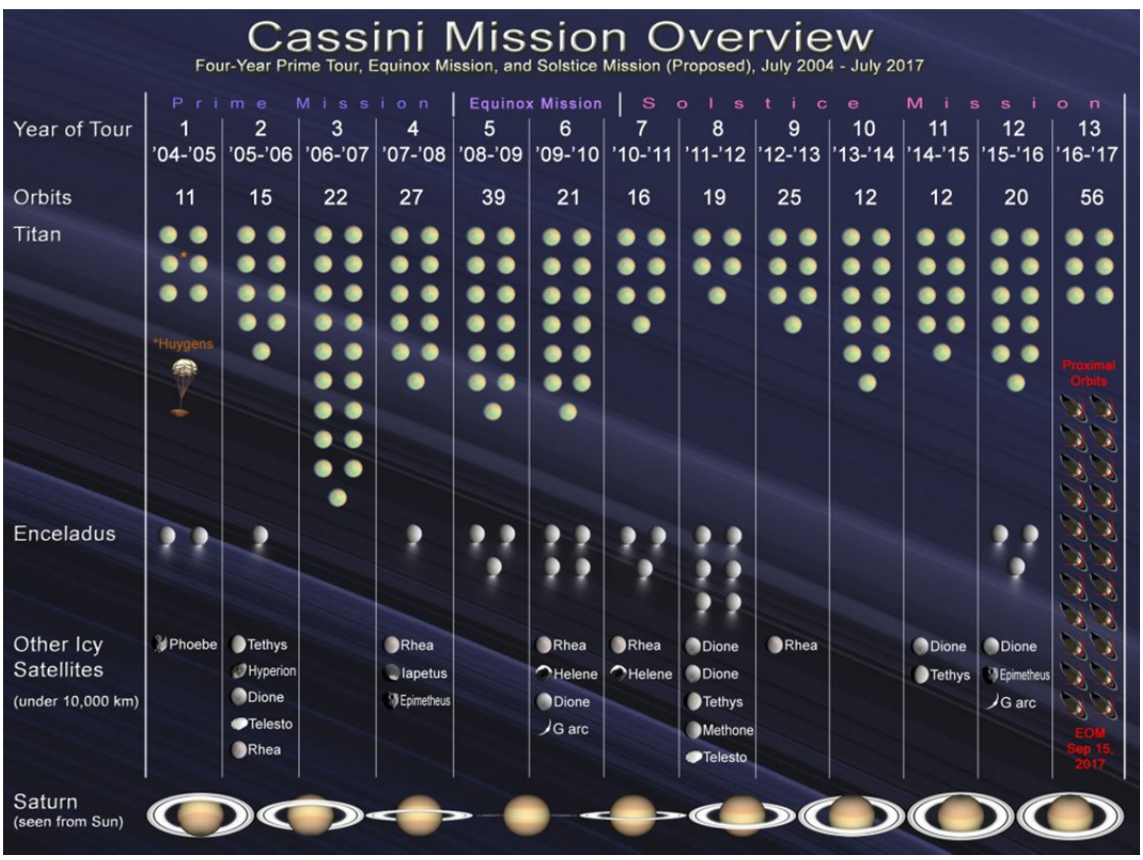

Figure 2-3. Cassini mission phases.

3 The Cassini RADAR Experiment

3.1 Cassini RADAR Overview

The Cassini RADAR instrument transmits and receives Ku-band microwave radiation. It operates in both passive (radiometer) and active (altimeter, SAR imaging, scatterometer) modes (Table 3-1) (Elachi et al. 2004).

Table 3-1. Instrument description.

RADAR MODES	CENTER FREQUENCY AND BANDWIDTH(S)
Imaging	13.78, GHz, with 0.425 MHz, 0.85 MHz bandwidth
Altimetry	13.78, GHz, with 4.25 MHz bandwidth
Scatterometry	13.78, GHz, with 0.10625 MHz bandwidth
Radiometry	13.78, GHz, with 125 MHz bandwidth
DURATION OPERATIONS	300 minutes +/- closest approach
PEAK OPERATING POWER	86 W
DATA RATES	1 kbps (radiometer only) 30 kbps (altimeter, scatterometer/radiometer) 365 kbps (SAR +/- radiometer) (usually limited to ~250 kbps)

In active mode the RADAR measures the returned energy from the transmitted signal. Ground processing can separate that energy by round trip time and Doppler shift. The return energy is used to determine the normalized radar cross section (NRCS) of the surface. NRCS is the ratio of the energy received to that which one would expect from a uniform scatterer. This quantity is related to the roughness at the scale of the wavelength of the transmitted signal (~2 cm) and the dielectric constant of the surface. It is also affected by the angle at which the radar beam impinges the surface and thus is modulated by the larger-scale shape of the surface. Such effects can depend upon both the incidence and azimuth of the observation, yielding variation in NRCS that is correlated with topographical features in RADAR imagery (i.e., lakes, mountains, rivers, dunes, etc.). Because return energy can be binned by delay and Doppler shift, one can produce geolocated SAR imagery and/or estimates of surface height depending upon the viewing geometry. As shown in Table 3-1, different signal bandwidths can be used to optimize the measurement of 1) precise NRCS quantities in scatterometer mode, 2) surface heights in altimetry mode, and 3) geolocated high-resolution (~500 m) imagery in SAR mode. Depending upon the accuracy of spacecraft attitude information among other error sources, obtaining SAR imagery and surface height information simultaneously is also possible in some cases.

In passive mode, the Cassini RADAR instrument measures the linearly polarized radiant power received through the antenna in a bandpass coincident with but much wider that the radar signal receiver (see Table 3-1). Passive measurements are acquired in all operational modes of the RADAR instrument. All radiant power observed in the Saturn system is thermal in origin. In the microwave region the power radiated by a thermal blackbody emitter is very nearly proportional to its physical temperature, and it is common usage to describe this power, whatever the source, in terms of the temperature of a blackbody that emits the equivalent power. Hence passive microwave measurements are reported in kelvins. In particular, the power collected by the antenna

is called the "antenna temperature." For an ideal antenna with a pencil beam and no sidelobes, the antenna temperature is the same as the "brightness temperature," or equivalent blackbody temperature, of the source observed in the beam of the antenna. In practice, and particularly for Cassini, the process of obtaining calibrated brightness temperatures from antenna temperature measurements is not straightforward, and caution must be exercised in the interpretation of all antenna temperature data reported from the Cassini RADAR radiometer. A summary of the calibration of the radiometer to obtain brightness temperatures is given in Section 5.

Active- and passive-mode Cassini RADAR observations during the Cassini mission are archived in the PDS. In addition to archiving the determined geophysical parameters such as NRCS, antenna temperature, and surface height, the raw radar returns and ancillary information needed to process them are also archived.

3.2 Experiment Description

3.2.1 RADAR Modes

3.2.1.a. Synthetic Aperture Radar (SAR). SAR is used to characterize Titan's surface morphology. The images returned have brightness variations that in some ways resemble traditional camera images; but in the case of SAR, image brightness represents normalized microwave energy backscattered from the surface (NRCS), which is a function of surface slope, dielectric properties, roughness, and the amount of volume scattering (e.g., Ulaby et al. 1982). Typical geomorphological investigations may include the identification and classification of landforms including impact craters, as well as aeolian and volcanic features. SAR resolution varies from 350 m at closest approach distances of ~950 km to over 1 km at the maximum range for standard SAR imaging. Thus, SAR image strips typically have high resolution in the center and lower resolution at both ends.

Ford et al. (1993) provides a guide to the interpretation of Magellan SAR data that also serves as a useful basis for understanding SAR in general and the Cassini SAR data. Users should keep in mind that SAR images are inherently "grainy" due to a phenomenon called speckle, and RADAR images have varying noise and varying resolution along each strip. Brightness in Cassini RADAR images does not necessarily link to the appearance of the surface to the eye; brightness can be caused by surface roughness, slope shading (just as in optical images), and subsurface volume scattering.

Radar images contain geometric distortions from topography, which enable stereo mapping, but can in severe (high-slope) cases, cause surfaces to appear to overlap themselves (not generally a problem on Titan where slopes are low) (Ford et al. 1993).

In places on Titan, multiple Cassini RADAR images have been obtained. But these multiple views of the surface took place with differing geometries, and therefore caution should be used in interpreting apparent surface differences. When two images from different geometries are compared, there will be not only geometric parallax but also illumination differences, so it can be extremely difficult to determine if there is any evidence for actual surface changes (Hayes et al. 2011).

3.2.1.b. Altimetry. The altimetry data have two broad applications. One is to use the aggregate of all datatakes to define a geoid for Titan and identify whether there is a frozen-in rotational or tidal bulge. The second application is to generate topographic

profiles that characterize landforms (e.g., impact craters, mountains), an important constraint on geophysical models. Altimetry is obtained when the RADAR is pointed within a fraction of a beam width (0.35 deg) of nadir. The 4.25-MHz bandwidth results in a range resolution of approximately 30 m.

3.2.1.c. Scatterometry. Scatterometry data have near-global coverage, and can be used as a "basemap" for SAR, and as a broad characterization of global terrains. The data indicate the backscatter efficiency at various incidence angles at relatively low resolution (real aperture resolution depends on range to surface). As an independent constraint on surface roughness, scatterometry data are an important complement to radiometry data in order to constrain surface composition.

3.2.1.d. Radiometry. Polarized brightness temperatures of the observed scene are obtained from the antenna temperature measurements (see Section 5). The microwave brightness temperature of a solid surface contains information on many properties besides physical temperature; e.g., emission angle, polarization, dielectric constant, porosity, surface and subsurface roughness, etc. The interpretation of brightness temperature generally depends on available ancillary information such as visible and IR imaging and the RADAR active return, and in conjunction with such observations can provide uniquely valuable information about surface properties of Titan, the icy satellites, and the rings. Such information may include bulk dielectric constant and likely composition (e.g., organics with low dielectric constant or water ice with high dielectric constant), surface or subsurface roughness or physical state, or physical temperature. For Saturn's atmosphere the only significant source of opacity is ammonia vapor, and the thermal radiation at the RADAR wavelength of 2.2 cm comes from the ammonia cloud-forming region around 1–2 bar pressure. The measured brightness temperature reflects the mean atmospheric temperature in the region of absorption, and is generally indicative of the cloud-level ammonia humidity.

3.2.2 Secondary RADAR Data Types

3.2.2.a. HiSAR. Synthetic aperture imagery is occasionally obtained at altitudes greater than 10000 km above the target body. In these circumstances, nominal SAR mode data suffers from excessive noise due to poor signal-to-noise ratio (SNR). In such cases, we utilize a lower resolution (1–5 km) version of SAR imaging with resolution that is between nominal SAR (~500 m) and scatterometry (>10 km). To maintain adequate SNR, only the central high-gain beam is used. At higher altitudes, the central beam spans a wider area, so useful swath widths in the range of 70 km to 150 km can still be obtained. Instead of relying on spacecraft motion to sweep the beam across the surface, these imaging segments pan the central beam across the surface by turning the spacecraft. These images extended the area covered by imaging and are useful for mapping the extent of moderate resolution features such as mountains and lakes that are not apparent in lower resolution scatterometer data.

3.2.2.b. SARTopo. Because multiple antenna beams (feeds) are employed in SAR imaging, we can use an amplitude monopulse technique to compare overlapping regions between the beams and thereby estimate surface heights (Stiles et al. 2009). This technique depends upon accurate knowledge of spacecraft attitude and the antenna gain pattern. It enables two or more surface-height profiles to be obtained along the long dimension of each SAR image. These profiles have approximately 10 km spatial

resolution and 100 m height accuracy. By providing coincident surface heights with SAR imagery, the SARTopo technique greatly improves the interpretability of the imagery. Although SARTopo heights have not been archived in PDS to date, it is planned to archive them by the end of 2012. SARTopo data in the form of SAR images with pseudocolor height profiles are available in peer-reviewed journal papers (Stiles et al. 2009, Zebker et al. 2009a, b).

3.2.2.c. SAR Stereo. When overlapping SAR images are obtained at different times, it is often possibly to determine surface heights using stereo techniques closely related to those employed for optical images. The stereo mapping process can be divided broadly into two steps: identifying corresponding points (or features) in two different images and using the pixel coordinates of those points to solve for the ground-coordinates of the feature. The first step is essentially an image-processing problem and is the same for optical or radar images, though the latter may have greater problems from noise. The geometric calculations of radargrammetry differ from those of photogrammetry in that they are based on the principles by which SAR images are formed, i.e., a pixel corresponds to a circle of constant range from the spacecraft at the time of imaging, rather than to a ray emanating from the camera in a constant direction. The Cassini RADAR Science Team (CRST) produces Digital Topographic Models (DTMs) from stereo data by using a commercial system that includes flexible image matching capabilities and that allows the user to write “sensor model” code describing the geometry of the images (Kirk et al. in prep.).

3.3 Typical RADAR Observation of Titan

An encounter that fully utilizes the RADAR instrument starts as the spacecraft approaches Titan, obtaining only radiometer measurements for up to 3 hours (Figure 3-1). Next, when the spacecraft is within about 30,000 km the transmitter is turned on and scatterometer measurements are taken. Altimetry follows when Titan is close enough (~10000 km) for useful data to be taken at the wider bandwidth. Then, about 15 minutes before closest approach at an range of about 5000 km, SAR observation begins. On the outbound portion of the pass these transitions occur in reverse. High SAR observations are obtained during nominal scatterometer or altimeter time periods when data volume and viewing geometry constraints allow. In practice, observation time during Titan (and other target) passes are mostly shared with other instruments, vary in altitude, and are otherwise constrained so for any individual encounter, the combination of observations varies.

3.4 Titan Coverage

Figures 3-2 and 3-3 provide a global overview of SAR coverage from the Cassini Prime and Equinox missions. Figure 3-4 shows coverage anticipated in the Solstice Mission. Tables 3-2 through 3-7 provide detailed information for SAR passes in all three phases. By the end of the Prime Mission, SAR coverage of Titan was approximately 30%; at the end of the Equinox it was 41%. By the end of the Solstice mission, anticipated SAR coverage of Titan will be more than 60%. Scatterometer and radiometer coverage of Titan will be close to 100% by end of mission.

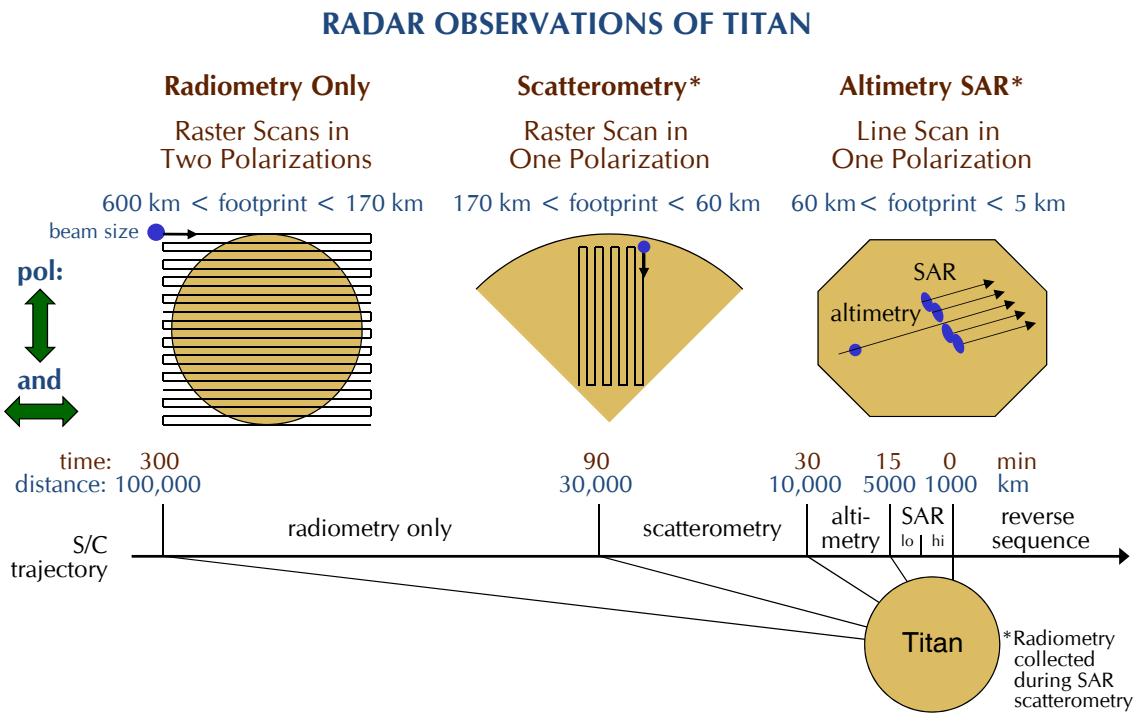

Figure 3-1. Typical SAR data pass at Titan (courtesy M. Janssen).

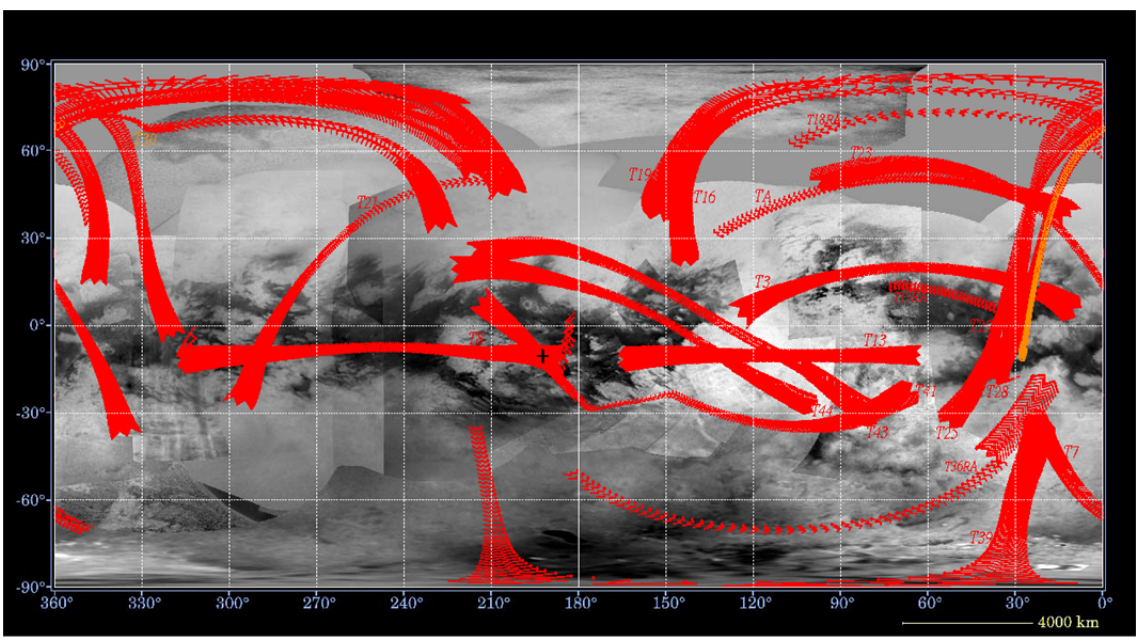

Figure 3-2. Titan SAR coverage from the Prime Mission. The swaths are shown on an ISS basemap.

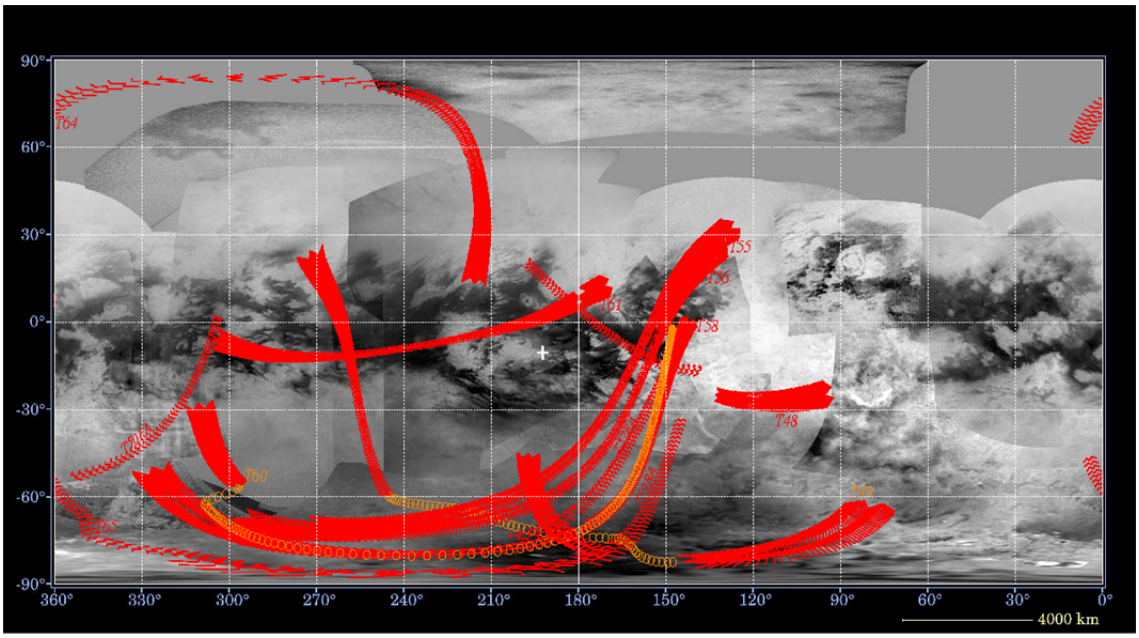

Figure 3-3. Titan SAR coverage from the Equinox (XM) mission. The swaths are shown on an ISS basemap.

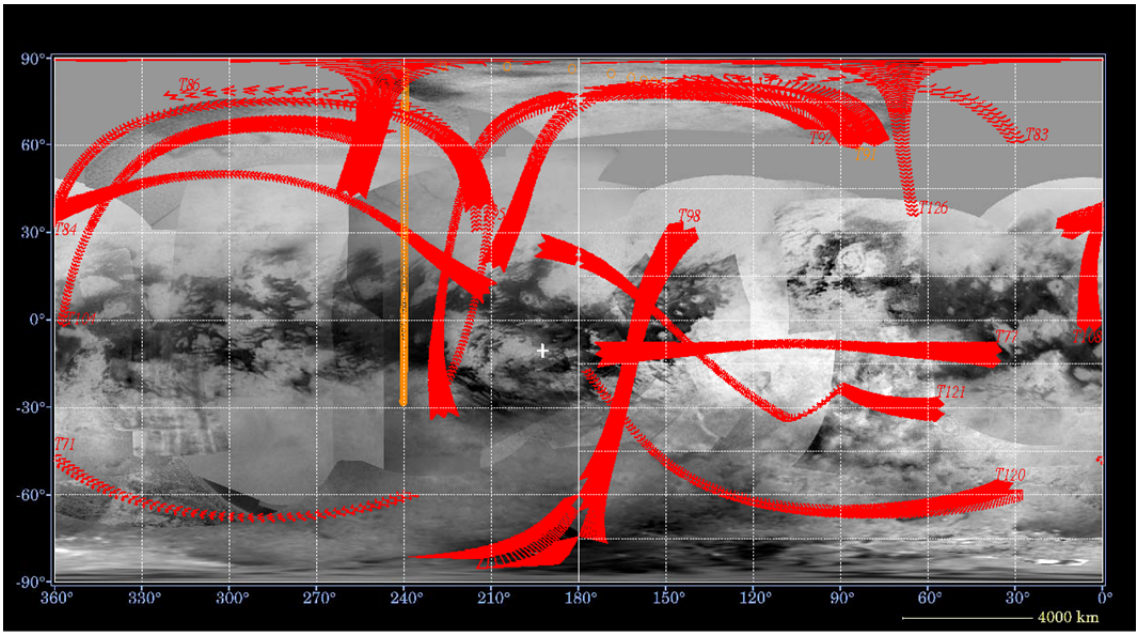

Figure 3-4. Titan SAR coverage from the Solstice (XXM) mission. The swaths are shown on an ISS basemap.

Table 3-2. Titan coverage in the Prime Mission, Part I.

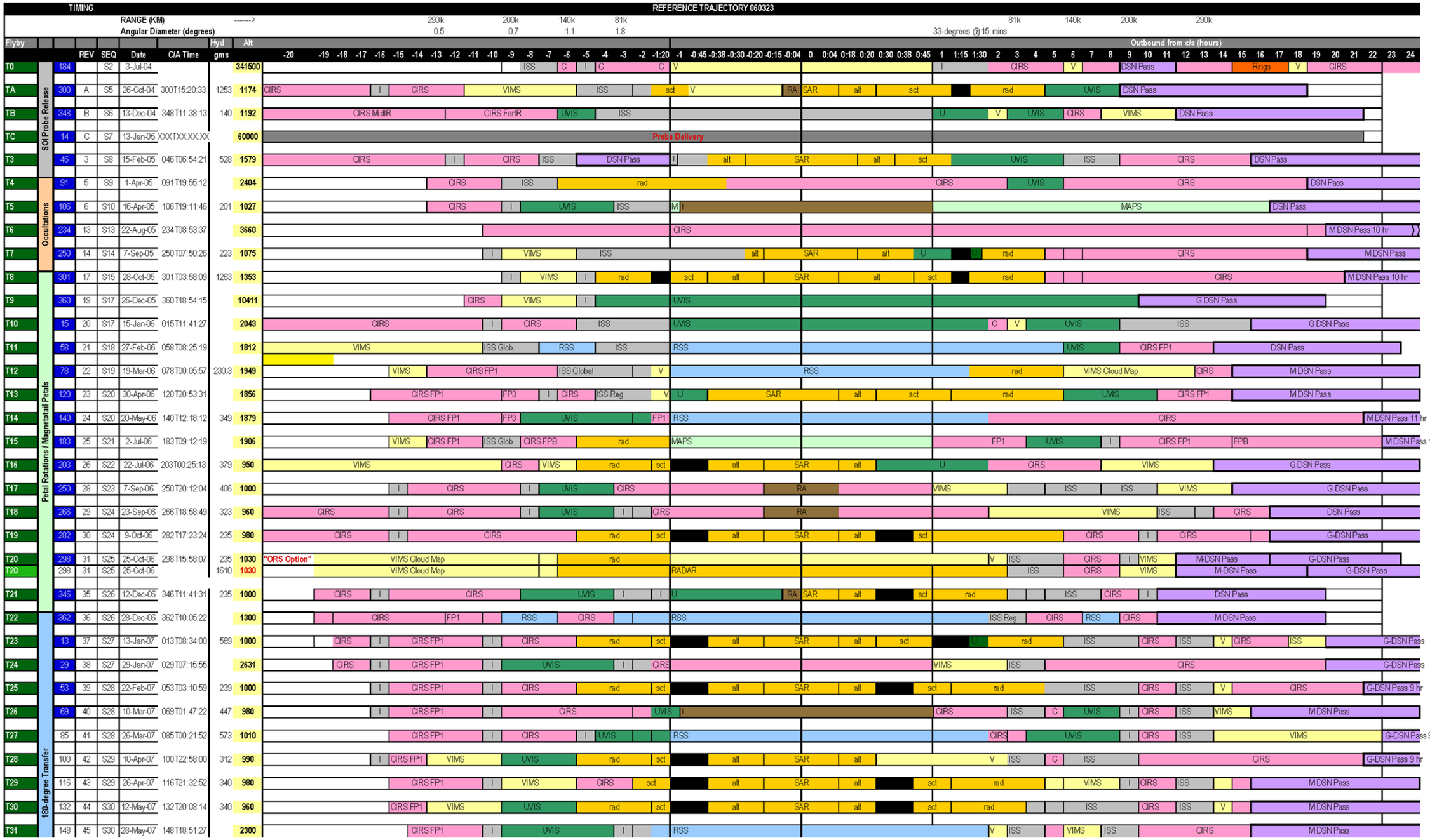

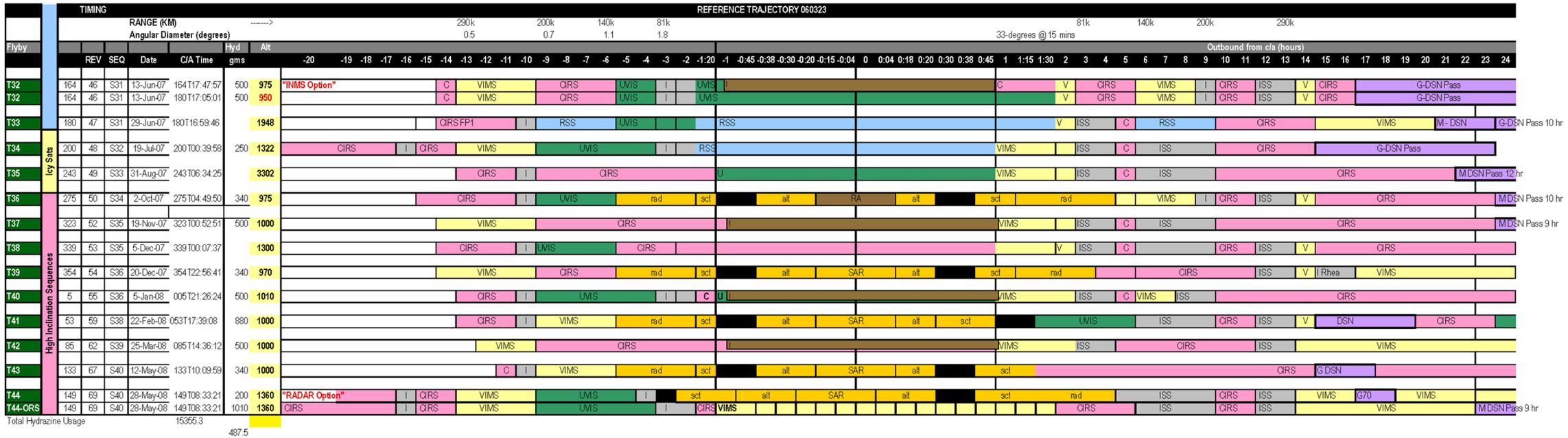

This document has been reviewed and determined not to contain export-controlled technical data.

Table 3-3. Titan coverage in the Prime Mission, Part II.

Flyby	O/B Lit?	In/Out	Occ	LST	S/C North Lat	S/C Long	Flyby	Event Name at Event Time Only	SCET Date (MM/DD/YYYY HH:MM:SS) ET	S/C Range (km)	S/C Altitude wrt Triaxial Ellipsoid (km)	S/C West Longitude SMEQPM Date (deg)	S/C Inertial Velocity (km/s)	S/C Radial Inertial Velocity (km/s)	S/C Tangential Inertial Velocity (km/s)	Central Body Angular Diameter (mrad)	Phase = Sun-Central_ Body-S/C Angle (deg)	Sun-S/C Central_ Body Angle (deg)	S/C Local True Solar Time wrt Central Body (hh:mm)	Subsolar Latitude wrt Central Body (deg)	Subsolar West Longitude wrt Central Body SMEQPM Date (deg)		C/A Phase				
	Illum.	Bound		Dec-Hr	(deg)																	Speed		Lat	Lon	Alt. Miles	Speed MPH
T0	UNLIT OUTBOUND ILLUMINATION	IN					T0																				
TA		IN		11.00	38.8		TA	TA_0ATI	15:31:09	3,749.50	1,174.50	88.5	6.06	-0.003	6.06	1514	90.9	89.1	16.44	-23.2	159.7						
TB		IN	U	10.47	59.1		TB	TB_0BTI	11:39:20	3,767.50	1,192.50	84.2	6.055	-0.001	6.055	1505	101.5	78.5	16.54	-22.8	157.9						
TC		IN		10.47	0.1		TC	TC_0CTI	11:13:03	62,578.60	60,003.60	-108.2	5.402	0	5.402	82.3	92.9	87.1	5.47	-22.5	158.7						
T3		IN		10.33	29.9		T3	T3_03TI	6:58:57	4,153.80	1,578.80	68.9	5.956	0	5.956	1337.3	98.5	81.5	17.48	-22.2	156						
T4		Out		5.27	33.4		T4	T4_05TI	20:06:20	4,978.40	2,403.40	118.7	5.926	0.006	5.926	1087.2	66.4	113.6	9.25	-21.8	79.9						
T5		Out		5.27	74		T5	T5_06TI	19:12:50	3,605.70	1,030.70	-87.7	6.061	0.007	6.061	1590.8	127.2	52.8	23.09	-21.6	79.7						
T6		Out		5.00	-58.5		T6	T6_13TI	8:54:41	6,367.40	3,792.40	102.7	5.858	0	5.858	832.7	43.1	136.9	10.09	-20.3	75						
T7		Out	U	4.93	-67		T7	T7_14TI	8:13:11	3,600.00	1,025.00	-51.9	6.071	0	6.071	1594	84.5	95.5	20.27	-20.1	75						
T8		IN		9.27	1.2		T8	T8_17TI	4:16:13	3,928.00	1,353.00	-113.9	5.937	-0.009	5.937	1429.8	104.8	75.2	4.59	-19.6	140.9						
T9		Out		3.00	-0.2		T9	T9_19TI	19:00:34	12,983.70	10,408.70	110.4	5.615	0.001	5.615	399.3	67.1	112.9	7.36	-18.9	44.6						
T10		IN	UV	8.47	0.1		T10	T10_20TI	11:42:31	4,618.20	2,043.20	-109.2	5.824	-0.001	5.824	1182.9	120.5	59.5	3.5	-18.6	128.5						
T11		Out		1.13	0		T11	T11_21TI	8:26:24	4,388.10	1,813.10	107.4	5.865	0.007	5.865	1254.2	92.5	87.5	5.49	-18.1	14.7						
T12		IN	R	6.40	0.1	250.6	T12	T12_22TI	0:07:01	4,526.10	1,951.10	-109.4	5.824	0	5.824	1210.4	148	32	1.48	-17.9	97.7	5.824	148.001	0.118	250.6	1210.559	13028.288
T13		Out	U	23.13	0.1	106.309	T13	T13_23TI	20:59:19	4,429.50	1,854.50	106.3	5.844	0.001	5.844	1240.7	120.7	59.3	3.5	-17.3	-15.9	5.844	120.659	0.105	106.309	1152.795	13073.028
T14	LIT	IN	R	4.40	0.4	249.898	T14	T14_24TI	12:19:15	4,453.90	1,878.90	-110.2	5.836	-0.007	5.836	1232.9	163	17	23.47	-17.1	66.7	5.836	163.019	0.405	249.898	1167.081	13055.132
T15	UN	Out		21.20	-0.4	105.537	T15	T15_25TI	9:21:52	4,480.80	1,905.80	105.6	5.834	0.003	5.834	1224.4	147.9	32.1	1.5	-16.5	-46.7	5.834	147.846	-0.387	105.537	1183.851	13050.658
T16	LIT OUTBOUND ILLUMINATION	IN	U	2.40	85.2	316.238	T16	T16_26TI	0:26:31	3,525.00	950	-43.8	5.966	0	5.966	1638.1	105.3	74.7	17.17	-16.3	35.6	5.966	105.33	85.164	316.238	590.0621	13345.942
T17		IN	V	2.27	23	56.74	T17	T17_28TI	20:13:52	3,525.00	950	56.6	5.985	-0.003	5.985	1638.1	44.7	135.3	10.28	-15.6	33.7	5.976	44.562	22.829	56.74	621.118	13368.312
T18		IN		2.27	71	357.002	T18	T18_29TI	18:55:47	3,525.00	950	-3.2	5.979	0	5.979	1638.1	89.9	90.1	14.25	-15.4	33.1	5.965	89.828	70.905	357.002	596.2733	13343.705
T19		IN		2.20	60.7	357.512	T19	T19_30TI	17:26:36	3,525.00	950	-2.5	5.983	0.001	5.983	1638.1	80.9	99.1	14.19	-15.2	32.4	5.967	80.959	60.76	357.512	608.6957	13348.179
T20		IN		2.13	7.5	44.339	T20	T20_31TI	15:54:41	3,525.00	950	43.3	5.993	0	5.993	1638.1	25.3	154.7	11.13	-15	31.7	5.968	24.54	6.119	44.339	639.7516	13350.416
T20		IN		2.13	7.5		T20	T20_31TI	15:54:41	3,525.00	950	43.3	5.993	0	5.993	1638.1	25.3	154.7	11.13	-15	31.7						
T21		IN	U	2.00	43.9	265.028	T21	T21_35TI	11:38:29	3,525.00	950	-93.9	5.969	0	5.969	1638.1	123.9	56.1	20.14	-14.3	29.7	5.947	124.839	43.358	265.028	621.118	13303.439
T22		IN		1.93	40.2	357.578	T22	T22_36TI	10:03:06	4,075.00	1,500.00	-2.4	5.927	0	5.927	1368	61.6	118.4	14.05	-14.1	28.9	5.931	61.965	40.593	357.578	807.4534	13267.647
T23		IN	U	1.93	30.5	357.929	T23	T23_37TI	8:36:47	3,525.00	950	-2.1	5.984	0	5.984	1638.1	53.1	126.9	14.01	-13.9	28.2	5.965	53.279	30.688	357.929	621.118	13343.705
T24		IN	V	1.87	32.8	330.07	T24	T24_38TI	7:14:38	5,301.30	2,726.30	-30.6	5.838	0	5.838	1014.4	72.4	107.6	15.52	-13.7	27.6	5.83	71.905	32.707	330.07	1634.161	13041.71
T25		Out		13.80	30.3	16.252	T25	T25_39TI	3:11:16	3,525.00	950	16	6.253	0	6.253	1638.1	161.2	18.8	0.35	-13.4	-155.1	6.232	161.262	30.322	16.252	621.118	13940.984
T26		Out	UV	13.80	31.7	357.872	T26	T26_40TI	1:47:56	3,525.00	950	-2.1	6.255	0	6.255	1638.1	149.5	30.5	1.45	-13.1	-155.7	6.237	149.501	31.677	357.872	608.6957	13952.169

Flyby		In/Out	Occ	LST	S/C North Lat	S/C Long	Flyby	Event Name at Event Time Only	SCET Date (MM/DD/YYYY HH:MM:SS) ET	S/C Range (km)	S/C Altitude wrt Triaxial Ellipsoid (km)	S/C West Longitude SMEQPM Date (deg)	S/C Inertial Velocity (km/s)	S/C Radial Inertial Velocity (km/s)	S/C Tangential Inertial Velocity (km/s)	Central Body Angular Diameter (mrad)	Phase = Sun-Central_ Body-S/C Angle (deg)	Sun-S/C Central_ Body Angle (deg)	S/C Local True Solar Time wrt Central Body (hh:mm)	Subsolar Latitude wrt Central Body (deg)	Subsolar West Longitude wrt Central Body SMEQPM Date (deg)	Speed	C/A Phase	Lat	Lon	Alt. Miles	Speed MPH
		Bound		Dec-Hr	(deg)																							
T27	LIT OUTBOUND ILLUMINATION	Out	R	13.73	41.1	357.983	T27	T27_41TI	0:22:37	3,525.00	950	-2	6.254	0	6.254	1638.1	144	36	1.42	-12.9	-156.4	6.232	144.128	40.926	357.983	627.3292	13940.984
T28		Out		13.67	50.4	358.148	T28	T28_42TI	22:57:29	3,525.00	950	-1.9	6.253	0	6.253	1638.1	137.2	42.8	1.39	-12.7	-157	6.234	137.392	50.149	358.148	614.9068	13945.458
T29		Out		13.67	59.7	358.369	T29	T29_43TI	21:32:33	3,525.00	950	-1.6	6.252	0.002	6.252	1638.1	129.6	50.4	1.35	-12.5	-157.7	6.234	129.805	59.381	358.369	608.6957	13945.458
T30		Out		13.60	68.9	358.894	T30	T30_44TI	20:08:43	3,525.00	950	-1.2	6.251	0.004	6.251	1638.1	121.4	58.6	1.31	-12.2	-158.3	6.236	121.701	68.637	358.894	596.2733	13949.932
T31		Out	R	13.60	76.8	359.961	T31	T31_45TI	18:51:53	5,000.70	2,425.70	0	6.129	0	6.129	1081.8	114.3	65.7	1.24	-12	-158.8	6.123	114.418	76.618	359.961	1428.571	13697.151
T32		Out	UV	13.53	84.5	0.903	T32	T32_46TI	17:47:35	3,525.00	950	1.2	6.252	0.001	6.252	1638.1	106.9	73.1	1.18	-11.8	-159.1	6.237	106.987	84.45	0.903	605.5901	13952.169
T32		Out	UV	13.53	84.5		T32	T32_46TI	17:47:35	3,525.00	950	1.2	6.252	0.001	6.252	1638.1	106.9	73.1	1.18	-11.8	-159.1						
T33		Out		13.53	8.1	294.887	T33	T33_47TI	17:03:44	4,519.10	1,944.10	-65	6.184	0	6.184	1212.5	95.6	84.4	5.43	-11.5	-159.1	6.172	95.521	8.233	294.887	1209.938	13806.764
T34		IN		18.80	1.3	244.652	T34	T34_48TI	0:38:50	3,875.40	1,300.40	-115.4	6.246	0	6.246	1453.5	34	146	14.07	-11.3	-83.6	6.232	34.322	1.284	244.652	821.118	13940.984
T35		Out	UV	11.53	63.5	110.569	T35	T35_49TI	6:36:02	5,787.30	3,212.30	110.9	6.101	0.005	6.101	922.2	87	93	16.01	-10.6	171.3	6.085	86.873	62.915	110.569	2050.932	13612.145
T36		Out		11.47	-59.9	108.983	T36	T36_50TI	4:55:02	3,525.00	950	109	6.326	0	6.326	1638.1	67.5	112.5	16.08	-10.2	171.1	6.302	67.364	-59.828	108.983	605.5901	14097.574
T37		Out		11.40	-22.1	117.366	T37	T37_52TI	0:59:26	3,525.00	950	117.6	6.319	0	6.319	1638.1	51.3	128.7	15.27	-9.5	169.6	6.292	51.304	-21.378	117.366	621.118	14075.204
T38		Out		11.40	-78.9	175.079	T38	T38_53TI	0:07:20	3,875.00	1,300.00	175	6.297	0	6.297	1453.7	69.7	110.3	11.37	-9.2	169.4	6.286	69.809	-78.969	175.079	807.4534	14061.782
T39		Out		11.33	-70.1	176.593	T39	T39_54TI	22:54:00	3,525.00	950	176.6	6.333	0	6.333	1638.1	61.3	118.7	11.29	-9	169	6.324	61.379	-70.168	176.593	602.4845	14146.788
T40		Out	UV	11.33	-12.2	130.409	T40	T40_55TI	21:26:00	3,525.00	950	130.7	6.322	0	6.322	1638.1	37.1	142.9	14.3	-8.7	168.3	6.307	37.506	-11.755	130.409	627.3292	14108.759
T41		Out	U	11.20	-34.7	151.727	T41	T41_59TI	17:40:12	3,525.00	950	151.8	6.358	0	6.358	1638.1	30.1	149.9	13	-8	166.9	6.329	30.226	-34.879	151.727	621.118	14157.973
T42		Out		11.13	-27.1	156.427	T42	T42_62TI	14:36:12	3,525.00	950	156.6	6.367	0	6.367	1638.1	21.3	158.7	12.35	-7.5	165.5	6.336	21.39	-27.171	156.427	621.118	14173.632
T43		Out		11.00	17.1	137.165	T43	T43_67TI	10:11:05	3,525.00	950	138	6.36	0	6.36	1638.1	34.8	145.2	13.42	-6.8	163.5	6.33	35.815	17.948	137.165	621.118	14160.21
T44		Out		10.93	12.4	150.137	T44-RADA	T44_69TI	8:34:18	3,923.10	1,348.10	149.5	6.315	0	6.315	1432	23.1	156.9	12.52	-6.6	162.7	6.29	21.221	10.663	150.137	844.7205	14070.73
T44-ORS		Out		10.93	12.4		T44-ORS	T44_69TI	8:34:18	3,923.10	1,348.10	149.5	6.315	0	6.315	1432	23.1	156.9	12.52	-6.6	162.7						
		Earth	R	INMS		Flank In		T45_78TI	2:20:35	6,555.00	3,980.00	165.4	6.115	0	6.115	807.4	6.5	173.5	11.37	-5.6	159.8						
		Solar	UV	+MAG		Tail																					
		Stellar	U	Hi-Res		Flank Out																					
						Nose																					

Flank In
Tail
Flank Out
Nose

Table 3-4. Titan coverage in the Equinox Mission, Part I.

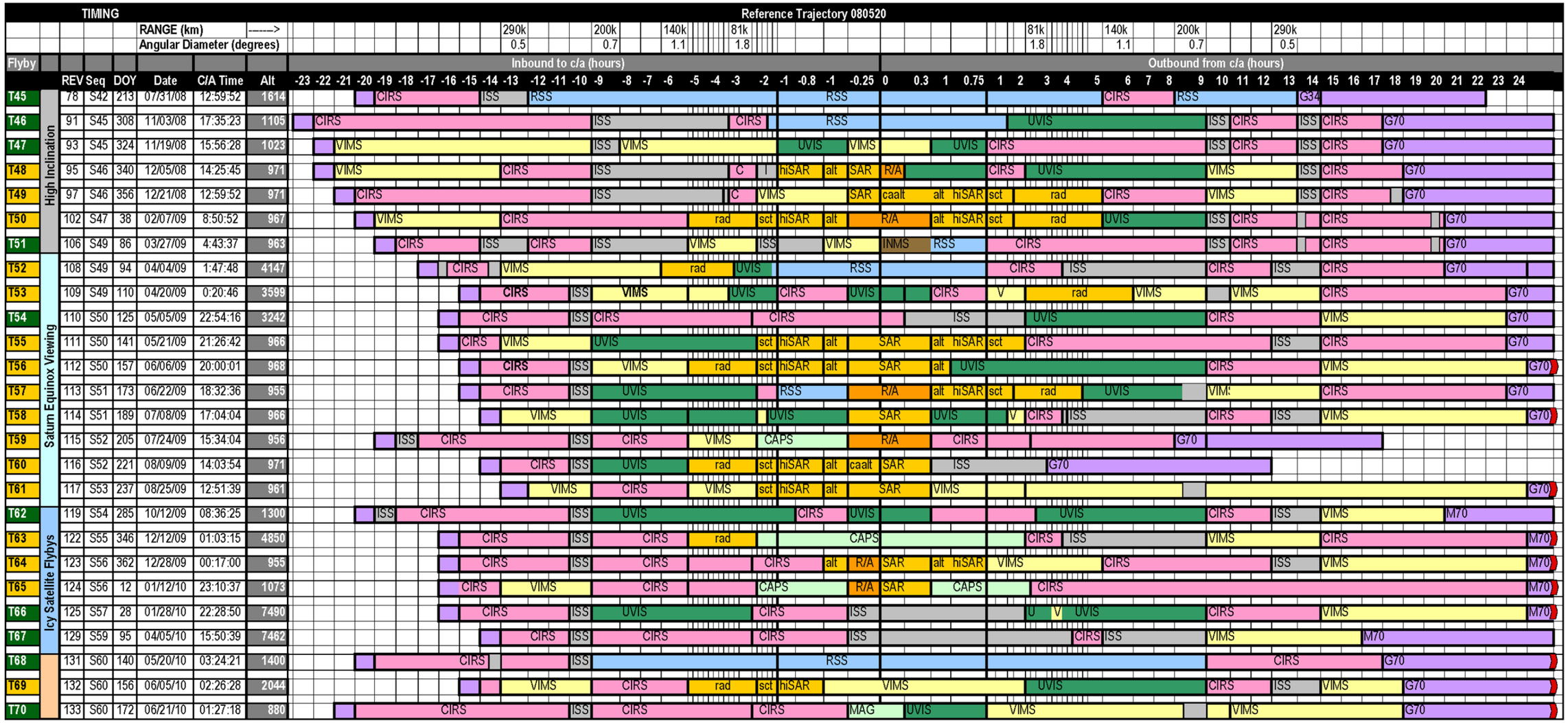

Table 3-5. Titan coverage in the Equinox Mission, Part II.

Flyby	O/B Lit?	In/Out	Occ	LST	Recover?	C/A LAT	C/A LON	Phase @C/A	Flyby	Vinf	Latitude	Longitude	Latitude	Longitude	Latitude	Longitude	Latitude	Longitude		DSN Pass 1 Start	DSN Pass 1 End	DSN Pass 2 Start	DSN Pass 2 End
	Illum.	Bound		Dec-Hr																			
T45	U	OUT		11		-43.31	195.4	48.7	T45	6.238									2008 JUL 31 02:12:56.13	02:12:56	08	213/02:12:56	T45 C/A
T46	U	OUT	R	10.50		-3.51	339.91	171	T46	6.262	-34.21	60.81	25.99	205.75	-39.46	61.98	23.31	278.08	2008 NOV 03 17:34:50.97	17:34:50	08	308/17:34:50	T46 C/A
T47	U	OUT	U	10.50		-21.56	177.6	28.1	T47	6.272									2008 NOV 19 15:56:01.87	15:56:01	08	324/15:56:01	T47 C/A
T48	U	OUT	U	10.50		-10.28	178.78	25	T48	6.269									2008 DEC 05 14:25:19.42	14:25:19	08	340/14:25:19	T48 C/A
T49	U	OUT		10.40		-43.85	236.81	83.6	T49	6.272									2008 DEC 21 12:59:29.29	12:59:29	08	356/12:59:29	T49 C/A
T50	H	OUT		10.20		-33.67	306.32	136	T50	6.276	-75.75	243.56	-5.75	216.46	-70.81	250.55	-10.84	264.16	2009 FEB 07 08:50:19.78	08:50:19	09	038/08:50:19	T50 C/A
T51	H	OUT		10.00		-30.27	234.8	86.6	T51	6.266									2009 MAR 27 04:43:12.27	04:43:12	09	086/04:43:12	T51 C/A
T52		IN	RU	22.00		-2.81	176.29	151	T52	5.768	63.83	247.63	-2.38	261.94	48.99	239.95	12.89	221.79	2009 APR 04 01:47:02.38	01:47:02	09	094/01:47:02	T52 C/A
T53		IN	UV	22.00		-7.74	177.61	148	T53	5.803	75.36	255.74	-17.09	265.84	60.34	239.55	-2.81	216.28	2009 APR 20 00:19:40.85	00:19:40	09	110/00:19:40	T53 C/A
T54		IN		22.00		-13.78	177.78	146	T54	5.812	81.46	269.93	-26.71	268.31	64.27	239.3	-11.54	213.53	2009 MAY 05 22:53:08.08	22:53:08	09	125/22:53:08	T54 C/A
T55		IN		22.00		-22.03	177.77	141	T55	5.978	80.49	35.33	-45.05	276.8	85.54	246.64	-36.94	201.67	2009 MAY 21 21:25:23.16	21:25:23	09	141/21:25:23	T55 C/A
T56		IN	U	22.00		-32.10	177.96	135	T56	5.978	78.7	40.79	-51.44	279.21	85.02	241.84	-43.6	198.49	2009 JUN 06 19:58:32.59	19:58:32	09	157/19:58:32	T56 C/A
T57		IN	R	22.00		-42.17	178.12	128	T57	5.979	78.14	42.96	-56.95	281.23	83.34	238.4	-49.8	195.62	2009 JUN 22 18:31:14.35	18:31:14	09	173/18:31:14	T57 C/A
T58		IN	U	22.00		-52.25	178.38	120	T58	5.961	79.67	42.27	-61.54	282.74	79.32	234.52	-54.88	193.74	2009 JUL 08 17:03:06.93	17:03:06	09	189/17:03:06	T58 C/A
T59		IN		22.00		-62.31	179.05	112	T59	5.975	82.87	39.02	-66.78	285.73	75.3	232.8	-61.58	189.42	2009 JUL 24 15:31:51.04	15:31:51	09	205/15:31:51	T59 C/A
T60		IN		21.90		-72.49	179.98	104	T60	5.977	86.99	263.39	-71.1	287.14	64.9	231.56	-67.06	188.02	2009 AUG 09 14:03:26.78	14:03:26	09	221/14:03:26	T60 C/A
T61	L	IN		21.80		-19.34	237.12	85.8	T61	5.968									2009 AUG 25 12:49:09.63	12:49:09	09	237/12:49:09	T61 C/A
T62		IN	UV	21.70		-61.47	68.805	99.3	T62	5.993	-11.9	228.72	-71.04	352.51	-11.54	230.16	-74.29	98.38	2009 OCT 12 08:32:33.10	08:32:33	09	285/08:32:33	T62 C/A
T63		OUT		17.00		33.20	114.78	124	T63	5.681									2009 DEC 12 00:54:38.83	00:54:38	09	346/00:54:38	T63 C/A
T64		OUT		17.00		81.77	172.17	85.9	T64	5.932									2009 DEC 28 00:09:45.50	00:09:45	09	362/00:09:45	T64 C/A
T65		OUT		17.00		-81.92	358.35	95.1	T65	5.928									2010 JAN 12 23:05:42.11	23:05:42	10	012/23:05:42	T65 C/A
T66		OUT	V	17.00		-52.75	297.07	69.1	T66	5.692									2010 JAN 28 22:26:59.43	22:26:59	10	028/22:26:59	T66 C/A
T67		IN		21		0.00	240.35	73	T67	5.674									2010 APR 05 15:50:26.48	15:50:26	10	095/15:50:26	T67 C/A
T68		OUT		16		-49.09	116.61	112	T68	5.878					-75.36	309.08	-86.73	44.42	2010 MAY 20 03:24:01.87	03:24:01	10	140/03:24:01	T68 C/A
T69		OUT		16		87.29	9.356	87.3	T69	5.832									2010 JUN 05 02:26:13.02	02:26:13	10	156/02:26:13	T69 C/A
T70		OUT		16		83.52	171.67	82.4	T70	5.93									2010 JUN 21 01:27:17.05	01:27:17	10	172/01:27:17	T70 C/A
		Earth					Flank In																

Table 3-6. Titan SAR coverage in the Solstice Mission, Part I.

TIMING — REFERENCE TRAJECTORY 091005

RANGE (km) ------> 290k 200k 140k 81k 81k 140k 200k 290k

Angular Diameter (degrees) 0.5 0.7 1.1 1.8 33-degrees @ 15 mins

Outbound from c/a (hours): -14 -13 -12 -11 -10 -9 -8 -7 -6 -5 -4 -3 -2 -1 -.75 -.5 -.25 0 0.25 .5 .75 1 2 3 4 5 6 7 8 9 10 11 12 13 15 15 16 17 18 19 20 21 22 23 24 25

Flyby		REV	SEQ	Date	DOY	C/A Time	Alt	Outbound from c/a (hours)
T71	In - 0	134	S61	07/07/10	188	00:22:45	1005	CIRS; rad; CAPS; R/A; CAPS; rad; VIMS
T72	In - 0	138	S63	09/24/10	267	18:38:41	8174.9	CIRS; VIMS; UVIS; VIMS
T73	In - 0	140	S64	11/11/10	315	13:37:02	7920.7	CIRS; CAPS; CIRS; VIMS; G70
T74	Equatorial - 1	145	S66	02/18/11	049	16:04:11	3650.7	CAPS; CIRS; C70
T75	Equatorial - 1	147	S67	04/19/11	109	05:00:39	10053	CAPS; UVIS; G70
T76	Equatorial - 1	148	S68	05/08/11	128	22:53:44	1873.2	CIRS; VIMS; UVIS; VIMS; CIRS; G70
T77	Equatorial - 1	149	S68	06/20/11	171	18:32:01	1358.7	UVIS; sct; HiSAR; alt; SAR; alt; HiSAR; sct; CIRS; VIMS; CIRS; G70
T78	Equatorial - 1	153	S70	09/12/11	255	02:50:05	5821.4	CIRS; V; UVIS; CAPS; UVIS; G70
T79	Equatorial - 1	158	S71	12/13/11	347	20:11:24	3585.8	CAPS; VIMS; CIRS; C70
T80	Equatorial - 1	159	S71	01/02/12	002	15:13:37	29415	CIRS; ISS; rad; VIMS; G70
T81	Equatorial - 1	160	S72	01/30/12	030	13:39:47	31131	CIRS; UVIS; ISS; UVIS; CIRS; G70
T82	Equatorial - 1	161	S72	02/19/12	050	08:43:17	3803.3	CIRS; ISS; CIRS; M70
T83	Equatorial - 1	166	S73	05/22/12	143	01:10:11	955	VIMS; CIRS; sct; HiSAR; alt; R/A; SAR; alt; HiSAR; sct; rad; VIMS; CIRS; M70
T84	Inclined - 1	167	S73	06/06/12	159	00:07:21	959	VIMS; CIRS; sct; HiSAR; alt; SAR; alt; HiSAR; sct; UVIS; CIRS; G70
T85	Inclined - 1	169	S74	07/24/12	206	20:03:08	1012	VIMS; CIRS; CIRS; VIMS; G70
T86	Inclined - 1	172	S75	09/26/12	270	14:35:39	956	CIRS; UVIS; CIRS; R/A; alt; CIRS; UVIS; CIRS
T87	Inclined - 1	174	S76	11/13/12	318	10:22:10	973	VIMS; NAV / INMS; VIMS; CIRS; G70
T88	Inclined - 1	175	S76	11/29/12	334	08:57:00	1014	CIRS; CIRS; VIMS; CIRS; C70; CIRS
T89	Inclined - 1	181	S77	02/17/13	048	01:56:37	1978.2	RSS; CIRS; M70
T90	Inclined - 1	185	S78	04/05/13	095	21:43:32	1400	CIRS; CIRS; VIMS; CIRS; M70
T91	Inclined - 1	190	S78	05/23/13	143	17:32:55	969.8	CIRS; rad; sct; HiSAR; alt; SAR; alt; HiSAR; sct; rad; ISS; CIRS; M70
T92	Inclined - 1	194	S79	07/10/13	191	13:21:48	964	ISS; CIRS; rad; sct; HiSAR; alt; SAR; alt; HiSAR; VIMS; ISS; G70
T93	Inclined - 1	195	S79	07/26/13	207	11:56:23	1400	ISS; CIRS; UVIS; ISS; VIMS; ISS; CIRS; VIMS; C70
T94	Inclined - 1	197	S80	09/12/13	255	07:43:57	1400	ISS; ISS; VIMS; CIRS; UVIS; VIMS; C70
T95	Inclined - 1	198	S80	10/14/13	287	04:56:28	961	ISS; CIRS; rad; ISS; HiSAR; alt; R/A; alt; HiSAR; sct; rad; CIRS; G70
T96	Inclined - 1	199	S81	12/01/13	335	00:41:19	1400	ISS; ISS; VIMS; CIRS; CIRS; VIMS; C70
T97	Inclined - 1	200	S82	01/01/14	001	21:59:42	1400	ISS; CIRS; UVIS; VIMS; CIRS; UVIS; CIRS; C70
T98	Inclined - 1	201	S82	02/02/14	033	19:12:39	1235.7	CIRS; ISS; rad; sct; HiSAR; alt; SAR; alt; HiSAR; sct; rad; CIRS; C70
T99	Inclined - 1	202	S82	03/06/14	065	16:26:48	1500	RSS; C70
T100	Inclined - 1	203	S83	04/07/14	097	13:41:15	963	ISS; CIRS; VIMS; CIRS; VIMS; INMS; CIRS; UVIS; CIRS; C70
T101	Inclined - 1	204	S83	05/17/14	137	16:12:16	2993.8	UVIS; WP; RSS; WP; CIRS; C70
T102	Inclined - 1	205	S84	06/18/14	169	13:28:25	3658.6	ISS; CIRS; RSS; CIRS; ISS; C70

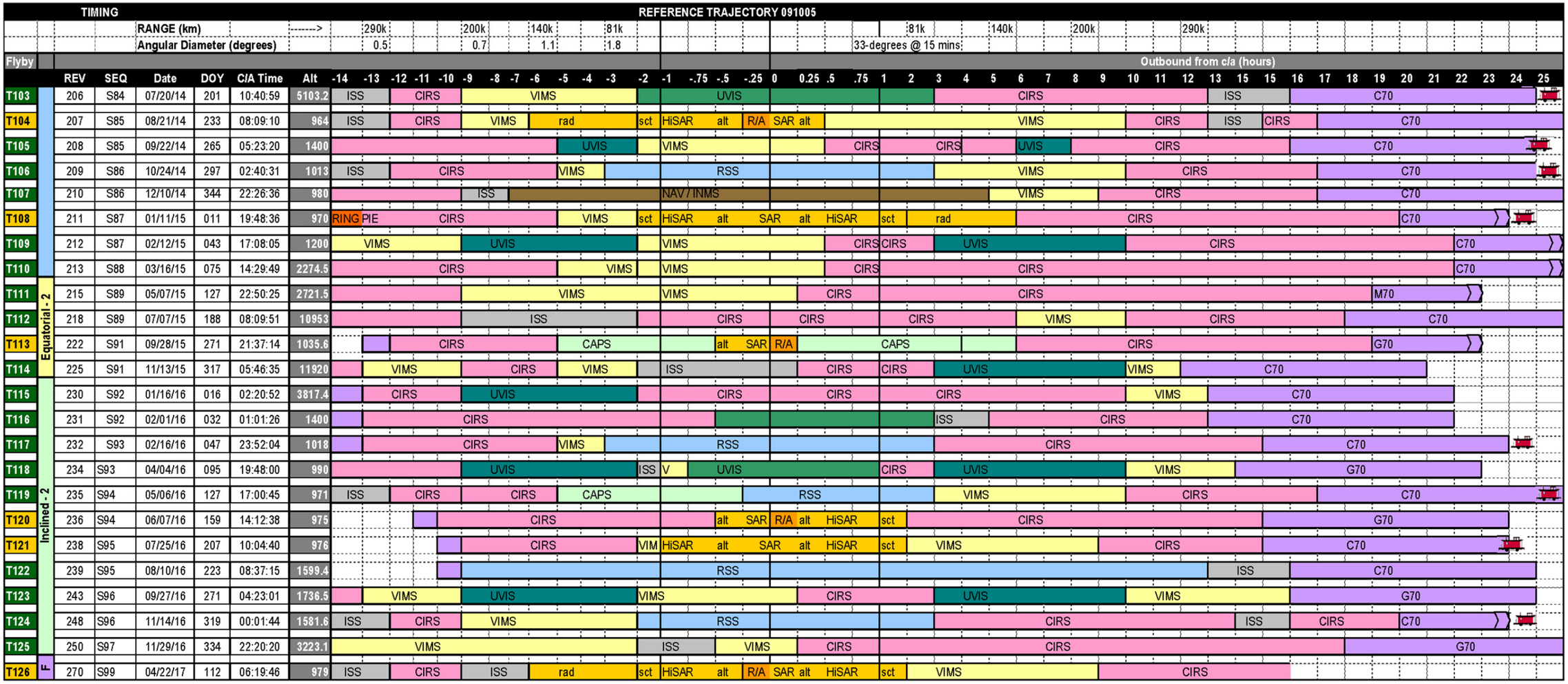
TIMING
REFERENCE TRAJECTORY 091005
RANGE (km) ------> 290k 200k 140k 81k 81k 140k 200k 290k
Angular Diameter (degrees) 0.5 0.7 1.1 1.8 33-degrees @ 15 mins
Flyby
Outbound from c/a (hours)
REV SEQ Date DOY C/A Time Alt
-14 -13 -12 -11 -10 -9 -8 -7 -6 -5 -4 -3 -2 -1 -.75 -.5 -.25 0 0.25 .5 .75 1 2 3 4 5 6 7 8 9 10 11 12 13 15 15 16 17 18 19 20 21 22 23 24 25
T103 206 S84 07/20/14 201 10:40:59 5103.2 ISS CIRS VIMS UVIS CIRS ISS C70
T104 207 S85 08/21/14 233 08:09:10 964 ISS CIRS VIMS rad sct HiSAR alt R/A SAR alt VIMS CIRS ISS CIRS C70
T105 208 S85 09/22/14 265 05:23:20 1400 UVIS VIMS CIRS CIRS UVIS CIRS C70
T106 209 S86 10/24/14 297 02:40:31 1013 ISS CIRS VIMS RSS VIMS CIRS C70
T107 210 S86 12/10/14 344 22:26:36 980 ISS NAV / INMS VIMS CIRS C70
T108 211 S87 01/11/15 011 19:48:36 970 RING PIE CIRS VIMS sct HiSAR alt SAR alt HiSAR sct rad CIRS C70
T109 212 S87 02/12/15 043 17:08:05 1200 VIMS UVIS VIMS CIRS CIRS UVIS CIRS C70
T110 213 S88 03/16/15 075 14:29:49 2274.5 CIRS VIMS VIMS CIRS CIRS C70
T111 215 S89 05/07/15 127 22:50:25 2721.5 VIMS VIMS CIRS CIRS M70
T112 218 S89 07/07/15 188 08:09:51 10953 ISS CIRS CIRS CIRS VIMS CIRS C70
T113 222 S91 09/28/15 271 21:37:14 1035.6 CIRS CAPS alt SAR R/A CAPS CIRS G70
T114 225 S91 11/13/15 317 05:46:35 11920 VIMS CIRS VIMS ISS CIRS CIRS UVIS VIMS C70
T115 230 S92 01/16/16 016 02:20:52 3817.4 CIRS UVIS CIRS CIRS CIRS VIMS C70
T116 231 S92 02/01/16 032 01:01:26 1400 CIRS ISS CIRS C70
T117 232 S93 02/16/16 047 23:52:04 1018 CIRS VIMS RSS CIRS C70
T118 234 S93 04/04/16 095 19:48:00 990 UVIS ISS V UVIS CIRS UVIS VIMS G70
T119 235 S94 05/06/16 127 17:00:45 971 ISS CIRS CIRS CAPS RSS VIMS CIRS C70
T120 236 S94 06/07/16 159 14:12:38 975 CIRS alt SAR R/A alt HiSAR sct CIRS G70
T121 238 S95 07/25/16 207 10:04:40 976 CIRS VIM HiSAR alt SAR alt HiSAR sct VIMS CIRS C70
T122 239 S95 08/10/16 223 08:37:15 1599.4 RSS ISS C70
T123 243 S96 09/27/16 271 04:23:01 1736.5 VIMS UVIS VIMS CIRS UVIS VIMS G70
T124 248 S96 11/14/16 319 00:01:44 1581.6 ISS CIRS VIMS RSS CIRS ISS CIRS C70
T125 250 S97 11/29/16 334 22:20:20 3223.1 VIMS ISS VIMS CIRS CIRS G70
T126 270 S99 04/22/17 112 06:19:46 979 ISS CIRS ISS rad sct HiSAR alt R/A SAR alt HiSAR sct VIMS CIRS
Equatorial - 2
Inclined - 2
F

Table 3-7. Titan SAR coverage in the Solstice Mission, Part II.

Flyby	O/B Lit? Illum.	In/Out Bound	C/A LAT (deg)	C/A LON	Phase @C/A (deg)	Flyby	Flyby	LST	Altitude	Sub S/C Lat	Sub S/C Long	Sub S/C Phase Angle	Date	Day	Day of Week	In/Out	Alt (km)	km/s	Phase (deg)	C/A Time
T71	LIT OUTBOUND ILLUMINATION	Out	-56.2	304	82	T71	134TI_T71	16.04	1005	-56.23	303.57	82	2010-188T00:22:45	07/07/10	Wed	Outbound	1005	5.9	82	188T00:22:45
T72		Out	-14.7	290	60	T72	138TI_T72	15.96	8174.9	-14.73	290.47	60	2010-267T18:38:41	09/24/10	Fri	Outbound	8174.9	5.7	60	267T18:38:41
T73		Out	-35.5	108	121	T73	140TI_T73	15.83	7920.7	-35.49	108.23	121	2010-315T13:37:02	11/11/10	Thu	Outbound	7920.7	5.6	121	315T13:37:02
T74		IN	0.7	245	62	T74	145TI_T74	20.62	3650.7	0.67	244.53	62	2011-049T16:04:11	02/18/11	Fri	Inbound	3650.7	5.8	62	049T16:04:11
T75		Out	0.1	107	101	T75	147TI_T75	14.25	10052.8	0.06	106.86	101	2011-109T05:00:39	04/19/11	Tue	Outbound	10052.8	5.6	101	109T05:00:39
T76		IN	0.0	248	47	T76	148TI_T76	19.79	1873.2	0.04	247.63	47	2011-128T22:53:44	05/08/11	Sun	Inbound	1873.2	5.9	47	128T22:53:44
T77		Out	0.1	106	73	T77	149TI_T77	12.25	1358.7	0.08	105.97	73	2011-171T18:32:01	06/20/11	Mon	Outbound	1358.7	5.9	73	171T18:32:01
T78		IN	-0.2	60.2	159	T78	153TI_T78	17.55	5821.4	-0.19	60.23	159	2011-255T02:50:05	09/12/11	Mon	Inbound	5821.4	5.8	159	255T02:50:05
T79		Out	7.7	291	100	T79	158TI_T79	12.79	3585.8	7.68	290.89	100	2011-347T20:11:24	12/13/11	Tue	Outbound	3585.8	5.8	100	347T20:11:24
T80		IN	-59.9	247	76	T80	159TI_T80	18.65	29415.3	-59.90	247.17	76	2012-002T15:13:37	01/02/12	Mon	Inbound	29415.3	5.5	76	002T15:13:37
T81		Out	-60.0	105	96	T81	160TI_T81	12.69	31130.6	-59.98	104.91	96	2012-030T13:39:47	01/30/12	Mon	Outbound	31130.6	5.4	96	030T13:39:47
T82		IN	9.8	61.4	143	T82	161TI_T82	18.34	3803.3	9.78	61.44	143	2012-050T08:43:17	02/19/12	Sun	Inbound	3803.3	5.8	143	050T08:43:17
T83		Out	72.3	128	71	T83	166TI_T83	13.62	955	72.34	127.99	71	2012-143T01:10:11	05/22/12	Tue	Outbound	955	5.9	71	143T01:10:11
T84		Out	39.1	282	75	T84	167TI_T84	13.64	959	39.10	282.47	75	2012-159T00:07:21	06/06/12	Thu	Outbound	959	5.9	75	159T00:07:21
T85		Out	61.6	149	58	T85	169TI_T85	13.69	1012	61.63	149.25	58	2012-206T20:03:08	07/24/12	Tue	Outbound	1012	5.9	58	206T20:03:08
T86		Out	62.4	200	47	T86	172TI_T86	13.44	956	62.45	200.09	47	2012-270T14:35:39	09/26/12	Wed	Outbound	956	5.9	47	270T14:35:39
T87		Out	11.4	125	68	T87	174TI_T87	13.22	973	11.44	124.68	68	2012-318T10:22:10	11/13/12	Tue	Outbound	973	5.9	68	318T10:22:10
T88		Out	25.6	148	44	T88	175TI_T88	13.24	1014	25.60	147.93	44	2012-334T08:57:00	11/29/12	Thu	Outbound	1014	5.9	44	334T08:57:00
T89		Out	20.7	155	35	T89	181TI_T89	13.19	1978.2	20.74	154.86	35	2013-048T01:56:37	02/17/13	Sun	Outbound	1978.2	5.8	35	048T01:56:37
T90		Out	-16.8	130	69	T90	185TI_T90	12.87	1400	-16.83	129.68	69	2013-095T21:43:32	04/05/13	Fri	Outbound	1400	5.8	69	095T21:43:32
T91		Out	46.2	240	50	T91	190TI_T91	12.86	969.8	46.16	239.52	50	2013-143T17:32:55	05/23/13	Thu	Outbound	969.8	5.9	50	143T17:32:55
T92		Out	37.0	234	46	T92	194TI_T92	12.91	964	37.01	234.47	46	2013-191T13:21:48	07/10/13	Wed	Outbound	964	5.9	46	191T13:21:48
T93		Out	28.2	249	58	T93	195TI_T93	12.84	1400	28.23	249.00	58	2013-207T11:56:23	07/26/13	Fri	Outbound	1400	5.8	58	207T11:56:23
T94		Out	17.1	206	21	T94	197TI_T94	12.50	1400	17.14	205.98	21	2013-255T07:43:57	09/12/13	Thu	Outbound	1400	5.8	21	255T07:43:57
T95		Out	8.2	205	25	T95	198TI_T95	12.40	961	8.19	205.26	25	2013-287T04:56:28	10/14/13	Mon	Outbound	961	5.9	25	287T04:56:28
T96		IN	-13.9	143	50	T96	199TI_T96	12.52	1400	-13.90	143.38	50	2013-335T00:41:19	12/01/13	Sun	Inbound	1400	5.8	50	335T00:41:19
T97		IN	-14.3	177	35	T97	200TI_T97	12.50	1400	-14.34	176.75	35	2014-001T21:59:42	01/01/14	Wed	Inbound	1400	5.8	35	001T21:59:42
T98		IN	-22.9	177	44	T98	201TI_T98	12.29	1235.7	-22.91	176.92	44	2014-033T19:12:39	02/02/14	Sun	Inbound	1235.7	5.9	44	033T19:12:39
T99		IN	-31.4	177	53	T99	202TI_T99	12.05	1500	-31.39	177.04	53	2014-065T16:26:48	03/06/14	Thu	Inbound	1500	5.8	53	065T16:26:48
T100		IN	-37.0	188	60	T100	203TI_T100	12.00	963	-37.02	187.92	60	2014-097T13:41:15	04/07/14	Mon	Inbound	963	5.9	60	097T13:41:15
T101		Out	-37.0	162	158	T101	204TI_T101	23.97	2993.8	-37.02	161.61	158	2014-137T16:12:16	05/17/14	Sat	Outbound	2993.8	5.7	158	137T16:12:16

Flyby	O/B Lit?	In/Out	C/A LAT	C/A LON	Phase @C/A	Flyby	Flyby	LST	Altitude	Sub S/C Lat	Sub S/C Long	Sub S/C Phase Angle	Date	Day	Day of Week	In/Out	Alt (km)	km/s	Phase (deg)	C/A Time
	Illum.	Bound	(deg)		(deg)															
T102	UNLIT OUTBOUND ILLUMINATION	Out	-36.6	178	165	T102	205TI_T102	23.77	3658.6	-36.58	178.46	165	2014-169T13:28:25	06/18/14	Wed	Outbound	3658.6	5.6	165	169T13:28:25
T103		Out	-31.5	179	171	T103	206TI_T103	23.76	5103.2	-31.52	178.77	171	2014-201T10:40:59	07/20/14	Sun	Outbound	5103.2	5.6	171	201T10:40:59
T104		Out	34.2	360	12	T104	207TI_T104	23.87	964	34.23	359.83	12	2014-233T08:09:10	08/21/14	Thu	Outbound	964	5.8	12	233T08:09:10
T105		Out	43.5	0.31	21	T105	208TI_T105	23.90	1400	43.53	0.31	21	2014-265T05:23:20	09/22/14	Mon	Outbound	1400	5.8	21	265T05:23:20
T106		Out	37.1	322	31	T106	209TI_T106	23.71	1013	37.15	322.33	31	2014-297T02:40:31	10/24/14	Fri	Outbound	1013	5.8	31	297T02:40:31
T107		Out	53.8	57	56	T107	210TI_T107	23.35	980	53.85	56.97	56	2014-344T22:26:36	12/10/14	Wed	Outbound	980	5.8	56	344T22:26:36
T108		Out	69.0	1.16	46	T108	211TI_T108	23.35	970	69.05	1.16	46	2015-011T19:48:36	01/11/15	Sun	Outbound	970	5.8	46	011T19:48:36
T109		Out	78.4	3.14	55	T109	212TI_T109	23.49	1200	78.45	3.14	55	2015-043T17:08:05	02/12/15	Thu	Outbound	1200	5.8	55	043T17:08:05
T110		Out	75.0	94	70	T110	213TI_T110	23.52	2274.5	74.99	94.02	70	2015-075T14:29:49	03/16/15	Mon	Outbound	2274.5	5.7	70	075T14:29:49
T111		IN	-1.1	67	34	T111	215TI_T111	6.23	2721.5	-1.13	66.96	34	2015-127T22:50:25	05/07/15	Thu	Inbound	2721.5	5.7	34	127T22:50:25
T112		Out	0.6	294	78	T112	218TI_T112	0.92	10953.1	0.59	293.86	78	2015-188T08:09:51	07/07/15	Tue	Outbound	10953.1	5.6	78	188T08:09:51
T113		IN	-1.1	61.4	42	T113	222TI_T113	6.71	1035.6	-1.11	61.37	42	2015-271T21:37:14	09/28/15	Mon	Inbound	1035.6	5.8	42	271T21:37:14
T114		Out	-14.4	122	92	T114	225TI_T114	2.55	11919.7	-14.35	122.47	92	2015-317T05:46:35	11/13/15	Fri	Outbound	11919.7	5.5	92	317T05:46:35
T115		Out	-8.4	300	99	T115	230TI_T115	2.67	3817.4	-8.45	300.41	99	2016-016T02:20:52	01/16/16	Sat	Outbound	3817.4	5.7	99	016T02:20:52
T116		Out	-83.6	175	120	T116	231TI_T116	2.63	1400	-83.59	175.35	120	2016-032T01:01:26	02/01/16	Mon	Outbound	1400	5.8	120	032T01:01:26
T117		Out	-38.7	285	122	T117	232TI_T117	2.59	1018	-38.72	284.68	122	2016-047T23:52:04	02/16/16	Tue	Outbound	1018	5.9	122	047T23:52:04
T118		Out	-63.0	245	138	T118	234TI_T118	2.24	990	-63.01	245.20	138	2016-095T19:48:00	04/04/16	Mon	Outbound	990	5.9	138	095T19:48:00
T119		Out	-59.9	178	138	T119	235TI_T119	2.08	971	-59.94	178.16	138	2016-127T17:00:45	05/06/16	Fri	Outbound	971	5.9	138	127T17:00:45
T120		Out	-36.6	147	124	T120	236TI_T120	2.18	975	-36.58	146.52	124	2016-159T14:12:38	06/07/16	Tue	Outbound	975	5.9	124	159T14:12:38
T121		Out	-7.0	129	101	T121	238TI_T121	2.24	976	-6.99	129.09	101	2016-207T10:04:40	07/25/16	Mon	Outbound	976	5.9	101	207T10:04:40
T122		Out	9.3	126	92	T122	239TI_T122	2.15	1599.4	9.31	126.02	92	2016-223T08:37:15	08/10/16	Wed	Outbound	1599.4	5.8	92	223T08:37:15
T123		Out	21.0	126	88	T123	243TI_T123	1.76	1736.5	20.97	125.96	88	2016-271T04:23:01	09/27/16	Tue	Outbound	1736.5	5.8	88	271T04:23:01
T124		Out	36.2	122	80	T124	248TI_T124	1.72	1581.6	36.21	121.98	80	2016-319T00:01:44	11/14/16	Mon	Outbound	1581.6	5.8	80	319T00:01:44
T125		Out	41.4	128	82	T125	250TI_T125	1.81	3223.1	41.43	127.73	82	2016-334T22:20:20	11/29/16	Tue	Outbound	3223.1	5.7	82	334T22:20:20
T126		Out	66.4	94.3	61	T126	270TI_T126	1.32	979	66.42	94.35	61	2017-112T06:19:46	04/22/17	Sat	Outbound	979	5.8	61	112T06:19:46
		Earth		Flank In																
		Solar		Tail																
		Stellar		Flank Out																
				Nose																

3.5 Other RADAR Coverage

3.5.1 Rings

Radiometry at 2-cm wavelength provides a unique window on the physical and compositional properties of Saturn's rings. The dominant emission from the rings at this wavelength is scattered disk thermal emission. Pure ice is basically transparent, so that the measurements are sensitive to trace amounts of contaminants. The microwave approach uniquely samples bulk rather than surface properties of particles. The RADAR team's objectives at Saturn are therefore to investigate the structural and compositional properties of the rings by determining their scattering properties from passive observations at different aspects in relation to the disk, and by searching for thermal properties in evidence of intrinsic thermal emission. Sets of prioritized observations were developed and are shown in Table 3-8.

Table 3-8. Ring objectives and observations.

REV	REQUEST	DATE	DATA RECEIVED (KB)
S10	RADAR_006RI_PO8RINGS001_PRIME	12-Apr-05	31942.8
S14	RADAR_014RI_PO8RINGS001_PRIME	3-Sep-05	21987
S23	RADAR_028RI_PO1RINGS002_PRIME	10-Sep-06	152038
S23	RADAR_028RI_045MATCH001_PRIME	11-Sep-06	18065.2
S27	RADAR_038RI_038MATCH1001_PRIME	27-Jan-07	35910
S27	RADAR_038RI_038MATCH2001_PRIME	4-Feb-07	32991.6
S28	RADAR_039RI_39R1MATCH001_PRIME	23-Feb-07	28302.4
S34	RADAR_050RI_PO8RINGS001_PRIME	28-Sep-07	88403.2
S34	RADAR_051RI_PO2RINGS002_PRIME	23-Oct-07	8831.2
S35	RADAR_052RI_PO8RINGS001_PRIME	14-Nov-07	3576565
S35	RADAR_052RI_PO2RINGS002_PRIME	16-Nov-07	8626
S40	RADAR_066RI_046MATCH001_PRIME	4-May-08	46420.8

3.5.2 Icy Satellites

The Cassini RADAR obtained scatterometry and radiometry observations of Saturn's icy satellites (Mimas, Dione, Enceladus, Tethys, Phoebe, Hyperion, Iapetus, Rhea). RADAR scatterometry observations measured the object's radar reflectivity and aided in constraining composition and structure of the top decimeter of the surface of the icy satellites (Ostro et al. 2006, 2010). Radiometric observations will help constrain the thermal properties of the surfaces and search for "hot spots" if there is cryovolcanic activity, as has been proposed for Enceladus. A list of RADAR icy satellites observations is given in Table 3-9.

During most of the icy satellite observations the RADAR operates at very high ranges of 50,000 to 420,000 km where SAR and altimetry observations are not possible due to low signal levels. Some HiSAR data is available for three icy satellites including one observation each for Iapetus, Rhea, and Enceladus. An additional observation including HiSAR and nominal altitude SAR of Enceladus is planned to occur in November 2012. For all the other icy satellite observations, only disk integrated scatterometry and radiometry data are collected. In some cases, the central beam is about half the apparent

Table 3-9. Icy satellites observations.

REV	REQUEST	DATE	DATA RECEIVED (KB)
S01	RADAR_000PH_SCATTRAD001_PRIME	11-Jun-04	2705.6
S01	RADAR_000PH_2SCATTRAD001_PRIME	11-Jun-04	285030.4
S06	RADAR_00BDI_SCATTRADL002_PRIME	15-Dec-04	S/C Commanding Error*
S07	RADAR_00BIA_SCATTRADL001_PRIME	31-Dec-04	318295.6
S07	RADAR_00CIA_SCATTRADL001_PRIME	1-Jan-05	1259213.6
S08	RADAR_003EN_SCATTRAD001_PRIME	17-Feb-05	495953.2
S09	RADAR_004EN_SCATTRAD001_PRIME	9-Mar-05	397586.4
S12	RADAR_011RH_SCATTRADL001_PRIME	14-Jul-05	212123.6
S14	RADAR_015TE_SCATTRAD003_PRIME	24-Sep-05	248960.8
S14	RADAR_015HY_SCATTRAD001_PRIME	26-Sep-05	392669.2
S15	RADAR_016DI_SCATTRAD001_PRIME	11-Oct-05	314343.6
S16	RADAR_017IA_SCATTRAD001_PRIME	12-Nov-05	321898
S16	RADAR_018RH_SCATTRAD001_PRIME	27-Nov-05	698675.6
S18	RADAR_021TE_SCATTRADL001_PRIME	25-Feb-06	290570.8
S19	RADAR_022RH_SCATTRAD001_PRIME	21-Mar-06	738347.6
S22	RADAR_027DI_SCATTRADL001_PRIME	16-Aug-06	147956.8
S22	RADAR_027RH_SCATTRADL001_PRIME	17_aug-06	157783.6
S23	RADAR_028EN_SCATTRAD003_PRIME	10-Sep-06	152038
S25	RADAR_032EN_SCATTRADL001_PRIME	9-Nov-06	144567.2
S25	RADAR_033DI_SCATTRAD002_PRIME	21-Nov-06	163826
S27	RADAR_039HY_SCATTRADL001_PRIME	15-Feb-07	246278
S30	RADAR_045RH_SCATTRADL001_PRIME	27-May-07	259500
S30	RADAR_045RH_SCATTRADL002_PRIME	27-May-07	
S31	RADAR_047MI_SCATTRAD001_PRIME	28-Jun-07	264.3
S31	RADAR_047RH_SCATTRADL001_PRIME	28-Jun-07	224
S32	RADAR_048TE_SCATTRADL001_PRIME	20-Jul-07	206172.8
S33	RADAR_049RH_SCATTRAD001_PRIME	29_aug-07	225157.6
S33	RADAR_049IA_SCATTRAD003_PRIME	9-Sep-07	561237.2
S33	RADAR_049IA_SCATTRAD004_PRIME	9-Sep-07	291482.8
S33	RADAR_049IA_SCATTRAD001_PRIME	10-Sep-07	330888.8
S33	RADAR_049IA_SCATTRAD002_PRIME	11-Sep-07	155397.2
S33	RADAR_049IA_SCATTRAD005_PRIME	12-Sep-07	S/C Safing Incident**
S34	RADAR_050DI_SCATTRAD001_PRIME	30-Sep-07	274975.6
S34	RADAR_050EN_SCATTRAD001_PRIME	30-Sep-07	115178
S35	RADAR_053MI_SCATTRAD001_PRIME	3-Dec-07	297965.6
S38	RADAR_061EN_SCATTRAD001_PRIME	12-Mar-08	243815.6
S38	RADAR_061EN_SCATTRAD002_PRIME	12-Mar-08	199644.4
S39	RADAR_064MI_SCATTRAD001_PRIME	11-Apr-08	222700
S44	RADAR_088EN_SCATTRAD001_PRIME	9-Oct-08	402131
S54	RADAR_120EN_SCATTRAD001_PRIME	2-Nov-09	444828
S57	RADAR_126MI_SCATTRAD001_PRIME	13-Feb-10	190402.8
S58	RADAR_127RH_SCATTRAD001_PRIME	2-Mar-10	428822.4

* This activity did not get downlinked.

** Instrument execution block did not execute.

angular size of the target body, and a multipoint observation is conducted to look for large-scale variation in surface properties. In other cases, the central beam is larger in angular extent than the target body, and a single stare centered on the target is conducted.

Radiometry data are collected during the scatterometer integrations and also during a small raster scan centered on the target body. The raster scan provides on- and off-target measurements to help calibrate the radiometer. The scatterometer integrations usually involve transmitting a single frequency carrier and then recording the Doppler-shifted and spread echoes from the target for five to twenty minutes. Even though the transmitted pulses are very narrow bandwidth tones, the received echo power is spread out in the frequency domain by Doppler variation, which arises from a combination of the relative motion of the spacecraft and the rotation of the target body. For the icy satellites, the Doppler variation ranges from a few hundred Hz up to about 4 kHz. The pulsed nature of the transmit events also introduces grating lobes spaced at the pulse repetition frequency (PRF) (Ostro et al. 2006). This causes the echo power spectrum to be repeated at intervals of the PRF. To make processing easier, the PRF is set to a frequency higher than the predict Doppler spread of the target body so that the central spectral peak is separated from the grating lobes, which shows the natural variation of the echo power over the target body. The measured echoes are processed in the frequency domain to provide an echo power spectrum and a low-noise disk-integrated radar cross-section measurement. In some cases a chirped pulse is transmitted to allow for range processing. Range processing is limited by the range spread within the antenna beam footprint projected on the surface of the icy satellite. If the range spread is large enough to cover the pulse repetition interval, then different ranges within the beam footprint will be ambiguous making interpretation of range-Doppler images difficult. Low SNR at the typical ranges of RADAR icy satellite observations can also make range-Doppler results less useful. For these reasons, chirped pulses are used only when there is sufficient predicted SNR and some ambiguity free illuminated area.

3.5.3 Saturn

Cassini radiometry data can be used to analyze the emission from Saturn at the wavelength of ~2 cm, which is entirely thermal in origin and originates in the ammonia cloud region since the dominant atmospheric absorber is ammonia vapor. Inside of observation distances of 6 Saturn radii (Rs [1 Rs ~60,000 km: Titan orbits at 20 Rs]), the spatial resolution (of ~2600 km) is comparable to the horizontal scale of the mid-latitude jets, planetary waves, and other features (cf. Sromovsky et al. 1983, Allison et al. 1990). The observed planetary wave structure will provide an important diagnostic of the static stability at deeper atmospheric levels. Ammonia variations will provide an indication of upwelling and downwelling and possibly trace the “potential vorticity” field (cf. Allison 2000). Data collected are listed in Table 3-10.

Table 3-10. Saturn observations.

REV	REQUEST	DATE	DATA RECEIVED (KB)
S14	RADAR_015SA_GLOBALMAP001_PRIME	23-Sep-05	34291.2
S14	RADAR_015SA_GLOBALMAP002_PRIME	23-Sep-05	
S14	RADAR_015SA_GLOBALMAP003_PRIME	24-Sep-05	7942
S37	RADAR_058SA_2POLAR001_PRIME	8-Feb-08	28690
S38	RADAR_059SA_1POLAR001_PRIME	20-Feb-08	267398.4
S46	RADAR_095SA_NORTHPOL001_PRIME	1-Dec-08	112001.2
S46	RADAR_095SA_SOUTHPOL001_PRIME	3-Dec-08	86784.4
S46	RADAR_097SA_NORTHPOL001_PRIME	17-Dec-08	114592.8
S46	RADAR_097SA_SOUTHPOL001_PRIME	18-Dec-08	123758.3
S54	RADAR_119SA_GLOBALMAP001_PRIME	13-Oct-09	44718.4
S55	RADAR_122SA_GLOBALMAP002_PRIME	9-Dec-09	51984
S61	RADAR_135SA_GLOBALMAP001_PRIME	24-Jul-10	50669
S67	RADAR_146SA_GLOBALMAP001_PIE	20-Mar-11	expecting

4 RADAR Data Product Overview

The RADAR instrument collects returns, digitizes, and delivers digital data to the spacecraft. Together with other instruments' data, they are stored on the spacecraft Solid State Recorder (SSR) and downlinked, generally at the next scheduled communication opportunity with a DSN complex (Imbriale 2003) where digital data is extracted and returned to the Cassini operations center at JPL. Individual instrument data are separated and stored on the Cassini Distributed Object Manager (DOM).

RADAR telemetry is extracted from the Cassini DOM and processed at JPL to produce time ordered RADAR frames (Level 0). For routine processing, the data extraction occurs after the Project has produced the best possible filled and cleaned telemetry files, approximately 2 days after downlink. This Level 0 data is then further processed to produce three types of Cassini RADAR data products: Burst Ordered Data Products (BODPs) (Level 1), BIDRs (Level 2), and Digital Map Products (DMPs) (Levels 3 and above). BODPs and BIDRs are produced at JPL; DMPs are produced at the United States Geological Survey (USGS) in Flagstaff, Arizona. BODPs are data sets at various stages of processing that are organized as time-ordered records for each burst. The BIDR and DMP data sets are downstream from production of BODPs. Production of the DMPs also makes use of several types of auxiliary data files (altimeter and radiometry summary files and SARTopo files) produced at JPL that are not currently being archived. When these intermediate products are added to the archive, the Data Users Guide will be updated to provide a description of them. Each type of product is briefly described here and in the software interface specification (SIS) documents contained in each archived PDS volume.

Like all planetary data, Cassini RADAR data are archived in NASA's PDS (http://pds.jpl.nasa.gov/) (see Section 9). PDS is organized by nodes, each of which archives a science discipline (Atmospheres, Geosciences, Planetary Plasma Interactions, Rings and Small Bodies, Engineering, Imaging, and Navigation and Ancillary Data). Cassini RADAR data are archived in the Imaging Node, physically located at the USGS facility in Flagstaff, and on the Internet at http://img.pds.nasa.gov/. The Cassini RADAR Science Team delivers data products to the PDS at regular intervals throughout the mission lifetime, typically within one year of data acquisition. At the Imaging node web site all data products may be downloaded, and search engines are available to aid in locating those of interest. The governing documents for all Radar data products are the SISs, which contain detailed information about each product. These are: BIDR SIS V.2.0, April 2008; BODP SIS V2.0, June 2008, Volume SIS V.1.5, May 2008; and Radar Map Products Volume SIS V1.0, August 2004. They are available in the DOCUMENTS directory of each archived PDS data volume.

4.1 Burst Ordered Data Products (BODPs)

BODPs are data files with a data set IDs of CO-SSA-RADAR-3-?BDR-V1.0, where the "?" can be S, L, or A. They include engineering telemetry, radar operational parameters, raw echo data, instrument viewing geometry, and calibrated science data (ref BODP SIS). BODP files contain time-ordered fixed length records. BODP come in three different record formats:

- Short Burst Data Record (SBDR)
- Long Burst Data Record (LBDR)
- Altimeter Burst Data Record (ABDR), plus the ABDR summary file

For each data pass, the ground processing occurs in the following manner: an SBDR record is produced for every burst throughout the pass; an LBDR file (or up to two files depending on data volume) is produced which only contains records for the middle portion of the pass during which the transmitter was on; and an ABDR file is produced which contains records for only the periods (typically one inbound, one outbound) in which the radar is in altimeter mode. One data field in each record is a burst identifier, which uniquely distinguishes a burst from all other bursts in the mission; records in different files that correspond to the same burst have the same burst ID.

All of the data types are in tables, with rows corresponding to a single time period referred to as a burst. Each record corresponds to the full set of relevant data for an individual radar burst. The Cassini RADAR is operated in "burst mode," where the radar transmits a number of pulses in sequence, then waits to receive the return signals. For the BODP, "burst" refers to an entire measurement cycle including transmit, receipt of echo, and radiometric (passive) measurements of the naturally occurring radiation emitted from the surface. Even when the transmitter is turned off and only passive measurements are made, the measurement cycle is still referred to as a burst.

4.1.1 Product Overview

Burst Ordered Data Products (BODPs) are fixed header length, fixed record length files. The header is an attached PDS label. All of the BODPs contain binary data. Radar values have all been decoded and are stored in 32-bit floating point format; other ancillary data is stored as 32-bit integers, 32-bit floating point or 64-bit IEEE floating point as appropriate (ref: BODP SIS), or fixed length character strings for text variables such as time tags.

To read a particular data value from a particular data field, the header length, the record size, and the byte offset of the data field within the record must be known. As a UTC time tag is included in each record, the data one reads can be restricted to a particular time interval. To further facilitate temporal segmentation of the data, a Cassini RADAR Transition (CRT) file is provided for each Titan pass. This file maintains a temporally ordered list of the times and transition types for all radar mode transitions, such as radiometry to scatterometry mode switches. The Volume SIS contains more information about CRT file formats.

4.1.2 Short Burst Data Record (SBDR)

The SBDR includes instrument telemetry and calibrated science data in burst order. It excludes raw echo data and altimeter profiles. For every Titan RADAR pass, an SBDR record is produced for every burst throughout the pass (e.g., for 43200 bursts, record size is 1273 bytes, and file size is 55 MB). The SBDR data record is divided into three consecutive segments from three different levels of processing: 1) the engineering data segment, 2) the intermediate-level data segment (mostly spacecraft geometry), and 3) the science data segment (antenna temperature, backscatter, surface height, measurement geometry, etc.). Three geophysical quantities are in the science data segment: the NRCS σ_0 obtained from the scatterometer measurement; the antenna

temperature determined from the radiometer measurement; and the measured distance from the gravitational center of the body (local radius). The antenna temperature is computed for every burst; the NRCS is computed for all bursts with active-mode data with the exception of distant observations for which a single burst is insufficient to obtain a useful measurement. For every burst in altimeter mode, the local radius is estimated. In addition, ancillary parameters including intermediate values (e.g., receiver temperature, total echo energy, system gain, etc.), analytical estimates of the standard deviation of the residual error in each of the three primary measurements, and measurement geometry are computed. In order to ease the identification of surface features from NRCS maps, the effects of incidence angle are removed by a global average model to compute a "corrected" version of NRCS. For Titan passes, the raw backscatter values have been multiplied by the function f(I),

where I is the incidence angle,

and f(I) = 0.2907/(f1(I)+f2(I)+f3(I)),

for f1(I)=2.8126*(cos(I)^4+893.9677*sin(I)^2)^(-1.5),

f2(I)=0.5824*(cos(I)^4+34.1366*sin(I)^2)^(-1.5),

and f3(I)=0.3767*cos(I)^1.9782.

For targets other than Titan, incidence angle corrections have only been computed for observations in which we have SAR data. In those cases the specific equation for the correction is documented in the PDS label for the incidence angel corrected BIDR files (filename prefix = BIF). In addition, SAR ancillary data are included in the science data segment when available. The SAR images themselves are stored in the BIDR files.

For active- and passive-mode measurements, measurement geometry information is included. Separate data fields for each are reported, as differences in passive- and active-mode measurement times can cause the two cases to differ, although some active- and passive-mode quantities are likely to be identical (e.g., polarization orientation angle). Active-mode geometry is calculated for the time halfway between the midpoint of the transmission and the midpoint of the active-mode receiver window. Passive geometry is calculated for the time at the midpoint of the passive receiver window (summed radiometer windows). For each case, the full set of measurement geometry includes the polarization orientation angle, emission/incidence angle, azimuth angle, the measurement centroid, and four points on the 3-dB gain contour of the measurement. The centroid and contour points are in latitude and longitude, using the west longitude positive planetodetic coordinate system. Since Titan is treated as a sphere, these coordinates are identical to the standard planetographic coordinates used in the SAR imagery (BIDR) data set. The rectangular coordinates (X,Y, and Z) of this system are defined such that the positive Z-axis is North (in the direction of the spin axis +83.4279 degrees declination, +39.4827 degrees right ascension); the positive X-axis is in the equatorial plain and directed toward the prime meridian; and the Y-axis completes the orthogonal right-hand-rule system. The latitude and longitude are defined by:

Lon = 360 - atan2(Y,X);
Lat = asin(Z);

For more details see the BIDR SIS, BIDRSIS.PDF, in the DOCUMENTS directory of each PDS volume.

For non-spherical bodies, the BODP latitudes and longitudes differ from those used in the BIDR. For image projection convenience and convention, the relatively small number of non-Titan SAR images are projected onto a reference sphere whose radius is documented in the labels of the BIDR files. (Other than Titan, only Rhea, Iapetus, and Enceladus have SAR imagery available.) However, the latitudes and longitudes in the BODP data files are planetodetic. The BODP coordinate system is defined by:

$$X' = x/radx,\ Y' = y/rady,\ Z' = z/radz$$
$$Lon = 360 - atan2(Y',X');$$
$$Lat = asin(Z');$$

Where x,y,z are the rectangular coordinates (coordinate system defined the same as above) of a point on the triaxial body with radii = (radx,rady,radz).The science data segment is usually not computed for non-Titan bodies with the exception of radiometric observations of Saturn and its rings, so these fields are flagged as invalid for those observations. The exceptional cases are those in which SAR observations of the non-Titan bodies were obtained. For most non-Titan icy satellite observations, only a single antenna temperature or backscatter measurement is computable, rather than values for each burst. This limitation is due to SNR effects due to the long distance from which the radar observations are obtained in order to avoid impacting observations from the other Cassini instruments.

4.1.3 Long Burst Data Record (LBDR)

The LBDR is the same as the SBDR but includes a raw echo data array as well. The array comprises 32,768 32-bit IEEE floating-point values, and contains the active-mode time-sampled data obtained during the receive window. The data is encoded before downlink from the spacecraft to minimize the data transfer rate, and is then decoded during ground processing. The length of the array corresponds to the maximum amount of echo data that can ever be obtained from a single burst. In the array, only the first N elements, floating point values typically in the range [-127.5, 127.5] sampled consecutively at a rate of B=2*Bandwidth Hz, are valid data. The decompression algorithm occasionally produces values outside the nominal range to account for situations in which saturation occurs due to exceeding the dynamic range of the digital to analog converter. N is stored in the raw_active_mode_length data field and B is in the adc_rate field in the engineering data segment. The raw_active_mode_rms field in the engineering data segment contains the root mean square of the N sampled echo data values. The BAQ_mode field identifies the specific compression algorithm used. See the BODP SIS for a full description of this field. For a description of the block-adaptive quantizer (BAQ) compression algorithm, see Kwok and Johnson (1989).

When the BAQ_mode field is set to 3, it signifies the compressed scatterometer mode, where all data samples are not downlinked from the spacecraft. In this mode, absolute values of the samples are summed across all corresponding sample positions in each pulse repetition interval (PRI) and downlinked. To track any dc bias, a summation of signed values over the entire receive window is also downlinked. These data are stored in the LBDR raw echo data array as one PRI worth of summed magnitudes, plus one summed value at the end. Thus, if there are 50 PRI in the receive window with 250 samples in one PRI, then the LBDR raw echo data array will contain 250 floating point values, each a sum of 50 magnitudes, followed by one floating value containing the sum

over all 50*250 samples. The value of N is set to 50, so the user needs to separately load the dc bias value at the end. The one PRI worth of summed magnitudes are intended to provide a profile of the echo while still reducing the downlinked data volume by a factor equal to the number of PRI in the receive window. These values can be further summed to a single value that is proportional to the average power assuming that the radar echo power is normally distributed. This assumption is expected to hold for radar echoes from natural distributed targets that contain many scattering centers. Since it is a summation, the values may be outside the nominal range.

4.1.4 Altimeter Burst Data Record (ABDR)

The ABDR is the same as the SBDR but includes altimeter profiles that are range-compressed active-mode data obtained while the radar is in altimeter mode and the radar beam is pointed within less than beamwidth of nadir. The profile is an array of floating point values with the number of values stored in the altimeter_profile_length data field in the science data segment. The active-mode data is segmented by pulse during range compression, and each pulse is correlated with a real-valued replica of the chirped transmit waveform to distribute the energy within each returned pulse into range bins. The replica waveform used is a digital-step chirp with identical starting frequency, step duration, step frequency, and number of steps to the transmitted signal. The modulation of the analog dealiasing filter on the return signal is treated as an ideal filter. Any inaccuracy in the chirp generator used to produce the transmitted signal is also ignored. It is possible to use rerouted-chirp measurements obtained during each observation to correct for these errors, but this has not been done for the archived data set (See Sec 8.4 on an enhanced altimeter product produced by Peter Ford). The number of pulses, the range for the first sample of the altimeter profile and the range step are data fields that can be found in the science data segment. The number of range bins can be obtained by dividing the profile length by the number of pulses; the array is arranged so that the range bins for each pulse are contiguous. A simple altimeter product containing basic location and surface height information is included as an ASCII comma-separated-value (csv) file.

4.1.5 Data Validation and Archiving

All of the BODPs have attached PDS labels, and the data products conform to PDS standards for file formats and labels. PDS labels are stored as ASCII character strings. A sample PDS label can be found in the BODP SIS (V2.0, June 2008). Validating or ensuring the quality of the products and their readiness for release is the responsibility of the CRST.

4.2 Basic Image Data Products (BIDRs)

BIDR data files are single-pass, calibrated and gridded SAR image data, with a data set ID of CO-SSA-RADAR-5-BIDR-V1.0. They are designated CODMAC (Committee of Data Management and Computation) level-5 data. The BIDR products are all gridded (raster) maps of Titan derived from SAR data and stored as PDS image files, and are generated at more than one word type (e.g., byte vs. floating point) and resolution. The BIDR is produced in an oblique cylindrical coordinate system, where the great circle corresponding to the ground track of the spacecraft around closest approach is defined to be 0 degrees latitude. The prime meridian of the oblique cylindrical coordinate

intersects this great circle at the point of closest approach to the reference sphere. The extent of each BIDR product is the minimum bounding rectangle of the area of coverage in this projection for nominal SAR. This projection was chosen to minimize the amount of "dead space" (pixels not containing data) in the minimum bounding rectangle around image strips that are oriented essentially randomly on Titan. For distant HiSAR observations the oblique cylindrical projection can be much less optimal, but it is retained for the sake of simplicity.

4.2.1 Data Format and Description

BIDRs are produced at the Jet Propulsion Laboratory by the CRST in full-resolution floating-point format. Several different files containing different steps in the processing of the backscatter images and supplementary maps of key variables (sometimes known informally as "backplanes," though each map is contained in a separate data file) are produced for each SAR observation. One of these backplanes is the beam mask backplane, which denotes which of the five radar beams (antenna feeds) was used to produce each SAR pixel. The values contained in the beam mask image are 16-bit integers. The five least significant bits are used to indicate the beams, and the other 11 bits are always zero. Integer values of 1, 2, 4, 8, and 16 denote beams 1, 2, 3, 4, and 5, respectively. This format allows us to represent the case in which pixels are averaged from multiple beams, but multiple-beam averaging was never used in the SAR processing. Each SAR pixel value comes from a single beam. For more information about the beam mask backplane, see the BIDR SIS.

Different image versions and supplementary backplane files are identified by the third letter in the BIDR filenames. The first two letters in all BIDRs filenames are "BI." The primary images are the BIF files that contain floating point NRCS data from which systematic biases due to thermal and quantization noise, and systematic variation due to incidence angle have been removed. The quantization noise results from BAQ scheme that is used to compress the data on the spacecraft before downlink to Earth. This compression induces an offset and a scaling term to the SAR data, which can then be accounted for in the noise subtraction approach. Thermal noise is caused mainly by system noise in the radar with a minor contribution due to emission from Titan's surface. The latter effect is estimated based on Titan's observed gross radiometric characteristics; the former is dealt with by using estimates made from engineering test data. The incidence angle correction algorithm used for Titan is the sum of three component models: two Hagfors components and a diffuse component (see the BIDR SIS V2.0, April 2008 for details). BIDRs from non-Titan observations use different incidence angle models appropriate to the specific body observed. In all cases the labels of the BIF files contain the precise equations and associated parameters used to perform the incidence angle correction.

There are two other NRCS images produced at JPL: BIU files, which have no corrections for incidence angle or noise, and BIS files, which are noise-corrected but not incidence-angle corrected. Coregistered images of ancillary data are also produced by JPL including latitude (BIT), longitude (BIN), incidence angle (BIE), beam mask (BIM) and number of looks (BIL) backplane images. BIM and BIL backplanes are 8-bit images. All others are 32-bit floating point format images. The values in the BIF, BIU, and BIS NRCS backplanes are linear-scale, unitless quantities. BIF files are converted

to 8-bit (BIB)-format log-scale images at various resolutions by the USGS Flagstaff Astrogeology Team; both the USGS and JPL files are archived. The-8 bit images from the USGS are returned to JPL and archived together with the full-resolution floating-point images. See the BIDR SIS for more information.

BIDRs are generated from BODPs (described above, and in SIS); the encoded raw active-mode data in the BODP (LBDR) files are decoded and processed into SAR images by the CRST. Geometric data used as inputs include a description of the shape and orientation of the RADAR beams derived from in-flight geometric calibration (stored as antenna gain pattern files in the CALIB directory of each archived PDS volume); mission-provided spacecraft pointing histories; and Titan and spacecraft ephemerides provided by the Cassini project. Each BIDR file contains data from all the antenna beams (up to 5) used in each observation. For the NRCS images, each pixel contains information from the beam with the highest data quality for that pixel. The planetographic latitude/west longitude system is used to produce the latitude and longitude BIDR backplanes. Each BIDR is projected onto the oblique cylindrical map projection described at the beginning of Section 4.3.

Multiple imaging segments can be obtained per spacecraft pass. Each of these segments contains all BIDR file types at each resolution. The “SXX” tag in their filenames distinguishes files from different segments such that “XX” is the 2-digit segment identifier. Typically segment S01 is the primary SAR imaging segment. Other segments contain High-SAR data or turns at the beginning and end of the SAR observation. Occasionally the nominal SAR imaging period is split into multiple segments due to an unusual spacecraft pointing profile. See the BIDR SIS for a complete specification of the file names.

4.2.2 Data Validation and Archiving

The CRST validates the BIDRs for scientific integrity as well as compliance with PDS standards. BIDRs are archived as binary files, with the initial records containing a PDS label. Each BIDR is assigned a string that uniquely identifies the type of data product, bit type, resolution, and location of the data on Titan. This string is used both as the value of the PRODUCT_ID keyword in the PDS labels and, with extension “.IMG” as the filename for that product. For more information about BIDR filename conventions see the BIDR SIS, and in Appendix 5.

4.3 Digital Map Products (DMPs)

The DMPs are high-level gridded (raster) maps of Titan produced by the USGS, Flagstaff from the lower-level JPL products just described (SBDR, BIDR, and supplement files). The USGS cartographic system Integrated Software for Imagers and Spectrometers (ISIS) is used for this processing, augmented by the commercial stereoanalysis package SOCET SET for production of stereo topographic maps. A total of eight DMP data sets are produced, as shown in Table 4-1.

Table 4-1. Cassini RADAR Digital Map Products.

DATA SET ID	CODMAC LEVEL	DESCRIPTION
CO-SSA-RADAR-5-PRDR-V1.0	5	Calibrated and gridded single-pass radiometer data
CO-SSA-RADAR-5-PSDR-V1.0	5	Calibrated and gridded single-pass scatterometer data
CO-SSA-RADAR-5-GRDR-V1.0	5	Mosaicked or modeled multipass radiometer data
CO-SSA-RADAR-5-GSDR-V1.0	5	Mosaicked multipass scatterometer data
CO-SSA-RADAR-5-GTDR-V1.0	5	Mosaicked altimetric and SAR topographic data
CO-SSA-RADAR-5-MDIR-V1.0	5	Mosaicked multipass SAR image data
CO-SSA-RADAR-5-RIDR-V1.0	5	Coregistered multilook SAR image sets
CO-SSA-RADAR-5-DTM-V1.0	5	Digital Topographic Models

The majority of these data sets include, in addition to a primary product (e.g., for the PSDR and GSDR a map of NRCS measured by the scatterometer), associated data products showing the variation of related parameters (e.g., incidence angle, resolution, and so on). The purpose of these products is to make as much of the information in the BIDRs and especially the BODPs accessible to the research community in a simple and straightforward map format, obviating the need to understand and process the lower level products. The initial delivery of DMPs, which is currently in preparation, will contain data from the Prime Mission (Ta through T44) and will include all of the data products except DTMs. Data from the extended missions and DTMs will be added in subsequent deliveries.

The contents of the eight DMP data sets are summarized below.

4.3.1 Pass Radiometry Data Records (PRDRs)

Each PRDR is a global map of Titan in Equirectangular (cylindrical) projection containing in gridded form the brightness temperature of the surface (or associated information) based on one sequence obtained on one Titan flyby pass. PRDRs are provided for the scatterometry, altimetry, and SAR sequences, as well as for radiometry-only scans. Each PRDR brightness temperature map is produced in three forms (calibrated antenna temperature, antenna temperature with sidelobe contributions subtracted, and sidelobe-corrected temperature normalized to standard viewing geometry of normal incidence) and is accompanied by companion files in identical map projection, indicating respectively the resolution (beam footprint diameter at 3 dB power contour), emission angle, polarization angle, and ground azimuth angle at which each observation in the map was obtained. The sidelobe-corrected temperatures are calculated by CRST members at JPL and are supplied to the USGS for processing in a “radiometer summary file” that is not currently included in the BODP archive, but which may be added at a later date. See Figure 4-1 for examples.

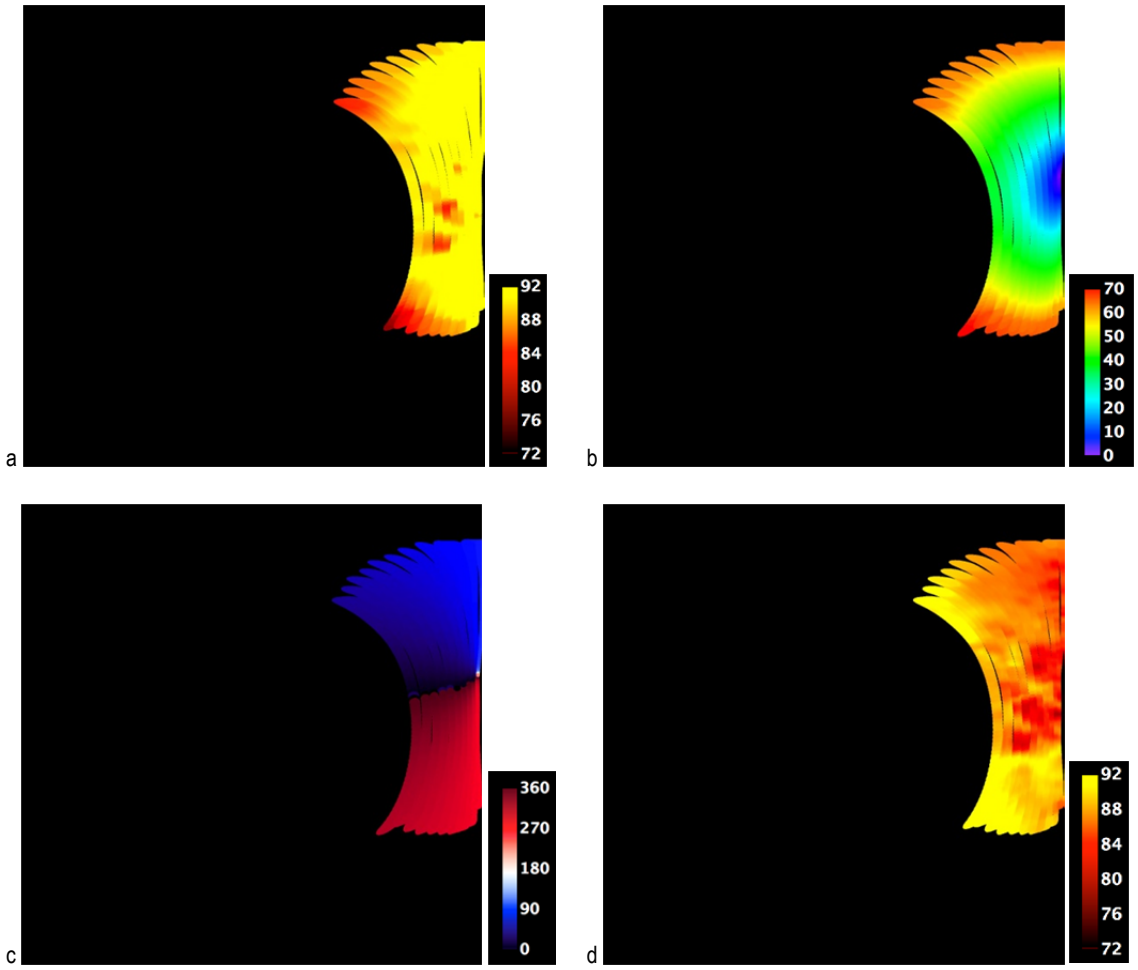

Figure 4-1. Examples of PRDR products: a) sidelobe-corrected brightness temperature, b) emission angle, c) polarization angle, d) brightness temperature corrected to normal incidence, based on emission and polarization angles. All products contain data from Ta Sequence 4 and show the western hemisphere (latitude -90° to 90°, longitude 0° to 90°W) in simple cylindrical projection with north at top. NOTE that these color figures and those below are derived from the DMPs for illustrative purposes. The actual DMPs are raster maps of floating point or integer data, not color images.

4.3.2 *Pass Scatterometry Data Records (PSDRs)*

The PSDR resembles the PRDR in format and also contains gridded data for a single sequence of one Titan flyby. The primary mapped quantity in the PSDR, however, is NRCS, which is provided in three forms analogous to those used for BIDR products (calibrated data, data normalized to standard viewing geometry, and normalized data converted to 8-bit integer form with a logarithmic scaling). Real-aperture cross-section values are measured during altimetry and SAR as well as scatterometry mode operation of the RADAR, and PSDRs are provided for all three active modes. As for the PRDR, the PSDR includes maps of resolution and the emission, polarization, and azimuth angles. See Figure 4-2.

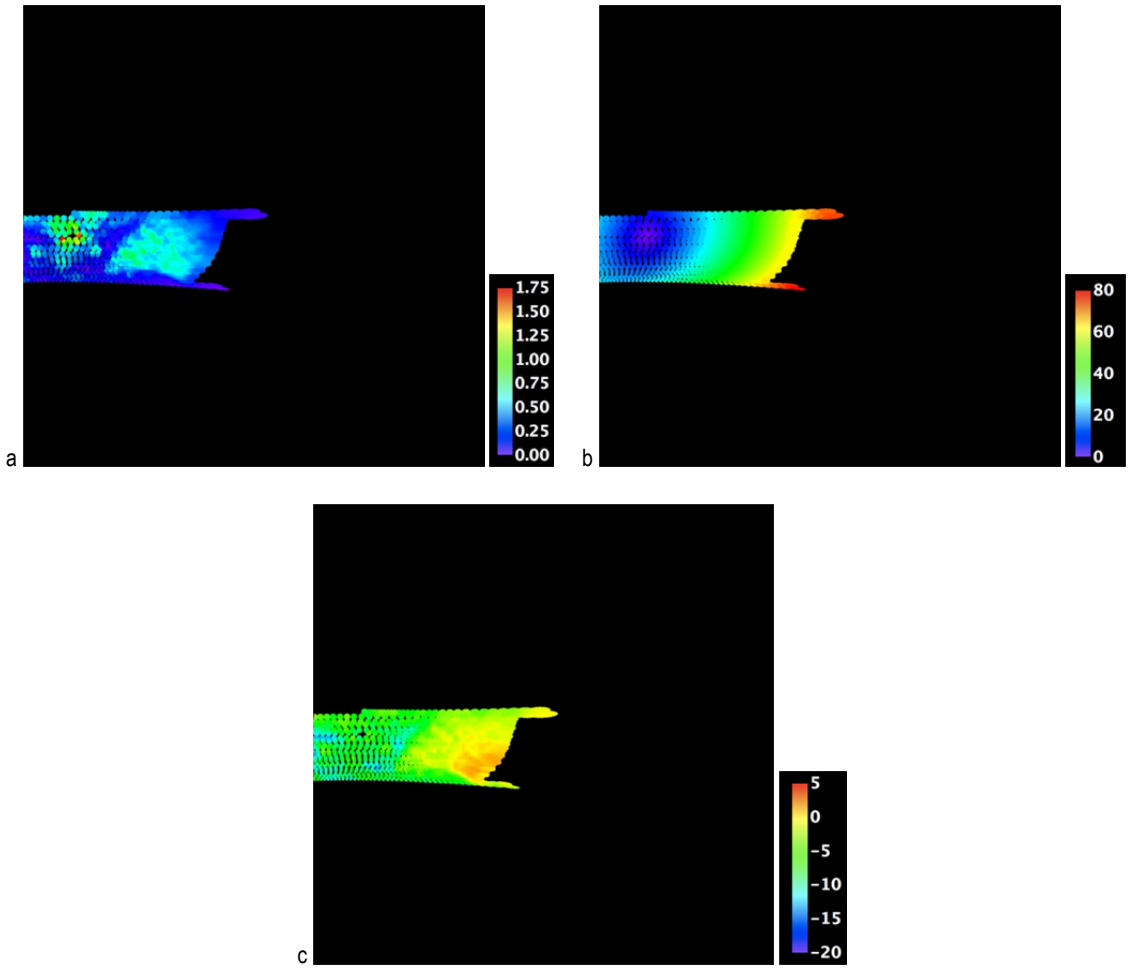

Figure 4-2. Examples of PSDR products: a) NRCS, b) incidence or emission angle, c) NRCS normalized to standard incidence angle and scaled logarithmically in decibels (dB). All products show data from T8 sequence 7 for the western hemisphere.

4.3.3 *Global Radiometry Data Records (GRDRs)*

The GRDR is a mosaic of gridded radiometric brightness temperature data (corrected to normal emission) assembled from the complete set of individual PRDR products. Where data from multiple PRDRs are available at a given grid location, that with the highest corresponding resolution (smallest footprint diameter) is selected. The GRDR includes maps of the resolution and emission, polarization, and azimuth angles for data used in the brightness temperature mosaic, as well as an index map from which it is possible to determine the PRDR from which any given pixel in the GRDR derives. The GRDR data set also includes three additional maps produced by more sophisticated modeling of all available radiometry observations at each grid point, performed by CRST members at JPL. These include a more accurate and detailed brightness temperature map than that obtained by mosaicking the PRDRs, a map of inferred dielectric constant, and a map of volume scattering fraction. See Figure 4-3.

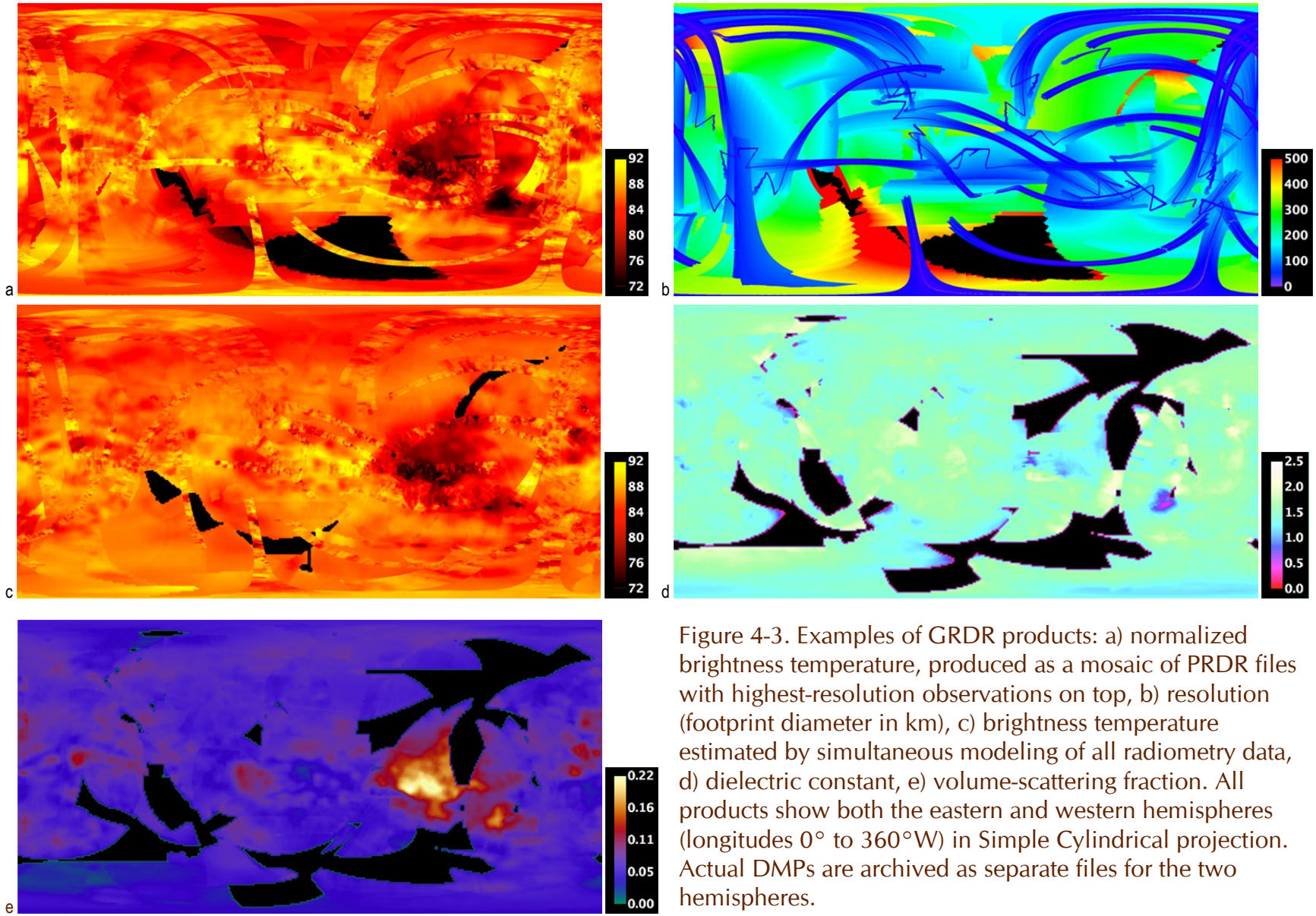

Figure 4-3. Examples of GRDR products: a) normalized brightness temperature, produced as a mosaic of PRDR files with highest-resolution observations on top, b) resolution (footprint diameter in km), c) brightness temperature estimated by simultaneous modeling of all radiometry data, d) dielectric constant, e) volume-scattering fraction. All products show both the eastern and western hemispheres (longitudes 0° to 360°W) in Simple Cylindrical projection. Actual DMPs are archived as separate files for the two hemispheres.

4.3.4 Global Scatterometry Data Records (GSDRs)

The GSDR is a mosaic of backscatter cross-section data (corrected to a reference incidence angle) assembled from the PSDRs by the same process used to generate the GRDR from PRDRs. It also includes maps of the resolution and the incidence, emission, and polarization angles of the included data and an index map showing the source PSDR for each pixel. See Figure 4-4.

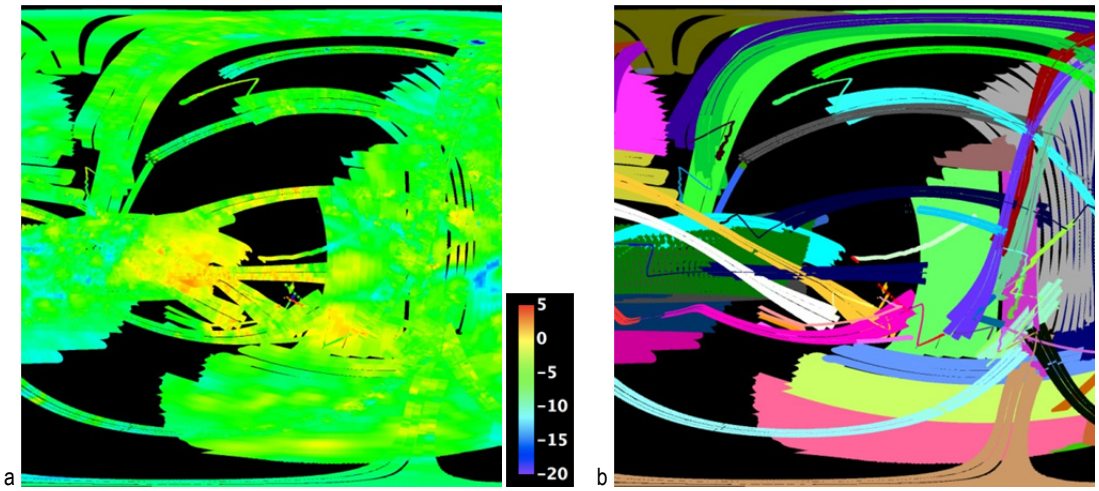

Figure 4-4. Examples of GSDR products: a) NRCS scaled logarithmically to dB; b) index map indicating the PSDR from which each pixel derives data by a unique numerical code value. Both products show the western hemisphere.

4.3.5 Global Topography Data Records (GTDRs)

The GTDR is a mosaic of absolute elevation values obtained on multiple Titan flybys. Pass-by-pass topographic files ("PTDRs" equivalent to the PRDR and PSDR) are not archived because the amount of overlap between topographic observations from different flybys is extremely small. The GTDR contains both altimetric data and "SARTopo" elevations derived by monopulse analysis of overlapping beams in the SAR images. These data are contained respectively in an altimeter summary file and a SARTopo file produced by the RADAR engineering team at JPL. These files are not currently included in the BODP archive, but may be added at a later date. See Figure 4-5.

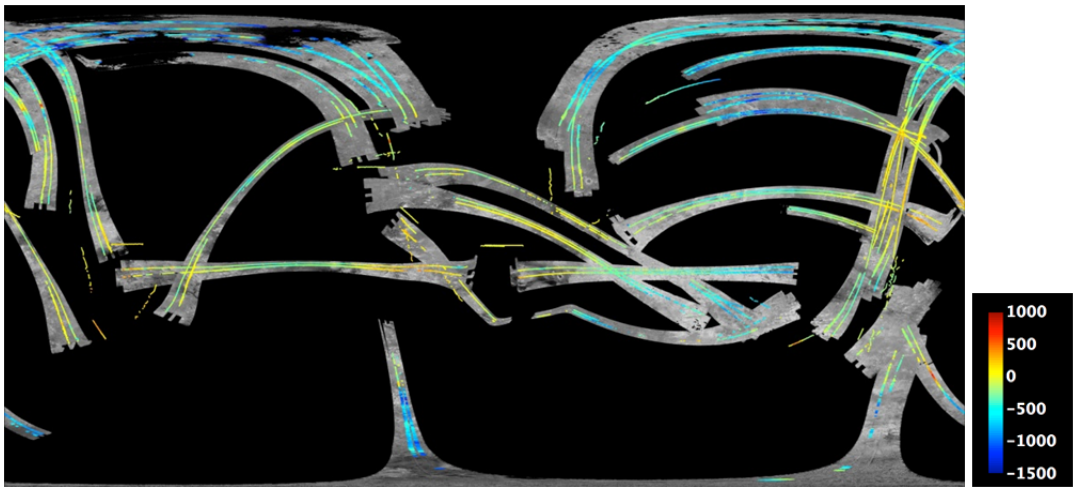

Figure 4-5. The GTDR. Color coded elevation values are shown here superimposed on an image mosaic (MIDR) and both hemispheres are shown in Simple Cylindrical projection. The actual GTDR product contains only the numerical elevation data without the images, and is archived in separate files for the two hemispheres.

4.3.6 Mosaicked Image Data Records (MIDRs)

Each MIDR is a mosaic of SAR image data assembled from the BIDRs obtained on multiple Titan passes. MIDRs are archived at full resolution (in multiple quadrangles) and reduced resolutions (multiple quadrangles and a global map divided into files for the eastern and western hemispheres) as described in Tables 4-2 and 4-3. Three complete sets of mosaics are produced: one containing data from the main full resolution SAR swaths, one containing all other SAR sequences (both start and end segments adjacent to main swaths and high altitude SAR) and one containing all data. See Figure 4-6.

4.3.7 Repeat Image Data Records (RIDRs)

The RIDR product is designed to facilitate comparison of overlapping (repeat) SAR image coverage. A RIDR set will be produced for each of the 15 map quadrangles (Table 4-2, Figure 4-6) in which two or more SAR images (BIDRs) overlap. The RIDR will consist of two or more separate files, each containing the SAR data from one of the overlapping BIDRs, resampled to a common map projection and common extent. Files showing the emission (incidence) angle for each BIDR are also provided. The map projection used (see Section 4.2) will depend on the location and extent of the overlap area: equirectangular for low to middle latitudes, polar stereographic for high latitudes, and oblique cylindrical (matching one of the component BIDRs) for a few image pairs with parallel ground tracks and very long overlap areas.

Table 4-2. Extents of Cassini RADAR Digital Map Product quadrangles.

QUADRANGLE	CENTER LON	CENTER LAT	LON RANGE	LAT RANGE
00N090	90°	0°	0° to 180°	-90° to 90°
00N270	270°	0°	180° to 360°	-90° to 90°
78N180	0°	77.75°	0° to 360°	65.5° to 90°
43N045	45°	43.5°	0° to 90°	21.5° to 65.5°
43N135	135°	43.5°	90° to 180°	21.5° to 65.5°
43N225	225°	43.5°	180° to 270°	21.5° to 65.5°
43N315	315°	43.5°	270° to 360°	21.5° to 65.5°
00N036	36°	0°	0° to 72°	-21.5° to 21.5°
00N108	108°	0°	72° to 144°	-21.5° to 21.5°
00N180	180°	0°	144° to 216°	-21.5° to 21.5°
00N252	252°	0°	216° to 288°	-21.5° to 21.5°
00N324	324°	0°	288° to 360°	-21.5° to 21.5°
43S045	45°	-43.5°	0° to 90°	-65.5° to 21.5°
43S135	135°	-43.5°	90° to 180°	-65.5° to 21.5°
43S225	225°	-43.5°	180° to 270°	-65.5° to 21.5°
43S315	315°	-43.5°	270° to 360°	-65.5° to 21.5°
78S180	0°	-77.75°	0° to 360°	-90° to -65.5°
90N000	0°	90°	0° to 360°	56° to 90°
90S000	0°	-90°	0° to 360°	-90° to -56°

Table 4-3. Data types[1] of Cassini Digital Map Products at various scales.

PRODUCT	PIXELS/DEGREE				
	2	8	32	128	256
PSDR, PRDR, GSDR, GRDR, GTDR[2]	8	8, 32			
Emission, polarization, azimuth, and resolution maps for above[2]		32			
Index maps for GSDR, GRDR[2]		16			
MIDR, global format in 2 hemispheres	8	8	8, 32		
MIDR, 15 quad format[2]		8	8	8, 32	
Products including “main swath” SAR data (TjjjS01 BIDRs)					
RIDR[2]			8	8, 32	8, 32
DTM, radarstereogrammetric			8, 32		
DTM, radarclinometric				8, 32	
Products including only non-main-swath BIDRs					
RIDR[2]			8	8, 32	

[1] 8 = 8-bit (byte) unsigned integer; 16 = 16-bit LSB integer; 32 = 32-bit PC real.
[2] Including polar regions in polar stereographic projection.

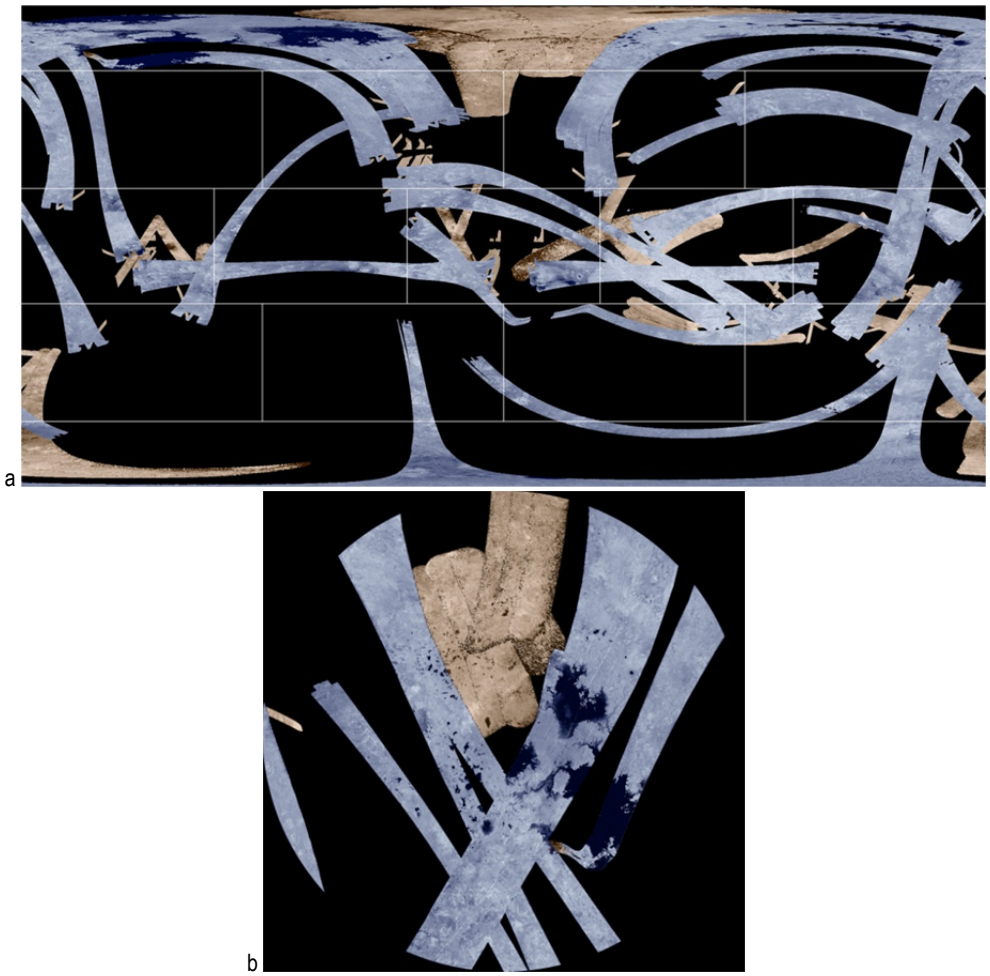

Figure 4-6. Examples of MIDR products: a) global mosaic in Simple Cylindrical projection, with outlines of the 15 quadrangles used for full-resolution mosaics shown, b) north polar region in Polar Stereographic projection. Both products show data from SAR main swaths in blue tint and data from other, generally lower resolution sequences in brown tint to distinguish them. The actual MIDR products consist of separate mosaics of these two types of data plus a combined mosaic, all presented without color.

4.3.8 Digital Topographic Models (DTMs)

Where suitable data are available, DTMs may be generated (Figure 4-7). Some DTMs are produced by radar-stereogrammetric analysis of overlapping SAR image pairs. Other DTMs are made by radarclinometric (shape-from-shading) analysis of portions of individual images. Each DTM is a gridded data product containing absolute or relative elevation values. Stereo DTMs will be produced in Equirectangular or Polar Stereographic projection, depending on latitude. Radarclinometric DTMs will be archived both in the Oblique Cylindrical projection of the source BIDR and in either Equirectangular or Polar Stereographic projection.

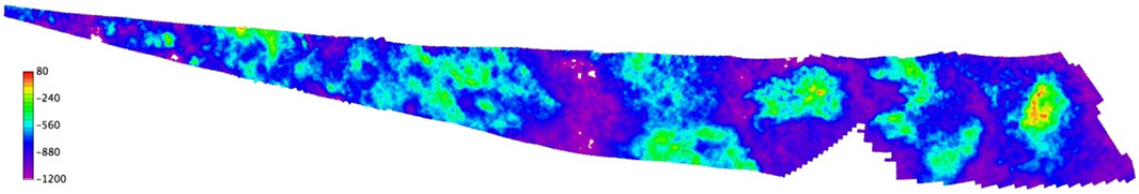

Figure 4-7. Example of a DTM. Color-coded elevation values are shown for the overlap between the northern ends of the T25 and T28 SAR strips, covering the area adjacent to and partly overlapping Kraken Mare. Polar stereographic projection, with north approximately at top (the figure has been rotated to fit more conveniently on the page).

4.3.9 PDS Label Format for DMPs

All Radar DMPs are archived as binary files, the initial record of which is a PDS label. Each DMP will be assigned a string that uniquely identifies the type of data product, bit type, resolution, location of the data on Titan, and (where applicable) input data set. This string will be used both as the value of the PRODUCT_ID keyword in the PDS labels and, with extension ".IMG" as the filename for that product. Table 4-4 lists the primary and supplementary products for each type of DMP, along with the first three letters of the file name, which uniquely identify them, the data set variable (listed in the catalog files in the DMP archive volume) and data type. For a full description of the DMP file naming convention, see the DMP SIS. File information in the label includes image dimensions, bits/pixel and precise pixel type, and location of image in the file. Map projection information includes planet name and radii, projection, scale, parameters (e.g., rotations for oblique projection), latitude-longitude extent, and offset of projection center relative to file boundaries. Source data information includes spacecraft, instrument names, input data time/clock range, input product names, data set name, physical units, scaling to data number, processing institution and processing date.

Table 4-4. Primary and supplementary mapped quantities for Cassini DMPs.

DATA SET	PRODUCT ID BEGINS WITH	DATA SET VARIABLE[1]	DATA TYPE[2]	DESCRIPTION AND SOURCE
PRDR	PRU	T_B	32	Calibrated antenna temperature, K (BODP antenna_temp)
	PRS	T_B	32	PRU values with antenna sidelobe contributions subtracted (Radiometer Summary File antenna_temp_sidelobe_corr)
	PRF	T_B	32	PRS values, corrected to normal emission by Fresnel formula
	PRB	T_B	8	PRF values scaled linearly to 8 bit range
	PRE	EMA	32	Emission angle, degrees (BODP pass_emission_angle)
	PRP	POL	32	Polarization angle, degrees, between electric vector of received signal and plane containing emission direction and local vertical (BODP pass_pol_angle)
	PRZ	AZI	32	Azimuth angle, degrees, between projection of emission direction onto ground and north (BODP pass_azimuth_angle)
	PRR	RES	32	Resolution, km, defined as long axis dimension of beam footprint (BODP pass_major_width)
PSDR	PSU	S_0	32	Backscatter cross section, unitless, in physical (linear) scale (BODP sigma0_uncorrected)
	PSF	S_0	32	PSU value, normalized to reference emission angle by Titan backscatter model (BODP sigma0_corrected)
	PSB	S_0	8	PSF value, scaled logarithmically (as dB) to 8-bit range
	PSE	EMA	32	Emission angle, degrees (BODP act_emission_angle)
	PSP	POL	32	Polarization angle, degrees, between electric vector of received signal and plane containing emission direction and local vertical (BODP act_pol_angle)
	PSZ	AZI	32	Azimuth angle, degrees, between projection of emission direction onto ground and north (BODP act_azimuth_angle)
	PSR	RES	32	Resolution, km, defined as long axis dimension of beam footprint (BODP act_major_width)
GRDR	GRF	T_B	32	As PRF
	GRB	T_B	8	As PRB
	GRE	EMA	32	As PRE
	GRP	POL	32	As PRP
	GRZ	AZI	32	As PRZ
	GRR	RES	32	As PRR
	GRI	IDX	16	Index uniquely identifying the observation sequence from which values at each pixel are derived (appears as OBSERVATION_ SEQUENCE_INDEX in index files)
	GRH	T_B	32	Brightness temperature, K, corrected to normal emission, estimated by modeling all available radiometric observations
	GRG	T_B	8	GRH values scaled linearly to 8-bit range
	GRD	DIE	32	Dielectric constant, estimated by modeling multipolarization radiometric observations, unitless
	GRC	DIE	8	GRD values scaled linearly to 8-bit range
	GRV	VOL	32	Fractional contribution of volume scattering, estimated by modeling all available radiometric observations, unitless
	GRW	VOL	8	GRV values scaled linearly to 8-bit range

DATA SET	PRODUCT ID BEGINS WITH	DATA SET VARIABLE[1]	DATA TYPE[2]	DESCRIPTION AND SOURCE
GSDR	GSF	S_0	32	As PSF
	GSB	S_0	8	As PSB
	GSE	EMA	32	As PSE
	GSP	POL	32	As PSP
	GSZ	AZI	32	As PSZ
	GSR	RES	32	As PSR
	GSI	IDX	16	As GRI
GTDR	GTF	ELE	32	Elevation, m, relative to reference sphere of 2575 km radius (ABDR Summary File MLE surface height or SARTopo File Elevation)
	GTB	ELE	8	GTF value scaled linearly to 8-bit range
MIDR	MIF	S_0	32	Backscatter cross section corrected for additive noise and normalized to reference emission angle by Titan backscatter model, unitless, in physical (linear) scale (BIDR BIF pixel value)
	MIB	S_0	8	MIB value, scaled logarithmically (as dB) to 8-bit range
RIDR	RIS	S_0	32	Backscatter cross section corrected for additive noise, unitless, in physical (linear) scale (BIDR BIS pixel value)
	RIF	S_0	32	As MIF
	RIB	S_0	8	As MIB
	RIE	EMA	32	Emission angle, degrees (BIDR BIE pixel value)
	RIZ	AZI	32	Azimuth angle, degrees (BODP act_azimuth_angle)
DTM	DTF	ELE	32	Elevation, m—may be absolute referenced to 2575-km sphere (stereo) or relative (radarclinometry)
	DTB	ELE	8	DTF values scaled linearly to 8-bit range

[1] Value of DATA_SET_VARIABLE field of index files.
[2] Where 8 = 8-bit unsigned integer, 16 = 16-bit LSB integer, 32 = 32-bit PC real.

4.3.10 Validation and Archiving of DMPs

DMPs will be validated for both scientific integrity and compliance with PDS standards. Validation is the responsibility of the Cassini Science Archive Working Group Data Validation Team and the CRST. Further details of the labels and processing conducted on these data can be found in the DMP SIS.

5 Calibration

This section briefly summarizes the techniques use to calibrate the various radar and radiometer data products. For a more complete description of the radar calibration see West et al. (2009). The discussion below is highly condensed from this reference. Also refer to Wye et al. (2007d) for a discussion of scatterometry calibration. Radiometer calibration is discussed thoroughly in Janssen et al. (2009).

Active-mode radar observations measure the level of backscattering from the target of interest. Backscattering denoted σ_0 is the NRCS. The definition of this fundamental quantity is given in many standard radar textbooks. Normalization in this case means dividing out the projected area on the surface of the pixel or footprint of interest from the backscattering cross-section that has units of area. The radar instrument measures received power (P_s) which is converted to σ_0 by the radar equation: $Ps = X\ \sigma_0$. Here, X includes terms such as the antenna gain, the range to the target, etc. The value of P_s is obtained by applying a receiver gain conversion constant (C) to the raw counts from the echo buffer (or from the SAR processing algorithm) converting them to units of power, and then subtracting an estimate of the noise power that corresponds to the measurement. The noise power (P_n) is computed using an estimate of the receiver noise temperature (T_r) applied to the measurement bandwidth (B): $P_n = kT_rB$.

Calibration of the active-mode radar data then consists of two main tasks. First the value of P_s is determined using the conversion constant and the receiver noise temperature. These vary with bandwidth and with the attenuator setting used in the observation. SAR processing uses fixed values that were determined from post-launch engineering test measurements as described in West et al. (2009). Real aperture (scatterometer) results in the SBDR files are also computed using fixed values, except that the noise level is estimated directly from noise only data that is usually available in scatterometer observations (see Wye et al. 2007d). Second, the value of X is determined from the measurement geometry and some prelaunch values (peak antenna gain, attenuator setting values). The active-mode calibration is tied to the passive radiometer calibration through the receiver noise temperature which is used to set the conversion constant C when observing known reference sources. The same antenna gain pattern characteristics determined by the radiometer calibration (see Janssen et al. 2009) are applied to the active-mode calibration ensuring consistent active/passive calibrations.

The calculation of X includes the attenuator setting and any BAQ bias correction. Attenuation is set in the receiver chain to prevent saturation of the digital data which is restricted to the range -127 to +128. For scatterometer measurements, attenuation is almost always set to 9 dB which provides a reasonable range for the low SNR signals commonly encountered in scatterometry. SAR and altimeter mode data use an on-board algorithm called auto-gain to automatically step the attenuator in 2 dB increments until the digital data is comfortably in-range. Auto-gain attenuator steps can occur on each instruction boundary and this helps the instrument to follow unknown variation of the target reflectivity. In a few cases (e.g., T49), some altimetry data is still saturated because there was insufficient time or too few instructions to allow the attenuation to step quickly enough. A similar algorithm called auto-rad automatically adjusts the radiometer integration window length to avoid saturating the radiometer data. Auto-rad

is always used for radiometry, except during SAR imaging where it is more important to keep the burst rate high. This requires setting a fixed radiometer integration window length that was selected to be 35 ms based on early analysis of system performance. Both attenuation settings and radiometer integration periods are reported in the downlinked telemetry and need to be included in active and passive calibration. SAR data (including high-altitude imaging scatterometry) usually uses 8-2 BAQ to compress each 8 bit sample to 2 bits. The BAQ algorithm is designed for unity gain, but sometimes introduces a bias factor which needs to be corrected as described in West et al. (2009).

The conversion constant C, the receiver temperature Tr, and the radar equation factor X are all subject to absolute and relative errors that constrain the error budget for σ_0. The overall 3-sigma absolute uncertainty for σ_0 is about 1.3 dB. This uncertainty comes mainly from uncertainty in the transmit power (measured prelaunch at 48.1 W), and statistical uncertainty in the determined values of C. There are also relative errors the user should be aware of, both statistical and systematic. Systematic errors are lowest for scatterometry scans where the relative error (3-sigma) is about 0.6 dB. In between Titan flybys, the systematic relative error is dominated by the uncertainty in C which is 0.9 dB (3-sigma). Statistical uncertainties (denoted K_{pc}) are usually lower than systematic uncertainties for real aperture observations. For SAR observations, however, K_{pc} errors can be much larger. In areas of low backscatter and combined with a low number of looks, the statistical error can be many dB. Averaging pixels together can reduce such statistical errors, albeit at the expense of image resolution.

The absolute calibration of the RADAR radiometer antenna temperature measurements requires 1) an accounting for contributions from outside the main beam (the beam pattern correction) to obtain brightness temperatures of the observed scene, and 2) a calibration of the radiant power received by the antenna and measured by the radiometer. A definition of terms used in microwave radiometry along with the fundamentals of calibration will be found in Janssen (1993). The calibration of the Cassini radiometer is described in Janssen et al. (2009). Work is in progress at present to update this calibration using all the data acquired during the Prime and Equinox missions, and will appear in press by early 2012. The current state of the calibration is summarized here. The PDS archive containing Cassini RADAR radiometer files is accompanied by documentation that includes periodic updates to the radiometric calibration factor.

Overall, up to the present (end of the Equinox mission), the RADAR radiometer has obtained nearly a million individual antenna temperature measurements on Titan, at all angles of incidence and polarization, and at ranges from 1000 km to 100,000 km, in 210 individual observing segments obtained during 39 Titan passes. In addition, Titan was observed unresolved at ranges exceeding 1,000,000 km as a control on possible time dependences of the measurements. Titan's polarized emission was imaged at low resolution by scanning during that portion of selected Titan flybys where the range varied from about 30,000 to 100,000 km (see Figure 3-1). Maps of effective dielectric constant (equivalent dielectric constant of a nominal simple dielectric surface) were constructed from these measurements. The polarization allows all brightness measurements obtained from the antenna measurements to be referenced to their

nominal values at normal incidence, which allows direct comparison with one another and the construction of a normal-incidence brightness temperature map. Sidelobe contributions were accounted for sequentially from low to high resolution by constructing, at first, a very low-resolution map (range >50,000 km) where the antenna beam was sufficiently well known to correct for the sidelobe contributions, and then using this map as a base onto which successively higher-resolution data were added. Simultaneously a one-dimensional sidelobe pattern was iteratively determined by using it to compute and remove sidelobe contributions and adjusting it to minimize the residuals in fitting higher-resolution segments to the accumulating map. Figure 5-1 shows the resulting beam pattern and residuals.

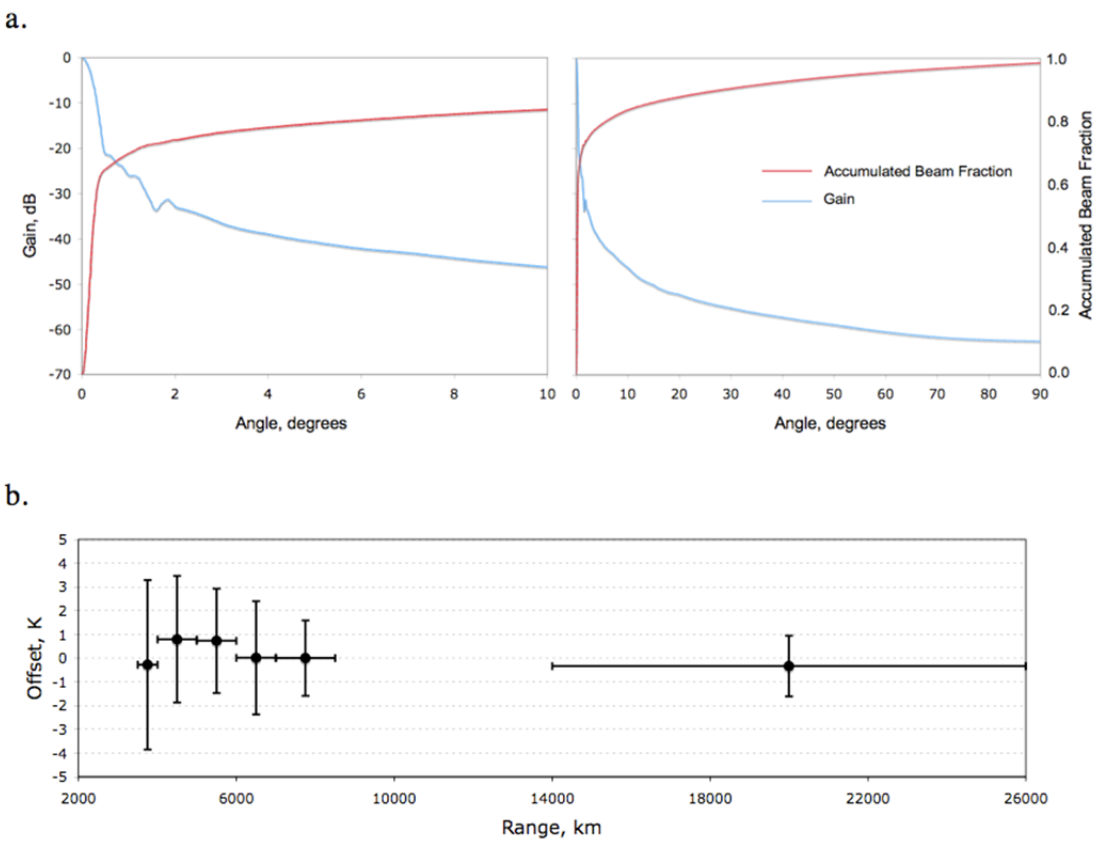

Figure 5-1. a) The radiometer beam gain determined in the mosaicking process used to obtain the global map shown in Fig. 4-3. The full two-dimensional beam shape was determined inside 2° from Sun scans, and the more distant sidelobes were solved for by assuming azimuthal symmetry in the minimization of residuals in the construction of the brightness mosaic. b) Residuals in the mosaicking process after fitting a one-dimensional far sidelobe pattern. The individual segments were given a final offset adjustment to best fit the accumulating map, so that the residual point-by-point systematic errors are much fewer than those in the figure.

The intrinsic noise in individual antenna temperature measurements is about 0.1 K, insignificant in the present context. The final residual systematic errors incurred in the map mosaicking process were evaluated to be about 1 K by comparing the variation in

normal-incidence brightness temperature among measurements in different segments at the same locations on Titan. The distant observations were used to correct for possible time dependencies in the observationsto allow for 1) a possible drift in the radiometer gain, and/or 2) a likely change in Titan's global average temperature as the Sun distance changes during the mission. Originally the dependence of Titan's average disk brightness on viewing geometry was obtained by fitting a "light curve" as a function of subspacecraft longitude to the observations along with an assumed linear time dependence. The present calibration using the distant Titan data makes use of the actual accumulating map to account for the viewing geometry dependence of the Titan whole-disk brightness.

The absolute calibration is obtained using Titan itself. Originally we took the Huygens probe surface temperature measurement of 93.6 K near the equator as our calibration temperature reference, using a model for the equator-to-pole temperature gradient to extend this temperature to the globe, assuming no day-to-night or other systematic temperature variations. At present we use the Composite Infrared Spectrometer (CIRS) results for surface temperature distribution (Jennings et al. 2009), a practice that eliminates many of the uncertainties in this procedure. Knowledge of the surface temperature distribution allows us to establish an absolute brightness map once we establish an emissivity reference on Titan's surface. There are in fact two areas on Titan that have well-understood thermoelectric properties and can serve as emissivity references: 1) the dune fields, and 2) Titan's seas, both of which can be argued to have an emissivity of about 0.98 based a combination of supporting radar, radiometric polarization, and Visible and Infrared Mapping Spectrometer (VIMS) data. As illustrated in Figure 5-2, the observed brightnesses of the dunes and the seas in both the north and south yield a consistent story for the absolute calibration.

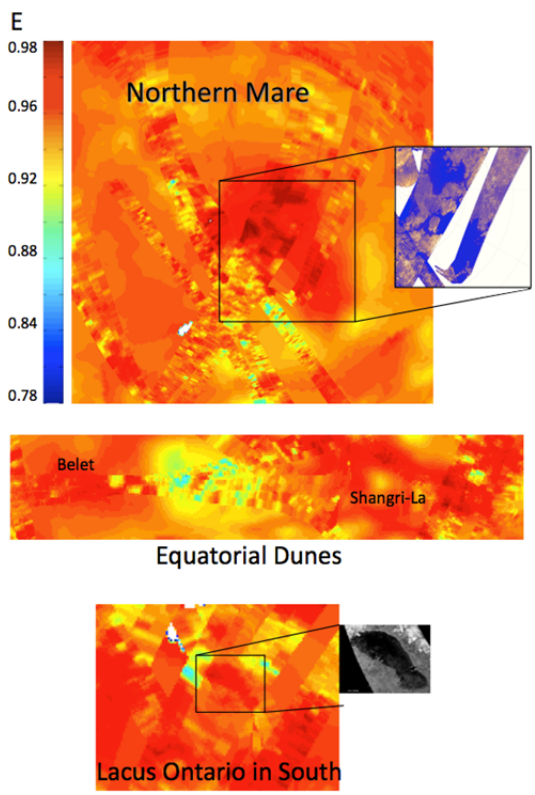

Figure 5-2. Absolute emissivity maps in the vicinity of the equatorial dunes (center panel), seas in the north (top panel) and Ontario in the south (bottom panel). The dielectric constant of both the dunes and the methane seas (~1.7) yields an emissivity of 0.98 with a small uncertainty, providing a consistent case for the absolute calibration of the Titan brightness map to about 1 K.

6 Titan SAR Swath Summary

Table 6-1 provides a summary of the Ta–T71 SAR swaths, including date obtained, longitude and latitude range, incidence angle range, and range and azimuth resolution (from A. Hayes). A brief description of the morphologic features within each swath is given below; descriptions for swaths Ta–T30 are adapted from Lopes et al. (2010), given in tabular format in Appendix 3.

Table 6-1. Characteristics of SAR swaths Ta–T71.

Swath	Segment	Date	Longitude Range (deg E)			Latitude Range (deg)			Incidence Angle (deg)			Polarization Angle (deg)			Azimuth Angle (deg)			Range Resolution (km)			Azimuth Resolution (km)		
			Mean	Min	Max	Mean	Min	Max	Mean	Min	Max	Mean	Min	Max	Mean	Min	Max	Mean	Min	Max	Mean	Min	Max
T0A	1	10/26/2004	-65.381	-133.69	-5.7813	44.21	29.469	53.344	22.447	2.8079	45.339	172.21	124.98	185.23	93.715	22.819	181.87	0.77488	0.27343	3.8176	0.37353	0.24215	1.2942
T03	1	2/15/2005	-65.111	-133.84	-0.8125	13.668	-2.7813	22.5	20.24	1.8435	28.768	176.8	130.09	183.17	275.77	234.62	346.68	0.48568	0.32313	4.8052	0.49462	0.24661	1.9253
T07	1	9/7/2005	-7.3877	-28.281	17.656	-52.332	-72.344	-28.156	21.623	9.1783	34.127	2.2782	-1.2697	13.27	212.57	196.33	230.52	0.45569	0.27633	0.96616	0.35817	0.24843	0.72797
T08	1	10/28/2005	112.63	41.656	177.25	-9.3305	-18.156	-3.4375	21.226	5.4893	28.052	6.9196	-0.5499	61.358	-97.841	-143.6	-80.717	0.49842	0.33624	3.239	0.45757	0.24691	1.7312
T08	2	10/28/2005	46.686	41.719	50.594	-6.7627	-17.625	4.1875	20.451	4.3338	28.052	48.373	19.316	127.43	229.21	145.22	253.38	0.74668	0.39886	4.456	1.3272	0.98278	3.2275
T08	3	10/28/2005	176.05	172.28	179	-5.5409	-16.813	5.875	12.465	2.2275	23.961	11.201	-0.5499	179.66	250.44	88.417	268.09	1.8213	0.75922	7.9396	0.60355	0.4956	1.0273
T13	1	4/30/2006	-116.95	-170.47	-62.281	-10.169	-17.25	-4.1875	20.689	8.9772	27.809	8.1877	-6.5668	55.002	262.75	219.85	276.02	0.47455	0.32711	1.365	0.4257	0.24818	1.4753
T13	2	4/30/2006	-167.45	-170.5	-165.03	-5.3598	-16.781	6.7188	14.729	2.0845	26.314	48.043	2.1266	177.84	225.81	92.042	267.76	1.1421	0.40044	5.3362	1.2065	0.90206	2.8988
T13	3	4/30/2006	169.77	161.03	178.28	-7.4075	-12.25	-1.0625	16.032	3.9262	23.472	317.16	314.22	323.22	221.91	215.11	225.55	2.0978	1.431	6.7018	2.7471	2.4389	3.3547
T15	2	7/2/2006	-30.942	-48.938	-13.375	-31.272	-38.844	-24.313	36.564	35.63	37.634	15.194	10.179	19.793	232.31	227.16	237.95	-1*	-1	-1	-1	-1	-1
T15	3	7/2/2006	-42.462	-48.875	-36.313	-23.099	-28.688	-17.531	37.44	37.231	37.634	19.049	18.313	19.793	227.99	227.16	228.81	-1	-1	-1	-1	-1	-1
T16	1	7/22/2006	-63.157	-150.13	19.969	59.207	13.281	82.438	24.37	10.627	38.924	2.9217	-61.373	65.458	252.72	0.00151	359.99	0.46278	0.245	1.9076	0.44308	0.24712	1.9076
T16	2	7/22/2006	-145.56	-154.34	-136.78	22.925	18.5	29.188	15.431	2.2961	27.07	48.848	39.699	62.098	315.33	306.13	324.83	1.2944	0.43223	5.2165	1.4252	0.59523	1.6516
T16	3	7/22/2006	18.616	13.094	23.844	16.982	13.5	21	14.899	2.4062	21.536	313.22	302.22	318.21	220.93	219.25	230.21	1.2554	0.59182	4.8893	1.2963	0.62116	1.4323
T17	1	9/7/2006	-50.366	-69.25	-32.406	9.8669	2.4688	15.688	35.509	30.627	43.991	-13.5	-44.14	15.293	-91.293	-112.24	-67.677	0.27813	0.25028	0.31972	0.27473	0.25051	0.34989
T18	1	9/23/2006	-40.704	-106.38	14.438	64.544	34.094	74.688	29.273	20.085	44.349	-0.027	-59.41	57.114	-123.35	-141.81	-95.871	0.37773	0.29486	0.44923	0.31591	0.25039	0.4769
T19	1	10/9/2006	-47.459	-160.44	46.531	61.231	-6.2813	86.969	23.979	10.723	37.982	174.33	104.86	241.31	17.67	-179.95	179.99	0.53405	0.25201	2.6114	0.45382	0.24704	3.1799
T19	2	10/9/2006	-144.13	-152.38	-136.31	42.352	38.188	47.031	16.029	2.8489	24.633	122.37	110.53	127.58	219.77	212.91	227.69	1.4924	0.69371	5.5269	2.051	0.92184	2.288
T19	3	10/9/2006	35.846	30.281	41.719	-3.5092	-5.0625	-1.125	14.287	3.0335	21.635	226	223.45	239.87	329.81	318.53	335.81	1.3355	0.59093	5.1261	1.4375	0.62133	1.9026
T19	4	10/9/2006	43.27	35.031	52.719	-2.224	-15.438	11.438	22.273	19.307	26.271	223.64	211.98	227.46	338.41	333.88	349.38	0.73141	0.59093	1.1842	1.0396	0.51962	1.3507
T20	2	10/25/2006	-142.19	-176.97	-98.031	2.9029	-13.75	13.875	31.491	19.025	60.365	-13.18	-66.839	53.072	280.06	225.61	323.88	3.0601	2.1323	3.9842	6.7354	3.4725	12.291
T20	3	10/25/2006	-122.88	-145.78	-98.031	3.4475	-10.063	13.438	33.328	22.79	42.509	-20.23	-66.839	28.463	286.34	245.51	323.88	2.5852	2.1032	4.2802	5.3616	3.3776	10.168
T20	4	10/25/2006	-137.87	-145.59	-130.81	20.502	5.625	34.875	23.697	4.4243	27.64	27.281	-36.797	28.463	246.43	243.23	305	4.5836	3.5926	17.924	4.4916	3.6943	7.1054
T21	1	12/12/2006	116.51	55.969	167.25	27.586	-29.781	52.406	27.568	9.9739	56.011	178.58	119.1	251.96	-35.677	-92.745	-10.689	0.47222	0.23692	2.2751	0.44673	0.24993	2.6
T21	2	12/12/2006	60.582	58.125	62.625	-21.317	-27.969	-14.656	15.031	2.4702	22.73	237.67	234.7	243.93	288.52	275.65	300.68	1.1635	0.65073	4.0047	1.6954	0.84037	1.9166
T23	1	1/13/2007	-25.725	-101.19	32.75	22.506	-40.156	59.094	23.611	9.0085	37.382	1.5178	-67.214	62.463	224.7	187.87	266.37	0.51236	0.25544	2.1775	0.43811	0.24798	1.6754
T23	2	1/13/2007	-94.8	-98.188	-89.938	55.486	49.156	61.313	16.145	2.8368	21.811	48.478	40.477	60.139	250.18	241.23	252.74	1.103	0.59457	4.1345	1.3879	0.6866	1.5551
T23	3	1/13/2007	26.147	17.656	32.688	-35.327	-40.094	-27.563	14.135	2.2554	26.372	-52.18	-67.214	-36.108	241.38	229.7	264.09	1.3695	0.64332	4.3828	1.0932	0.55601	1.3771
T25	1	2/22/2007	31.04	-57.813	148.5	52.52	-35.375	85.688	23.687	10.262	37.427	178.25	118.25	245.41	155.55	0.10877	359.94	0.49512	0.25518	2.0553	0.39394	0.23787	1.5828
T25	2	2/22/2007	-46.408	-53.625	-39.281	-32.012	-33.375	-30.281	15.507	2.0935	21.008	131.65	120.92	146.95	195.5	189.44	204.96	1.2918	0.60228	5.0606	1.1855	0.59783	1.4021
T28	1	4/10/2007	46.065	-42.969	156.47	52.941	-20.625	80.938	20.902	7.433	34.722	176.15	100.06	257.01	155.4	0.02158	359.84	0.62335	0.27637	5.3181	0.44773	0.23805	3.1052
T28	2	4/10/2007	-33.944	-43.063	-25.5	-16.082	-20.75	-10.469	19.962	2.8423	25.127	118.39	97.623	138.54	214.09	195.18	238.51	1.7517	0.51959	7.6081	1.3653	0.65693	3.1052
T29	1	4/26/2007	53.322	-39.469	163.84	62.326	-4.2813	86.469	23.446	7.2268	37.989	176.28	96.912	248.91	153.16	0.01263	359.97	0.47983	0.25199	2.718	0.43654	0.23643	1.9271
T29	2	4/26/2007	-30.257	-34.938	-26.188	-2.0318	-3.8438	-0.375	11.998	1.7736	18.071	115.49	90.929	134.64	185.5	172.79	207.99	1.0418	0.61396	5.1664	1.1107	0.97861	1.3158
T30	1	5/12/2007	88.278	26.813	140.78	60.229	29.75	72.656	25.874	10.543	46.617	11.714	-68.314	49.316	217.37	180.32	260.81	0.52113	0.23615	2.031	0.57057	0.35227	2.289
T30	2	5/12/2007	17.564	3.6875	31.125	71.867	68.875	73.656	17.905	2.7002	34.966	45.889	2.3711	177.34	260.45	147.78	318.91	1.017	0.35436	3.3759	0.38423	0.2461	0.51406
T30	3	5/12/2007	135.32	126.31	142.28	34.485	29.813	41.969	16.22	2.5838	26.364	312.09	291.69	324.66	240.08	228.91	257.2	1.2206	0.4401	4.8919	1.3552	0.57005	2.289
T36	1	10/2/2007	-30.309	-45.219	-13.094	-29.199	-49.375	-12.781	25.618	2.3096	60.768	180.15	2.0521	244.24	-39.301	-112.59	144.73	0.91147	0.23284	4.7196	0.89591	0.37463	3.4823
T36	3	10/2/2007	246.6	164.44	334.88	-57.409	-71.781	-38.125	40.066	22.14	60.768	180.66	115.54	242.07	-38.463	-179.99	179.97	0.30407	0.22854	0.86985	0.33341	0.23785	0.83506
T36	4	10/2/2007	163.22	150.28	178.38	2.5661	-20.063	23.594	25.398	6.9026	67.881	-58.07	-83.384	1.5529	88.804	30.06	115.26	1.6916	1.2391	2.7565	2.555	1.2385	4.6643
T39	1	12/20/2007	20.025	-179.97	180	-76.935	-90	-27.25	28.148	6.181	57.379	179.45	110.1	240.11	10.57	-179.89	179.95	0.43293	0.2396	2.9036	0.40957	0.23432	2.4151
T39	3	12/20/2007	164.34	154.78	172.47	8.1148	-11	25.375	22.982	6.3597	50.662	276.74	255.31	351.34	31.849	-49.131	58.968	0.94337	0.47071	2.521	1.3704	0.85586	2.8076
T39	4	12/20/2007	-3.2719	-18.688	12.281	-51.887	-64.25	-38.281	44.568	41.572	46.829	212.97	212.51	213.19	356.14	353.93	358.03	0.44397	0.42745	0.46806	1.9878	1.934	2.0792
T39	5	12/20/2007	35.235	-10.938	108.16	-76.698	-86.719	-38.219	44.796	42.128	46.829	212.96	212.51	213.16	356.31	354.34	358.03	0.44215	0.42745	0.46319	1.9891	1.934	2.0792

Swath	Segment	Date	Longitude Range (deg E)			Latitude Range (deg)			Incidence Angle (deg)			Polarization Angle (deg)			Azimuth Angle (deg)			Range Resolution (km)			Azimuth Resolution (km)		
			Mean	Min	Max	Mean	Min	Max	Mean	Min	Max	Mean	Min	Max	Mean	Min	Max	Mean	Min	Max	Mean	Min	Max
T39	6	12/20/2007	38.982	-1.3438	106.38	-75.533	-85.813	-38.281	46.105	45.188	46.829	212.82	212.51	213	357.3	356.55	358.03	0.43231	0.42745	0.43878	2.0281	1.9624	2.0792
T39	7	12/20/2007	-8.9882	-32.219	14.938	-37.472	-41.281	-30.5	23.806	2.3467	46.829	177.71	111.5	213.48	5.6531	-26.925	50.761	1.2218	0.42745	7.6047	1.5251	0.52837	2.1363
T41	1	2/22/2008	-102.6	-149	-61.25	-28.968	-37.063	-16.656	27.92	14.29	41.626	9.2731	-0.14154	59.145	87.757	58.566	109.96	0.38941	0.23227	1.4851	0.43268	0.23249	1.7617
T41	2	2/22/2008	-153.31	-162.44	-143.97	-24.384	-27.125	-21.813	27.062	5.6203	41.626	1.8604	-0.033234	13.458	58.324	44.312	63.504	0.41645	0.23227	1.609	0.24124	0.23284	0.25493
T41	3	2/22/2008	166.33	141.34	190.19	-10.095	-29.75	12.844	14.127	4.66	25.163	191.29	163.97	264.38	220.24	147.61	246.54	0.95303	0.37027	6.6475	0.5773	0.24424	4.9777
T43	1	5/12/2008	211.09	140.09	285.69	5.7906	-35.75	31.094	24.599	6.4777	41.709	178.05	106.55	339.85	249.47	191.25	307.18	0.92677	0.45596	3.664	1.5249	1.1691	2.3328
T43	4	5/12/2008	-101.11	-135.5	-67.25	-33.369	-37.281	-23.969	21.224	10.15	25.625	169.85	122.34	292.06	273.64	245.63	293.8	0.57963	0.49789	0.65789	1.6367	1.4364	1.832
T44	1	5/28/2008	197.05	134.63	264.66	2.4165	-32.438	25.406	19.533	7.5288	27.015	178.7	129.33	246.81	248.71	211.46	289.49	0.50756	0.36068	2.1103	0.38914	0.23285	2.0435
T48	1	12/5/2008	-116.2	-137.31	-96.25	-26.464	-33.313	-20.656	20.437	12.375	37.884	22.427	-3.6395	63.769	65.707	31.16	82.159	-1*	-1	-1	-1	-1	-1
T48	2	12/5/2008	-129.26	-137.22	-118.09	-20.837	-26.031	-16.469	32.476	16.106	67.19	24.473	-3.6234	54.305	55.413	25.794	82.097	-1	-1	-1	-1	-1	-1
T48	3	12/5/2008	190.02	131.13	241.91	2.3192	-18.344	46.313	41.823	31.827	75.312	-1.5	-66.766	54.305	56.841	21.629	125.7	-1	-1	-1	-1	-1	-1
T48	4	12/5/2008	-147.75	-178.47	-116.56	-55.188	-59.438	-47.781	31.346	27.005	36.689	134.17	128.87	139.81	213.12	200.69	223.62	-1	-1	-1	-1	-1	-1
T48	5	12/5/2008	-104.93	-110.97	-99.438	-32.611	-37.656	-26.469	15.435	2.0589	23.834	49.346	40.75	58.503	48.051	40.153	52.447	-1	-1	-1	-1	-1	-1
T49	1	12/21/2008	-117.31	-164.78	-67.406	-63.631	-85.656	-14	17.824	2.291	68.681	151.19	20.207	180.31	-12.7	-97.127	100.32	-1	-1	-1	-1	-1	-1
T49	2	12/21/2008	105.44	81.344	139	-22.524	-64.188	28.438	25.11	9.1034	38.289	181.67	71.362	253.57	196.13	134.77	236.57	-1	-1	-1	-1	-1	-1
T49	3	12/21/2008	82.814	75.375	90.125	4.1504	-7.4063	15.844	25.265	20.497	31.621	79.872	67.048	211.48	234.02	178.34	241.72	-1	-1	-1	-1	-1	-1
T50	1	2/7/2009	22.29	-17.656	61.656	-33.359	-58	17.5	40.466	31.898	59.465	178	118.5	241.15	145.46	101.04	171.35	0.27051	0.22683	0.31223	0.30657	0.23778	0.52409
T50	5	2/7/2009	88.383	71.938	102.56	49.037	24.5	62.844	27.379	6.1685	64.598	-115.4	-179.77	-94.699	92.688	58.661	161.17	2.1587	1.4331	3.0974	2.1142	0.86831	3.7434
T55	1	5/21/2009	161.04	75.906	238.41	-37.159	-76.781	37.344	23.969	8.8763	38.596	170.39	0.092717	359.91	-40.216	-162.26	12.004	0.51739	0.25234	2.4948	0.5608	0.24686	4.6821
T55	2	5/21/2009	-121.96	-142.72	-91.844	27.921	15.688	40.688	18.967	2.8532	30.409	85.35	-40.153	174.15	-47.944	-106.57	6.2993	1.0937	0.43213	8.2725	1.8096	0.47563	4.6821
T55	3	5/21/2009	129.76	67.219	219.66	-73.687	-82.656	-53.219	25.336	6.8409	39.124	198.95	161.76	245.34	-85.891	-162.43	10.64	0.78198	0.43224	2.991	1.2923	0.4881	2.0883
T55	4	5/21/2009	-133.42	-141.13	-125.5	33.847	32.844	34.906	14.921	2.3195	22.393	116.45	63.11	131.03	-11.614	-94.027	9.5008	1.3672	0.59878	4.7879	1.4836	0.70028	2.5405
T55	5	5/21/2009	94.248	82	105.38	-66.531	-71.031	-62.281	15.346	3.9174	21.536	227.71	163.3	237.3	216.59	208.27	294.03	1.193	0.59101	3.1524	1.2314	0.62748	1.6892
T56	1	6/6/2009	149.11	47.5	233.13	-45.635	-76.688	29.656	24.125	10.005	38.476	174.03	82.466	243.35	-41.814	-179.89	179.9	0.49698	0.253	2.2186	0.52386	0.24863	3.0836
T56	2	6/6/2009	-126.59	-142.13	-102.16	20.354	8.9063	31.25	21.602	5.7644	33.239	108.7	48.642	170.69	-48.875	-100.32	8.8682	0.92174	0.4361	5.5732	1.9319	0.48185	3.3014
T56	3	6/6/2009	-137.71	-144.84	-130.53	26.013	25.063	27.094	15.834	2.0065	22.026	125.62	113.6	131.62	-3.2823	-97.489	17.426	1.3931	0.59635	5.2251	1.4992	0.68627	3.1363
T56	4	6/6/2009	72.901	59.531	85.906	-64.935	-67.031	-62.281	13.033	2.3537	20.867	229.89	225.81	238.41	194.63	184.91	209.94	1.4416	0.62388	4.7754	1.2584	0.69212	1.4005
T57	1	6/22/2009	142.73	42.094	230.41	-59.964	-81.938	15.938	41.929	32.047	75.433	179.58	111.61	256	-21.172	-179.95	179.51	0.26738	0.18885	0.30965	0.33417	0.24734	1.1555
T57	2	6/22/2009	99.52	59.438	141.22	-44.203	-52.688	-37.094	34.102	3.1516	39.501	2.3548	-1.764	7.1029	33.192	3.2819	38.066	-1	-1	-1	-1	-1	-1
T58	1	7/8/2009	131.54	23.875	223.63	-58.695	-82.156	5.6563	24.577	10.773	49.247	181.93	134.58	274.33	-29.494	-180	179.97	0.45633	0.24766	3.1556	0.40165	0.24767	2.5733
T58	2	7/8/2009	-147.72	-150.03	-140.69	-17.889	-37	3.1563	20.575	13.558	60.723	185.39	146.17	278.93	-27.728	-89.311	5.9096	0.52069	0.33409	0.66693	0.40949	0.29937	0.83754
T58	3	7/8/2009	79.015	40.531	112.97	-56.465	-58.969	-50.969	14.348	13.121	15.874	224.26	218.08	229.39	168.73	164.76	172.8	1.0145	0.70807	1.4189	0.90248	0.53327	1.0758
T59	1	7/24/2009	126.96	25.594	220.66	-71.726	-88.25	-22.781	39.878	32.022	55.52	179.45	120.93	239.65	7.6452	-179.92	179.73	0.26997	0.23536	0.31067	0.31049	0.24777	0.49608
T61	1	8/25/2009	125.66	50.438	193.91	-3.7113	-14.813	18.094	23.977	10.394	37.968	2.508	-58.5	65.98	94.236	53.851	126.65	0.47391	0.2488	1.9912	0.40049	0.24675	1.9346
T61	2	8/25/2009	-157.51	-162.22	-152.31	-7.0873	-14.719	0.0625	15.722	10.603	21.052	72.635	39.73	96.03	287.33	263.91	320.05	1.2362	0.8743	1.6834	2.2374	1.2042	3.5291
T61	3	8/25/2009	-157.84	-161.69	-154.16	-7.4785	-13.906	-1.375	15.727	10.603	21.052	72.693	39.73	96.03	287.27	263.91	320.05	1.2358	0.8743	1.6834	2.2402	1.2097	3.5291
T61	4	8/25/2009	-159.81	-165.47	-154.75	-4.961	-13.125	1.8438	15.575	2.38	21.052	72.222	39.73	96.03	287.72	263.91	320.05	1.2699	0.8743	7.7322	2.2173	1.1565	3.5291
T61	5	8/25/2009	-169.75	-170.34	-169.13	11.699	10.094	13.313	21.248	18.135	22.057	53.289	49.403	58.679	65.87	61.099	69.287	0.79142	0.60159	1.3972	1.2684	0.71539	1.4363
T61	6	8/25/2009	57.159	53.594	60.75	1.0501	-2.6875	4.6563	26.338	23.175	32.26	-25.82	-33.98	-12.729	93.761	79.701	102.75	0.47153	0.3014	0.89994	0.93067	0.52453	1.0311
T64	1	12/28/2009	72.771	-13.875	151.13	73.632	11.688	85.469	27.478	10.93	54.228	3.1737	-62.18	57.855	208.96	162.57	307.75	0.43552	0.23608	1.8964	0.39758	0.24842	1.6636
T65	1	1/12/2010	121.36	-7.6	282.19	-76.801	-84.75	-41.156	28.231	2.3268	47.457	54.264	-179.97	179.97	37.805	-62.969	163.14	-1	-1	-1	-1	-1	-1
T65	2	1/12/2010	175.57	163.09	185.94	-68.869	-72.25	-64.563	28.67	19.125	47.313	25.537	-0.84174	85.396	-12.996	-64.925	16.547	-1	-1	-1	-1	-1	-1
T65	5	1/12/2010	141.79	117.22	176.81	-43.863	-72.344	-2.1875	32.572	17.815	69.125	147.89	3.1916	359.3	2.019	-178.96	179.98	-1	-1	-1	-1	-1	-1
T69	2	6/5/2010	-45.24	-61.72	35.2188	25.641	-10.25	57.281	36.229	11.78	69.922	226.84	0.063931	359.98	147.11	0.04652	359.89	-1	-1	-1	-1	-1	-1
T71	1	7/7/2010	61.359	-18.625	148.84	-52.644	-69.25	-30.219	40.113	30.331	61.909	-0.144	-66.932	65.293	218.47	0.08028	359.86	-1	-1	-1	-1	-1	-1

* Values of -1 indicate no range information available.

6.1 Swath Descriptions

Ta. The Ta pass consisted of inbound scatterometry and radiometry, Ion and Neutral Mass Spectrometer (INMS) ride-along SAR, SAR imaging, followed by altimetry and outbound scatterometry and radiometry. The Ta SAR swath crosses the mid-northern latitudes in an approximately E-W direction, from ~32°N, 130°W to 53°N, 10°W. Ganesa Macula, radar-bright lobate features, and two circular features with associated lobate deposits are located in the swath. All of these features are interpreted to be superposed on the surrounding plains units (Lopes et al. 2010). Channels interpreted to be fluvial in origin also are located throughout the swath, along with small, isolated hills (Elachi et al. 2005b; Stofan et al. 2006).

T3. T3 had inbound and outbound altimetry along with SAR imaging. The T3 SAR swath is located in the low northern latitudes in an ~E-W direction, from 3°S, 0.4°W to 22.5°N, 133°W (Elachi et al. 2006a). Abundant dunes are located throughout the swath, along with two impact craters: Menrva (~450 km diameter, 19.6°N, 87.1°W) and Sinlap (~70 km diameter, 11.3°N, 16.1°W). The dune fields in T3 are superposed on both intermediate and low backscatter plains. Isolated hills are also seen in the swath between 16-21°N and 39-54°W and between 1-11°N and 10° and 23°W and small circular features of unknown origin near 15°N, 33°W. Fluvial channels—including the wide anabranching network Elivagar Flunima and a few small features interpreted as cryovolcanic flows (Lopes et al. 2007a) are also seen. Principal results of T3 were discussed in Elachi et al. (2006a). An early discussion of Titan craters is in Lorenz et al. (2007).

T7. The plan for T7 was to collect inbound and outbound radiometry and altimetry, with SAR imaging. T7 SAR is a partial swath extending from 31°S, 23°W to 70°S, 11°E. Channels are ubiquitous throughout the swath, but are particularly concentrated in the intermediate to bright unit in the swath center that terminates abruptly into a relatively radar-dark unit. A circular feature in the eastern portion of the swath appears to be an eroded impact crater. Results of T7 and T8 are discussed primarily in Lunine et al. (2008).

*T8.*The T8 pass consists of inbound radiometry, scatterometry and altimetry, SAR imaging, and then outbound radiometry, scatterometry and altimetry. T8 SAR, covering the equatorial region, has closely-spaced dunes that cover much of the swath and led to the secure recognition of these features (e.g., Lorenz et al. 2006b). Linear mountain ranges extend from 13–5°S and 198–225°W (e.g., Radebaugh et al. 2008). A few channels interpreted to be fluvial in origin are seen, as well as small circular features of unknown origin. T8 also, by design, imaged the Huygens landing site with radar for the first time.

T13. The T13 pass includes HiSAR and SAR, along with outbound altimetry, scatterometry, and radiometry. T13 SAR includes the central portion of Xanadu (from 10°S, 65°W to 12°S, 170°W), essentially equatorial, like T8 . The Xanadu radar-bright terrain has a “crinkled,” hummocky texture and a rugged surface cut by channels, and is characterized by irregular but not regionally raised topography (Radebaugh et al. 2010). Some circular features within Xanadu may be eroded impact craters (Wood et al. 2010). The plains adjacent to Xanadu have abundant dunes. Also to the west of Xanadu is

Guabonito, an 80-km-across possibly eroded impact basin (Wood et al. 2010, Lopes et al. 2010). A T13 HiSAR observation observed the Huygens landing site.

T15. The T15 pass consisted of radiometry data collection and HiSAR data only.

T16. T16 had inbound radiometry, scatterometry, and altimetry; SAR; then outbound altimetry. The T16 swath, the first obtained in the north polar region, has scattered lakes north of about 70°N (Stofan et al. 2006, Hayes et al. 2008a, Mitchell et al. in prep.]). Some lakes are only partially filled with dark material interpreted to be liquid hydrocarbons (Stofan et al. 2006, Lopes et al. 2007b), while other basin-shaped features without dark fill are interpreted as empty lakes (e.g., Hayes et al. 2008a). Channels are seen across the swath, along with some small hills, radar-bright patches. Dunes are located only at the southern end of T16.

T17. T17 was a SAR ride-along with INMS. T17 is a partial swath containing the impact crater Ksa (29 km) (Wood et al. 2010). The swath also covers part of the Fensal sand sea dunes (e.g., Radebaugh et al. 2008).

T18. T18 was an INMS ride-along, SAR only. T18 extends over the north polar lakes area. The southern portions of the swath have mottled plains, few channels and no dunes.

T19. T19 had inbound and outbound radiometry, scatterometry and altimetry, along with SAR imaging. The SAR swath extends from 2°S, 318°W to 42°N, 160°W, over the northern lake district. Bright, featureless patches occur throughout the swath, as well as dunes in the southernmost extent of the swath. Channels are seen throughout the region, particularly in association with the lakes. Some circular features of unknown origin are seen (Wood et al. 2010).

T20. The T20 pass consisted of HiSAR imagery and radiometry only.

T21. T21 was an INMS ride-along, with SAR, and outbound altimetry, scatterometry and radiometry. The T21 swath, 25°S, 290°W to 50°N, 195°W, is mostly characterized by dark, relatively featureless plains, scattered bright patches, dunes and streaks. Linear mountains with interspersed dunes cover about half the swath. A number of circular features of unknown origin are defined by a faint bright ring (Wood et al. 2010).

T23. T23 SAR was accompanied by inbound and outbound altimetry, scatterometry and radiometry. T23 contains a region of overlap with the Ta swath, including Ganesha. Also in the swath are abundant dunes, channels, and hills, the northern part of a bright flow, and a partial circular feature with morphology similar to that of Guabonito.

T25. T25 was a full Radar pass, with inbound and outbound radiometry, scatterometry, and altimetry, along with SAR imaging. The T25 SAR swath, located in the mid northern latitudes, has a possible cryovolcanic feature at 15°S, 40°W (Sotra Facula), surrounded by lobate deposits (Lopes et al. in prep.). The swath also is characterized by linear hills surrounded by fields of dunes, and some circular features that may be of impact origin (Wood et al. 2010). The swath covers part of the northern lakes region, including Mare Ligeia.

T28. T28 has inbound radiometry, scatterometry and altimetry, SAR, then outbound altimetry. The SAR swath covers the northern lakes region including the large seas. Near the seas, the plains are more textured and cut by channels, while to the south the intermediate to dark plains have dune fields and streaks, small hills, and circular to oval

bright rim features of unknown origin (Lopes et al. 2010). Significant overlap exists between T25 and T28, permitting stereo DEM generation (Kirk et al. in prep.). Lake-surface backscatter is discussed in Notarnicola et al. (2009).

T29. T29 was a full pass with inbound and outbound radiometry, scatterometry and altimetry, along with SAR imaging. The T29 SAR swath covers terrain similar to the T25 and T28 swaths. It has dark to intermediate plains, some lakes, circular features of unknown origin, and fields of dunes at low latitudes.

T30. T30 was also a full pass, with inbound and outbound radiometry, scatterometry and altimetry, along with SAR imaging. The inbound half of the pass was devoted to altimetry as it covered the previous SAR swaths T28/T29. The long pass of altimetry not only provides unique height data, it also allows diagnosing of some of the features of the altimetry measurement. A detailed discussion of altimetry observations is given in Zebker et al. (2009a).The T30 SAR swath also images the north polar seas (indeed, it was targeted specifically to observe Kraken Mare, initially suggested in ISS imaging). An inventory of lake/sea volume and dune sands was conducted by Lorenz et al. (2008b). In the radar-bright, often hummocky terrain surrounding the seas, channels are common. Radar-bright streaks to the south of the seas have also been identified in ISS images (Lopes et al. 2010, Perry et al. 2007). T30 featured the first “atmospheric sounding” altimetry/scatterometry observation to detect, or at least estabilish an upper limit on, rainfall (Lorenz et al. 2008g). These observations were also done on T36(1), T39(1), T41(1), T43(1), T44(1), T48(1), T49(2), T50(2), T60(2),T 61(1), and T64(2). The numbers in parentheses indicate the number of separate atmospheric probe measurements, each of which consists of two segments—a tone and a chirp measurement using scatterometer mode to give a low noise floor and 4 seconds total of data. Most of these observations have just one pair positioned at the lower altitude edge of altimetry while the beam is still close to nadir to avoid surface echo return. A few have two pairs positioned at either edge of an altimeter segment.

T36. T36 was a ride-along SAR pass with INMS, broken up into SAR imaging segments (S01 and S02), covering a variety of terrains in the mid-southern latitudes, and partially overlapping T7. It has multiple patches of bright to mottled plains and hummocky terrain cut by channels. It has circular features of unknown origin, including some that resemble empty lakes. The pass also had inbound and outbound radiometry, scatterometry and altimetry.

T39. T39 has an imaging segment as well as inbound and outbound scatterometry and altimetry. T39 is a partial ride-along, with regular SAR pointing on the inbound side, and ride-along SAR (with INMS) for the first 5 minutes after closest approach. Like T36, T39 has a sweeping turn across the surface of Titan that begins after the INMS ride-along ends, and ends at the start of outbound altimetry. Additional SAR imaging is performed during the turn. The T39 swath over the south polar region has patches of hummocky terrain surrounded by plains of intermediate backscatter, labyrinth terrain (Malaska et al. 2011), apparent sedimentary deposits, a few lakes near the pole, and abundant channels (Stofan et al. 2008). Some dunes are seen at the northernmost portion of the swath.

T41. T41 has three short SAR segments (S01, S02, and S03) due to an unusual pointing design. It is right-looking and switches to left-looking in the middle. It overlaps T13 and

sweeps to the east to connect to the T17 ride-along swath. The inbound imaging is right-looking and covers the Hotei region (Soderblom et al. 2009). The outbound imaging is left-looking to cover the probe landing site. The inbound segment contains lobate flow features in Tui Regio (Barnes et al. 2006), with channels draining down towards it from mountainous terrain in Xanadu. The closest approach segment is characterized by mottled to featureless plains. The outbound swath has dunes, streaks and patches of radar-bright hummocky terrain.

T43. T43 has a SAR imaging observation as well as inbound and outbound scatterometry, radiometry and altimetry. At the end of the outbound altimetry, two short observations in scatterometry mode are inserted to look for echo energy coming back from the atmosphere. The SAR swath is left-looking and was adjusted to collect data over the Tortola Facula (Sotin et al. 2005), and to provide better altimeter track crossings. The T43 SAR swath crosses the equatorial region at Xanadu (Radebaugh et al. 2010), covering its mountainous and hummocky terrains between the T13 and T41 swaths. The swath also contains featureless to mottled plains, circular features and dunes. SARTopo and altimetry data through T43 were used to estimate Titan's global shape (Zebker et al. 2009b).

T44. For T44, data volume for this pass was reduced from the nominal value owing to DSN allocation changes to support the Phoenix landing on Mars. No hi-altitude imaging was performed, and data rates were reduced from normal values in several places. Most of the main SAR swath was preserved at the nominal rate. At the start of the inbound altimetry, some special nadir pointed calibration observations were inserted in all four modes to collect data for radiometric cross-calibration. At the end of the outbound altimetry, two short scatterometry observations were done to look for echo energy coming back from Titan's atmosphere. The T44 swath also covers Xanadu, showing channels cutting much of the mountainous terrain. Also in the swath are regions of plains with dunes. Lorenz and Radebaugh (2009) present a map of dunes observed with SAR throughout the Prime Mission, Ta–T44.

T48. The T48 swath is a ride-along swath, with accompanying HiSAR and inbound radiometry, scatterometry and altimetry, and outbound radiometry. It covers the margin of Xanadu and the flow-like features of Tui Regio, also seen in T41. Also seen are channels, and dark equatorial plains with dunes.

T49. T49 consisted of a south polar SAR pass, a switch to altimetry data collection, back to SAR crossing T8 to T21, then to altimetry, with HiSAR data collection and outbound scatterometry and radiometry. The SAR imaging contains hummocky and lobate terrains in the first segment, and dark plains with dunes in the second segment. The altimetry observation includes coverage of Ontario Lacus: Wye et al. (2009b) present the constraints placed by the echo shape and amplitude on the roughness of Ontario; Lorenz et al. (2010b) compare Ontario with Racetrack Playa in Death Valley.

T50. T50 was a ride-along pass, with inbound and outbound scatterometry and radiometry and HiSAR. There is an outbound high-altitude image segment, two sweep turn image segments, and the ride-along swath that extends from approximately T8 to T7. It covered the area of the VIMS cloud source (Rodriguez et al. 2009) and mountains to the east of the T7 swath. Dunes, numerous patches of bright hummocky materials, and some channels characterize the plains in this region.

T55. The T55 observation consisted of inbound and outbound HiSAR, with the inbound HiSAR near Ta, altimetry, regular SAR crossing T48 to the south pole, then a switch back to altimetry, scatterometry, and radiometry. The swath overlaps portions of the T39 swath, and contains a great diversity of terrains including lobate deposits, hummocky and labyrinth terrain, and channels in the south polar regions extending to dune-filled plains close to the equator.

T56. T56 was HiSAR, followed by altimetry, regular SAR, altimetry, then outbound radiometry and scatterometry. The swath extends from the equatorial region to the south polar region, covering plains with dunes and circular features of unknown origin, hummocky and mountainous terrain, and lobate deposits.

T57. The T57 observation was a ride-along over Ontario Lacus, followed by altimetry, HiSAR, altimetry, radiometry, and scatterometry. The swath covers, along with a portion of Ontario, plains with dunes, streaks, hummocky and mountainous terrain and circular features of unknown origin.

T58. The T58 pass is a partial pass that consisted of inbound scatterometry calibration and HiSAR. The T58 SAR swath covers Ontario Lacus in the south polar region, as well as empty lakes, channels and labyrinth terrain in that region. Further from Ontario, the swath is characterized by plains with streaks and dunes, as well as hummocky terrains.

T59. T59 is a ride-along pass with inbound and outbound radiometry and HiSAR. T59 is adjacent to T58, and cuts across the southern latitudes, with its complex plains regions with dunes, streaks, circular features of unknown origin, channels and hummocky and mountainous terrains.

T61. T61 has an inbound high-altitude SAR imaging division to provide a special dunes observation between 3°S, 156°W and 12°S, 160°W, with 26.5-degree slews, to provide incidence and azimuth viewing angle diversity to study dune geometry and backscatter response. Incidence angles vary between 11° and 23°; azimuth angles vary between 250° and 320°. T61 begins with a scatterometry raster, followed by the special dunes observation, followed by an atmospheric probe observation, and then regular altimetry and a SAR imaging pass that overlaps T8 coverage in the equatorial region. The T61 swath covers a portion of Adiri, with its linear hummocky mountains and dunes to the Belet sand sea. Atmospheric probe observations (like that on T30) use tone only transmissions in scatterometer mode to achieve a very low noise floor. They are conducted during low altitude altimetry passes so that backscatter signals from the atmosphere can be separated from the surface response, and they are intended to look for methane “rain” drops that might be within the beam footprint.

T64. T64 was an excursion back to the northern hemisphere, extending from northern mid-latitudes to the lakes region near the north pole. The pass has no radiometry or scatterometry, but did include a dual polarization experiment crossing the northern part of the T43 pass. This experiment involved two high-altitude imaging scans using orthogonal polarizations to look for polarization variation of features observed in the T43 swath. To the south of the lakes, the plains are relatively featureless, with patches of hummocky terrain and some bright streaks. The pass had no radiometry or scatterometry, but did include a dual polarization experiment crossing the northern part of T43.

T65. T65 has two segments, one veering a portion of Ontario Lacus, and the other cutting across the diverse terrains of the southern hemisphere.

T69. T69 consists of HiSAR and radiometry only.

6.2 Ontario Lacus: A Case Study

A recent series of studies of Ontario Lacus near the south pole of Titan illustrate the benefit of utilizing multiple radar data sets to address scientific problems. Ontario is one of the few lakes in the south polar region, and the largest, with an area over 15,600 km^2 (Figure 6-1). The nature of the lake, the surrounding terrain, and lacustrine processes at Ontario have been determined through the combined utilization of SAR image, altimetry and radiometry data (Wye et al. 2009b, Wall et al. 2010, Hayes et al. 2010).

SAR images of Ontario at 350- to 500-m-resolution cell sizes in the T57 and T58 swaths obtained in 2009 reveals the complex shoreline of Ontario, with a relatively smooth northern shore resembling a terrestrial wave modified beach (Figure 6-1) (Wall et al. 2010). Multiple lineations parallel to the lake edge along this shoreline suggest higher lake levels in the past; a higher shoreline for Ontario was observed in ISS images in 2005 (Turtle et al. 2009, Barnes et al. 2009). The western shoreline of Ontario has more rugged terrain, with lake liquids flooding low-lying areas. To the southwest, a delta has formed in the lake at the terminus of a broad channel ~1 km wide. The delta has an area of over 140 km^2, much smaller than terrestrial deltas fed by similar-size rivers. Wall et al. (2010) interpret this to indicate low sediment supply, slow flow velocity and a low sediment transport capability.

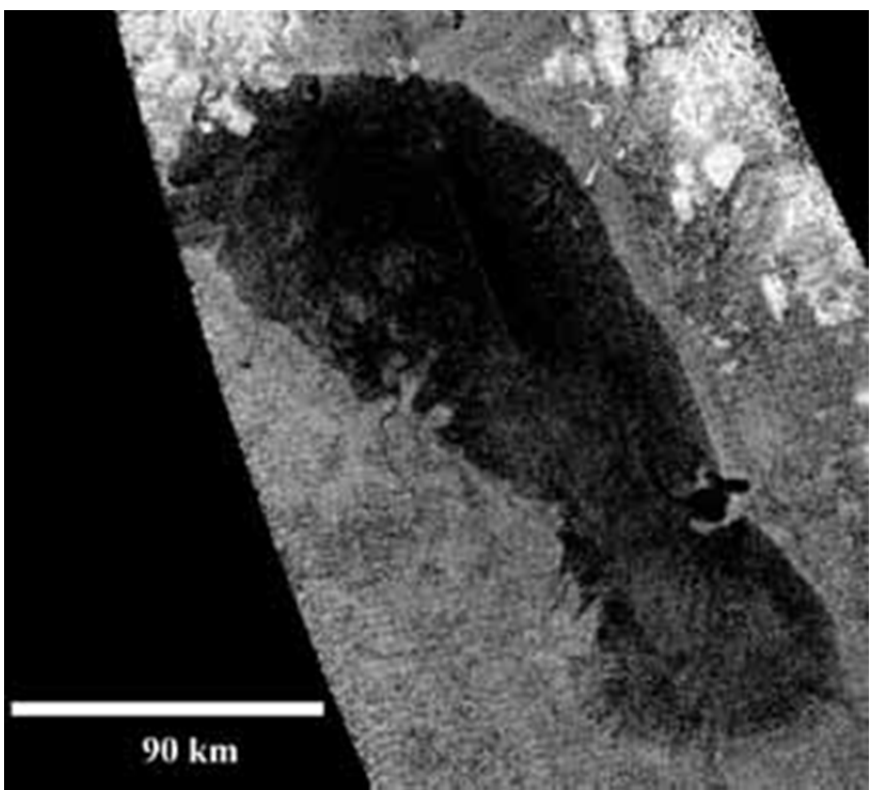

Figure 6-1. Cassini RADAR image (PIA13172) of Ontario Lacus.

Altimetry data indicate the lake lies in a shallow depression, with the mountainous terrain to the west of the lake having elevations of 300-500 m. The region tilts to the west, possibly indicating the lake has formed within a graben (Wall et al. 2010). At the time the altimetry data were taken, the lake surface was extremely smooth (Wye et al. 2009b), indicating no wave activity. The apparent wave-modified beach indicates that the lake surface is more dynamic at times, likely relate to seasonal cycling (e.g., Wall et al. 2010).

The lake is characterized by high emissivity, with a maximum brightness temperature of 88.5 K (with absolute calibration of ~1–1.5 K [Janssen et al. 2009]) corresponding to a physical temperature of 90.0–90.8 K, allowing for a methane-ethane mixture (i.e., Paillou et al. 2008b, Wall et al. 2010). This slightly cooler-than-average temperature (~92 K [Jennings et al. 2009]), if real, could result from evaporative cooling (e.g., Mitri et al. 2007).

The radar backscatter of the lake surface decreases exponentially away from the shoreline, consistent with attenuation of the radar signal in a deepening liquid (Hayes et al. 2010a). From this, Hayes et al. (2010) estimated a loss tangent for the liquid consistent with liquid hydrocarbons and calculated a bathymetry map for Ontario. Hayes et al. (2011) utilized these data and the recession observed between the ISS and radar observations to calculate a reduction in the depth of the lake between 2005 and 2009 of 4 ±1.3 m.

These studies illustrate the importance of utilizing all available data sets to fully characterize processes on Titan. SAR data provides morphologic and surface properties information, altimetry data can constrain the properties of the lake surface as well as help constrain the origin of the surrounding terrain, while the radiometry data provide insight into the lake liquid composition and state. In addition, comparison to other Cassini data sets such as ISS and VIMS data, allow more complete interpretations of lake character and evolution.

7 Data Outages, Anomalies, and Related Data Issues

In all planetary missions, including Cassini, anomalies occur that affect data return in various ways. It is important to note that while this section points out some of the times when various parts of the Cassini systems (which include not only the spacecraft and ground systems but also planners, sequencers, spacecraft engineers, mission operators, DSN station operators, managers, scientists, etc.) in some way didn't work right. To keep a proper perspective, the reader is reminded that most of the time these systems perform flawlessly; in fact, the Cassini systems are remarkable in that they have had so few of these issues. Most issues have been small, and the amount of data lost has been minimal relative to that of other planetary missions. In this section we first report anomalies in spacecraft, commanding, or ground system that resulted in known loss or corruption of RADAR data. Second, we report anomalies for which there are no known issues with RADAR data, in the hope that if later researchers should find issues with the related data they may be able to better characterize them with the knowledge of coincident problems.

Before we review these events, some introduction to the details of the Cassini and Cassini RADAR ground system terminology is necessary. During the event planning period, each RADAR observation is given a unique identifier of the format tt_nnn_s, where tt is an abbreviated identification of the target (e.g., ti = Titan), nnn is the Saturn orbit number, and s (if supplied) is a number showing the temporal order of the observation within the pass or Saturn orbit as appropriate. Note that due to the late change of Huygens' deployment, the first three orbits of Saturn were called a, b, and c (shown in this ID as 00a, etc.), followed by the number 3 and so on. Thus ti_00b_1 is the first observation of Titan in Saturn orbit b.

All instances of missing data are indicated in the comprehensive downlink spreadsheet provided in Appendix 4.

7.1 Major Data Outages and Corruption

Anomalies have their most obvious effect when data are lost completely. Data loss can result from failure of the instrument to acquire data, failure of the spacecraft to collect, store, or transmit data, or failure of the ground system to receive and process data properly. Less obvious, and potentially more damaging to subsequent research, are data that are present but corrupted. Processing of SAR-mode data is inherently resistant to errors, since it tends to combine data taken at separate times, but this is not necessarily a good thing, as the resulting compressed image data may appear to be normal but have different quantitative characteristics (e.g., number of looks, SNR, etc.) caused by the corrupted raw data.

7.1.1 Dione/Mimas 00b (Total Loss)

On December 16, 2004, substantial gaps in all science data were noticed immediately following that day's downlink. RADAR data were received from the instrument warm-up period but not during actual science data acquisition. Investigation revealed that during data acquisition, a command timing error caused the science data to be not recorded on the SSR. All RADAR science data were lost. RADAR observations

di_00b_1 and mi_00b_1of Dione and Mimas respectively, were completely lost. For further details see JPL ISA Z85233[2].

7.1.2 The T7 Anomaly

On September 9, 2005, a Cassini downlink to the Goldstone 70-m antenna (DSS14) failed when the antenna refused to point correctly. The antenna operator investigated and found that the antenna had been instructed to point to the spacecraft location in the year 2023 rather than 2005. After correcting the incorrect date the antenna pointed and the remainder of the downlink was received. Unfortunately, the playback from the spacecraft was also imperfect and revealed a flight software error involving the way that data playbacks from the spacecraft were managed. Following this pass the flight software was fixed (see ISA Z87618, ECR 104281, P/FR Z87475 for details).

From a data standpoint, the net result is that the T7 SAR data terminate at approximately 170°W, 70°S, as shown by the dashed line in Figure 7-1. Some data degradation may be present at the SE end of the data, just prior to the end.

Following the Titan T13 encounter on May 12, 2006, when the spacecraft was expected to downlink, the ground system did not acquire its signal. A failure in the spacecraft's power subsystem's solid-state power switches (see Section 2.1) was diagnosed, but the downlink transmission was lost. A second downlink was performed, and most of the radar data were recovered, but minor losses remain. The net effect is that the T13 swath does not extend as far to the east as planned.

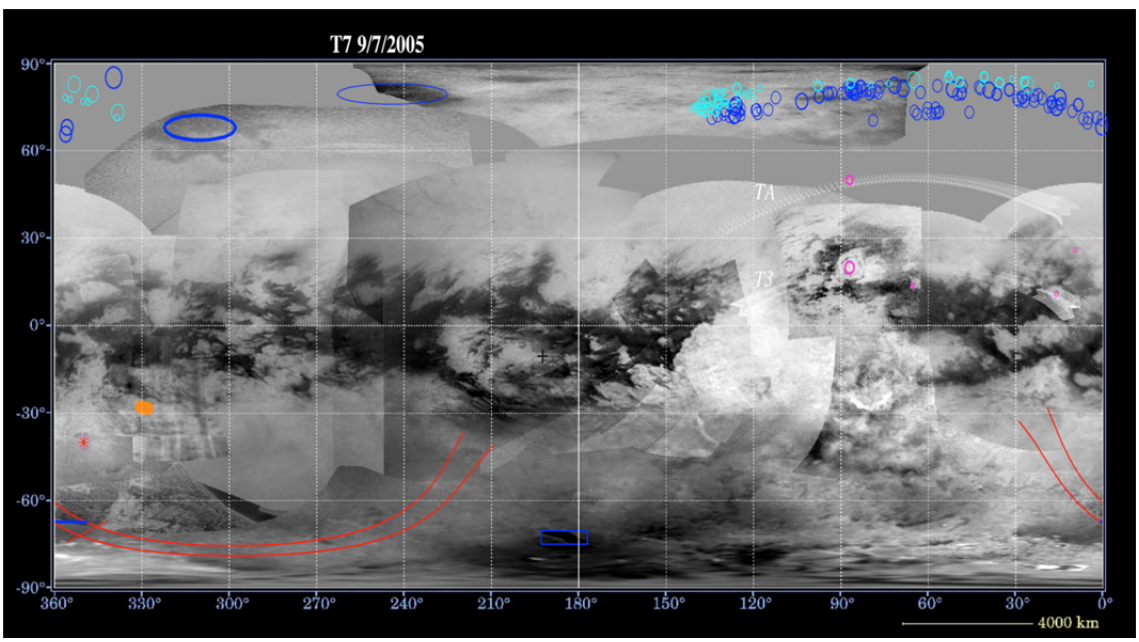

Figure 7-1. T7 planned swath with actual coverage limit marked (red dashed line at lower left). Note that the horizontal scale in this figure does not follow convention.

[2] JPL ISAs (Incident/Surprise/Anomaly reports), ECRs (Engineering Change Requests), P/FRs (Problem/Failure Reports) and DRs (Discrepancy Reports) can be obtained from the Jet Propulsion Laboratory, 4800 Oak Grove Drive, Pasadena CA 91109 USA.

7.1.3 The T60 Anomaly

On August 9, 2009, the spacecraft was to downlink Titan pass T60 to the Goldstone, CA DSN antenna complex, using the 70-m antenna (DSS-14). DSS-14 experienced an azimuth antenna bearing problem when tracking the Mars Reconnaissance Orbiter spacecraft prior to the start of the Cassini track and could not be moved. A 34-m antenna, DSS-25, was "borrowed" from the Kepler and New Horizons projects; it was able to communicate with Cassini and provided uplink and coherent tracking for navigation. Unfortunately, the downlink telemetry data rate was too high for the smaller antenna and the entire downlink, including T60, was lost. For further details, see JPL Discrepancy Report DR G109608, "All TLM from T60 lost, ALC problem."

7.1.4 Iapetus 49

Cassini's solid-state power switches have turned themselves off spontaneously several times during the mission, probably because of cosmic ray interference. On September 11, 2007, one such event turned off Travelling-Wave Tube Amplifier A, which sent the spacecraft into safing. RADAR Iapetus Pass 49, scheduled for later that same day, did not execute (ISA# Z91542).

7.1.5 The T64 Anomaly

On Dec 29, 2009, a Cassini downlink to the antenna complex in Madrid, Spain, was significantly affected by heavy rain. Seventy-six minutes of telemetry were lost due to both rain and an incorrect set of parameters used for the receiver (downlink controller table). Even though a second, redundant playback of the spacecraft solid-state recorder was planned and executed, the redundant playback was in the same pass and was also affected. As a result, data from Titan Pass T64 were very noisy. When these noisy data were processed through the Cassini ground processing software, incorrect bits resulted in lost data packets, which in turn caused the Cassini RADAR data processor to lose entire frames of data The resulting SAR data contain many gaps, some large (DR M105593).

It is sometimes possible to recover corrupted data by rerunning the ground software that detects valid data, and attempts at recovering some of the T64 losses are underway at this writing (Figure 7-2). If significant amounts of data are recovered, this pass will be redelivered to PDS.

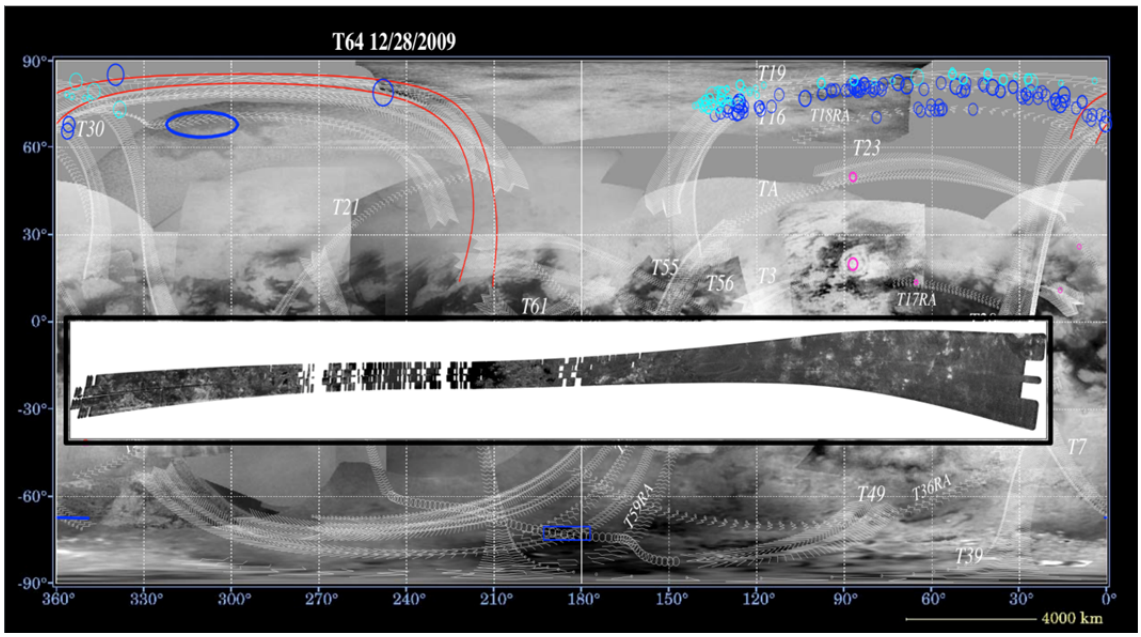

Figure 7-2. T64 planned swath and actual data prior to recovery efforts (inset, in oblique cylindrical projection).

7.2 Other Experiment Anomalies

Numerous minor anomalies have occurred, in instrument commanding and in spacecraft and ground systems, that have had minor effects on data products. It is common, for example, when telemetry modes are changed for a variety of reasons or receiving antennas are swapped (for example, due to Earth's rotation), to lose a small number of data packets. Miscellaneous "bit hits" occur in all data, including RADAR, for reasons that are often not known. These events can cause much larger losses, as ground processing software often excludes entire packets of data when only a few bits are missing. Such losses generally result in a lower number of looks rather than image gaps and would thus go unnoticed. Some quantitative use of the data will be affected. Missing packets in SAR mode, for example, may reduce the number of looks and thus the "grainy" aspects of the images, which could affect data analysis; other modes may be affected differently. Similar effects have resulted at ends of observations where data volume had to be trimmed to fit allocations (see below). For the benefit of users facing the latter effect, a spreadsheet listing all RADAR data takes and associated command history and lost data is included in Appendix 4.

7.3 Complexities to Consider When Interpreting SAR Images

Special care is needed when interpreting SAR images. Synthetic aperture image construction includes complexities that may be unfamiliar to researchers who are used to optical imagery. First, the viewing geometry can dramatically affect the images. In extreme cases, when two images of the same region have been observed from different orientations, one image may even look like a photographic negative of the other.

Less extreme cases in which the contrast of individual features is reversed or the edges of features appear to move slightly are more common. Radar returns are highly

dependent on look geometry. Researchers unfamiliar with SAR often infer changes over time in scenes where the only real change is the viewing geometry.

A second complication for SAR interpretation occurs in dark regions. There is often a strong temptation to assign meaning to fuzzy features near the noise floor. Often such features are purely due to noise. A good indicator for this is the presence of negative backscatter values in the floating point (BIF*.IMG or BIS*.IMG) noise-subtracted BIDR files. Negative backscatter is physically impossible but statistically meaningful. It means there is insufficient evidence to conclude that any radar energy returned from the surface. It occurs only in regions where the signal level is much less than thermal noise. One should not assign meaning to features in any region with a large number of negative values (~25% or more) unless one can formally show statistical significance using an accurate model of radar noise. An added complication for Cassini SAR in dark regions is that the central narrow antenna beam (Beam 3) has much higher signal-to-noise ratio than the wider beams on either side of it. When contrast stretching dark regions, it is common to observe seams along the edge of the center beam where the noise variance drops off rapidly. In this event there may be useful information in the Beam 3 portion of the data even if the other beams detect no signal, but only if the Beam 3 region contains few negative values. The (BIM*.IMG) beam mask BIDR files can be used to determine which beam contributes to each pixel in the image.

Linear artifacts are a third important feature of SAR imagery. Artifacts that look like bright or dark lines running along the long dimension of the SAR swath between beams or at the edges of the swath are common. These artifacts are primarily caused by residual errors in calibration due to surface topography. This effect is utilized by the SARTopo technique to estimate surface heights along the beam seams. A repeated pattern of lines in the orthogonal direction (perpendicular to the long axis of the SAR strips) can also occur. This effect is most pronounced when the number of independent looks for each pixel is less than 4. The number of looks for each pixel is contained in the BIL*.IMG BIDR files. A common rule of thumb for artifacts is that if it looks artificial it probably is. For a good tutorial on the interpretation of SAR images, see Ford et al. (1993).

8 Case Studies in Quantitative Use of Cassini RADAR Data

Most scientific analyses of Cassini RADAR data performed to date have used SAR imagery, altimeter surface heights, scatterometer backscatter values (sigma-0), or radiometer temperatures. These are the primary scientific measurements in the data set. The SAR imagery is contained in the BIDR files. The other values are in the SBDR files. Both of these data sets are archived by PDS. A handful of more data intensive studies have utilized intermediate or ancillary data and/or used different data types in combination in a manner in which the relationship between the various data elements is crucial to the investigations. These studies have sometimes even involved reprocessing data from raw radar returns. In this section, we describe four previous studies and briefly describe what a user would need to know to replicate these studies. The goal of this section is to provide interested users with enough background to get them started on similar data intensive analyses of their own.

8.1 Case 1: Topography from SAR Data

In Stiles et al. 2009 a technique (SARTopo) is described that estimates Titan surface heights using SAR mode data. The primary benefit of the technique is the production of height profiles along the long dimension of each Cassini SAR image of Titan. As mentioned in section 3.2.2.b., it is planned to archive these profiles in PDS by the end of 2012. To produce these height profiles, the authors took advantage of the fact that Cassini obtains overlapping SAR imagery from multiple beams (antenna feeds) (see also Section 3 above). The overlap between beams is small and is not included in the BIDR image records themselves. Instead, an algorithm is used to select the beam with the highest quality imagery and only that data is used. To produce the SARTopo heights, it was necessary to reprocess individual beam images from the raw echo returns. The technique depends on the precise manner in which the location and magnitude of each SAR pixel are affected by variation in surface height. Understanding the relationship between surface height and SAR imagery is important not only to estimate surface heights, but also to understand how surface height variation can impact other quantitative studies of SAR imagery. (See Case 2 below for an example of such effects.)

In SAR, unlike optical imagery, the image pixels can be located on the target body without precise knowledge of the observer's orientation (e.g., spacecraft attitude). Instead, all that is required is knowledge of the shape of the target body and the location and velocity of the observer with respect to that body. SAR processing produces pixels by breaking up the return energy of the radar signal into round trip time and Doppler frequency bins. One can compute the distance (range) from the spacecraft to the ground location of each pixel from its round trip time. Similarly one can compute the relative velocity with respect to the spacecraft of each pixel from its Doppler. At that point, one has three critical pieces of information about the location of the pixel: 1) the pixel is on the surface of a sphere whose radius is the range and whose center is the spacecraft location; 2) it is on a cone centered on the spacecraft velocity vector, whose circumscribed angle is determined by the relative velocity of the ground location (and thus by the Doppler); and 3) it is on the surface of the target body. By intersecting the range sphere and the Doppler cone with a model of the surface of the target body, we

obtain the locus of possible locations of the pixel. For typical SAR geometry and a spherical target body, there are only two points that intersect all three surfaces. The two points are far enough apart that a very coarse knowledge of spacecraft attitude (tens of degrees) is sufficient to select the correct pixel location. Once pixel locations are determined, they are used to project the SAR image onto the target body and to calibrate the image. Errors in the presumed shape of the target body lead to both mislocation (incorrect placement on the target body) and miscalibration (applying incorrect correction factors to pixel values due to poor knowledge of where the pixel falls in the antenna gain pattern).

Of course, "errors in the presumed shape" are just another name for surface heights. Because the surface of Titan is typically within 1 km of the reference sphere the resultant mislocation error is usually small. Miscalibration is also small except in regions near the edge of beams. The SARTopo technique estimates surface heights from observed SAR miscalibrations. Cassini's antenna has multiple beams (feeds), so that some points on the ground are observed from two different beams. For different beams, the mislocation error due to surface height is the same, but the miscalibration error is different and of opposite sign. Nonzero surface heights, therefore, result in apparent differences in pixel values between overlapping single beam SAR images. The SARTopo technique first processes single beam SAR images for all 5 Cassini beams and 17 candidate surface heights (-2 km to +2 km from the 2575-km-radius Titan reference sphere in steps of 250 m). It then determines the surface height profiles that minimize the difference between the overlapping SAR images. Sources of error that affect SAR pixel calibration also affect SARTopo height estimation. The three largest sources of error are 1) spacecraft attitude knowledge error, 2) thermal and speckle noise, and 3) SAR ambiguities. Although, SAR location accuracy is insensitive to spacecraft attitude error, calibration accuracy is not. The gain of the antenna varies with the angle between the antenna beam boresight and the observation vector. If the beam boresight points directly at a pixel location, the antenna gain of the pixel is high. As the boresight moves away from the pixel, its gain quickly decreases. For this reason, a precise knowledge of the orientation of the beam (and thus the spacecraft attitude) is needed for calibration. A network of overlapping SARTopo and nadir altimetry profiles from different Titan flybys is used to correct systematic height errors due to spacecraft attitude. Errors due to thermal and speckle noise are reduced by averaging height estimates from hundreds of SAR pixels, thus trading spatial resolution for height accuracy. SAR ambiguity errors occur at particular region in the SAR imagery. SARTopo heights from this region are discarded. Figure 8-1 is a global map of all SARTopo heights obtained during the primary and first extended Cassini missions.

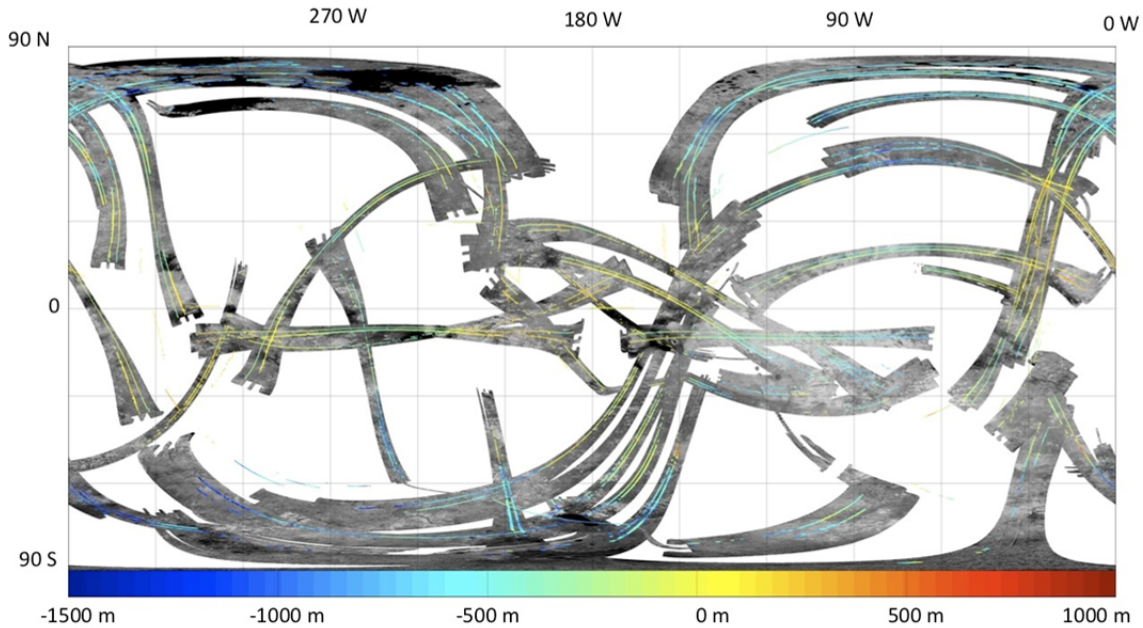

Figure 8-1. Global map of Titan surface heights for Cassini RADAR flybys in prime and first extended mission (Ta–T65 inclusive). Nadir altimetry height profiles can be distinguished because they are not parallel to and/or not within SAR swaths.

Because the SARTopo technique involves reprocessing SAR images, it requires raw radar echo data, instrument transmit and receive parameters, antenna gain patterns, calibration constants, spacecraft ephemeris, and spacecraft attitude data as input. All of these are available in the Long Burst Data Record files, instrument configuration files, or other files archived in PDS. The processing of the SAR images from the raw data involves three steps: 1) Synthetic Aperture Processing: Energy in the raw echoes in broken up in to 2-D image bins corresponding to range and Doppler (azimuth); 2) Calibration: Raw counts are converted to a geophysical quantity NRCS that corresponds to the ratio of the returned energy to what one would expect from a uniform scatterer; 3) Geolocation: The location on Titan from which the energy in each image pixel was scattered is determined. Because SARTopo has to do a full reprocessing of the images, it requires input data to do all three of these tasks. This is a

superset of the data needed to do each of the other example studies. Tables 8-1 through 8-3 list the full set of parameters needed for each step and how to find them in the PDS volume. The parameters in the LBDR files are reported for each radar measurement cycle (burst). The configuration file parameters are contained in the single configuration file archived with each PDS volume. At most four to five instances of each a parameter (organized as keyword/value pairs) are contained in the configuration file. The multiple instances correspond to different radar modes (SAR high-resolution, SAR low-resolution, and altimeter low-resolution [scatterometer]) or different antenna beam numbers (1–5). For each radar measurement cycle, the beam number is available and so are the radar_mode and receiver_bandwidth (rc_bw) parameters that can be used to determine the mode. Special calibration modes are indicated by flag bits in the calibration source (csr) parameter in the LBDR files. Locations and descriptions of all parameters in the LBDR files are detailed in the DOCUMENTS/BODPSIS.PDF file included in each PDS volume.

Table 8-1. Data needed to perform synthetic aperture processing.

PARAMETER DESCRIPTOR	SYMBOL	FILE IN PDS VOLUME	PARAMETER NAME(S)
Raw radar echo counts	$s(t)$	DATA/LBDR/LBDR*.ZIP	Sampled Echo Data (See Section 2.3.4 of BODPSIS.PDF)
Spacecraft velocity	v	DATA/LBDR/LBDR*.ZIP	sc_vel_target_x, sc_vel_target_y,sc_vel_target_z
Spacecraft position	u_{sc}	DATA/LBDR/LBDR*.ZIP	sc_pos_target_x, sc_pos_target_y, sc_pos_target_z
Beam boresight orientation	u_{bore}	DATA/LBDR/LBDR*.ZIP	act_centroid_lat, act_centroid_lon (Boresight location on reference sphere can be used to compute the boresight orientation)
Pulse repetition interval	t_p	DATA/LBDR/LBDR*.ZIP	PRI
Number of pulses transmitted	N_p	DATA/LBDR/LBDR*.ZIP	num_pulses
Chirp start frequency	f_c	DATA/LBDR/LBDR*.ZIP	chirp_start_freq
Chirp step frequency	Δf_c	DATA/LBDR/LBDR*.ZIP	chirp_freq_step
Chirp length	Δt_c	DATA/LBDR/LBDR*.ZIP	chirp_length
Number of chirp steps	N_c	DATA/LBDR/LBDR*.ZIP	num_chirp_steps
Transmit frequency	f	CALIB/CONFIG	Keyword = carrier_frequency
Beam number	b	DATA/LBDR/LBDR*.ZIP	beam_number
Radar mode	m	DATA/LBDR/LBDR*.ZIP	radar_mode
Sampling frequency	f_{adc}	DATA/LBDR/LBDR*.ZIP	adc_rate
Receive window delay	t_{rx}	DATA/LBDR/LBDR*.ZIP	rx_window_delay
Receive window length	Δt_{rx}	DATA/LBDR/LBDR*.ZIP	rx_window_pri (units are PRI)
Measurement start time	t_0	DATA/LBDR/LBDR*.ZIP	t_ephem_time
Transmit delay	t_{tx}	DATA/LBDR/LBDR*.ZIP	transmit_time_offset
Receiver bandwidth	B	DATA/LBDR/LBDR*.ZIP	rc_bw

Table 8-2. Data needed to calibrate SAR imagery.

PARAMETER DESCRIPTOR	SYMBOL	FILE IN PDS VOLUME	PARAMETER NAME(S)
Antenna gain pattern	G	CALIB/BEAMPAT/BEAM*_V01.PAT	See DOCUMENT/VOLSIS.PDF for description
Spacecraft position	p	DATA/LBDR/LBDR*.ZIP	sc_pos_target_x, sc_pos_target_y, sc_pos_target_z
Beam boresight orientation	u_{bore}	DATA/LBDR/LBDR*.ZIP	act_centoid_lat, act_centroid_lon
Attenuator gain	G_a	DATA/LBDR/LBDR*.ZIP	at1_tot, at3_tot, at4_tot for beams (1,2), (3), and (4,5) respectively.
Transmit frequency	f	CALIB/CONFIG/PCF*.CFG	Keyword=carrier_frequency
Transmit power	P_t	CALIB/CONFIG/PCF*.CFG	Keyword = Pt
System noise temperature	T_r	CALIB/CONFIG/PCF*.CFG	Keyword = SYSTEM_TEMPERATURE_XXXX where XXXX is ALTH, ALTL,SARH or SARL depending on radar mode
Echo-count-to-power conversion factor	C	CALIB/CONFIG/PCF*.CFG	Keyword = squared_deviation_of_system_noise _input_at_XXXX where XXXX is ALTH, ALTL, SARH or SARL depending on radar mode.
Beam number	b	DATA/LBDR/LBDR*.ZIP	beam_number
Radar mode	m	DATA/LBDR/LBDR*.ZIP	radar_mode

Table 8-3. Data needed to geolocate SAR imagery.

PARAMETER DESCRIPTOR	SYMBOL	FILE IN PDS VOLUME	PARAMETER NAME(S)
Spacecraft velocity	v	DATA/LBDR/LBDR*.ZIP	sc_vel_target_x, sc_vel_target_y, sc_vel_target_z
Spacecraft position	u_{sc}	DATA/LBDR/LBDR*.ZIP	sc_pos_target_x, sc_pos_target_y,sc_pos_target_z
Titan pole location	u_{pole}	DATA/LBDR/LBDR*.ZIP	pole_right_ascension, pole_declination
Titan rotation angle	ω	DATA/LBDR/LBDR*.ZIP	target_rotation_angle
Titan spin rate	$d\omega/dt$	DATA/LBDR/LBDR*.ZIP	target_rotation_rate
Beam boresight orientation	u_{bore}	DATA/LBDR/LBDR*.ZIP	act_centroid_lat, act_centroid_lon
Transmit frequency	f	CALIB/CONFIG/PCF*.CFG	Keyword=carrier_frequency

8.2 Case 2: Titan Pole and Spin Rate Estimation

The second example study is detailed in Stiles et al. (2008). As was done for Venus using Magellan data in Davies (1992), the authors of this study used SAR imagery of the same features taken months and years apart to refine the pole location and spin rate of Titan. For the purposes of this discussion we refer to the technique as SAR Spin Model Estimation (SARSME). The authors used apparent misregistrations of the observed features to constrain the motion of Titan's surface about its pole during the time period observed.

SARSME is a three-step procedure. First, one selects a set of recognizable landmarks that have each been observed in two different SAR images obtained at different times. Second, one locates the landmarks in the inertial frame using the Doppler frequency and range of each landmark, and the spacecraft's inertial frame position and velocity vectors. Finally, one estimates the spin state parameters by minimizing the misregistration error, that is, the apparent movement in Titan body fixed coordinates of

the landmarks between observation times. In this manner, Stiles et al 2008 fit a 6-parameter spin model including: the right ascension and declination of Titan's pole, and Titan spin rate at 19:16:25 UTC on Aug 1, 2006, and the first derivatives of these three parameters with respect to time. The strongest conclusion of the study was that the obliquity (angle between Titan's pole and the normal vector to its orbit) was 0.3 degrees not 0 degrees as had been assumed previously (Davies et al., 1989). When this obliquity was accounted for, the RMS misregistration of the observed features dropped from 20 km to 2 km.

SARSME is complementary to SARTopo. While SARTopo estimates heights from SAR calibration error and is insensitive to location error, SARSME estimates the location of Titan's pole and its spin rate using SAR location error and is insensitive to calibration error. Because calibration accuracy depends strongly upon attitude knowledge, SARTopo's largest error source is attitude knowledge error. Because SAR geolocation does not depend on spacecraft attitude, SARSME is insensitive to attitude error. Because of the relationship between the two techniques, each can be used to refine the results of the other. Using SARSME to obtain a better spin model for Titan, allows one to better geolocate SAR data and its colocated SARTopo measurements. As we mentioned before, SARTopo height accuracy is not directly affected by location error. Both single beam images used in SARTopo have the same location error, so one can use the differences in their pixel values to determine a height estimate without concern for misregistration error. Nonetheless a more accurate knowledge of the location of the height measurements on the surface of Titan is useful. An accurate spin model is also needed to properly align SARTopo profiles and nadir altimetry profiles from different Titan flybys as is required to correct SARTopo for attitude errors. Conversely, SARTopo heights can also be used to refine SARSME spin models. The primary error source in SARSME involves human error in the matching up of landmarks between SAR images. Differences in resolution between SAR passes make it hard to match up features, thereby compounding this error. One can reasonably assume that feature-matching error is random, so that one can beat down the errors by acquiring a large number of landmarks. The second largest error source is errors in locating the features due to errors in the presumed shape of Titan. This error source is not random, because Titan's shape diverges from a sphere in a systematic (nonrandom) manner that is primarily due to its observed oblateness. SARTopo heights or a shape model derived from those heights (Zebker et al. 2009a) can reduce systematic errors in the SARSME fits.

The data needed to perform SARSME is the same as that needed to do SAR geolocation (Table 8-3) with the additions of the primary BIDR images (DATA/BIDR/BIF*.IMG) and the latitude (DATA/BIDR/BIT*.IMG), longitude (DATA/BIDR/BIN.IMG) and beam number mask (DATA/BIDR/BIM*.IMG) backplanes. Landmarks are found in the SAR images and located by their line and sample in each image. The line and sample is used to look up the apparent longitude and latitude in the backplanes. The inertial coordinates of each feature can then be determined by inverting the SAR geolocation process to recover the Doppler and range estimates from the latitudes and longitudes. To do this inversion ones needs the Titan pole, rotation angle, and rotation rate and spacecraft velocity and position originally used to do the geolocation. Pixels in the SAR image are averaged from multiple single look (single measurement cycle) SAR images.

However, it is sufficient to pick the measurement cycle (burst) with the correct beam number mask that has a boresight (u_{bore}) closest to the landmark. One can then look up all the relevant parameters for the selected measurement in the LBDR file.

8.3 Case 3: SAR Stereo

Three developments have been crucial in bringing us to the current state in which detailed stereo DTMs can be derived for a large and growing collection of areas of Titan. The first is the acquisition of the overlapping SAR images required as inputs. Prior to T18 (the eighteenth numbered flyby of Cassini past Titan) on 2006 September 23, RADAR had acquired seven SAR images, none of which overlapped. Beginning with T18, nearly every new image has overlapped at least one and sometimes several prior images, and this trend can be expected to continue. Not only are the voids in the map of Titan being filled, so that incidental overlaps are more likely, but, in addition, mission designers are now aware of the value of stereo imaging for understanding the satellite and are deliberately searching for stereo opportunities. Because of these effects, the rate at which stereo pairs accumulate is accelerating over time. The second step has been the identification and elimination of major errors in Titan cartography and geodesy resulting from the lack of an accurate model of Titan's rotation prior to the mission. The rotation modeling SARSME technique described above has led to the production of reprocessed images that coregister much more accurately, facilitating stereo comparison efforts. The final key ingredient for extensive stereo mapping has been the development of the needed software tools. Useful "spot" measurements of relative elevations were obtained in a few cases shortly after the acquisition of the stereo pairs by making manual measurements of the parallax between features in two images and then using a simplified version of the imaging geometry to convert parallaxes to height differences (Kirk et al. 2007a, b). The formulae for converting parallax to height are given below. To go beyond point measurements and collect DTMs of extensive areas requires more sophisticated software that combines automated and manual image measurement capabilities, and the ability to derive reliable absolute as well as relative heights, which requires a full model of the geometry of image formation, known as a "sensor model."

The approach taken by CRST members at the USGS (Kirk et al., in revision) has been to adapt a commercial stereo mapping software system for use with RADAR data by developing the needed sensor model and taking advantage of the other features the system provides. This approach works because radargrammetry is analogous to photogrammetry as commonly carried out with images from optical cameras (Slama 1980), though it is based on a slightly different geometrical construction. In either discipline, an image represents a two-dimensional projection of a three-dimensional world, and a given pixel could correspond to one or more points along a given curve in space. In the more familiar case of optical images this curve is a straight line through the detector pixel and the optical center of the camera (hence the term "colinearity equations" for the fundamental principle of photogrammetry), but for a SAR image it is a circle of constant range and Doppler frequency centered on the flight path. Note that while uncertainties in the location and velocity of the spacecraft will affect the range and Doppler measurements, the pointing of the spacecraft does not enter into the measurements. This insensitivity of the image-formation process to pointing simplifies the analysis of the images and leads to greater accuracy because an error source that is

important in photogrammetry can be ignored. If the same point can be identified in two images, the location of the point can be determined as the intersection of the two corresponding curves (or, in the presence of measurement errors, midway between the closest approach of two curves that do not precisely intersect). The precision of an elevation estimate from stereo then depends on three factors: the error ρ (in pixels) with which corresponding points in two images can be measured; the resolutions of the images; and the geometry of intersection of the circular loci for the two images, which determines the ratio of parallax to height. The dimensionless matching error ρ is often taken to be 0.2 pixel for optical images, but can be expected to be larger for radar images both because of the influence of speckle noise and because the pixel separation is chosen to deliberately oversample the true resolution. The CRST generally produces DTMs of Titan from the "full-resolution" 256 pixel/degree images. The ground-sample distance (GSD) of these images is 175 m, roughly a factor of 2 smaller than the best resolution obtained near closest approach, which is on the order of 300 m (Elachi et al. 2004). Empirical comparisons of stereo and SARTopo data suggest that a matching precision of $\rho = 1.4$ pixels can be obtained (Kirk et al. in prep.).

It is simplest to begin by considering pairs of images with parallel flight tracks, in which case the circular loci are coplanar, and the geometry is fully characterized by the incidence angles of the images. Because the illumination in radar images comes from the spacecraft, there are conflicting requirements on the incidence angles. Image matching is most successful when the resemblance between the images is maximized, requiring same-side illumination and viewing with incidence angles as similar as possible. Unfortunately, this also minimizes the strength of stereo and increases the vertical errors. Conversely, opposite-side viewing provides very strong stereo convergence but can make the identification of matching points in the images much more difficult. More complex imaging geometries, in which the image strips cross at an angle α, are intermediate between the same-side and opposite-side cases in both ease of matching and stereo strength, but are generally closer to the opposite-side case. The limits of acceptable imaging depend critically on the terrain, however. Leberl et al. (1992a) found that Magellan stereo pairs with $\alpha > 30°$ were not useful, but this was for rugged terrain near the north pole of Venus in which the images dominantly showed slope shading. Howington-Kraus et al. (2006) found that, in the Venusian lowlands, where relief is subtle and most of the information in the image comes from intrinsic backscatter variations (which do not change appearance with the illumination) rather than shading, opposite-side imaging is preferred in practice. The situation for most of Titan is similar, with low slopes and strong intrinsic variations in radar brightness, so that opposite-side or high-angle stereo pairs will be useful except perhaps in some mountainous areas (Kirk et al. in prep.). For two images with incidence angles i_1 and i_2, matching uncertainty ρ in pixels, and ground sample distance *GSD* between pixels in meters the expected vertical precision (EP) is:

$$EP = \frac{\rho GSD}{p/h}, \tag{1}$$

where p/h is the parallax-to-height ratio set by the imaging geometry. For the simple case of parallel image tracks, this is (Leberl et al. 1992b),

$$p/h = \left|\cot(i_1) \mp \cot(i_2)\right|, \tag{2}$$

where the minus sign applies to same-side imaging and the plus sign to opposite-side imaging. For a nominal pair of Cassini RADAR high-resolution SAR images with $i_1 = 10°$, $i_2 = 20°$, Eq. 1 and 2 give $EP = 80$ m for same-side imaging but 30 m for opposite-side. For the case of images that cross at an angle α, the expression for the parallax-height ratio generalizes to

$$p/h = \sqrt{\cot^2(i_1) + \cot^2(i_2) - 2\cot(i_1)\cot(i_2)\cos(\alpha)}. \tag{3}$$

Because of the need to compare finite image areas (e.g., matching patches no smaller than 3–5 pixels across), the minimum spacing for independent height estimates or "posts" is normally given as 3–5 pixels but the case of radar is more likely limited to several times the actual resolution. The CRST typically produces Titan DTMs with a post spacing of 8 pixels or 32 posts/degree (~1.4 km/post). This spacing may oversample the achievable resolution for DTMs made with images of lower resolution (i.e., the ends of the image strips, obtained at distances greater than closest approach).

The data required to do SAR stereo are the same as those required for SARSME. The 8 bit/pixel logarithmically scaled BIDRs are used as the images for feature matching, and information about the beam, burst, and time of observation of a given pixel and the spacecraft position and velocity at this time are derived from the corresponding SBDR. To speed the sensor model calculation, the appropriate burst identifier for each pixel is precomputed from the SBDR information and stored in a burst ID map file in the same projection as the image.

8.4 Case 4: Altimetry Refinement

Higher spatial- and range-resolution altimeter products have been produced under the Cassini Data Analysis Program (CDAP) by using Doppler beam sharpening or "synthetic aperture altimetry" (Raney 1998). The technique depends on noting that the returned signal can be divided by Doppler frequency as well as range. Along-track footprints are preassigned based on the Doppler resolution. Thus there is no direct relationship of the output samples to the original bursts, although information on the center burst is provided. The samples are counted relative to periapsis. The transmitted chirp waveform from the loop back calibration is used for the range compression. The Doppler shift correction for the vertical velocity must be included in the compression.

A few of the questions that arose in the course of this investigation are covered here.

The altimeter uses the center beam of the radar which actually uses the spacecraft's main antenna (approximately 4 m). The beam pattern was measured with sun scans during cruise. The measured beam patterns are available in the CALIB/BEAMPAT directory of the regular data packages in PDS. The altimeter bandwidth is 4.25 MHz; it is sampled at 10 MHz. No direct inflight calibration of the bandpass has been done. The samples in the LBDR signal array are real values with data compression undone. However, they have not been adjusted for attenuator settings. The nominal attenuator settings available in the data have been checked and found to be reasonable, but not adjusted for small differences from nominal. Also, the transmitted power is not measured in flight, so a prelaunch value is used.

According to the CDAP work, each footprint record will be preceded by a header containing the following fields:

- Originating burst ID, making it easy to locate the burst within the ABDR or LBDR
- Burst time (UTC)
- Frequency offset
- Range walk correction
- Antenna gain correction

The information for each synthetic sample is

1. Footprint counter (periapsis = 0)
2. Latitude and longitude of the footprint center
3. Footprint dimensions along- and across-track
4. Number of time steps in the echo profiles
5. Length of each time step
6. Time t (UTC) at which Cassini passes over the mid-point of the footprint
7. Cassini state vector (location and velocity) at time t in Titan corotating coordinates
8. Cassini state vector (location and velocity) at time t in Titan-centered J2000 frame
9. Horizontal and vertical components of Cassini velocity at time t
10. Round-trip delay (seconds) to first range bin
11. Atmospheric correction to time delay
12. Range to footprints (range-walked and non-range-walked)
13. Array of Fourier components contributing to this footprint

As of the writing of this guide, data produced under this task have not been archived, so the proposed contents have not been verified.

9 Obtaining Cassini RADAR Data Products

The PDS archives and distributes scientific data from NASA planetary missions, astronomical observations, and laboratory measurements, under the direction of NASA's Science Mission Directorate. The intent of the PDS is to ensure the long-term usability of NASA data, stimulate research, and is a world-wide resource for scientists, as well as the public. PDS products must be peer-reviewed, well-documented, and easily accessible through an online catalog system. The PDS works with project teams to help them design products that can be released quickly and easily used.

The PDS is made up of eight nodes: Atmospheres, Geosciences, Planetary Plasma Interactions, Rings, Small Bodies, Engineering, Imaging, and Navigation and Ancillary data. The nodes are geographically distributed around the U.S., and several have "sub-nodes" to support a specific aspect of the node's discipline. An expert in the subject discipline leads each node, and each node has an advisory group.

Cassini data are due to the PDS 9-12 months after acquisition, delivered every three months. PDS must still validate those data before they are considered archived. This may result in a delay between the time that Cassini delivers data and the time when PDS makes the data available. Alternately, PDS may choose to put data online while they are being validated. PDS urges caution when using any data that have been released to PDS for less than three months.

RADAR data sets are archived by the PDS Imaging Node at the Jet Propulsion Laboratory at http://pds-imaging.jpl.nasa.gov/. Under Cassini via the "Tools and Tutorials" link, the user can download a document entitled "How to Obtain Cassini Data" that contains a great deal of information on how to navigate the PDS site to obtain data. Under "All Data Holdings," a list of Cassini and other data sets held at the imaging node is found.

To download Cassini RADAR data from the PDS imaging node site, the user can either utilize the "Data Portal" or the "Data Volumes Index." A complete set of links can be found at http://pds-imaging.jpl.nasa.gov/portal/cassini_mission.html (Figure 9-1).

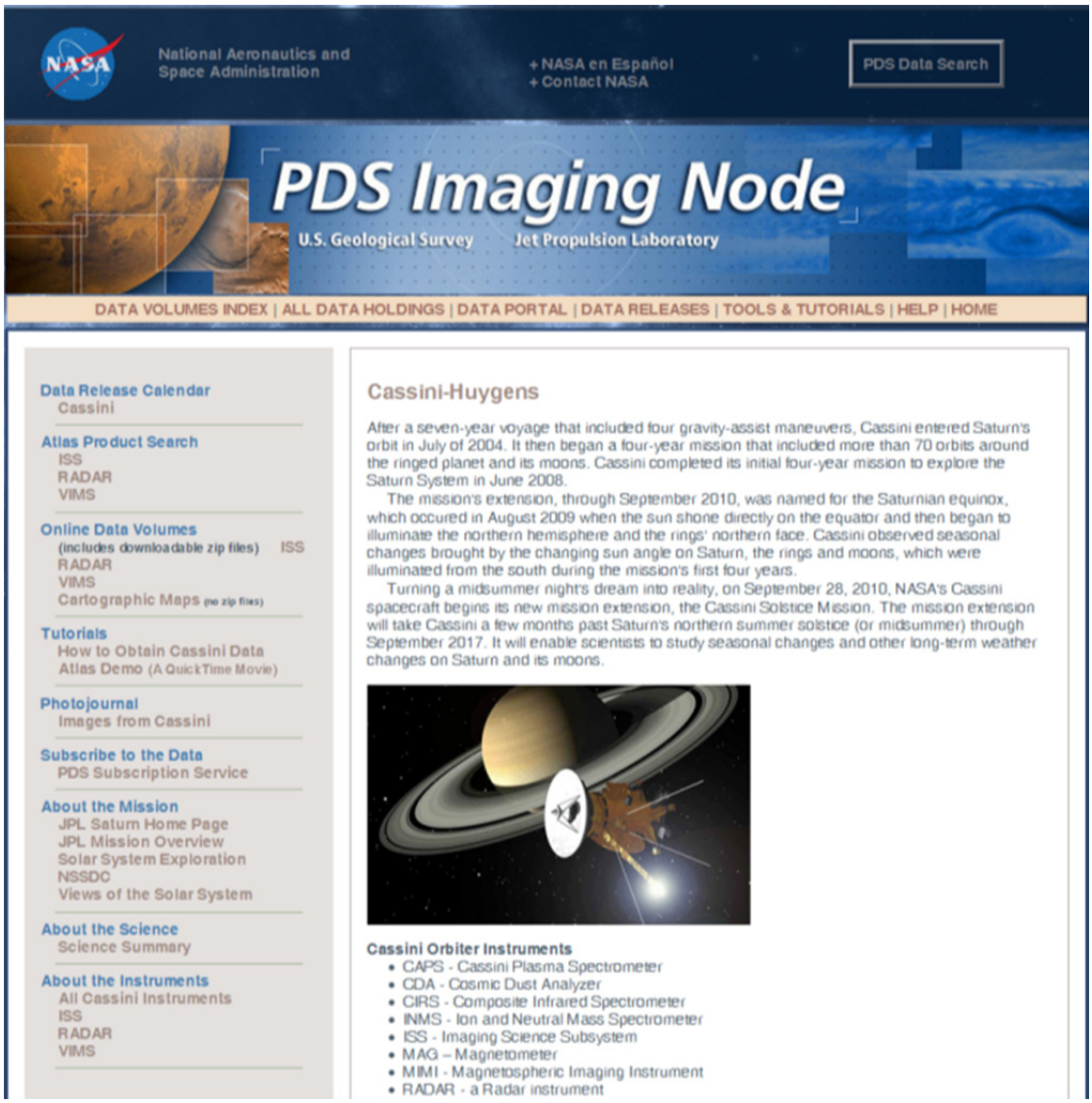

Figure 9-1. Links at left on this page of the NASA PDS Imaging Node Web site provide direction for using Cassini data.

In addition, a number of RADAR data products are publicly available through the NASA Planetary Photojournal (http://photojournal.jpl.nasa.gov/target/Titan) (Figure 9-2). Over 400 images of Titan from Cassini-Huygens are at this site, all with press-release captions. Also at the Photojournal site are JPEG files of all of the released Cassini RADAR swaths (Appendix 3).

Figure 9-2. PIA07368. Cassini RADAR images of an impact crater on Titan.

The Gazetteer of Planetary Nomenclature (http://planetarynames.wr.usgs.gov/) contains labeled images of features on Titan, as well as all of the other bodies in the solar system. The International Astronomical Union (IAU) Working Group for Planetary System Nomenclature (WGPSN) is responsible identifying types of features to be named and for providing names for individual features so that they can be easily referenced. To date, over 95 features on Titan have been named, with feature types including: Albedo Feature, Arcus, Crater, Facula, Fluctus, Flumen, Insula, Labyrinthus, Lacuna, Lacus, Large ringed feature, Macula, Mare, Planitia, Regio, and Virga. The Gazetteer contains the locations and labeled images for each feature, as well as definitions of feature types.

10 Information for Educators

Saturn, with its many moons and exotic rings, provides endless opportunities for engaging students of all ages and abilities. The Cassini education Web site (http://saturn.jpl.nasa.gov/education/overview/) provides links to materials and programs aimed at students in elementary through high school, with programs as diverse as the "Reading, Writing, and Rings" program for elementary school students to podcasts aimed at older students.

For Titan-specific exercises, see http://saturn.jpl.nasa.gov/education/educationK4Program/educationK4Lit12b/

- "Titan and the Other Moons of Saturn" provides a good introduction to Titan for younger students, with both a language arts and a science focus.
- "All About Titan and the Huygens Probe" provides another exercise for elementary school children with both a language arts and a science focus

At http://saturn.jpl.nasa.gov/education/EDUCATION58Program/edu58kitchen/, middle school students can learn the basics of radar using the exercise "Unveiling Titan's Surface" (Figure 10-1). Students make measurements of topographic features and draw maps based on these, in a way that is analogous to making radar measurements of topography through vegetation (on Earth) or through clouds (on Venus, Titan, and Earth).

National Aeronautics and Space Administration

Educational Product	
Educators & Students	Grades 5–12

EB-2001-12-006-JPL

Educational Brief

CASSINI SCIENCE INVESTIGATION

Unveiling Titan's Surface

Objective

To make measurements of topographic features and to draw maps based on these data. This will be done in a way that is analogous to making radar measurements of topography through vegetation (on Earth) or through clouds (on Venus, Titan, and Earth).

Time Required: 1–2 hours

Saturn System Analogy: Titan's surface unveiled by Cassini radar

Keywords: Contour Map, Radar, Relief, Topography

MATERIALS

- A sturdy cardboard shoe box, shipping carton with its top, or boot box
- Green styrofoam (commonly used in floral arrangements) cut to fit in the bottom of the box
- A tool for shaping the styrofoam (a large spoon will suffice)
- A sharpened pencil or similar object to punch holes in the box top
- A plastic coffee stirrer (about 5 inches long) or other long thin object like a bicycle spoke, a wooden kebab skewer, or a chopstick — to use as a depth gauge
- Adhesive tape and a ruler or tape measure
- A blank 3- by 5-inch index card
- Graph paper: several pieces with the same grid size

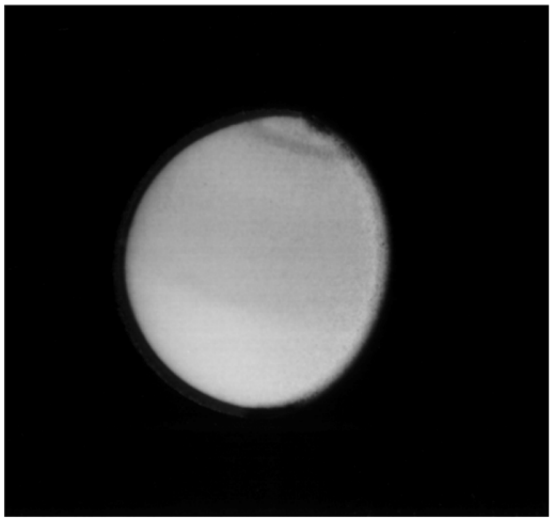

Titan, Saturn's largest moon, as seen by the Voyager 2 spacecraft.

Discussion

Titan's visibly opaque atmosphere shrouds the satellite's surface from our eyes. When the two Voyager spacecraft imaged Titan during their 1980 and 1981 flybys, scientists saw only the haze and cloud tops of the moon's thick, nitrogen-rich atmosphere.

Unlike a photographic camera that needs an outside light source, radar provides its own illumination. Cassini's radar will project pulses of radar energy toward Titan to strike the surface and echo back to the instrument. The amount

Unveiling Titan's Surface EB-2001-12-006-JPL
JPL 400-1021 05/02

Figure 10-1. First page from "Unveiling Titan's Surface" student investigation.

11 Appendix 1: References and Bibliography

Aharonson, O., 2008: Titan's global asymmetry in lake distribution and implications, *Amer. Geophys. Union*.

Aharonson, O., A. G. Hayes, J. I. Lunine, R. D. Lorenz, M. D. Allison, and C. Elachi, 2009: An asymmetric distribution of lakes on Titan as a possible consequence of orbital forcing. *Nature Geosci*., **2**, doi:10.1038/NGEO698.

Allison, M. D., 2000: A similarity model for the windy jovian thermocline. *Planet. Space Sci*., **48**, 753–774.

Allison, M. D., D. A. Godfrey, and R. F. Beebe, 1990: A wave dynamical interpretation of Saturn's polar hexagon. *Science*, **247**, 1061–1063, doi:10.1126/science.247.4946.10611990.

Artemieva, N., and J. I. Lunine, 2005: Impact cratering on Titan II. Global melt, escaping ejecta and surface organics. *Icarus*, **175**, 522–533.

Barnes, J. W., R. H. Brown, E. P. Turtle, A. S. McEwen, R. D. Lorenz, M. Janssen, E. L. Schaller, M. E. Brown, B. J. Buratti, C. Sotin, C. Griffith, R. Clark, J. Perry, S. Fussner, J. Barbara, R. West, C. Elachi, A. H. Bouchez, H. G. Roe, K. H. Baines, G. Bellucci, J.-P. Bibring, F. Capaccioni, P. Cerroni, M. Combes, A. Coradini, D. P. Cruikshank, P. Drossart, V. Formisano, R. Jaumann, Y. Langevin, D. L. Matson, T. B. McCord, P. D. Nicholson, and B. Sicardy, 2005: A 5-micron-bright spot on Titan: Evidence for surface diversity. *Science*, **310**, 92–95.

Barnes, J. W., R. H. Brown, J. Radebaugh, B. J. Buratti, C. Sotin, S. Le Mouélic, S. Rodriguez, E. P. Turtle, J. Perry, R. Clark, K. H. Baines, and P. D. Nicholson, 2006: Cassini observations of flow-like features in western Tui Regio, Titan. *Geophys. Res. Lett*., **33**, L16204, doi:10.1029/2006GL026843.

Barnes, J. W., J. Radebaugh, R. H. Brown, S. Wall, L. Soderblom, J. Lunine, D. Burr, C. Sotin, S. Le Mouélic, B. J. Buratti, R. Clark, K. H. Baines, R. Jaumann, P. D. Nicholson, R. L. Kirk, R. Lopes, R. Lorenz, K. Mitchell, C. A. Wood, and the Cassini RADAR Science Team, 2007: Near-infrared spectral mapping of Titan's mountains and channels. *J. Geophys. Res*., **112**, E11006, doi:10.1029/2007JE002932.

Barnes, J. W., R. H. Brown, J. M. Soderblom, L. A. Soderblom, R. Jaumann, B. Jackson, S. Le Mouélic, C. Sotin, B. J. Buratti, K. M. Pitman, K. H. Baines, R. N. Clark, P. D. Nicholson, E. P. Turtle, and J. Perry, 2009: Shoreline features of Titan's Ontario Lacus from Cassini/VIMS observations. *Icarus*, **201**, 217–225.

Boubin, G. M., E. G. Reffet, J. Lunine, J. Radebaugh, R. M. Lopes, and the Cassini RADAR Science Team, 2005: Mapping and characterization of "cat scratches" on Titan. *Amer. Astron. Soc. Div. Planet. Sci. Mtg*., Cambridge, England, September.

Casarano, D., B. Ventura, C. Notarnicola, and F. Posa, 2007: Cassini RADAR: Observations of Titan's surface features. *Proc. 5th Intl. Symposium on Retrieval of Bio and Geophys. Parameters from SAR Data for Land Applications*, ESA, Bari, Italy, September 25–28.

Crapeau, M., S. Rodriguez, S. Le Mouélic, P. Paillou, C. Sotin, P. Encrenaz, S. D. Wall, 2006a: Benefits of combining RADAR altimeter and VIMS data: Example using Ta and T13 flybys, *First Eur. Planet. Sci. Congress*, Berlin, Germany, September.

Crapeau, M., S. Rodriguez, S. Le Mouélic, P. Paillou, C. Sotin, and S.D. Wall, 2006b: Cassini altimeter and VIMS complementarity: Example using observations over the same area from Ta and T13 Titan flybys. *38th Amer. Astron. Soc. Div. Planet. Sci. Mtg*., Pasadena, CA, October.

Cumming, I. G., and F. H. Wong, 2005: Digital processing of synthetic aperture radar data: Algorithms and implementation. Artech House, 660 pp.

Curlander, J. C., and R. N. McDonough, 1991: *Synthetic Aperture Radar: Systems and Signal Processing*. Wiley, 672 pp.

Davies, M. E., V. K. Abalakin, M. Bursa, G. E. Hunt, J. H. Lieske, B. Morando, R. H. Rapp, P. K. Seidelmann, A. T. Sinclair, and Y. S. Tjuflin, 1989: Report of the IAU/IAG/COSPAR working group on cartographic coordinates and rotational elements of the planets and satellites. *Celest. Mech. Dyn. Astron.*, **46**, 187–204.

Davies, M. E., T. R. Colvin, P. G. Rogers, P. W. Chodas, W. L. Sjogren, E. L. Akim, V. A. Stepanyantz, Z. P. Vlasova, and A. I. Zakharov, 1992, The rotational period, direction of the north-pole, and geodetic control network of Venus. *J. Geophys. Res. Planets*, **97**, 13141–13151.

Elachi, C., M. D. Allison, L. Borgarelli, E. Encrenaz, E. Im, M. A. Janssen, W. T. K. Johnson, R. L. Kirk, R. D. Lorenz, J. I. Lunine, D. O. Muhleman, S. J. Ostro, G. Picardi, F. Posa, C. G. Rapley, L. E. Roth, R. Seu, L. A. Soderblom, S. Vetrell, S. D. Wall, C. A. Wood, and H. A. Zebker, 2004: RADAR: The Cassini Titan Radar Mapper. *Space Sci. Rev*., **115**, 71–110, doi:10.1007/s11214-004-1438-9.

Elachi, C., S. D. Wall, M. D. Allison, Y. Anderson, R. Boehmer, P. Callahan, P. Encrenaz, E. Flamini, G. Francescetti, Y. Gim, G. Hamilton, S. Hensley, M. A. Janssen, W. T. K. Johnson, K. Kelleher, R. L. Kirk, R. M. Lopes, R. D. Lorenz, J. I. Lunine, D. O. Muhleman, S. J. Ostro, F. Paganelli, G. Picardi, F. Posa, L. E. Roth, R. Seu, S. Shaffer, L. A. Soderblom, B. Stiles, E. R. Stofan, S. Vetrella, R. A. West, C. A. Wood, L. Wye, and H. A. Zebker, 2005a: Cassini RADAR's first look at Titan. *Lunar Planet Sci. Conf*., League City, TX, March 14–18.

Elachi, C., S. D. Wall, M. D. Allison, Y. Anderson, R. Boehmer, P. Callahan, P. Encrenaz, E. Flamini, G. Francescetti, Y. Gim, G. Hamilton, S. Hensley, M. A. Janssen, W. T. K. Johnson, K. Kelleher, R. Kirk, R. Lopes, R. Lorenz, J. Lunine, D. Muhleman, S. Ostro, F. Paganelli, G. Picardi, F. Posa, L. Roth, R. Seu, S. Shaffer, L. Soderblom, B. Stiles, E. Stofan, S. Vetrella, R. West, C. Wood, L. Wye, and H. Zebker, 2005b: First views of the surface of Titan from the Cassini RADAR. *Science*, **308**, 970–974.

Elachi, C., S. Wall, M. Janssen, E. Stofan, R. Lopes, R. Kirk, R. Lorenz, J. Lunine, F. Paganelli, L. Soderblom, C. Wood, L. Wye, H. Zebker, Y. Anderson, S. Ostro, M. Allison, R. Boehmer, P. Callahan, P. Encrenaz, E. Flameni, G. Francescetti, Y. Gim, G. Hamilton, S. Hensley, W. Johnson, K. Kelleher, D. Muhleman, G. Picardi, F. Posa, L. Roth, R. Seu, S. Schaffer, B. Stiles, S. Vetrella, and R. West, 2006a: Titan Radar Mapper observations from Cassini's Ta and T3 fly-bys. *Nature*, **441**, 709–713, doi:10.1038/nature0486.

Elachi, C., S. D. Wall, M. D. Allison, Y.Anderson, R. Boehmer, P. Callahan, P. Encrenaz, E. Flamini, G. Francescetti, Y. Gim, G. Hamilton, S. Hensley, M. A. Janssen, W. T. K. Johnson, K. Kelleher, R. L. Kirk, R. M. Lopes, J. I. Lunine, K. Mitchell, D. O.

Muhleman, G. Ori, R. Orosei, S. J. Ostro, F. Paganelli, G. Picardi, F. Posa, L. E. Roth, R. Seu, S. Shaffer, L. A. Soderblom, B. Stiles, E. Stofan, S. Vetrella, R. West, C. A. Wood, L. Wye, and H. A. Zebker, 2006b: Cassini RADAR's third and fourth looks at Titan. *37th Lunar Planet. Sci. Conf.*, Abstract 1249.

English, M. A., L. M. Lara, R. D. Lorenz, P.R. Ratcliff, and R. Rodrigo, 1996: Ablation and chemistry of meteoric materials on Titan. *Advances in Space Research*, Vol.12,157–160.

Ford, J. P., J. J. Plaut, C. M. Weitz, T. G. Farr, D. A. Senske, E. R. Stofan, G. Michaels, and T. J. Parker, 1993: *Guide to Magellan Image Interpretation*, JPL Publication 93-24, Jet Propulsion Laboratory. [Available online at http://history.nasa.gov/JPL-93-24/jpl_93-24.htm.]

Franceschetti, G., and R. Lanari, 1999: *Synthetic Aperture Radar Processing*, CRC, 328 pp.

Franceschetti, G., P. S. Callahan, A. Iodice, D. Riccio, and S. D. Wall, 2006: Titan, fractals, and filtering of Cassini altimeter data. *IEEE Trans. Geosci. and Remote Sensing*, **44**(8), August.

Furfaro, R., J. S. Kargel, J. I. Lunine, W. Fink, and M. P. Bishop, 2010: Identification of cryovolcanism on Titan using fuzzy cognitive maps. *Planet. Space Sci.*, **58**, 761–779, doi:10.1016/j.pss.2009.12.003.

Hayes, A. G., 2010: Exploring lakes on Titan, *Astronomy Beat*, *Astron. Soc. Pacific*, **56**, September 20.

Hayes, A. G., O. Aharonson, K. Lewis, K. Mitchell, R. Lorenz, P. Callahan, J. Lunine, R. Lopes, S. Wall, C. Elachi, G. Mitri, R. Kirk, Y. Gim, E. Stofan, and the Cassini RADAR Science Team, 2008a: Hydrocarbon lakes on Titan: Distribution and interaction with a porous regolith, *Geophys. Res. Lett.*, **35**, L09204, doi:10.1029/2008GL033409.

Hayes, A. G,.O. Aharonson, D. Stevenson, J. Lunine, R. Lorenz, K. Mitchell, R. Lopes, B. Stiles, R. Kirk, S. Wall, and the Cassini RADAR Science Team, 2008b: Titan's global lake distribution and implied hydrocarbon hydrology from Cassini SAR, *Amer. Geophys. Union*, P11D-07.

Hayes, A. G., O. Aharonson, S. Wall, C. Sotin, A. Le Gall, R. Lopes, M. Janssen, and the Cassini RADAR Science Team, 2008c: Joint analysis of Titan's surface using the Cassini VIMS and RADAR instruments, *Bull. Amer. Astron. Soc.*, **40**, p. 457, DPS2008 P3406.

Hayes, A. G., A. S. Wolf, O. Aharonson, H. Zebker, R. Lorenz, P., Paillou, S. Wall, and C. Elachi, 2010: Bathymetry and absorptivity of Titan's Ontario Lacus. *J. Geophys. Res.: Planets*, **115**, September, E09009, doi:10.1029/2009JE003557.

Hayes, A. G., O. Aharonson, J. I. Lunine, R. L. Kirk, H. A. Zebker, L. C. Wye, R. D. Lorenz, E. P. Turtle, P. Paillou, G. Mitri, S. D. Wall, E. R. Stofan, K. L. Mitchell, C. Elachi, and the Cassini RADAR Science Team, 2011: Transient surface liquid in Titan's polar regions from Cassini, *Icarus*, **211**(1), 655–671, doi:10.1016/j.icarus.2010.08.017.

Howington-Krause, E., R. L. Kirk, D. Galuszka, and B. Redding, 2006: USGS Magellan stereomapping of Venus, *Eur. Planet. Sci. Congr.*, Berlin, September 18–22.

Iess, L., Nicole J. Rappaport, Robert A. Jacobson, Paolo Racioppa, David J. Stevenson, Paolo Tortora, John W. Armstrong, Sami W. Asmar, Gravity Field, Shape, and Moment of Inertia of Titan, doi: 10.1126/science.1182583 *Science* 327, 1367 (2010)

Imbriale, W. A., 2003: *Large Antennas of the Deep Space Network*, JPL Deep-Space Communications and Navigation Series, John Wiley and Sons, 302 pp. [Available online at http://onlinelibrary.wiley.com/book/10.1002/0471728497.]

Jacobsen, R. E., D. L. Roth, D. M. Burr, C. Phillips, and K. L. Mitchell, 2008: Identification, mapping, and measurement of Titan fluvial features. *Amer. Geophys. Union*.

Janssen, M. A., 1993: An introduction to the passive microwave remote sensing of atmospheres. Chapter 1, *Atmospheric Remote Sensing by Microwave Radiometry*, M. Janssen, Ed., Wiley & Sons, 1–35.

Janssen, M. A., R. Lorenz, C. Elachi, Y. Z. Anderson, R. A. Boehmer, Y. Gim, W. T. K. Johnson, K. D. Kelleher, R. M. Lopes, L. E. Roth, S. D. Wall, and R. D. West, 2005a: First mapping of Titan with the Cassini RADAR radiometer. *Bull. Amer. Astron. Soc.*, **36**, 1075.

Janssen, M. A., F. Paganelli, R. Kirk, R. D. Lorenz, R. M. Lopes, and the Cassini RADAR Science Team, 2005b: Titan's surface properties from the Cassini RADAR radiometer. *Bull. Amer. Astron. Soc*., **37**, 739.

Janssen, M. A., R. D. Lorenz, F. Paganelli, R. L. Kirk, R. M. Lopes, and the Cassini RADAR Science Team, 2007: Absolutely calibrated 2-cm radiometry of Titan and implications. *38th Amer. Astron. Soc. Div. Planet. Sci. Mtg*., Orlando, FL, October 7–12.

Janssen, M. A., M. Allison, S. Gulkis, R. D. Lorenz, and K. D. Kelleher, 2008: Saturn's thermal emission at 2-cm wavelength and implications for atmospheric composition and dynamics, *Amer. Geophys. Union Fall Mtg*., Abstract P11B-1278.

Janssen, M. A., R. D. Lorenz, R. West, F. Paganelli, R. M. Lopes, R. L. Kirk, C. Elachi, S. D. Wall, W. T. K. Johnson, Y. Anderson, R. A. Boehmer, P. Callahan, Y. Gim, G. A. Hamilton, K. D. Kelleher, L. Roth, B Stiles, A. Le Gall, and the Cassini RADAR Science Team, 2009: Titan's surface at 2.2-cm wavelength imaged by the Cassini RADAR radiometer: Calibration and first results. *Icarus*, **200**, 222–239, doi:10.1016/j.icarus.2008.10.017.

Janssen, M. A, A. Le Gall, and L. C. Wye, 2011: Anomalous radar backscatter from Titan's surface, *Icarus*, **212**, 321–328.

Jaumann, R., R. H. Brown, K. Stephan, J. W. Barnes, L. A. Soderblom, C. Sotin, S. Le Mouélic, R. N. Clark, J. Soderblom, B. J. Buratti, R. Wagner, T. B. McCord, S. Rodriguez, K. H. Baines, D. P. Cruikshank, P. D. Nicholson, C. A. Griffith, M. Langhans, and R. D. Lorenz, 2008: Fluvial erosion post-erosional processes on Titan. *Icarus*, **197**(2), 526–538.

Jennings, D. E., F. M. Flasar, V. G. Kunde, R. E. Samuelson, J. C. Pearl, C. A. Nixon, R. C. Carlson, A. A. Mamoutkine, J. C. Brasunas, E. Guandique, R. K. Achterberg, G. L. Bjoraker, P. N. Romani, M. E. Segura, S. A. Albright, M. H. Elliott, J. S. Tingley, S. Calcut, A. Coustenis, and R. Courtin, 2009: Titan's surface brightness temperatures. *Astrophys. J. Lett.*, **691**, L103–L105.

Johnson, W. T. K., 2008: The Cassini mission to Saturn: Innovative design of the Ku-band Titan radar mapper, *PIERS*.

Kirk, R. L., J. M. Barrett, E. Howington-Kraus, B. A. Archinal, G. Neukum, and the Cassini RADAR Science Team., 2005: Cassini RADAR observations of Titan: Passes Ta and

T3, and USGS topomapping with Mars Express HRSC and SRC Images (poster). *2nd Ann. Asia Oceanic Geosci. Soc. Conf.*, Singapore, 58-PS-A0955.

Kirk, R. L., E. Howington-Kraus, K. L. Mitchell, S. Hensley, B. W. Stiles, and the Cassini RADAR Science Team, 2007a: First stereoscopic radar images of Titan. *38th Lunar Planet. Sci. Conf.*, Abstract 1427, Lunar and Planetary Institute, Houston (CD-ROM).

Kirk, R. L., E. Howington-Kraus, B. W. Stiles, S. Hensley, K. L. Mitchell, and the Cassini RADAR Science Team, 2007b: Topography of Titan from Cassini RADAR stereo data, *Eos Trans. Amer. Geophys. Union Fall Mtg. Suppl.*, **88**(52), Abstract P22B-01.

Kirk, R. L., and E. Howington-Kraus, 2008a: Radargrammetry on three planets, *International Archives of Photogrammetry, Remote Sensing, and Spatial Information Sciences*, *XXXVII*, *Part 4, A Silk Road for Information from Imagery*, 973–980, Beijing, July 3–11, DVD-ROM.

Kirk, R. L., and E. Howington-Kraus, 2008b: Topography of Titan from stereoanalysis of Cassini RADAR images with a rigorous sensor model, *Titan After Cassini-Huygens Symposium*, Corpus Christi, TX, 7–11 July.

Kirk, R. L., P. Callahan, R. Seu, R. D. Lorenz, F. Paganelli, R. M. Lopes, C. Elachi, and the Cassini RADAR Science Team, 2005: Radar reveals Titan topography. *36th Lunar Planet. Sci. Conf.*, Abstract 2, Houston, TX.

Kirk, R. L., E. Howington-Kraus, B. Redding, T. L. Becker, E. M. Lee, B. W. Stiles, S. Hensley, A. Hayes, R. M. Lopes, R. D. Lorenz, K. Mitchell, J. Radebaugh, F. Paganelli, L. Soderblom, E. Stofan, C. Wood, S. Wall, and the Cassini RADAR Science Team, 2008: A three-dimensional view of Titan's surface features from Cassini RADAR Stereogrammetry. *Amer. Geophys. Union.*

Kirk, R. L., E. Howington-Kraus, B. L. Redding, T. L. Becker, E. M. Lee, B. W. Stiles, S. Hensley, A. G. Hayes, R. M. Lopes, K. L. Lorenz, K. L. Mitchell, J. Radebaugh, F. Paganelli, L. A. Soderblom, E. R. Stofan, C. A. Wood, S. D. Wall, and the Cassini RADAR Science Team, in revision: High-resolution topographic models of Titan's surface derived by radar stereogrammetry with a rigorous sensor model. *Icarus*, in revision.

Kossacki, K. J., and R. D. Lorenz, 1996: Hiding Titan's ocean: Densification and hydrocarbon storage in an icy regolith. *Planet. Space Sci.*, **44**, 1029–1037/

Kwok, R., and W. T. K. Johnson, 1989: Block adaptive quantization of Magellan SAR data. *IEEE Trans. Geosci. Remote Sensing*, **27**, 375–383.

Lara, L. M., R. D. Lorenz, and R Rodrigo, 1994: Liquids and solids on the surface of Titan: Results of a new photochemical model. *Planet. Space Sci.*, **42**, 5–14.

Laurence, A., R. H. Soderblom, R. H. Brown, J. M. Soderblom, J. W. Barnes, R. L. Kirk, C. Sotin, R. Jaumann, D. J. Mackinnon, D. W. Mackowski, K. H. Baines, B. J. Buratti, R. N. Clark, P. D. Nicholson, 2009: The geology of Hotei Regio, Titan: Correlation of Cassini VIMS and RADAR, *Icarus*, **204**, 610–618, doi:10.1016/j.icarus.2009.07.033.

Leberl, F. W., K. E. Maurice, J. K. Thomas, C. E. Leff, and S. D. Wall, 1992a: Images and topographic relief at the north pole of Venus. *J. Geophys. Res.*, **97**(E8), 13,667–13,674.

Leberl, F. W., J. K. Thomas, and K. E. Maurice, 1992b: Initial results from the Magellan Stereo Experiment. *J. Geophys. Res.*, **97**(E8), 13,675–13,689.

Le Gall, A. A., M. A. Janssen, R. D. Lorenz, L. Wye, P. Callahan, A. Hayes, H. Zebker, and F. Paganelli, 2008: Titan's dunes and interdunes: New insights from Cassini RADAR observations, *Amer. Geophys. Union*.

Le Gall, A. A., M. A. Janssen, R. D. Lorenz, L. Wye, P. S. Callahan, A. G. Hayes, F. Paganelli, and H. A. Zebker, 2009: Titan's dunes and interdunes: New insights from Cassini RADAR observations. *Amer. Geophys. Union Fall Mtg*.

Le Gall, A. A., M. A. Janssen, P. Paillou, R. D. Lorenz, S. D. Wall, and the Cassini RADAR Science Team, 2010: Radar-bright channels on Titan. *Icarus*, **207**, 948–958, doi:10.1016/j.icarus.2009.12.027.

Le Mouélic, S., P. Paillou, C. Sotin, S. Rodriguez, M. Crapeau, M. Hirtzig, M.H. Brown, S.D. Wall, Comparison between VIMS and RADAR data on Sinlap crater on Titan, First European Planetary Science Congress, Berlin, Germany, September 2006

Le Mouélic, S., P. Paillou, M. Janssen, J. Barnes, S. Rodriguez, C. Sotin, R.H. Brown, K. Baines, B. Buratti, R. Clark, M. Crapeau,P. Encrenaz, R. Jaumann, D. Geutner, F. Paganelli, L. Soderblom,G. Tobie, S. Wall, Joint analysis of Cassini VIMS and RADAR data:Application to the mapping of Sinlap crater on Titan, *J. Geophys. Res.*, **113**, E04003, doi:10.1029/2007JE002965, 2008.

Lopes, R. M. C., 2006: Titan: Cassini reveals a new world. *Space Exploration 2007*, B. Harvey, Ed., Praxis-Springer.

Lopes, R. M. C., C. Elachi, F. Paganelli, K. Mitchell, E. Stofan, C. Wood, R. Kirk, R. Lorenz, J. Lunine, S. Wall, and the Cassini RADAR Science Team, 2005a: Flows on the surface of Titan as revealed by the Cassini RADAR. *Amer. Astron. Soc. Planet. Sci. Mtg*., Cambridge, England, September.

Lopes, R. M. C., C. Elachi, E. Stofan, F. Paganelli, C. Wood, R. Kirk, R. Lorenz, A. D. Fortes, J. Lunine, L. A. Soderblom, S. D. Wall, and the Cassini RADAR Science Team, 2005b: Cryovolcanic features on Titan's surface as revealed by the Cassini RADAR, solicited talk, *Eur. Geosci. Union Mtg*., April.

Lopes, R. M. C., C. Elachi, E. Stofan, F. Paganelli, C. Wood, R. Kirk, R. Lorenz, A. D. Fortes, J. I. Lunine, S. D. Wall, and the Cassini RADAR Science Team, 2005c: Cryovolcanic features on Titan's surface as revealed by the Cassini RADAR. *36th Lunar Planet. Sci. Conf*., Abstract 1885.

Lopes, R. M. C., E. R. Stofan, C. Elachi, R. L. Kirk, R. Lorenz, J. I. Lunine, K. L. Mitchell, G. G. Ori, F. Paganelli, L. Soderblom, S. D. Wall, C. A. Wood, and the Cassini RADAR Science Team, 2005d: Geologic features on Titan's surface as revealed by the Cassini RADAR Mapper. *Eos Trans. Amer. Geophys. Union Fall Mtg., Suppl*., **85**(52), Abstract P44A-02.

Lopes, R. M. C., E. Stofan, F. Paganelli, K. Mitchell, C. Wood, R. Kirk, R. Lorenz, J. Lunine, S. Wall, and C. Elachi, 2005e: Geologic features on Titan's surface as revealed by the Cassini RADAR. *Geological Soc. Amer. Ann. Mtg*., Abstract 102-6.

Lopes, R. M. C., K. L. Mitchell, E. Stofan, J. Lunine, and Cassini RADAR Science Team, 2006a: Cryovolcanic features on Titan's surface as revealed by the Cassini RADAR. Invited talk, *AOGS Mtg*., Singapore, July.

Lopes, R. M. C., E. R. Stofan, F. Paganelli, K. L. Mitchell, R. Kirk, R. Lorenz, J. Lunine, L. A. Soderblom, S. D. Wall, C. Wood, J. Radebaugh, L. E. Robshaw, C. Elachi, and the Cassini RADAR Science Team, 2006b: Geologic features on Titan's surface as revealed by the Cassini Titan Radar Mapper. *37th Lunar Planet. Sci. Conf.*, Abstract 1347, League City, TX, March 13–17.

Lopes, R. M. C., K. L. Mitchell, E. R. Stofan, J. I. Lunine, R. Lorenz, F. Paganelli, R. L. Kirk, C. A. Wood, S. D. Wall, L.E. Robshaw, A. D. Fortes, C. D. Neish, J. Radebaugh, E. Reffet, S. J. Ostro, C. Elachi, M. D. Allison, Y. Z. Anderson, R. A. Boehmer, G. Boubin, P. S. Callahan, P. Encrenaz, E. Flamini, G. Franceschetti, Y. G. Gim, G. A. Hamilton, S. Hensley, M. A. Janssen, W. T. K. Johnson, K. Kelleher, D. O. Muhleman, G. Ori, R. Orosei, G. Picardi, F. Posa, L. E. Roth, R. Seu, S. Shaffer, L. A. Soderblom, B. Stiles, S. Vetrella, R. D. West, L. Wye, and H. A. Zebker, 2007a: Cryovolcanic features on Titan's surface as revealed by the Cassini Titan Radar Mapper, *Icarus*, **186**(2).

Lopes, R. M. C., K. L. Mitchell, S.D. Wall, G. Mitri, M. Janssen, S. Ostro,R. L. Kirk, A.G. Hayes, E.R. Stofan, J.I. Lunine, R.D. Lorenz, C.Wood, J. Radebaugh, P. Paillou, H. Zebker, F. Paganelli, and the Cassini RADAR Science Team, 2007b. The lakes and seas of Titan. *Eos*, **88**(51), 569–576.

Lopes, R. M. C., R. Peckyno, A. Le Gall, and M. A. Janssen, 2008a: Surface parameters of Titan feature classes from Cassini RADAR backscatter measurements. *Amer. Geophys. Union Fall Mtg.,* P21A-1318.

Lopes, R. M. C., E. R. Stofan, C. Wood, J. Radebaugh, R. Kirk, R. Lorenz, J. Lunine, S. D. Wall, K. L. Mitchell, and G. Mitri, 2008b: New views of Titan's surface geology from the Cassini RADAR, Invited Talk. *Eur. Geosci. Union*, Vienna, Austria, April 13–18, 2008

Lopes, R. M. C., S. D. Wall, E. R. Stofan, C. A. Wood, R. M. Nelson, K. L. Mitchell, J. Radebaugh, B. W. Stiles, L. W. Kamp, R. D. Lorenz, J. I. Lunine, M. A. Janssen, T. G. Farr, G. Mitri, R. Kirk, and F. Paganelli, 2008c: Cryovolcanism on Titan: Interpretations from Cassini RADAR data. *Amer. Geophys. Union Fall Mtg*., P52A-03.

Lopes, R. M. C., S. D. Wall, E. R. Stofan, C. A. Wood, J. R. Radebaugh, K. L. Mitchell, B. W. Stiles, R. M. Nelson, L. W. Kamp, M. A. Janssen, R. D. Lorenz, J. I. Lunine, T. Farr, G. Mitri, and P. Paillou, 2008d: Hotei Arcus and western Xanadu, Titan: Evidence for cryovolcanic activity, *Amer. Astron. Soc. Div. Planet. Sci*.

Lopes, R. M. C., E. R. Stofan, R. Peckyno, J. Radebaugh, K. L. Mitchell, G. Mitri, C. A. Wood, R. L. Kirk, S. D. Wall, J. I. Lunine, A. Hayes, R. Lorenz, T. Farr, L. Wye, J. Craig, R. J. Ollerenshaw, M. Janssen, A. Le Gall, F. Paganelli, R. West, B. Stiles, P. Callahan, Y. Anderson, P. Valora, L. Soderblom, and the Cassini RADAR Science Team, 2010: Distribution and interplay of geologic processes on Titan from Cassini RADAR data. *Icarus*, **205**, 540–558, doi:10.1016/j.icarus.2009.08.010.

Lopes, R. M. C., and the Cassini RADAR Science Team, 2011: Cryovolcanism on Titan: New results from Cassini RADAR and VIMS. In preparation.

Lorenz, R. D., 1993a: The life, death and afterlife of a raindrop on Titan. *Planet. Space Sci*., **41**(9), 647–655.

Lorenz, R. D., 1993b: Wake-induced dust cloud formation following impact of planetary landers. *Icarus*, **101**, 165–167.

Lorenz, R. D., 1994a: Crater lakes on Titan: Rings, horseshoes and bullseyes. *Planet. Space Sci*., **42**, 1–4.

Lorenz, R. D., 1994b: Huygens Probe impact dynamics. *ESA J*., **18**, 93–117.

Lorenz, R. D., 1995: Raindrops on Titan. *Adv. Space Res.*, 15, 317–320.

Lorenz, R. D., 1996: Pillow lava on Titan: Expectations and constraints on cryovolcanic processes. *Planet. Space Sci*., **44**, 1021–1028.

Lorenz, R. D., 1999: Calorimetric radar absorptivity measurement using a microwave oven, *Meas. Sci. Tech*., **10**(6), June, L29–L32.

Lorenz, R. D., 2002: Thermodynamics of geysers: Application to Titan. *Icarus*, **156**, 176–183.

Lorenz, R. D., 2005: Lifting Titan's veil, invited talk, *Amer. Inst. Physics, Industrial Physics Forum*, Gaithersburg, MD, 7 November.

Lorenz, R. D., 2006a: The exploration of Titan. *JHU-APL Technical Digest*, **27**,133–144.

Lorenz, R. D., 2006b: Surface modification processes on Titan. *Astrobiology Conf. (AbSciCon)*, Washington, DC , March.

Lorenz, R. D., 2006c: Titan's dynamic surface revealed by Cassini RADAR, *Royal Astron. Soc*., London, February.

Lorenz, R. D., 2007: Comments on "In situ atmospheric turbulence measurement using the terrestrial magnetic field—a compass for a radiosonde." *J. Atmos. Oceanic Tech*., **24**, 1520–1521.

Lorenz, R. D., 2008a: Atmospheric electricity hazards. *Space Sci. Rev*., **137**, 287–294.

Lorenz, R. D., 2008b: Effects of atmospheric electricity on chemistry. *Space Sci. Rev*., **137**, 295–299.

Lorenz, R. D., 2010: Titan and Enceladus: Icy cauldrons of organic synthesis, invited talk, *Pardee Symposium, GSA An. Mtg.*, Denver, CO, Oct. 31–Nov. 3.

Lorenz, R. D., and J. I. Lunine, 1996: Erosion on Titan: Past and present, *Icarus*, **122**, 79–91.

Lorenz, R. D., and S. E. Shandera, 2001: Physical properties of ammonia-rich ice: Application to Titan. *Geophys. Res. Lett*., **28**, 215–218.

Lorenz, R. D., and J. I. Lunine, 2005: The surface of Titan before Cassini. *Planet. Space Sci*., **53**, 557–576.

Lorenz, R. D., and J. Radebaugh, 2009: The global pattern of Titan's dunes: Radar survey from the Cassini Prime Mission. *Geophys. Res. Lett*., **36**, L03202, doi:10.1029/2008GL036850.

Lorenz, R. D., M. Bannister, P. M. Daniell, Z. Krysinski, M. R. Leese, R. J. Miller, G. Newton, P. Rabbetts, D. M. Willett, and J. C. Zarnecki, 1994: An impact penetrometer for a landing spacecraft. *Meas. Sci. Tech*., **5**, 1033–1041.

Lorenz, R. D., J. I. Lunine, J. A. Grier, and M. A. Fisher, 1995: Prediction of aeolian features on planets: Application to Titan paleoclimatology. *J. Geophys. Res., Planets*, **88**, 26,377–26,386.

Lorenz, R. D., C. P. McKay, and J. I. Lunine, 1997: Photochemically-driven collapse of Titan's atmosphere. *Science*, **275**, 642–644.

Lorenz, R. D., C. P. McKay, and J. I. Lunine, 1999: Analytic stability of Titan's climate: Sensitivity to volatile inventory. *Planet. Space Sci*., **47**, 1503–1515.

Lorenz, R. D., J. I. Lunine, C. P. McKay, and P. G. Withers, 2001: Entropy production by latitudinal heat flow on Titan, Mars and Earth. *Geophys. Res. Lett*., **28**, 415–418.

Lorenz, R. D., C. Elachi, B. Stiles, R. A. West, M. A. Janssen, R. M. Lopes, E. R. Stofan, F. Paganelli, C. A. Wood, R. L. Kirk, J. Lunine, and S. D. Wall, 2005a: Titan's elusive lakes? Properties and context of dark spots in Cassini Ta radar data. *36th Lunar Planet. Sci. Conf.*, Abstract 1682, League City, TX, Mar. 14–18.

Lorenz, R. D., E. Kraal, E. Eddlemon, J. Cheney, and R. Greeley, 2005b: Sea-surface wave growth under extraterrestrial atmospheres: Preliminary wind tunnel experiments with application to Mars and Titan. *Icarus*, **175**, 556–560.

Lorenz, R. D., J. I. Lunine, and W. Zimmerman, 2005c: Post-Cassini exploration of Titan: Science goals, instrumentation and mission concepts. *Adv. in Space Res*., **36**, 281–285.

Lorenz, R. D., and the Cassini RADAR Science Team, 2006a: Dunes on Titan (poster). *European Geophys. Soc.*, Vienna, Austria, April.

Lorenz, R. D., S. Wall, J. Radebaugh, G. Boubin, E. Reffet, M. Janssen, E. Stofan, R. Lopes, R. Kirk, C. Elachi, J. Lunine, F. Paganelli, L. Soderblom, C. Wood, L. Wye, H. Zebker, Y. Anderson, S. Ostro, M. Allison, R. Boehmer, P. Callahan, P. Encrenaz, G. G. Ori, G. Francescetti, Y. Gim, G. Hamilton, S. Hensley, W. Johnson, K. Kelleher, K. Mitchell, D. Muhleman, G. Picardi, F. Posa, L. Roth, R. Seu, S. Shaffer, B. Stiles, S. Vetrella, E. Flamini, and R. West, 2006b: The sand seas of Titan: Cassini RADAR observations of longitudinal dunes. *Science*, **312**, 724–727.

Lorenz, R. D., S. D. Wall, E. Reffet, G. Boubin, J. Radebaugh, C. Elachi, M. D. Allison, Y.Anderson, R. Boehmer, P. Callahan, P. Encrenaz, E. Flamini, G. Francescetti, Y. Gim, G. Hamilton, S.Hensley, M. A. Janssen, W. T. K. Johnson, K. Kelleher, R. L. Kirk, R. M. Lopes, J. I. Lunine, K. Mitchell, D. O. Muhleman, G. Ori, R. Orosei, S. J. Ostro, F. Paganelli, G. Picardi, F. Posa, L. E. Roth, R. Seu, S. Shaffer, L. A. Soderblom, B. Stiles, E. Stofan, S. Vetrella, R. West, C. A. Wood, L. Wye, and H. A. Zebker, 2006c: Radar imaging of giant longitudinal dunes: Namib Desert (Earth) and the Belet Sand Sea (Titan). *Lunar Planet. Sci. Conf. 37*, Abstract 1249.

Lorenz, R. D., C. A. Wood, J. I. Lunine, S. D. Wall, R. M. Lopes, K. L. Mitchell, F. Paganelli, Y. Z. Anderson, L. Wye, C. Tsai, H. Zebker, and E. R. Stofan, 2007: Titan's young surface: Initial impact crater survey by Cassini RADAR and model comparison. *Geophys. Res. Lett*., **34**, L07204, doi:10.1029/2006GL028971.

Lorenz, R. D., R. M. Lopes, F. Paganelli, J. I. Lunine, R. L. Kirk, L. A. Soderblom, E. Stofan, G. Ori, M. Myers, H. Miyamoto, B. Stiles, S. D. Wall, C. A. Wood, and the Cassini RADAR Science Team, 2008a: Fluvial channels on Titan: Meteorological paradigm and Cassini RADAR observations. *Planet. Space Sci*., **56**, 1132–1144.

Lorenz, R. D., K. L. Mitchell, R. L. Kirk, A. G. Hayes, H. A. Zebker, P. Paillou, J. Radebaugh, J. I. Lunine, M. A. Janssen, S. D. Wall, R. M. Lopes, B. Stiles, S. Ostro, G. Mitri, and E. R. Stofan, 2008b: Titan's inventory of organic surface materials. *Geophys. Res. Lett*., **35**, L02206, doi:10.1029/2007GL032118.

Lorenz, R. D., J. Radebaugh, S. Wall, R. Lopes, C. Wood, and the Cassini RADAR Science Team, 2008c: Dunes on Titan: Cassini RADAR overview. *European Geosciences Union*, Vienna, Austria, April 13–18.

Lorenz, R. D., B. Stiles, R. L. Kirk, M. Allison, P. Persi del Marmo, L. Iess, J. I. Lunine, S. J. Ostro, and S. Hensley, 2008d: Titan's rotation reveals an internal ocean and changing zonal winds. *Science*, **319**, 1649–1651.

Lorenz, R. D., B. Stiles, R. L. Kirk, M. Allison, P. Persi del Marmo, J. I. Lunine, S. J. Ostro, and the Cassini RADAR Science Team, 2008e: Titan's changing length of day: An internal water ocean and seasonal variation of atmospheric angular momentum. *Science*, **319**, 1649–1651, doi:10.1126/science.1151639.

Lorenz, R. D., B. Stiles, R. Kirk, P. Callahan, S. Hensley, H. Zebker, and O. Aharonson, 2008f: Hypsometry and slope statistics of Titan from Cassini RADAR SARTopo data. *Amer. Astron. Soc. Div. Planet. Sci. Mtg*.

Lorenz, R. D., R. D. West, and W. T. K. Johnson, 2008g: Cassini RADAR constraint on Titan's winter polar precipitation. *Icarus*, **195**, 812–816.

Lorenz, R. D., J. Radebaugh, S. D. Wall, R. Kirk, A. Le Gall, M. A. Janssen, H. Zebker, F. Paganelli, L. Wye, and J. Lunine, 2009: The dunes of Shangri-La: New Cassini RADAR results on patterns of aeolian features and the influence of topography. *Amer. Geophys. Union Fall Mtg*., Abstract P21A-1309.

Lorenz, R. D., P. Claudin, B. Andreotti, J. Radebaugh, and T. Tokano, 2010a: A 3-km atmospheric boundary layer on Titan indicated by dune spacing and Huygens data. *Icarus*, **205**(2), 719–721, doi:10.1016/j.icarus.2009.08.002.

Lorenz, R. D., B. Jackson, and A. Hayes, 2010b: Racetrack and Bonnie Claire: Southwestern US playa lakes as analogs for Ontario Lacus, Titan. *Planet. Space Sci*., **58**(4), 724–731.

Lorenz, R. D., C. Newman, and J. I. Lunine, 2010c: Threshold of wave generation on Titan's lakes and seas: Effect of viscosity and implications for Cassini observations. *Icarus*, **207**(2), 932–937, doi:10.1016/j.icarus.2009.12.004

Lorenz, R. D., E. P. Turtle, B. Stiles, A. Le Gall, A. Hayes, O. Aharonson, C. A. Wood, E. Stofan, and R. Kirk, 2011: Hypsometry of Titan. *Icarus*, **211**, 699–706.

Lunine, J. I., 2005: Numerical modeling of impact cratering on Titan with implications for the age of Titan's surface. *Lunar Planet. Sci. Conf. 36*, Abstract 1504.

Lunine, J. I., and D. J. Stevenson 1987: Clathrate and ammonia hydrates at high pressure—application to the origin of methane on Titan. *Icarus*, **70**, 61–77.

Lunine, J. I., and S. K. Atreya, 2008: The methane cycle on Titan. *Nature Geosci*., **1**, 160–164.

Lunine, J. I., D. J. Stevenson, and Y. L. Yung, 1983: Ethane ocean on Titan. *Science*, **222**, 1229–1230.

Lunine, J. I., C. Elachi, , S. D. Wall, M. D. Allison,Y. Anderson, R. Boehmer, P. Callahan, P. Encrenaz, E. Flamini, G. Franceschetti, Y. Gim, G. Hamilton, S. Hensley, M. A. Janssen, W. T. K. Johnson, K. Kelleher, R. L. Kirk, R. M. Lopes, R. Lorenz, D. O. Muhleman, R. Orosei, S. J. Ostro, F. Paganelli, P. Paillou, G. Picardi, F. Posa, J. Radebaugh, L. E. Roth, R. Seu, S. Shaffer, L. A. Soderblom, B. Stiles, E.R. Stofan, S. Vetrella, R. West, C. A. Wood, L. Wye, H. Zebker, G. Alberti E. Karkoschka B. Rizk,

E. McFarlane, C. See, and B. Kazeminejad: 2008: Titan diverse landscapes as evidenced by Cassini RADAR's third and fourth looks at Titan. *Icarus*, **195**, 414–433, doi: 10.1016/j.icarus.2007.12.022.

Malaska, M., J. Radebaugh, A. Le Gall, K. Mitchell, R. Lopes, and S. Wall, 2011: Evidence for an eroded upwarp near Sikun Labyrinthus, Titan. *42nd Lunar Planet. Sci. Conf.*, Abstract 1568, The Woodlands, TX, Mar7–11.

Mitchell, K. L., R. M. Lopes, R. L. Kirk, and the Cassini RADAR Science Team. 2005: Preliminary analysis of the rheological properties of a probable cryovolcanic flow on Titan, by radarclinometric analysis of Cassini RADAR data. *Amer. Aston. Soc. Div. Planet. Sci. Mtg*., Cambridge, England, September.

Mitchell, K. L., J. S. Kargel, R. M. Lopes, J. I. Lunine, G. Mitri, R. D. Lorenz, Petford, N. and Wilson, L. (2006a) Eruption of ammonia-water cryomagmas on Titan 1: Crystallisation and cooling during ascent, *37th Lunar Planet. Sci. Conf.*, Abstract 2355, Lunar and Planetary Institute, Houston (CD-ROM).

Mitchell, K. L., R. M. C. Lopes, L. E. Robshaw, Kargel, J. S., J. I. Lunine, R. D. Lorenz, Petford, N., E. R. Stofan, Wilson, L. and the Cassini RADAR Science Team (2006b) Eruption of ammonia-water cryomagmas on Titan 2: Eruption styles and landforms, *37th Lunar Planet. Sci. Conf.*, Abstract 2425, Lunar and Planetary Institute, Houston (CD-Rom).

Mitchell, K. L., E. R. Stofan, C. Elachi, J. I. Lunine, R. D. Lorenz, B. Stiles, S. Ostro, L. Soderblom, C. Wood, H. Zebker, S. Wall, M. Janssen, R. Kirk, R. Lopes, F. Paganelli, J. Radebaugh, L. Wye, Y. Anderson, M. Allison, R. Boehmer, P. Callahan, P. Encrenaz, E. Flamini, G. Francescetti, Y. Gim, G. Hamilton, S. Hensley, W. T. K. Johnson, K. Kelleher, D. Muhleman, P. Paillou, G. Picardi, F. Posa, L. Roth, R. Seu, S. Shaffer, S. Vetrella, R. West, and the Cassini RADAR Science Team, 2008: The Lakes of Titan, *GSA*, Houston, TX, October 5–9.

Mitchell, K. L., E. R. Stofan, J. Radebaugh, R. M. C. Lopes, P. Paillou, J. I. Lunine, S. D. Wall, R. D. Lorenz, A. Hayes, J. S. Kargel, B. Ventura, and the Cassini RADAR Science Team, 2011: Titan's north polar lake district: Insights from the Cassini Titan RADAR Mapper. In prep.

Mitri, G., and A. P. Showman, 2007: Thermal convection in ice-I shells of Titan and Enceladus. *Icarus*, **193**, 387–396, doi:10.1016/ j.icarus.2007.07.016.

Mitri, G., A. P. Showman, J. I. Lunine, and R. M. Lopes, 2008: Resurfacing of Titan by ammonia-water cryomagma, *Icarus*, **196**, 216–224.

Mitri G., A. P. Showman, J. I. Lunine, and R.D. Lorenz, 2007: Hydrocarbon lakes on Titan. *Icarus*, **186**, 385–394.

Mitri, G., M. T. Bland, R. M. C. Lopes, J. R. Radebaugh, Showman, A.P., J. I. Lunine, and the Cassini RADAR Science Team, 2008a: Mountains on Titan. *Amer. Astron. Soc. Div. Planet. Sci*.

Mitri, G., M. T. Bland, R. M. C. Lopes, and A. P. Showman, 2008b: Mountain building on Titan. *Eur. Geosci. Union*, Vienna, Austria, April 13–18.

Mitri, G., A. P. Showman, J. I. Lunine, and R. M. Lopes, 2008c: Cryovolcanism on Titan. *Amer. Geophys. Union Fall Mtg.*, P11D-05.

Mitri, G., M. T. Bland, A. P. Showman, J. R. Radebaugh, B. W. Stiles, R. M. C. Lopes, J. I. Lunine, R. Pappalardo, and the Cassini RADAR Science Team, 2010: Mountains on Titan: Modeling and observations. *J. Geophys. Res.*, **115**, E10002, doi:10.1029/2010JE003592.

Neish, C. D., R. D. Lorenz, R. L. Kirk, and L. C. Wye, 2010: Radarclinometry of the sand seas of Africa's Namibia and Saturn's moon Titan. *Icarus*, **208**, 385–394, doi:10.1016/j.icarus.2010.01.023

Neish, C. D., R. D. Lorenz, and R. L.Kirk, 2008: Radar topography of domes on planetary surfaces. *Icarus,* **196**, 552–564, doi:10.1016/j.icarus.2008.03.013.

Neish, C. D.; R. D. Lorenz, and D. P. O'Brien, 2006: The potential for prebiotic chemistry in the possible cryovolcanic dome Ganesa Macula on Titan. *Intl. J. Astrobio*., **5**(1).

Nelson, R. M., L. Kamp, R. M. C. Lopes, D. L. Matson, R. L. Kirk, B. W. Hapke, M. D. Boryta, F. E. Leader, W. D. Smythe, K. H. Baines, R. Jauman, C. Sotin, R. N. Clark, D. P. Cruikshank, P. Drossart, B. J. Buratti, R. H. Brown, M. Combes, G. Bellucci, J.-P. Bibring, F. Capaccioni, P. Cerroni, A. Coradini, V. Formisano, G Filacchione, R. Y. Langevin, T. B. McCord, V. Mennella, P. D. Nicholson, and B. Sicardy, 2008a: Saturn's Titan: Reports suggesting surface activity from Cassini VIMS and Radar observations. *39th Lunar Planet. Sci. Conf*., Abstract 1862.

Nelson, R. M., L. W. Kamp, R. M. C. Lopes, D. L. Matson, R. L. Kirk, B. W. Hapke, S. D. Wall, M. D. Boryta, F. E. Leader, W. D. Smythe, K. L. Mitchell, K. H. Baines, R. Jaumann, C. Sotin, R. N. Clark, D. P. Cruikshank, P. Drossart, J. I. Lunine, M. Combes, G. Bellucci, J.-P. Bibring, F. Capaccioni, P. Cerroni, A. Coradini, V. Formisano, G. Filacchione, Y. Langevin, T. B. McCord, V. Menella, P. D. Nicholson, B. Sicardy, P. G. J. Irwin, and J. C. Pearl, 2008b: Photometric changes on Saturn's Titan: Evidence for active cryovolcanism. *Geophys. Res. Lett*., **36**, L04202, doi:10.1029/2008GL036206.

Nelson, R. M., L. Kamp, R. M. C. Lopes, D. L. Matson, S. D. Wall, R. L. Kirk, K. L Mitchell, G. Mitri, B. W. Hapke, M. D. Boryta, F. E. Leader, W. D. Smythe, K. H. Baines, R. Jauman, C. Sotin, R. N. Clark, D. P. Cruikshank, P. Drossart, B. J. Buratti, R. H. Brown, J.Lunine, M. Combes, G. Bellucci, J.-P. Bibring, F. Capaccioni, P. Cerroni, A. Coradini, V. Formisano, G Filacchione, R. Y. Langevin, T. B. McCord, V. Mennella, P. D. Nicholson, B. Sicardy, 2008c: The changing surface of Saturn's Titan: Cassini observations suggest active cryovolcanism, *Amer. Geophys. Union*.

Nelson, R. M., L. Kamp, R. M. C. Lopes, D. L. Matson, S. D. Wall, R. L. Kirk, K. L Mitchell, G. Mitri, B. W. Hapke, M. D. Boryta, F. E. Leader, W. D. Smythe, K. H. Baines, R. Jauman, C. Sotin, R. N. Clark, D. P. Cruikshank, P. Drossart, B. J. Buratti, R. H. Brown, J. Lunine, M. Combes, G. Bellucci, J.-P. Bibring, F. Capaccioni, P. Cerroni, A. Coradini, V. Formisano, G Filacchione, R. Y. Langevin, T. B. McCord, V. Mennella, P. D. Nicholson, B. Sicardy, 2008d: Saturn's Titan: Cassini instruments document surface change suggesting cryovolcanism, *Amer. Astron. Soc. Div. Planet. Sci. Mtg*.

Nicholson, P. D., Richard G. French, Donald B. Campbell, Jean-Luc Margot, Michael C. Nolan, Gregory J. Black, and Heikki J. Salo, 2005: Radar imaging of Saturn's rings. *Icarus*, **177**, 32–62, doi:10.1016/j.icarus.2005.03.023.

Notarnicola, C., B. Ventura, D. Casarano, and F. Posa, 2009: Cassini RADAR data: Estimation of Titan's lake features by means of a Bayesian inversion algorithm. *IEEE Trans. Geosci. and Remote Sensing*, **47**(5), 1503–1511.

Notarnicola, C., B. Ventura, D. Casarano, F. Posa and M. Janssen, 2010: Titan lakes: Characterization of physical properties by combined electromagnetic models of SAR and radiometric data, *Italian J. Remote Sensing*, **42**(1), 37–54.

O'Brien, D., P., R. D. Lorenz, and J. I. Lunine 2005. Numerical calculations of the longevity of impact oases on Titan. Icarus 173, 243–253.

Ostro, S. J., R. D. West, M. A. Janssen, H. A. Zebker, L. C. Wye, J. I. Lunine, R. M. Lopes, K. Kelleher, G. A. Hamilton, Y. Gim, Y. Z. Anderson, R. A. Boehmer, R. D. Lorenz, and the Cassini RADAR Science Team, 2005: Cassini RADAR observations of Phoebe, Iapetus, Enceladus, and Rhea. *Eos Trans. Amer. Geophys. Union Fall Mtg. Suppl.*, **85**(52), Abstract P22A-01.

Ostro, S. J., R. D. West, M. A. Janssen, R. D. Lorenz, H. A. Zebker, G. J. Black, J. I. Lunine, L. C. Wye, R. M. Lopes-Gautier, S. D. Wall, C. Elachi, L. Roth, S. Hensley, K. Kelleher, G. A. Hamilton, Y. Gim, Y. Z. Anderson, R. A. Boehmer, W. T. K. Johnson, and the Cassini RADAR Science Team, 2006: Cassini RADAR observations of Enceladus, Thethys, Dione, Rhea, Iapetus, Hyperion, and Phoebe, *Icarus*, **183**, 479–490.

Ostro, S. J., R. D. West, L. C. Wye, C. A. Wood, P. Paillou, M. A. Janssen, B. Stiles, K. Kelleher, Y. Z. Anderson, R. A. Boehmer, P. Callahan, Y. Gim, G. A. Hamilton, W. T. K. Johnson, C. Veeramachaneni, and the Cassini RADAR Science Team, 2007: New Cassini RADAR results for Iapetus and Saturn's other icy satellites. *Amer. Geophys. Union Fall Mtg*.

Ostro, S. J., R. D. West, L. C. Wye, H. A. Zebker, M. A. Janssen, B. Stiles, K. Kelleher, Y. Z. Anderson, R. A. Boehmer, P. Callahan, Y. Gim, G. A. Hamilton, W. T. K. Johnson, C. Veeramachaneni, R. D. Lorenz, and the Cassini RADAR Science Team, 2010: New Cassini RADAR results for Saturn's icy satellites. *Icarus*, **206**, 498–506, doi:10.1016/j.icarus.2009.07.041.

Paganelli, F., C. Elachi, R. M. Lopes, R. A. West, B. Stiles, M. A. Janssen, E. R. Stofan, C. A. Wood, R. D. Lorenz, J. I. Lunine, R. L. Kirk, L. E. Roth, S. D. Wall, L. A. Soderblom, and the Cassini RADAR Science Team, 2005a: Channels and fan-like features on Titan surface imaged by the Cassini RADAR. *36th Lunar Planet. Sci. Conf*., League City, TX, March 14–18.

Paganelli, F., M. A. Janssen, R. M. Lopes, R. L. Kirk, R. D. Lorenz, and the Cassini RADAR Science Team, 2005b. Titan's surface from combined SAR and radiometry using the Cassini RADAR. *Eos Trans. Amer. Geophys. Union Fall Mtg. Suppl*., **85**(52), Abstract P44A-04.

Paganelli, F., M. A. Janssen, R. M. Lopes, E. Stofan, B. Stiles, R. West, L. Roth, S.D. Wall, R. D. Lorenz, J. L. Lunine, R. L. Kirk, L. Soderblom, C. Elachi, and the Cassini RADAR Science Team, 2006a: A look at Titan's surface from the Cassini RADAR SAR and radiometry data. *37th Lunar Planet. Sci. Conf*., Abstract 1497.

Paganelli, F., J. van Zyl, M. A. Janssen, B. Stiles, R. West, R. M. Lopes, E. Stofan, P. Callahan, L. Roth, S.D. Wall, T.G. Farr, C. Elachi, R.D. Lorenz, L. Soderblom, and the Radar

Team, 2006b: Titan electromagnetic response and surface roughness imaged by Cassini RADAR. *37th Lunar Planet. Sci. Conf.*, Abstract 1501.

Paganelli, F., M. A. Janssen, B. Stiles, R. West, R. D. Lorenz, J. I. Lunine, R. M. Lopes, E. R. Stofan, S. D. Wall, R. L. Kirk, L. Roth, C. Elachi, and the Cassini RADAR Science Team, 2007a: Titan's surface from the Cassini RADAR radiometry data during SAR mode. *Planet. Space Sci. Special Issue from EGU 2006*.

Paganelli, F., M. A. Janssen, B. Stiles, R. West, R. D. Lorenz, J. I. Lunine, S. D. Wall, P. Callahan, R. M. Lopes, E. Stofan, R. L. Kirk, W. T. K Johnson, L. Roth, C. Elachi, and the Cassini RADAR Science Team, 2007b: Titan's surface from the Cassini RADAR SAR and high-resolution radiometry data of the first five flybys. *Icarus,* **191**, 211–222.

Paganelli, F., P. Callahan, S. Hensley, R. D. Lorenz, J. I. Lunine, R. L. Kirk, B. W. Stiles, Y. Gim, R. West, M. A. Janssen, R. M. Lopes, E. R. Stofan, S. D. Wall, P. Paillou, and the Cassini RADAR Science Team, 2008a: A different look at Titan's dunes. *Amer. Geophys. Union*.

Paganelli, F., P. Callahan, S. Hensley; R. D. Lorenz; J. I. Lunine; R. L. Kirk; B. W. Stiles, Y. Gim, R. West, M. A. Janssen, R. M. Lopes, E. R. Stofan, S. D. Wall, P. Paillou, J. Radebaugh, and the Cassini RADAR Science Team, 2008b: Different appearance of Titan's dunes. *Amer. Geophys. Union Fall Mtg*.

Paganelli, F., M. A. Janssen, R. M. Lopes, E. Stofan, S. D. Wall, R. D. Lorenz, J. I. Lunine, R. L. Kirk, L. Roth, C. Elachi, and the Cassini RADAR Science Team, 2008c: Titan's surface from the Cassini RADAR radiometry data during SAR mode. *Planet. Space Sci.*, **56**(1), 100–108.

Paillou, P., M. Crapeau, C. Elachi, S. D. Wall, and P. Encrenaz, 2006a: Modeling SAR backscattering of bright flows and dark spots on Titan. *37th Lunar Planet. Sci. Conf.*, Houston, TX, March.

Paillou, P., M. Crapeau, C. Elachi, S. D. Wall, and P. Encrenaz, 2006b: Models of synthetic aperture radar backscattering for bright flows and dark spots on Titan. *J. Geophys. Res.*, **111**, E11011, doi:10.1029/2006JE002724.

Paillou, P., J. I. Lunine, G. Ruffié, P. Encrenaz, S. D. Wall, R. D. Lorenz, and M. A. Janssen, 2008a: Microwave dielectric constant of Titan-relevant materials. *Geophys. Res. Lett.*, **35**, L18202, doi:10.1029/2008GL035216.

Paillou, P., K. L. Mitchell, S. D. Wall, G. Ruffié, C. A. Wood, R. D. Lorenz, E. R. Stofan, J. I. Lunine, R. M. Lopes, and P. Encrenaz, 2008b: Microwave dielectric constant of liquid hydrocarbons: Application to the depth estimation of Titan's lakes. *Geophys. Res. Lett.*, **35**, L05202, doi:10.1029/2007GL032515.

Perry, J. E., E. P. Turtle, A. S. McEwen, D. D. Dawson, and C. C. Porco, 2007: Cassini ISS observations of Titan's trailing hemisphere. *Ices, Oceans, and Fire: Satellites of the Outer Solar System workshop*, Boulder, Colorado, Abstract 6064.

Petford, N., K. L. Mitchell, and R. M. C. Lopes, 2006: Flow rheology of congested ammonia-water cyromagmas on Titan. *Royal Astronomical Society Titan Mtg.*, February.

Radebaugh, J R.., 2008: The Mountains of Titan. *GSA*.

Radebaugh, J. R., 2009: Titan's sticky dunes? *Nature Geosci.*, **2**, 608–609, doi:10.1038/ngeo623.

Radebaugh, J. R., R. Lorenz, R. Kirk, J. Lunine, and the Cassini RADAR Science Team, 2005: Mountains on Titan observed by Cassini RADAR. *Lunar Planetary Sci. Conf. 37*, Abstract 1007.

Radebaugh, J. R., R. Lorenz, J. Lunine, S. Wall, G. Boubin, E. Reffet, R. Kirk, R. Lopes, L. Soderblom, and the Cassini RADAR Science Team, 2006a: Orientations of dunes on Titan: Implications for global winds, *Amer. Astronom. Soc. Div. Planet. Sci. Mtg. 38*, Pasadena, CA, October, Abstract 52.07.

Radebaugh, J. R., R. Lorenz, J. Lunine, S. Wall, G. Boubin, E. Reffet, R. Kirk, R. Lopes, E. Stofan, L. Soderblom, M. Allison, and the Cassini RADAR Science Team, 2006b: Longitudinal dunes on Titan as indicators of regional and local winds. *EOS Trans. Amer. Geophys. Union Fall Mtg. Suppl*., Abstract P12A-03.

Radebaugh, J. R., R. Lorenz, R. Kirk, J. Lunine, E. Stofan, R. Lopes, S. Wall, and the Cassini RADAR Science Team, 2007a: Mountains on Titan from Cassini RADAR. *Icarus*, **192**, 77–91, doi:10.1016/j.icarus.2007.06.020.

Radebaugh, J. R., R. Lorenz, J. Lunine, and the Cassini RADAR Science Team, 2007b: Longitudinal dunes on Titan: Distributions and indicators of winds. *Spring EGU Mtg*., Vienna, Austria, Abstract 04702.

Radebaugh, J. R., R. Lorenz, J. Lunine, S. Wall, G. Boubin, E. Reffet, R. Kirk, R. Lopes, E. Stofan, L. Soderblom, M. Allison, P. Callahan, and the Cassini RADAR Science Team, 2007c: Longitudinal dunes on Titan as indicators of global climate. *Workshop on Ices, Oceans, and Fire, Satellites of the Outer Solar System*, Boulder, CO, Abstract 6005.

Radebaugh, J. R., R. D. Lorenz, J. I. Lunine, S. Wall, G. Boubin, E. Reffet, R. L. Kirk, R. M. C. Lopes, E. R. Stofan, L. Soderblom, M. Allison, P. Callahan, and the Cassini RADAR Science Team, 2007d: Orientations of longitudinal dunes on Titan: Implications for global wind and climate. *Bull. Amer. Astron. Soc*., **39**(3), 57.02.

Radebaugh, J. R., R. Lorenz, J. Lunine, S. Wall, G. Boubin, E. Reffet, R. Kirk, R. Lopes, E. Stofan, L. Soderblom, M. Allison, P. Callahan and the Cassini RADAR Science Team, 2007e: Dunes on Titan from Cassini RADAR. *38th Lunar Planet. Sci. Conf.*, Abstract 1338.

Radebaugh, J. R., R. Lorenz, J. Lunine, S. Wall, C. Spencer, R. L. Kirk, R. M. Lopes, E. R. Stofan, M. Allison, P. Callahan, and the Cassini RADAR Science Team, 2007f: Titan's sand seas of longitudinal dunes as indicators of winds and sediment transport. *Eos Trans. Amer. Geophys. Union Fall Mtg. Suppl*., **88**(52), Abstract 10910.

Radebaugh, J. R., R. D. Lorenz, J. I. Lunine, S. D. Wall, G. Boubin, E. Reffet, R. L. Kirk, R. M. Lopes, E. R. Stofan, L. Soderblom, M. Allison, M. Janssen, P. P. Paillou Callahan, C. Spencer, and the Cassini RADAR Science Team, 2008. Dunes on Titan observed by Cassini RADAR. *Icarus*, **194**(2), 690–703, doi:10.1016/j.icarus.2007.10.015.

Radebaugh, J. R., R. Lorenz, T. Farr, P. Paillou, C. Savage, and C. Spencer, 2010: Linear dunes on Titan and Earth: Initial remote sensing comparisons, *Geomorphology*, **121**, 122–132. doi:10.1016/j.geomorph.2009.02.022.

Radebaugh, J. R., R. D. Lorenz, S. D. Wall, R. L. Kirk, C. A. Wood, J. I. Lunine, E. R. Stofan, R. M. C. Lopes, P. Valora, T. G. Farr, A. Hayes, B. Stiles, G. Mitri, H. Zebker, M. Janssen, L. Wye, A. Le Gall, K. L. Mitchell, F. Paganelli, R. D. West, E. L. Schaller,

and the Cassini RADAR Science Team, 2011: Regional geomorphology and history of Titan's Xanadu province, *Icarus*, **211**, 672–685, doi:10.1016/j.icarus.2010.07.022.

Raney, K., 1998: The delay/Doppler radar altimeter. *IEEE Trans. Geosci. and Remote Sensing*, **36**(5), September.

Reffet, E. G., G. M. Boubin, J. Lunine, J. Radebaugh, R. M. Lopes, and the Cassini RADAR Science Team, 2005: Cryovolcanic features on Titan: Interpretation of Cassini RADAR data. *Amer. Astron. Soc. Div. Planet. Sci. Mtg*., Cambridge, England, September.

Rodriguez, S., S. Le Mouélic, P. R. G. Tobie, K. H. Baines, J. W. Barnes, C. A. Griffith, M. Hirtzig, K. M. Pitman, C. Sotin, R. H. Brown, B. J. Buratti, R. N. Clark, and P. D. Nicholson, 2009: Global circulation as the main source of cloud activity on Titan. *Nature*, **459**, 678–682, doi:10.1038/nature08014.

Roth, L., 2005: Planetary radar exploration: The Cassini RADAR. *Joint Conf. Czech and Slovak Phys. Soc*., Kosice, Slovakia, September 5.

Rubin, D. M., and P. A. Hesp, 2009: Multiple origins of linear dunes on Earth and Titan. *Nature Geosci.*, **2**, 653–658, doi:10.1038/ngeo610.

Slama, C. C., 1980. *Manual of Photogrammetry*, 4th Ed. American Society of Photogrammetryand Remote Sensing, 1056 pp.

Soderblom, J. M., B. J. Buratti, R. Wagner, T. B. McCord, S. Rodriguez, K. H. Baines, D. P. Cruikshank, P. D. Nicholson, C. A. Griffith, M. Langhans, and R. D. Lorenz, 2008: Fluvial erosion post-erosional processes on Titan. *Icarus*, **197**(2), 526–538, October.

Soderblom, L. A., R. Kirk, J. I. Lunine, J. Anderson, K. Baines, J. Barnes, J. Barrett, R. Brown, B. Buratti, R. Clark, D. Cruikshank, C. Elachi, M. A. Janssen, R. Jaumann, E. Karkoschka, S. Le Mouélic, R. M. Lopes., R. D. Lorenz, T. McCord, P. Nicholson, J. R. Radebaugh, B. Rizk, C. Sotin, E. R. Stofan, T. Sucharski, M. Tomasko, and S. D. Wall, 2007a: Correlations between Cassini VIMS spectra and RADAR SAR images: Implications for Titan's surface composition and the character of the Huygens Probe Landing Site. *Planet. Space Sci*., **55**, 2025–2036, doi:10.1016/j.pss.2007.04.014.

Soderblom, L. A., M. Tomasko, B. Archinal, T. Becker, M. Bushroe, D. Cook, L. Doose, L. Galuszka, T. Hare, A. Howington-Kraus, E. Karkoschka, R. L. Kirk, J. I. Lunine, E. McFarlane, B. Redding, B. Rizk, M. Rosiek, C. See, and P. Smith, 2007b: Topography and geomorphology of the Huygens landing site on Titan. *Planet. Space Sci*., **55**, 2015–2024, doi:10.1016/j.pss.2007.04.015.

Soderblom, L. A., R. H. Brown, J. M. Soderblom, J. W. Barnes , R. L. Kirk, C. Sotin , R. Jaumann, D. J., Mackinnon, D. W. Mackowski, K. H. Baines, B. J. Buratti , R. N. Clark, and P. D. Nicholson, 2009: The geology of Hotei Regio, Titan: Correlation of Cassini VIMS and RADAR. *Icarus*, **204**, 610–618.

Sohl, F., W. D. Sears, and R. D. Lorenz, 1995: Tidal dissipation on Titan. *Icarus*, **115**, 278–294.

Sotin, C., C. Sotin, R. Jaunmann, B. J. Buratti, R. H. Brown, R. N. Clark, L.A. Soderblom, K. A. Baines, G. Bellucci, J.-P. Bribing, F. Capaccioni, P. Cerroni, A. Coradini, D. P. Cruikshank, P. Drossart, V. Formisano, Y. Langevin, D. L. Matson, T. B. McCord, R. M. Nelson, P. D. Nicholson, B. Sicardy, S. LeMouelic, S. Rodriguez, K. Stephan, and C. K. Scholz, 2005: Release of volatiles from a possible cryovolcano from near-infrared imaging of Titan. *Nature*, **435**, 786–789.

Sromovsky, L. A., H. E. Revercombe, R. J. Kraus, and V. E. Suomi, 1983: Voyager 2 observations of Saturn's northern mid-latitude cloud features: Morphology, motions and evolution. *J. Geophys. Res*., **88**, 8650–8666.

Stephan, K., R. Jaumann, R. H. Brown, J. M. Soderblom, L. A. Soderblom, J. W. Barnes, C. Sotin, C. A. Griffith, R. L. Kirk, K. H. Baines, B. J. Buratti, R. N. Clark, D. M. Lytle, R. M. Nelson, and P. D. Nicholson, 2010: Specular reflection on Titan: Liquids in Kraken Mare. *Geophys. Res. Lett*., **37**, L07104, doi:10.1029/2009GL042312.

Stiles, B W., Y. Gim, G Hamilton, S. Hensley, W. T. K. Johnson, J. Shimada, R. D. West, and P. Callahan, 2006: Ground processing of Cassini RADAR imagery of Titan. *Proc. IEEE Radar Conf*., Verona, NY.

Stiles, B. W., R. L. Kirk, R. D. Lorenz, S. Hensley, E. Lee, S. J. Ostro, M. D. Allison, P. S. Callahan, Y. Gim, L. Iess, P. Persi del Marmo, G. Hamilton, W. T. K. Johnson, R. D. West, and The Cassini RADAR Science Team, 2008: Determining Titan's spin state from Cassini RADAR images. *Astronom. J*. **135**, 1669–1680, doi:10.1088/0004-6256/135/5/1669.

Stiles, B. W., S. Hensley, Y. Gim, D. M. Bates, R. L. Kirk, A. Hayes, J. Radebaugh, R. D. Lorenz, K. L. Mitchell, P. S. Callahan, H. Zebker, W. T. K. Johnson, S. D. Wall, J. I. Lunine, C. A. Wood, M. A. Janssen, F. Pelletier, R. D. West, C. Veeramacheneni, and the Cassini RADAR Science Team, 2009: Determining Titan surface topography from Cassini SAR data. *Icarus*, **202**, 584–598, doi:10.1016/j.icarus.2009.03.032.

Stofan, E. R., C. Elachi, R. Lopes, R. Lorenz, R. L. Kirk, F. Paganelli, C. A. Wood, S. D. Wall, J. Lunine, L. Soderblom, and the Cassini RADAR Science Team, 2005: Mappping of Titan: First results from the Cassini RADAR. *36th Lunar Planet. Sci. Conf*., Abstract 1714.

Stofan, E. R., J. I. Lunine, R. M. Lopes, F. Paganelli, R. D. Lorenz, C. A. Wood, R. L. Kirk, S. D. Wall, C. Elachi, L. A. Soderblom, S. Ostro, M. Janssen, J. Radebaugh, L. Wye, H. Zebker, Y. Anderson, M. Allison, R. Boehmer, P. Callahan, P. Encrenaz, E. Flamini, G. Francescetti, Y. Gim, G. Hamilton, S. Hensley, W. T. K. Johnson, K. Kelleher, D. Muhleman, G. Picardi, F. Posa, L. Roth, R. Seu, S. Shaffer, B. Stiles, S. Vetrella, and R. West, 2006: Mapping of Titan: Results from the first two Titan radar passes. *Icarus*, **185**(2), 443–456, doi:10.1016/j.icarus.2006.07.015.

Stofan, E. R., C. Elachi, J. I. Lunine, R. D. Lorenz, B. Stiles, K. Mitchell, S. Ostro, L. Soderblom, C. Wood, H. Zebker, S. Wall, M. Janssen, R. Kirk, R. Lopes, F. Paganelli, J. Radebaugh, L. Wye, Y. Anderson, M. Allison, R. Boehmer, P. Callahan, P. Encrenaz, E. Flamini, G. Francescetti, Y. Gim, G. Hamilton, S. Hensley, W. T. K. Johnson, K. Kelleher, D. Muhleman, P. Paillou, G. Picardi, F. Posa, L. Roth, R. Seu, S. Shaffer, S. Vetrella, R. West, 2007: The lakes of Titan. *Nature*, **445**, doi:10.1038/nature05438.

Stofan, E. R., C. Elachi, J. I. Lunine, R. D. Lorenz, R. L. Kirk, R. M. Lopes, C. A. Wood, J. Radebaugh, S. D. Wall, K. L. Mitchell, L. A. Soderblom, P. Paillou, T. Farr, B. Stiles, P. Callahan, and the Cassini RADAR Science Team, 2008: Varied geologic terrains at Titan's south pole: First results from T39. *39th Lunar Planet. Sci. Conf*., Abstract 1492, Houston, TX.

Tobie, G., O. Grasset, J. I. Lunine, A. Mocquet, and C. Sotin, 2005: Titan's internal structure inferred from a coupled thermal-orbital model. *Icarus*, **175**, 496–502, doi:10.1016/j.icarus.2004.12.007.

Tobie, G., J. I. Lunine, and C. Sotin, 2006: Episodic outgassing as the origin of atmospheric methane on Saturn's moon Titan. *Nature*, **440**, 61–64.

Tokano, T., 2009: Limnological structure of Titan's hydrocarbon lakes and its astrobiological implication. *Astrobio.*, **9**(2), 147–164, doi:10.1089/ast.2007.0220.

Tokano, T., 2011: Precipitation climatology on Titan, *Science*, **331**, 1393, doi:10.1126/science.1204092.

Tokano, T., and R. D. Lorenz, 2006: GCM simulation of balloon trajectories on Titan, *Planet. Space Sci*., **54**, 685–694.

Tomasko, M. G., B. Archinal, T. Becker, B. Bézard, M. Bushroe, M. Combes, D. Cook, A. Coustenis, C. de Bergh, L. E. Dafoe, L. Doose, S. Douté, A. Eibl, S. Engel, F. Gliem, B. Grieger, K. Holso, E. Howington-Kraus, E. Karkoschka, H. U. Keller, R. Kirk, R. Kramm, M. Küppers, P. Lanagan, E. Lellouch, M. Lemmon, J. Lunine, E. McFarlane, J. Moores, G. M. Prout, B. Rizk, M. Rosiek, P. Rueffer, S. E. Schröder, B. Schmitt, C. See, P. Smith, L. Soderblom, N. Thomas, and R. West, 2005: Rain, winds and haze during the Huygens probe's descent to Titan's surface. *Nature*, **438**, 765–778, doi:10.1038/nature04126.

Tosi, F., R. Orosei, R. Seu, A. Coradini, J. I. Lunine, G. Filacchione, A. I. Gavrishin, F. Capaccioni, P. Cerroni, A. Adriani, M. L. Moriconi, A. Negrão, E. Flamini, R. H. Brown, L. C. Wye, M. Janssen, R. D. West, J. W. Barnes, S. D. Wall, R. N. Clark, D. P. Cruikshank, T. B. McCord, P. D. Nicholson, J. M. Soderblom, and the Cassini VIMS and RADAR Teams, 2010: Correlations between VIMS and RADAR data over the surface of Titan: Implications for Titan's surface properties. *Icarus*, **208**, 366–384, doi:10.1016/j.icarus.2010.02.003.

Turtle, E. P., J. Barnes, B. Buratti, G. Collins, S. Fussner, R. M. Lopes, R. D. Lorenz, J. I. Lunine, T. B. McCord, A. S. McEwen, R. M. Nelson, J. Perry, C. C. Porco, L. Soderblom, C. Sotin, and S. D. Wall, 2005: Exploring the surface of Titan with Cassini-Huygens. *Eos Trans. Amer. Geophys. Union Fall Mtg. Suppl*., **85**(52), Abstract P44A-01.

Turtle, E. P., J. E. Perry, A. S. McEwen, A. D. DelGenio, J. Barbara, R. A. West, D. D. Dawson, and C. C. Porco, 2009: Cassini imaging of Titan's high-latitude lakes, clouds, and south-polar surface changes. *Geophys. Res. Lett*., **36**, L02204, doi:10.1029/2008GL036186.

Turtle, E. P., J. E. Perry, A. G. Hayes, R. D. Lorenz, J. W. Barnes, A. S. McEwen, R. A. West, A. D. Del Genio, J. M. Barbara, J. I. Lunine, E. L. Schaller, T. L. Ray, R. M. C. Lopes, and E. R. Stofan, 2011a: Rapid and extensive surface changes near Titan's equator: Evidence of April showers. *Science*, **331**, 1414, doi:10.1126/science.1201063.

Turtle, E. P., J. E. Perry, A. G. Hayes, and A. S. McEwen, 2011b: Shoreline retreat at Titan's Ontario Lacus and Arrakis Planitia from Cassini imaging science subsystem observations. *Icarus*, in press, doi:10.1016/j.icarus.2011.02.005.

Ulaby, F. T., R. K. Moore, and A. K. Fung, 1982: *Radar Remote Sensing and Surface Scattering and Emission Theory.* Vol. 2, *Microwave Remote Sensing: Active and Passive*, Addison-Wesley Publishing Co., 609 pp.

Ventura, B., D. Casarano, C. Notarnicola., D. Di Rosa, and F. Posa, 2006a: Cassini RADAR data analysis: Inference of physical and morphological properties of selected Titan's surface features. *Proc. IEEE Gold Symposium*, Bari, Italy, December.

Ventura, B., D. Casarano, C. Notarnicola., D. Di Rosa, and F. Posa, 2006b: Modeling the eletromagnetic response of Titan's surface features observed by the Cassini RADAR. *Proc. EUROPTO 2006 SPIE Conf. on SAR Image Analysis, Modeling and Techniques IV*, Stockholm, Sweden, September.

Ventura, B., D. Casarano, C. Notarnicola., M. A. Janssen, and F. Posa, 2007a: Inferring Titan's surface features by means of Bayesian inversion algorithm applied to radar data. *Proc. Intl. Symposium Remote Sensing*, **6746**, Florence, Italy, September 17–20.

Ventura, B., D. Casarano, C. Notarnicola, and F. Posa, 2007b: Cassini RADAR: Investigation of Titan's surface parameters by means of Bayesian inversion technique and gravity-capillary waves modelling of liquid hydrocarbons surfaces. *Proc. IEEE Intl. Geosci. and Remote Sensing Symposium*, Barcelona, Spain, July 23–27.

Ventura, B., D. Casarano, C. Notarnicola, and F. Posa, 2007c: Double-layer backscattering model and Bayesian inversion for retrieval of Titan's surface parameters from Cassini RADAR data. *Proc. 5th Intl. Symposium on Retrieval of Bio and Geophys. Parameters from SAR Data for Land Applications, ESA Conf.*, Bari, Italy, September 25–28.

Wall, S. D., 2008: The Cassini RADAR investigation, *EUSAR*.

Wall, S. D., S. L. McConnell, C. E. Leff, R. S. Austin, K. K. Beratan, and Mark J. Rokey, 1995: *User Guide to the Magellan Synthetic Aperture Radar Images*, Jet Propulsion Laboratory.

Wall, S. D., C. Elachi, and the Cassini RADAR Science Team, 2005: An overview of Cassini RADAR Mapper observations of Titan. *AAS Div. Planet Sci. Mtg*., Cambridge, England, September.

Wall, S. D., R. M. Lopes, and the Cassini RADAR Science Team, 2008: Evidence for cryovolcanic activity on the surface of Titan, *IAVCEI Conf.*

Wall, S. D., M. A. Janssen, A. Le Gall, H. Zebker, L. Wye, and P. Paillou, 2009a: Cassini RADAR: What microwaves tell us about Titan, *PIERS*.

Wall, S. D., R. M. Lopes, E. R. Stofan, C. A. Wood, J. R. Radebaugh, S. M. Hörst, B. W. Stiles, R. M. Nelson, L. W. Kamp, M. A. Janssen, R. D. Lorenz, J. I. Lunine, T. G. Farr, G. Mitri, P. Paillou, F. Paganelli, and K. L. Mitchell, 2009b: Cassini RADAR images at Hotei Arcus and western Xanadu, Titan: Evidence for geologically recent cryovolcanic activity. *Geophys. Res. Lett*., **36**, L04203, doi:10.1029/2008GL036415.

Wall, S. D., A. Hayes, C. Bristow, R. Lorenz, E. Stofan, J. Lunine, A. Le Gall, M. Janssen, R. Lopes, L. Wye, P. Soderblom, P. Paillou, O. Aharonson, H. Zebker, T. Farr, G. Mitri, R. Kirk, K. Mitchell, C. Notarnicola, D. Casarano, and B. Ventura, 2010: Active shoreline of Ontario Lacus, Titan: A morphological study of the lake and its surroundings. *Geophys. Res. Lett*., **37**, L05202, doi:10.1029/2009GL041821.

West, R. D., Y. Anderson, B. Stiles, K. Kelleher, L. Wye, P. Callahan, A. Le Gall, Y. Gim, G. Hamilton, M. Janssen, R. L. Kirk, W. T. K. Johnson, R. Lorenz, C. Veeramachaneni, H. Zebker, and the Cassini RADAR Science Team, 2008a: Survey of Cassini Prime

Mission radar data on Titan. *40th Amer. Astron. Soc. Div. Planet. Sci., Bull. Amer. Astron. Soc.,* **40**, 449.

West, R. D., Y. Anderson, B. Stiles, K. Kelleher, L. Wye, P. Callahan, A. Le Gall, Y. Gim, G. Hamilton, M. Janssen, R. Kirk, W. T. K. Johnson, R. Lorenz, C. Veeramachaneni, H. Zebker, and the Cassini RADAR Science Team, 2008b: Cassini RADAR: Extended Mission Plans and Expected Results. *Amer. Geophys. Union*.

West, R. D., Y. Anderson, R. Boehmer, L. Borgarelli, P. Callahan, C. Elachi, Y. Gim, G. Hamilton, S. Hensley, M. A. Janssen, W. T. K. Johnson, K. Kelleher, R. Lorenz, S. Ostro, L. Roth, S. Shaffer, B. Stiles, S. Wall, L. C. Wye, and H. A. Zebker, 2009: Cassini RADAR sequence planning and instrument performance. *IEEE Trans. Geosci. and Remote Sensing*, **47**(6), 1777–1795, doi 10.1109/TGRS.2008.2007217.

Wood, C. A., R. Lorenz, R. Kirk, R. Lopes, K. Mitchell, and E. Stofan, 2010: Impact craters on Titan. *Icarus,* **206**, 334–344, doi:10.1016/j.icarus.2009.08.021.

Wye, L. C., H. A. Zebker, S. J. Ostro, R. D. West, Y. Gim, M. A. Janssen, R. D. Lorenz, S. Hensley, and the Cassini RADAR Science Team, 2005: Titan's surface observed with the Cassini RADAR scatterometer. *Amer. Geophys. Union Joint Assembly Mtg*., New Orleans, LA, May 23–27.

Wye, L. C., H. A. Zebker, and the Cassini RADAR Science Team, 2006a: A second look at reduction and analysis of low-resolution Cassini RADAR scatterometer Titan data. *Amer. Astron. Soc. Div. Planet. Sci*. *Mtg*., Oct 8–13.

Wye, L. C., H. A. Zebker, R. D. Lorenz, and the Cassini RADAR Science Team, 2006b: Modeling Titan's surface from Cassini RADAR's scatterometer and radiometer measurements. *37th Lunar Planet. Sci. Conf.*, Abstract 1473, March 15.

Wye, L. C., H. A. Zebker, M. Janssen, R. Lorenz, R. West, and the Cassini RADAR Science Team, 2007a: Composition of Titan's surface features constrained through backscatter modeling, *Workshop on Ices, Oceans, and Fires: Satellites of the Outer Solar System*, Boulder, CO, August 13–15.

Wye, L. C., H. A. Zebker, M. Janssen, R. Lorenz, R. West, Y. Gim, P. Paillou, and the Cassini RADAR Science Team, 2007b: Backscatter modelling of Titan's surface features using a comprehensive collection of Cassini RADAR data. *39th Amer. Astron. Soc. Div. Planet. Sci*. *Mtg.*, Orlando, FL, October 7–12.

Wye, L. C., H. A. Zebker, S. J. Ostro, R. D. West, and the Cassini RADAR Science Team, 2007c: Range-Doppler processing of Saturn's icy satellites using the Cassini RADAR scatterometer. *Amer. Geophys. Union Fall Mtg*., San Francisco, CA, December 10–14.

Wye, L. C., H. A. Zebker, S. J. Ostro, R. D. West, Y. Gim, R. D. Lorenz, and the Cassini RADAR Science Team, 2007d: Electrical properties of Titan's surface from Cassini RADAR scatterometer measurements. *Icarus*, **188**, 367–385.

Wye, L. C., H. A. Zebker, R. M. Lopes, R. Peckyno, A. Le Gall, and M. A. Janssen, 2009a: A backscatter analysis of Titan's surface features and their global distribution using Cassini RADAR data, *Bull. Amer. Aston. Soc*., **41**, 560.

Wye, L. C., H. A. Zebker, and R. D. Lorenz, 2009b: Smoothness of Titan's Ontario Lacus: Constraints from Cassini RADAR specular reflection data. *Geophys. Res. Lett*., **36**, L16201, doi:10.1029/2009GL039588.

Zebker, H. A., 2008: The shape of Saturn's moon Titan from radar scattering properties. *PIERS*, Cambridge, MA, July 2–6.

Zebker, H. A., and L. Wye, 2006: Electrical properties of Titan surface from Cassini scatterometer and radiometer measurements. *PIERS*, Cambridge, MA, March 27.

Zebker, H. A., B. Stiles, S. Hensley, P. Callahan, Y. Gim, R. D. Lorenz, and R. L. Kirk, 2008: Titan's shape from Cassini radar altimeter and SAR monopulse observations, *Amer. Geophys. Union Fall Mtg*.

Zebker, H. A., Y. Gim, P. Callahan, S. Hensley, R. Lorenz, and the Cassini RADAR Science Team, 2009a: Analysis and interpretation of Cassini Titan radar altimeter echoes. *Icarus*, **200**(1), 240–255.

Zebker, H. A., B. Stiles, S. Hensley, R. D. Lorenz, R. L. Kirk, and J. Lunine, 2009b: Size and shape of Saturn's moon Titan. *Science*, published online, *Science Express Reports*, April 2, doi:10.1126/science.1168905.

12 Appendix 2: Acronyms

AACS	attitude and articulation control subsystem
ABDR	Altimeter Burst Data Record
ASI	Agenzia Spaziale Italiana (Italian Space Agency)
ASIC	application-specific integrated circuit
AU	astronomical unit
BAQ	block-adaptive quantizer
BG	background
BIDR	Basic Image Data Record
BIE	incidence angle data
BIL	number of looks data
BIM	beam mask data
BIN	longitude data
BIS	image file with correction for noise but not incidence angle
BIT	latitude data
BIU	bus interface unit
BIU	image file without correction for incidence angle or noise
BODP	Burst-Ordered Data Product
CCSDS	Consultative Committee for Space Data Systems
CDAP	Cassini Data Analysis Program
CDS	command and data subsystem
CIRS	Composite Infrared Spectrometer
CO	carryover
CODMAC	Committee of Data Management and Computation
CRST	Cassini RADAR Science Team
CRT	Cassini RADAR Transition
DBE	double-bit error
DMP	Digital Map Product
DOM	Distributed Object Manager (Cassini project database)
DSN	Deep Space Network
DSS	Deep Space Station
DTM	Digital Topographic Model
DTN	data take number
DV	data volume
ECR	Engineering Change Request
ESA	European Space Agency

FSIV	Final Sequence Integration and Validation
GRDR	Global Radiometry Data Record
GSD	ground-sample distance
GSDR	Global Scatterometry Data Record
GTDR	Global Topography Data Record
HGA	high-gain antenna
HiSAR	high-altitude SAR imaging
IDAP	Immediate/Delayed Action Program
IEB	instrument execution block
IEEE	Institute of Electrical and Electronics Engineers
IAU	International Astronomical Union
INMS	Ion and Neutral Mass Spectrometer
ISA	Incident, Surprise, Anomaly Report
ISA	Italian Space Agency
ISS	imaging science subsystem
ITL	Incompressible Test List
IVP	inertial vector propagator
LBDR	Long Burst Data Record
LGA	low-gain antenna
LSB	least significant bit
MIDR	Mosaicked Image Data Record
MSS	mission sequence subsystem
NASA	National Aeronautics and Space Administration
ND	not determined
NRCS	normalized radar cross section
OTM	orbit trim maneuver
PDS	Planetary Data System
P/FR	Problem/Failure Report
PMS	propulsion module subsystem
PPS	power and pyrotechnics subsystem
PRDR	Pass Radiometry Data Record
PRF	pulse repetition frequency
PSDR	Pass Scatterometry Data Record
PSIV	Preliminary Sequence Integration and Validation
PDT	Pacific Daylight Time
PST	Pacific Standard Time

PTDR	Pass Topography Data Record
RADAR	Cassini Radio Detection and Ranging instrument
RFS	radio frequency subsystem
RIDR	Repeat Image Data Record
RL	resistive load
RMSS	RADAR Mapping Sequencing Software
RTG	radioisotope thermoelectric generator
S/C	spacecraft
SAB	SAR-altimetry burst
SAR	synthetic aperture radar
SARSME	SAR Spin Model Estimation
SBDR	Short Burst Data Record
SFDU	Standard Formatted Data Unit
SIS	software interface specification
SNR	signal-to-noise ratio
SOI	Saturn Orbit Insertion
SOP	Science Operation Plan
SOST	Satellites Orbiter Science Team
SSG	subsequence generation
SSR	solid-state recorder
SSUP	Science and Sequence Update Process
TCS	temperature control subsystem
TOST	Titan Orbiter Science Team
TWT	Target Working Team
USGS	United States Geological Survey
UTC	Coordinated Universal Time
VHSIC	very-high-speed integrated circuit
VIMS	Visible and Infrared Mapping Spectrometer
WGPSN	Working Group for Planetary System Nomenclature
WTK	William T. K. Johnson data volume
XM	Cassini's first extended mission, Equinox Mission
XXM	Cassini's second extended mission, Solstice Mission

This document has been reviewed and determined not to contain export-controlled technical data.

13 Appendix 3: Links to SAR Swaths on Photojournal Site

The table below provides a complete list of Cassini Titan RADAR Mapper SAR swaths, in order of acquisition. Swaths released to the Planetary Data System are published on the JPL Photojournal Web site (http://photojournal.jpl.nasa.gov). The Photojournal releases can be accessed directly via the links given, e.g. (for the T13 flyby) http://photojournal.jpl.nasa.gov/catalog/PIA8552.

ORBIT	ORIG. DATE	PIA	WEB LINK	TITLE
Ta	10/27/2004	13961	http://photojournal.jpl.nasa.gov/catalog/PIA13961	Ta RADAR Full Swath (PIA 13961)
T3	2/15/2005	13962	http://photojournal.jpl.nasa.gov/catalog/PIA13962	T3 RADAR Full Swath (PIA 13962)
T7	9/7/2005	13963	http://photojournal.jpl.nasa.gov/catalog/PIA13963	T7 RADAR Full Swath (PIA 13963)
T8	10/28/2005	13964	http://photojournal.jpl.nasa.gov/catalog/PIA13964	T8 RADAR Full Swath (PIA 13964)
T13	4/30/2006	8552	http://photojournal.jpl.nasa.gov/catalog/PIA8552	Titan (T13) Viewed by Cassini's RADAR—April 30, 2006
T16	7/22/2006	9112	http://photojournal.jpl.nasa.gov/catalog/PIA9112	PIA09112: Titan (T16) Viewed by Cassini's RADAR—July 22, 2006
T17	9/7/2006	9172	http://photojournal.jpl.nasa.gov/catalog/PIA9172	PIA09172: Titan (T17) Viewed by Cassini's RADAR—Sept. 7, 2006
T18	9/23/2006	9179	http://photojournal.jpl.nasa.gov/catalog/PIA9179	PIA09179: Titan (T18) Viewed by Cassini's RADAR—Sept. 23, 2006
T19	10/9/2006	13965	http://photojournal.jpl.nasa.gov/catalog/PIA13965	T19 RADAR Full Swath (PIA 13965)
T21	12/12/2006	13966	http://photojournal.jpl.nasa.gov/catalog/PIA13966	T21 RADAR Full Swath (PIA 13966)
T23	1/13/2007	13967	http://photojournal.jpl.nasa.gov/catalog/PIA13967	T23 RADAR Full Swath (PIA 13967)
T25	2/22/2007	9182	http://photojournal.jpl.nasa.gov/catalog/PIA9182	Titan (T25) Viewed by Cassini's RADAR—Feb. 22, 2007
T28	4/10/2007	9217	http://photojournal.jpl.nasa.gov/catalog/PIA9217	PIA09217: Titan (T28) Viewed by Cassini's RADAR—April 10, 2007
T29	4/26/2007	13968	http://photojournal.jpl.nasa.gov/catalog/PIA13968	T29 RADAR Full Swath (PIA 13968)
T30	5/12/2007	9218	http://photojournal.jpl.nasa.gov/catalog/PIA9218	PIA09218: Titan (T30) Viewed by Cassini's RADAR—May 12, 2007
T36	10/2/2007	13969	http://photojournal.jpl.nasa.gov/catalog/PIA13969	T36 RADAR Full Swath (PIA 13969)
T39	12/20/2007	13970	http://photojournal.jpl.nasa.gov/catalog/PIA13970	T39 RADAR Full Swath (PIA 13970)
T41	2/22/2008	11822	http://photojournal.jpl.nasa.gov/catalog/PIA11822	PIA11822: Skirting Xanadu's Southern Boundary
T43	5/12/2008	12988	http://photojournal.jpl.nasa.gov/catalog/PIA12988	PIA12988: Dunes, Tectonics and Possible Ice Volcanoes on Titan
T44	5/28/2008	12989	http://photojournal.jpl.nasa.gov/catalog/PIA12989	PIA12989: Xanadu's Channels and Dunes
T48[1]	12/5/2008	13950	http://photojournal.jpl.nasa.gov/catalog/PIA13950	T48 RADAR Full Swath (PIA 13950)
T49	12/21/2008	13951	http://photojournal.jpl.nasa.gov/catalog/PIA13951	T49 RADAR Full Swath (PIA 13951)
T50	2/7/2009	13952	http://photojournal.jpl.nasa.gov/catalog/PIA13952	T50 RADAR Full Swath (PIA 13952)
T55	5/21/2009	13953	http://photojournal.jpl.nasa.gov/catalog/PIA13953	T55 RADAR Full Swath (PIA 13953)
T56	6/6/2009	13954	http://photojournal.jpl.nasa.gov/catalog/PIA13954	T56 RADAR Full Swath (PIA 13954)

ORBIT	ORIG. DATE	PIA	WEB LINK	TITLE
T57	6/22/2009	13955	http://photojournal.jpl.nasa.gov/catalog/PIA13955	T57 RADAR Full Swath (PIA 13955)
T58	7/8/2009	13956	http://photojournal.jpl.nasa.gov/catalog/PIA13956	T58 RADAR Full Swath (PIA 13956)
T59	7/24/2009	13957	http://photojournal.jpl.nasa.gov/catalog/PIA13957	T59 RADAR Full Swath (PIA 13957)
T60		N/A	http://photojournal.jpl.nasa.gov/catalog/PIAN/A	(Lost due to DSN failure)
T61	8/25/2009	13958	http://photojournal.jpl.nasa.gov/catalog/PIA13958	T61 RADAR Full Swath (PIA 13958)
T64[2]	12/28/2009	13959	http://photojournal.jpl.nasa.gov/catalog/PIA13959	T64 RADAR Full Swath (PIA 13959)
T65	1/12/2010	13960	http://photojournal.jpl.nasa.gov/catalog/PIA13960	T71 RADAR Full Swath (PIA 13960)
T71[2]	7/7/2010	N/A	http://photojournal.jpl.nasa.gov/catalog/PIAN/A	(Currently in embargo)

[1] Run1 version only
[2] ql1 or ql2 version only

14 Appendix 4: Cassini RADAR Uplink/Downlink Spreadsheet

KEY:
- Event occurred
- Event IEB delivery was skipped
- Event ERROR

Notes at the end of the spreadsheet describe column headings and define acronyms used.

IEB	DTN	Seq #	BG vs SSR	IDAP	PSIV2 Delivery (Subseq)	EXECUTION Date (UTC)	EXECUTION Julian Day	EXECUTION TIME (UTC)	Duration Total (sec)	~End of Downlink (PST/PDT)	Actual DV (kbit)	NOTES
ph_000_1	31	S01	BG	no	04/20/2004	06/11/2004	163	11:08:36	10320	06/12/2004 by 4:46 pm	2705.6	WTK (4.0) files did not include all expected telemetry gaps. Total (ph1 & ph2)
ph_000_2	32	S01	SSR	YES Live IVP	04/20/2004	06/11/2004	163	14:08:52	41684	06/12/2004 by 4:46 pm	285030.4	287736
s04_engtest	33	S04	BG	no	08/17/2004	10/13/2004	287	22:50:00	3000	10/15/2004 by 3:58 am	289180	
ti_00a_1	34	S05	BG	YES	09/20/2004?	10/25/2004	299	0:01:00	21600	10/25/2004 at 10:45 am	476216	Missing 266 packets (15 gaps)
ta	35	S05	BG	YES	09/20/2004?	10/26/2004	300	10:20:39	36561	10/27/2004 at 3:30 am	562810	All packets recovered! All data are present!
ti_00a_2	36	S05	SSR	no	09/20/2004?	11/06/2004	311	16:53:00	19461	11/07/2004 at 9:02 am	99606	Missing 150 packets (4 gaps)
src_00b_1	37	S06	BG	no	10/19/2004	11/30/2004	335	16:25:00	35400	12/01/2004 at 9:04 am (or CO*)	35500	Handedit (shorttime by 1 minute) to meet DV
di_00b_1	38	S06	BG	YES Live IVP	10/19/2004	12/14/2004	349	21:57:30	18610	12/15/2004 at 8:36 am (or CO*)	0	S/C commanding error. THIS ACTIVITY DID NOT GET DOWNLINKED!
mi_00b_1	39	S06	BG	YES Live IVP	10/19/2004	12/15/2004	350	3:09:57	4023	12/15/2004 at 8:36 a+R33m (or CO*)	0	S/C commanding error. THIS ACTIVITY DID NOT GET DOWNLINKED!
ia_00b_1	40	S07 MIA	MIA-Mini	no	11/16/2004	12/31/2004	366	1:50:00	21900	12/31/2005 at 6:44 am (or CO)	318295.6	3 gaps: Total loss = 228 SABs
ia_00c_1	41	S07 MIA	MIA-Mini	no	11/16/2004	01/01/2005	001	13:05:00	38362	01/06/2005 at 5:07 am (last CO)	1259214	1 gap missing 2 SABs

IEB	DTN	Seq #	BG vs SSR	IDAP	PSIV2 Delivery (Subseq)	EXECUTION Date (UTC)	EXECUTION Julian Day	EXECUTION TIME (UTC)	Duration Total (sec)	~End of Downlink (PST/PDT)	Actual DV (kbit)	NOTES
ti_00c_1	42	S08	BG	no	12/09/2004	01/26/2005	026	13:05:00	17400	01/27/2005 at 2:37 am	14280.4	Missing 46 (FIN5) during warm-up
ti_00c_2	43	S08	BG	no	12/09/2004	01/28/2005	028	13:05:00	13800	1/29/2005 at 2:22 am (or CO)	9887.6	No gaps
engtest	44	S08	BG	no	12/09/2004	01/29/2005	029	14:05:00	6600	1/30/2005 19:52 (or CO)	282902.4	Power State Error due to IEB duration longer than it should be . . . OK
t3	45	S08	BG	YES	12/09/2004	02/15/2005	046	2:17:53	20819	02/15/2005* at 8:18 pm	639844	Two gaps: First missed 3496 SABs (FIN8). This was expected due to S&ER3. A second critical gap of 171 SABs (FIN243-249) at +11 CPA (46 seconds for SAR). Incorrect ND setting
en_003_1	46	S08	Mini-Seq	no	12/09/2004	02/17/2005	048	8:21:30	11190	02/18/2005 at 1:57 am	495953.2	No gaps!
en_004_1	47	S09	BG	YES	02/01/2005	03/09/2005	068	12:06:41	13200	03/09/2005 at 20:00* (CO)	397586.4	Telem gap at FIN5 for telemetry mode (missed 1423 SABs), plus Fin 58 drop 3 SABs, plus FIN134 dropped 99 SABs
t4	48	S09	BG	YES	02/01/2005	03/31/2005	090	14:38:06	29100	04/01/2005 at 15:36	157092	T4—rad and scat only (plus attn test) (missed 2701 SABs due to telem). WTK2seqsasf DV calculation incorrect for scat_compress
engtest	49	S09	BG	no	02/01/2005	04/08/2005	098	8:30:35	17580	04/08/2005 at 22:29	154333.2	
rings_006_1	50	S10	BG	no	03/16/2005	04/12/2005	102	9:35:00	31799	04/12/2005 at xx:xx	31942.8	1 gap missing 9 SABs at FIN 18
ti_006_1	51	S10	BG	YES, -9 sec	03/16/2005	04/17/2005	107	22:30:00	17729	04/18/2005 at 15:14 (or CO*2)	262899	Missing 9 SABs
src_006_1	52	S10	BG	no	03/16/2005	04/18/2005	108	3:28:45	24675	04/18/2005 at 15:14 (or CO*2)	70307.6	Missing 205 SABs

IEB	DTN	Seq #	BG vs SSR	IDAP	PSIV2 Delivery (Subseq)	EXECUTION Date (UTC)	Julian Day	TIME (UTC)	Duration Total (sec)	~End of Downlink (PST/PDT)	Actual DV (kbit)	NOTES
ti_010_1	53	S12	BG	no	05/23/2005	06/19/2005	170	0:45:00	13800	06/19/2005 at 16:04	6148.4	38 missing SABs (DSN gap)
ti_011_1	54	S12	BG	no	05/23/2005	07/11/2005	192	23:35:00	14700	07/12/2005 at 16:44	3655.6	S&ER3: Expect to drop 2520 SABs
rh_011_1	55	S12	BG	YES	05/23/2005	07/14/2005	195	4:15:00	20401	07/15/2005 at 2:54	212123.6	S&ER3: Expect to drop ~3200 SABs
engtest	56	S13	Mini-Seq	no	06/29/2005	08/23/2005	235	19:40:00	10195	8/24/2005 at 15:36	250625.2	DSN drop of 30 seconds (70 SABs)
src_013_1	57	S13	Mini-Seq	no	06/29/2005	08/23/2005	235	23:40:00	35803	8/24/2005 at 15:36	31730	Minus S&ER3 gap
									35803			
rings_014_1	58	S14	BG	no	08/04/2005	09/03/2005	246	5:00:00	33601	09/03/2005 at 19:44 (w CO?)	21987	Expect to drop ~11690 SABs due to S&ER3
t7	59	S14	BG	as expected 7:25:07	08/04/2005	09/07/2005	250	7:27:07	21720	09/09/2005 at ~11:00 (for RADAR)	179154.8	SSR problem lost data from -2 CPA until end. DSN problem lost data from start to -14:45. Plus multiple small gaps during downlink (one medium size gap (~42 SABs) causes a gap in image. Incorrect ND & RL setting
sa_015_1	60	S14	BG	no	08/04/2005	09/23/2005	266	11:30:00	47130	09/24/2005 at 18:34 (w CO?)	34291.2	Dropped 12036 SABs due to S&ER3. Second small gap of 122 SABs (OBS: Sat1&2)
te_015_1	61	S14	Mini-Seq	23:59:25	08/04/2005	09/23/2005	266	23:59:25	26895	same as above	248960.8	Planned/expected dropped 5364 SABs due to S&ER3
sa_015_2	62	S14	BG	no	08/04/2005	09/24/2005	267	5:04:00	9155	same as above	7942	OBS: Sat3. No dropped packets
hy_015_1	63	S14	BG	as expected 06:00:16	08/04/2005	09/26/2005	269	6:00:16	10306	09/26/2005 at 18:57 (w CO?)	392669.2	No gaps due to second downlink recovery!

This document has been reviewed and determined not to contain export-controlled technical data.

IEB	DTN	Seq #	BG vs SSR	IDAP	PSIV2 Delivery (Subseq)	EXECUTION Date (UTC)	EXECUTION Julian Day	EXECUTION TIME (UTC)	Duration Total (sec)	~End of Downlink (PST/PDT)	Actual DV (kbit)	NOTES
di_016_1	64	S15	BG	shift by -2 sec to 19:12:00	09/07/2005	10/11/2005	284	19:12:02	15771	10/12/2005 at 12:59	314343.6	Dropped only the expected 90 minutes of data due to S&ER3
t8	65	S15	BG	Live Update 18:37:20	09/07/2005	10/27/2005	300	18:37:20	53085	10/28/2005 at 23:30 (for RADAR)	791304.4	Dropped 4290 SABs due to S&ER3, 1 at FIN 33 (inbound scat), 2 at FIN 249 (SAR+4.5)
ti_017_1	66	S15	BG	no	09/07/2005	11/01/2005	305	3:55:00	14661	11/02/2005 at 10:43	4187.6	Dropped only the 10493 SABs due to S&ER3
ti_017_2	67	S15	BG	no	09/07/2005	11/11/2005	315	20:58:00	13801	11/12/2005 at 10:15	6178.8	One CCSDS packet drop (equal 8 SABs drop. At 4 sec BPD)
ti_017_3 / ia_017_1	68	S16	BG	as expected 17:50:25	10/18/2005	11/12/2005	316	17:50:25	24120	11/13/2005 at 11:16	321898	RMSS will create one IEB (ia_017_1). On downlink we will cut into two data files for the two targets and call the first one ti_017_3 FSIV: VIMS IEB load conflicts with our FLTSW load, shift our turn on sequence by ~20 minutes. New IEB duration, therefore new IEB required Gap of 152 SABs observed
rh_018_1	69	S16	BG	as expected 00:39:09	10/18/2005	11/27/2005	331	0:39:09	17605	11/27/2005 at 1:49	698675.6	There is a 2:40:00 gap expected due to S&ER3 (~5980 SABs)
ti_019_1	70	S16	BG	no	10/18/2005	12/13/2005	347	17:05:00	13800	12/14/2005 at 8:04	6186.4	No gaps expected
ti_019_2	71	S16	BG	no	10/18/2005	12/15/2005	349	0:45:00	15960	12/15/2005 at 8:05	8192.8	1 gap of 161 sec (160 SABs)
eng_019_1	72	S17	BG	no	11/15/2005	12/23/2005	357	15:42:10	10601	12/24/2005 at ~7:00	301773.2	Testbed had disk crash, so not tested on BB Two gaps, 65 sec (144 SABs) & 7 sec (14 SABs)
ti_021_1	73	S18	BG	no	12/15/2005	02/15/2006	046	10:42:00	13800	02/15/2006 at 21:00	6186.4	No gaps
ti_021_2	74	S18	BG	no	12/15/2005	02/16/2006	047	3:42:00	13800	02/17/2006 at 4:21	6186.4	No gaps
te_021_1	75	S18	BG	as expected 16:05:00	12/15/2005	02/25/2005	056	16:05:00	14670	02/26/2006 at 2:20	290570.8	Expected data drop of 9926 SABs during VIMS collection
src_021_1	76	S18	BG	no	12/15/2005	02/28/2006	059	13:26:00	35400	03/01/2006 at 2:03	27291.6	Two small gaps of 9 seconds and 138 seconds

This document has been reviewed and determined not to contain export-controlled technical data.

IEB	DTN	Seq #	BG vs SSR	IDAP	PSIV2 Delivery (Subseq)	EXECUTION Date (UTC)	Julian Day	TIME (UTC)	Duration Total (sec)	~End of Downlink (PST/PDT)	Actual DV (kbit)	NOTES
ti_022_1	77	S19	BG	no	02/09/2006	03/14/2006	073	8:11:11	18829	03/16/2006 at ~2:00 w/ CO	10160.2	No gaps
T12	78	S19	BG	NO IVP update. As expected 22:55:57	02/09/2006	03/18/2006	077	22:56:26	23670	03/19/2006 at 18:20	240334.8	High-res scat attempt. One expected gap due to telemetry
rh_022_1	79	S19	Mini-Seq	YES, LIVE. WITH MINI-SEQ	02/09/2006	03/21/2006	080	6:25:29	36571	03/22/2006 at ~2:00	738347.6	Stare, 5-point scat, raster
ti_023_1	80	S20	BG	no	03/29/2006	04/26/2006	116	17:29:00	17401	04/26/2006 at 22:15	9355.6	Rad (plus eng test)
ti_023_2	81	S20	BG	YES - OD-58 4/25/2006	03/29/2006	04/29/2006	119	17:14:00	17370	04/29/2006 at 22:00	159166.8	Scat (plus eng tests). 10 small gaps. Missing 129 SABs
T13	82	S20	BG	YES - OD-58 4/25/2006	03/29/2006	04/30/2006	120	20:23:15	33870	05/01/2006 at 14:30	610561.2	Full SAR pass, plus outbound Possibly an ITL test, so delivery required for SSG 1 gap: missing 1748 SABs
engtest	83	S20	BG	no	03/29/2006	05/12/2006	132	14:00:00	10200	05/12/2006 at 21:15	387554.4	Attn test. 6 small gaps
ti_024_1	84	S20	BG	no	03/29/2006	05/16/2006	136	9:30:00	15600	05/16/2006 at 22:00	9682.4	Rad (plus eng test). 1 gap of 69 SABs
ti_025_1	85	S21	BG	no	05/09/2006	07/01/2006	182	2:06:00	7200	07/01/2006 at 18:00	13452	Rad
T15	86	S21	BG	YES as expected 01:25:47	05/09/2006	07/02/2006	183	4:20:00	14400	07/03/2006 at 10:30:00	145144.8	Rad and scat

This document has been reviewed and determined not to contain export-controlled technical data.

IEB	DTN	Seq #	BG vs SSR	IDAP	PSIV2 Delivery (Subseq)	EXECUTION Date (UTC)	Julian Day	TIME (UTC)	Duration Total (sec)	~End of Downlink (PST/PDT)	Actual DV (kbit)	NOTES
T16	87	S22	BG	as expected 16:30:26	06/14/2006	07/21/2006	202	16:30:55	30269	07/22/06 Saturday 203 14:36P	779813.2	Inbound alt & full SAR. 4 unknown gaps
ti_026_1	88	S22	BG	no	06/14/2006	08/03/2006	215	0:09:59	19200	215 23:05U	13186.6	Gap of 9 sec. Missing 8 SABs
ti_027_1	89	S22	BG	no	06/14/2006	08/13/2006	225	8:09:59	16320	225 22:12U	13915.6	No gaps
di_027_1	90	S22	mini	mini 228T08:10:00	08/04/2006	08/16/2006	228	8:10:29	15571	229 22:21U	147956.8	1 early gap of 40 seconds
rh_027_1	91	S22	mini	mini 229T03:30:00	08/04/2006	08/17/2006	229	3:30:29	11670	229 22:21U	157783.6	No gaps
ti_027_2	92	S23	BG	no	07/25/2006	08/22/2006	234	15:11:00	51600	235 21:51U	58611	Include source scan and eng test (on & off target)
T17 (rider)	93	S23	BG	YES (I=-20s) 250T18:58:03	07/25/2006	09/07/2006	250	18:58:23	4910	09/08/06 Friday 251 13:06	62373.2	~4–5 minutes of SAR
en_028_1 (rings_028_1)*	94 95	S23	BG	IVP -3 252T21:06:07	07/25/2006	09/09/2006	252	21:06:40	31730	253 21:00U	152038	Includes rings_028_1 observation and eng test
rings_028_2	96	S23	BG	no	07/25/2006	09/11/2006	254	5:05:00	22800	254 21:00U	18065.2	Includes eng test
ti_029_1	97	S24	BG	no	08/22/2006	09/21/2006	264	4:50:00	17400	264T20:22U or 265T18:52U	111568	
T18 (rider)	98	S24	BG	IDAP 266T17:03:49	08/22/2006	09/23/2006	266	17:04:19	7980	267T20:00U	120885.6	~10 minutes of SAR
ti_030_1	99	S24	BG	no	08/22/2006	10/07/2006	280	5:05:00	16500	280T19:24U	87080.8	
T19	100	S24	BG	OD ~10/4 YES 282T09:15:07	08/22/2006	10/09/2006	282	9:15:37	48601	2006-283T19:00U 10/10/2006 3:00-12:00	889686.4	X-only rolling (INMS ride-along)

IEB	DTN	Seq #	BG vs SSR	IDAP	PSIV2 Delivery (Subseq)	EXECUTION Date (UTC)	Julian Day	TIME (UTC)	Duration Total (sec)	~End of Downlink (PST/PDT)	Actual DV (kbit)	NOTES
T20	101	S25	BG	OTM 78-OTM79-Sun22 YES	09/27/2006	10/25/2006	298	7:33:04	25800	299T11:15P	250169.2	High scat-SAR
ti_032_1/eng	102	S25	BG	no	09/27/2006	11/04/2006	308	18:17:00	15600	309T17:30	307466	
ti_032_2	103	S25	BG	no	09/27/2006	11/06/2006	310	17:35:00	15600	311T17:28	7532	
en_032_1	104	S25	mini	Mini	09/27/2006	11/08/2006	312	22:45:00	15000	UTC:313T17:28	144567.2	
ti_032_3	105	S25	BG	no	09/27/2006	11/13/2006	317	18:19:00	13800	UTC:318T16:59	3245	
di_033_1	106	S25	BG	OTM 80 YES, Mini	09/27/2006	11/20/2006	324	22:05:00	21000	UTC:326T09:15	163826	
ti_033_1	107	S26	BG	no	10/24/2006	11/25/2006	329	2:05:00	17400	UTC:329T16:30	6992	
T21	108	S26	BG	YES	10/24/2006	12/12/2006	346	9:02:01	23640	12/13/2006 at 5:30	541701	Double-bit errors (DBEs) on the SSR are corrupting the data, All data are present, but ~4 minutes of data have not gone into the preprocessor (scatmode) due to the DBEs (FYI: 2 ITL runs)
src_035_1/eng	109	S26	BG	no	10/24/2006	12/19/2006	353	15:23:00	35400	UTC:354T14:48	57243.2	
ti_037_1	110	S27	BG	YES +24seconds	11/30/2006	01/11/2007	011	23:09:02	17338	UTC:012T13:34	250465.6	Rad/eng or scat or high SAR. Dropped 2 SABs
T23	111	S27	BG	YES	11/30/2006	01/13/2007	013	0:43:31	46140	UTC:014T13:34	804429.6	Full pass (0.5, 0.5, 2.0 pointing). Dropped 711 SABs; however some expected ~561. Missing ~150
ti_037_2	112	S27	BG	YES	11/30/2006	01/14/2007	014	13:40:10	12770	UTC:015T05:36	133950	Rad/eng or scat or high SAR
ti_037_3	113	S27	BG	no	11/30/2006	01/15/2007	015	13:35:00	15600	UTC:016T05:36	3947.6	Rad
ti_037_4	114	S27	BG	no	11/30/2006	01/18/2007	018	17:25:00	15600	UTC:019T12:51	7448	Rad
ti_037_5	115	S27	BG	no	11/30/2006	01/20/2007	020	22:50:00	15600	UTC:021T12:36	6095.2	Rad
rings_038_1	116	S27	BG	no	11/30/2006	01/27/2007	027	13:41:02	46199	UTC:028T12:12	35910	Rings rad/eng, lot of little gaps, we did get hit by DBE
ti_038_1	117	S27	BG	no	11/30/2006	02/03/2007	034	6:15:00	13800	UTC:035T11:37	4658.8	Rad
rings_038_2	118	S27	BG	no	11/30/2006	02/04/2007	035	17:57:00	40800	UTC:036T12:37	32991.6	Rings rad/eng
hy_039_1	119	S27	BG	NO, just let BG trig go (+30) 2/7 OTM 93	11/30/2006	02/15/2007	046	20:00:00	19440	UTC:047T10:52	246278	Scat/eng

IEB	DTN	Seq #	BG vs SSR	IDAP	PSIV2 Delivery (Subseq)	EXECUTION Date (UTC)	Julian Day	TIME (UTC)	Duration Total (sec)	~End of Downlink (PST/PDT)	Actual DV (kbit)	NOTES
T25	120	S28	BG	YES	01/24/2007	02/21/2007	052	19:17:24	45660	UTC:054T11:26:00 2/23-FRI@3:26 PST	555940	Some double-bit hits on SSR
rings_039_1	121	S28	BG	no	01/24/2007	02/23/2007	054	10:17:10	32390	UTC:055 10:22	28302.4	
ti_039_1	122	S28	BG	no	01/24/2007	02/26/2007	057	11:41:00	17400	UTC:058 02:36	9750.8	
ti_040_1	123	S28	BG	no	01/24/2007	03/05/2007	064	10:41:00	13801	UTC:065 02:21	6178.8	
ti_040_2	124	S28	BG	YES	01/24/2007	03/08/2007	067	15:26:00	15540	UTC:068 09:21	395298.8	Distant scat, with eng
ti_040_3	125	S28	BG	no	01/24/2007	03/13/2007	072	19:35:00	13800	UTC:073 09:06	3252.8	
T28	126	s29	BG	YES	02/28/2007	04/10/2007	100	15:03:30	30211	UTC: 101T16:00 - 102T7:00	742010.8	Use PDT kernel for RMSS runs for SSG runs
T29	127	s29	BG	YES	02/28/2007	04/26/2007	116	16:47:58	34461	PST: 117 6:15 117 15:45	871925	
src_043_1	128	s29	BG	no	02/28/2007	04/28/2007	118	10:20:00	35400		31289.2	
ti_043_1	129	s29	BG	no	02/28/2007	04/29/2007	119	8:50:00	13800		3260.4	
ti_043_2	130	s29	BG	no	02/28/2007	05/01/2007	121	22:06:10	13730		1140	
T30	131	s30	BG	no	04/10/2007	05/12/2007	132	12:24:58	44221	PST: 133: 05:30 133 14:30	819865.2	
ti_044_1	132	s30	BG	missed IDAP! BG trig only	04/10/2007	05/13/2007	133	22:18:00	15600		197326.4	Possibly use altimeter instead of SAR
rh_045_1	133	s30	BG	YES	04/10/2007	05/27/2007	147	7:40:00	19800			
engtest	134	s30	BG	no	04/10/2007	06/08/2007	159	5:30:30	16500		292	
mi_047_1	135	s31	mini	Mini	06/23/2007	06/27/2007	178	23:48:00	15989	UTC 180 03:20	264.3	
rh_047_1	136	s31	mini	Mini	06/23/2007	06/28/2007	179	11:35:00	14070	UTC 180 03:20	224	
ti_048_1	137	s32	BG		06/13/2007	07/15/2007	196	11:41:00	13800		5183.2	
te_048_1	138	s32	mini	Mini	06/13/2007	07/20/2007	201	14:35:00	13800		206172.8	Dropped 47 SABs. FIN51-55

This document has been reviewed and determined not to contain export-controlled technical data.

IEB	DTN	Seq #	BG vs SSR	IDAP	PSIV2 Delivery (Subseq)	EXECUTION Date (UTC)	Julian Day	TIME (UTC)	Duration Total (sec)	~End of Downlink (PST/PDT)	Actual DV (kbit)	NOTES
ti_049_1	139	s33	BG		07/12/2007	08/26/2007	238	22:20:00	54001		573.8	
rh_049_1	140	s33	BG	YES, plus 4 s	07/12/2007	08/29/2007	241	19:32:00	43320	Thursday by 4:00pm	225157.6	
ia_049_1	141	s33	BG	YES, 0shift	07/12/2007	09/08/2007	251	21:50:00	53700		561237.2	
ia_049_2	142	s33	BG	YES, 0shift	07/12/2007	09/09/2007	252	21:34:00	30360		291482.8	
ia_049_3	143	s33	BG	YES, 0shift	07/12/2007	09/10/2007	253	8:44:00	40861		330888.8	
ia_049_4	144	s33	BG	YES, 0shift	07/12/2007	09/10/2007	253	22:20:00	25800		155397.2	
ia_049_5	145	s33	BG	YES, 0shift	07/12/2007	09/11/2007	254	20:25:00	58201		0	S/C safing incident: IEB did not execute
rings_050_1	146	s34	BG		08/27/2007	09/27/2007	270	22:11:00	46200		88403.2	Including engineering test
di_050_1	147	s34	BG	YES, 0shift	08/27/2007	09/29/2007	272	21:05:00	21000		274975.6	
en_050_1	148	s34	BG	YES, 0shift	08/27/2007	09/30/2007	273	3:03:15	48436		115178	missing last 25 minutes in ROME file, but OK is SFDU. Double bit errors are confusing ROME SW
T36	149	s34	BG		08/27/2007	10/01/2007	274	18:32:43	53700		791684.4	Using new SAR ping-pong mode
ti_051_1	150	s34	BG		08/27/2007	10/20/2007	293	20:35:30	19200		187438.8	Including engineering test
rings_051_1	151	s34	BG		08/27/2007	10/23/2007	296	18:05:00	19200		8831.2	
ti_051_2	152	s34	BG		08/27/2007	10/27/2007	300	0:20:00	39000		310156	Source scan, may need to split the downlink
rings_052_1	153	s35	BG		10/02/2007	11/14/2007	318	18:02:15	37364		3576565	Engineering tests??
ti_052_1	154	s35	BG		10/02/2007	11/16/2007	320	0:05:00	15599		5183.2	
rings_052_2	155	s35	BG		10/02/2007	11/16/2007	320	18:35:00	19199		8626	
mi_053_1	156	s35	BG	Mini-Seq	10/02/2007	12/02/2007	336	21:05:00	21567		297965.6	
T39	157	s36	BG		11/12/2007	12/20/2007	354	15:17:53	44401	Saturday 12/22 @ 2:15 am	691159.2	
ti_057_1	158	s36	BG		11/12/2007	01/22/2008	022	21:05:00	13799		4294	
sa_058_1	159	s37	BG		12/12/2007	02/08/2008	039	19:19:14	38146		28690	
sa_059_1	160	s38	BG		01/22/2008	02/20/2008	051	1:12:07	54533		267398.4	
T41	161	s38	BG		01/22/2008	02/22/2008	053	7:22:07	40740		805919.2	
en_061_1	162	s38	BG	IDAP	01/22/2008	03/12/2008	072	3:21:12	46921		243815.6	Two parts or two IEBs?
en_061_2	163	s38	BG	IDAP	01/22/2008	03/12/2008	072	16:31:57	15495		199644.4	Two parts or two IEBs?
mi_064_1	164	s39	BG	IDAP	02/20/2008	04/11/2008	102	9:24:30	6599		222700	

This document has been reviewed and determined not to contain export-controlled technical data.

IEB	DTN	Seq #	BG vs SSR	IDAP	PSIV2 Delivery (Subseq)	EXECUTION Date (UTC)	Julian Day	TIME (UTC)	Duration Total (sec)	~End of Downlink (PST/PDT)	Actual DV (kbit)	NOTES
rings_066_1	165	s40	BG		03/25/2008	05/04/2008	125	7:51:00	46200		46420.8	Lots of small DSN gaps, ~450
T43	166	s40	BG		03/25/2008	05/12/2008	133	23:51:58	43019	Tue May 13 @4:30	930642.8	
T44	167	s40	BG		03/25/2008	05/28/2008	149	3:29:32	35699	Thurs May 29 @3:30	609056.4	
******* EXTENDED MISSION ******* EXTENDED MISSION ******* EXTENDED MISSION ******* EXTENDED MISSION *******												
sat rings en_088_1	168 169 170	s44	BG	IDAP	08/12/2008	10/10/2008	284	9:36:00	15940	10/11/2008 @6:00am	402131	
ti_092_1	171	s45	BG		09/08/2008	11/06/2008	311	12:05:00	19199	11/13/2008 2:00am	7508.8	
sa_095_1	172	s46	BG		10/20/2008	12/01/2008	336	5:21:00	31799		112001.2	
sa_095_2	173	s46	BG		10/20/2008	12/03/2008	338	0:02:08	27531		86784.4	
T48	174	s46	BG		10/20/2008	12/05/2008	340	5:15:45	34020		395025.2	
sa_097_1	175	s46	BG		10/20/2008	12/16/2008	351	23:53:00	34319		114592.8	
sa_097_2	176	s46	BG		10/20/2008	12/17/2008	352	23:04:08	31731		123758.3	Lots of small gaps
T49	177	s46	BG		10/20/2008	12/21/2008	356	10:04:52	29999	357 19:29	746631.1	9 one SAB gaps?
ti_098_1	178	s46	BG		10/20/2008	12/23/2008	358	19:35:00	15599		11840.8	
ti_099_1	179	s46	BG		10/20/2008	01/07/2009	007	15:22:08	14331		10624.8	
src_100_1	180	s47	BG		11/18/2008	01/18/2009	018	14:22:00	31431		218614	
T50	181	s47	BG		11/18/2008	02/07/2009	038	23:10:51	56099		696578	Dropped 3 SABs: FIN104*1, FIN227*2
ti_103_1	182	s47	BG		11/18/2008	02/11/2009	042	22:09:00	15599		5768.4	
ti_104_1	183	s48	BG		01/14/2009	02/20/2009	051	15:34:58	12602		6786.8	
ti_105_1	184	s48	BG		01/14/2009	03/13/2009	072	21:30:00	13799		0	LOST OBSERVATION due to the S/C thruster swap. The background sequence suspended for 10 days. Restarted the BG on day 78
ti_106_1	185	s48	BG		01/14/2009	03/19/2009	078	10:41:11	14928		6254.8	

IEB	DTN	Seq #	BG vs SSR	IDAP	PSIV2 Delivery (Subseq)	EXECUTION Date (UTC)	Julian Day	TIME (UTC)	Duration Total (sec)	~End of Downlink (PST/PDT)	Actual DV (kbit)	NOTES
T52	186	s49	BG		02/19/2009	04/03/2009	093	16:52:45	20062		23620.8	Rad & compressed scat only
ti_108_1	187	s49	BG		02/19/2009	04/15/2009	105	18:27:58	15601		5707.6	
ti_108_2	188	s49	BG		02/19/2009	04/16/2009	106	10:32:58	41101		15975.2	
T53	189	s49	BG		02/19/2009	04/20/2009	110	22:50:43	26701		39428.8	Rad & compressed scat only: Dropped 11 unexpected SABs as FIN13
ti_109_1	190	s49	BG		02/19/2009	04/22/2009	112	18:00:00	15599		8443.6	Zero drops
ti_110_1	191	s50	BG		03/31/2009	05/08/2009	128	16:56:00	15599		11833.2	Zero drops
ti_110_2	192	s50	BG		03/31/2009	05/11/2009	131	16:11:00	15599		11377.2	Zero drops
T55	193	s50	BG		03/31/2009	05/21/2009	141	12:31:41	41060		956186.4	Full pass
ti_111_1	194	s50	BG		03/31/2009	05/24/2009	144	6:44:00	15599		11377.2	Zero drops
T56	195	s50	BG		03/31/2009	06/06/2009	157	11:05:01	33719		811239.2	Ends at +26 min, include rerouted chirp engineering test. Lots of one-second gaps??
ti_112_1	196	s50	BG		03/31/2009	06/11/2009	162	14:50:00	41060		11377.2	Zero drops
src_112_1	197	s51	BG		05/06/2009	06/16/2009	167	7:16:03	40800		30270.8	
ti_113_1	198	s51	BG		05/06/2009	06/18/2009	169	19:30:03	15601		5707.6	One 9-second gap (FIN11)
T57	199	s51	BG		05/06/2009	06/22/2009	173	18:11:58	20448		420044.4	Dropped 4 SABs (FIN:69, 69, 165, 168)
T58	200	s51	BG		05/06/2009	07/08/2009	189	11:54:06	19561		478359.2	Missing 2 packet (fin158)
T59	201	s52	BG		06/16/2009	07/24/2009	205	10:24:03	19199		134368	Ride-along SAR (+/-5.2 min only)
T60	202	s52	BG		06/16/2009	08/09/2009	221	5:08:53	33359		0	DSN problems, downlink dropped! NO DATA!
T61	203	s53	BG		07/22/2009	08/25/2009	237	7:31:38	20399		746639.2	~4 small gaps?
ti_117_1	204	s53	BG		07/22/2009	09/07/2009	250	14:38:00	15600		11787.6	Lots of little gaps
sa_119_1	205	s54	BG		09/01/2009	10/13/2009	286	20:00:03	55202		44718.4	2 gaps
ti_120_1	206	s54	BG		09/01/2009	10/29/2009	302	12:30:00	15599		11833.2	
en_120_1	207	s54	BG		09/01/2009	11/01/2009	305	22:18:58	29879		444828	Lots of gaps….in SAB report
sa_122_1	208	s55	BG		10/06/2009	12/09/2009	343	22:45:58	51722		51984	
T63	209	s55	BG		10/06/2009	12/11/2009	345	22:18:58	24302		42491.6	

This document has been reviewed and determined not to contain export-controlled technical data.

IEB	DTN	Seq #	BG vs SSR	IDAP	PSIV2 Delivery (Subseq)	EXECUTION Date (UTC)	Julian Day	TIME (UTC)	Duration Total (sec)	~End of Downlink (PST/PDT)	Actual DV (kbit)	NOTES
T64	210	s56	BG		11/16/2009	12/27/2009	361	19:21:59	20879		465659	Lots of gaps, even with dual downlink. Betty Wilson provides additional packet that may recover some
T65	211	s56	BG		11/16/2009	01/12/2010	012	18:00:36	19520		241140	All data present!!
src_124_1	212	s56	BG		11/16/2009	01/18/2010	018	10:40:00	40800		368022.4	No gaps
mi_126_1	213	s57	BG		12/02/2000	02/13/2010	044	11:20:58	16081		190402.8	No gaps
rh_127_1	214	s58	BG		01/20/2010	03/02/2010	061	9:54:59	24937		428822.4	FIN 70 dropped 2 SABs
ti_128_1	215	s58	BG		01/20/2010	03/22/2010	081	2:53:59	15601		5791	
ti_130_1	216	s59	BG		03/02/2010	04/30/2010	120	5:01:59	15601		11833.2	Zero dropped
src_131_1	217	s60	BG		04/13/2010	05/25/2010	145	13:06:08	38872		540.3	No gaps
T69	218	s60	BG		04/13/2010	06/04/2010	155	17:13:27	31979		312808	4-minute radiometry gap only
ti_132_1	219	s60	BG		04/13/2010	06/07/2010	158	7:18:00	29219		5776	No gaps, only expected telem gap
T71	220	s61	BG	PSIV May 18	05/14/2010	07/06/2010	187	15:27:45	53400	7/8 @ 4am	352320	
sa_135_1	221	s61	BG	PSIV May 18	05/14/2010	07/24/2010	205	19:20:00	56939		50669	
ti_138_1	222	s63	BG		07/29/2010	09/26/2010	269	6:23:08	17331		10024	No gaps
ti_140_1	223	s64	BG		08/30/2010	11/13/2010	317	4:05:00	17399			LOST DUE TO S/C SAFING
sa_141_1	224	s64	BG		08/30/2010	11/21/2010	325	11:05:08	17399			Engineering and TWT health-check. LOST DUE TO S/C SAFING
ti_144_1	225	s66	BG		11/23/2010	01/29/2011	029	0:04:00	17400		11400	
sa_146_1	226	s67	BG		01/23/2111	03/20/2011	079					Only one off-target case. Stays on target at the end
ti_147_1	227	s67	BG		01/23/2111	04/20/2011	110					
eng_147_1	228	s67	BG		01/23/2111	04/21/2011	111					Next TWT turn on
T77	229	s68	BG			06/20/2011	171					
ti_150_1	230	s69	BG									
	231	s69	BG									
	232	s69	BG									

IEB	DTN	Seq #	BG vs SSR	IDAP	PSIV2 Delivery (Subseq)	EXECUTION Date (UTC)	EXECUTION Julian Day	EXECUTION TIME (UTC)	Duration Total (sec)	~End of Downlink (PST/PDT)	Actual DV (kbit)	NOTES
	233	s70	BG									
	234	s70	BG									
	235	s70	BG									
	236	s71	BG									
	237	s71	BG									
	238	s71	BG									
	239	s72	BG									
	240	s72	BG									
	241	s72	BG									
	242	s73	BG									
	243	s73	BG									
	244	s73	BG									

This document has been reviewed and determined not to contain export-controlled technical data.

Notes for uplink/downlink spreadsheet: column descriptions, acronym definitions, and other notes (as of 2/2/2011). Key columns of the Cruise worksheet are reproduced above.

HEAD	DESCRIPTION: NOTES, ACRONYMS
IEB	Instrument execution block: This column is really the name of the observation: Two letters for target, rev. number, times during the rev.
DTN	Data take number: For cruise, we used 1–21; for tour we started at 31. Maximum value is 255, so it may roll over.
Seq #	Sequence number: Project-supplied number for uplink planning units. For cruise, we used 1–21; for tour we started at 31.
BG vs SSR	Background (sequence) vs solid-state recorder: Used to keep track of the location in S/C memory of where our IEB will reside until it is transferred to the RADAR. Typically part of the BG sequence, unless there were memory space issues.
IDAP	Immediate/Delayed Action Program: A method to "trigger" the IEB within the RADAR. Normally the trigger time of the IEB is placed in the BG sequence. However, to allow for late pointing adjustments, this "trigger" instruction can be placed in an IDAP. Note that BG sequence commands are determined months ahead of time. An IDAP timing can be adjusted within a few days of execution to account for target/timing changes. IVP = inertial vector propagator PSIV = Preliminary Sequence Integration and Validation
PSIV2 Delivery (Subseq)	Preliminary sequence integration and validation delivery date (Port 2): There are various delivery windows that the RADAR team can use to deliver commands. Typically we used the second port of the PSIV process.
Execution Date (UTC)	Date of execution: The UTC execute start date of the IEB, calculated from the Julian Day in Column M.
Execution Julian Day	The day of execution of the start time of the IEB.
Execution Time (UTC)	This is rounded typically to the nearest second of trigger time.
Duration Total (sec)	Total seconds of IEB time (trigger to halt), converted to hours and minutes.
~End of Downlink (PST/PDT)	Date (and sometimes time, Pacific Standard/Daylight Time) when the downlink window is complete: This was used so that the IO Team would know the earliest time to query for the data. CO = Carryover, meaning that we may get only some of the data on that downlink and will have to wait for the rest on the next downlink.
Actual DV (Mbit)	Actual amount of data volume allocation to RADAR for that observation DV = data volume
Notes	Notes of potential use to data users. DBE double-bit error FSIV = Final Sequence Integration and Validation ITL = Incompressible Test List ND = not determined [confirm] RL = resistive load RMSS =RADAR Mapping Sequencing Software SAB = SAR-altimetry burst, where SAR=synthetic aperture radar SFDU = Standard Formatted Data Unit SSG = subsequence generation WTK = William T. K. Johnson data volume. The original command format for the IEBs was given the name "WTK" files for the lead scientist/engineer who developed the tools (and a large portion of the RADAR). This is a data volume estimator tool in bits.

	COLORS
Green	Task/observation complete as expected.
Yellow	Typically some note on the observation or task.
Orange/ other colors	Typically minor issues.
Red	Science data was lost and/or error in commanding.

15 Appendix 5: BIDR PDS Label, Primary Data Set, 32-Bit Data

Source: Appendix A, BIDR SIS

```
PDS_VERSION_ID = PDS3
/* FILE FORMAT AND LENGTH */
RECORD_TYPE = FIXED_LENGTH
RECORD_BYTES = 160
FILE_RECORDS = 183
LABEL_RECORDS = 23
/* POINTERS TO START RECORDS OF OBJECTS IN FILE */
^IMAGE = 24
/* IMAGE DESCRIPTION */
DATA_SET_ID = "CO-SSA-RADAR-5-BIDR-V1.0"
DATA_SET_NAME = "CASSINI ORBITER SSA RADAR 5 BIDR V1.0"
PRODUCER_INSTITUTION_NAME = "JET PROPULSION LABORATORY"
PRODUCER_ID = JPL
PRODUCER_FULL_NAME = "Inst Lead Charles Elachi contact Bryan Stiles"
PRODUCT_ID = BIFQI42N253_D035_T00A_V01
PRODUCT_VERSION_ID = 1
INSTRUMENT_HOST_NAME = "CASSINI ORBITER"
INSTRUMENT_HOST_ID = CO
INSTRUMENT_NAME = "CASSINI RADAR"
INSTRUMENT_ID = RADAR
TARGET_NAME = TITAN
START_TIME = YYYY-DOYThh:mm:ss.sss
STOP_TIME = YYYY-DOYThh:mm:ss.sss
SPACECRAFT_CLOCK_START_COUNT = nnnnnnnnn
SPACECRAFT_CLOCK_STOP_COUNT = nnnnnnnnn
PRODUCT_CREATION_TIME = YYYY-DOYThh:mm:ss.sss
SOURCE_PRODUCT_ID = LBDR_08_031_V01
MISSION_PHASE_NAME = TOUR
MISSION_NAME ="CASSINI-HUYGENS"
SOFTWARE_VERSION_ID ="V1.0"
/* DESCRIPTIONS OF OBJECTS CONTAINED IN FILE */
OBJECT = IMAGE
```

LINES = 160

LINE_SAMPLES = 40

SAMPLE_TYPE = "PC_REAL"

SAMPLE_BITS = 32

CHECKSUM = nnnnnnnnn

SCALING_FACTOR = 1.00000000

OFFSET = 0.00000000

MISSING_CONSTANT = 16#FF7FFFFB#

NOTE = "

Data values in this Basic Image Data Record are synthetic aperture radar (SAR) normalized backscatter cross-section values. The values are physical scale (not in dB) and have been normalized in order to remove variations in the image due to incidence angle variations among the measurements. The raw backscatter values are multiplied by the function f(I) of incidence angle, I, in degrees of the form XXXXXXXXX."

END_OBJECT = IMAGE

OBJECT = IMAGE_MAP_PROJECTION

^DATA_SET_MAP_PROJECTION = "DSMAP.CAT"

MAP_PROJECTION_TYPE = OBLIQUE CYLINDRICAL

A_AXIS_RADIUS = 2575.000000 <km>

B_AXIS_RADIUS = 2575.000000 <km>

C_AXIS_RADIUS = 2575.000000 <km>

FIRST_STANDARD_PARALLEL = "N/A"

SECOND_STANDARD_PARALLEL = "N/A"

POSITIVE_LONGITUDE_DIRECTION = WEST

CENTER_LATITUDE = 0.000000 <deg>

CENTER_LONGITUDE = 0.000000 <deg>

REFERENCE_LATITUDE = 30.000000 <deg>

REFERENCE_LONGITUDE = 150.000000 <deg>

LINE_FIRST_PIXEL = 1

LINE_LAST_PIXEL = 160

SAMPLE_FIRST_PIXEL = 1

SAMPLE_LAST_PIXEL = 40

MAP_PROJECTION_ROTATION = 90.0

MAP_RESOLUTION = 8.0 <pix/deg>

MAP_SCALE = 5.61777853 <km/pix>

MAXIMUM_LATITUDE = 46.13792 <deg>

MINIMUM_LATITUDE = 37.160353 <deg>

```
EASTERNMOST_LONGITUDE = 93.703090 <deg>
WESTERNMOST_LONGITUDE = 120.701079 <deg>
LINE_PROJECTION_OFFSET = -240.500000
SAMPLE_PROJECTION_OFFSET = -80.500000
OBLIQUE_PROJ_POLE_LATITUDE = 58.525051 <deg>
OBLIQUE_PROJ_POLE_LONGITUDE = 310.574599 <deg>
OBLIQUE_PROJ_POLE_ROTATION = 157.535316 <deg>
OBLIQUE_PROJ_X_AXIS_VECTOR = ( -0.75000000, -0.43301270, 0.50000000 )
OBLIQUE_PROJ_Y_AXIS_VECTOR = ( 0.56759575, -0.80945648, 0.15038374 )
OBLIQUE_PROJ_Z_AXIS_VECTOR = ( 0.33961017, 0.39658568, 0.85286853 )
LOOK_DIRECTION = LEFT
COORDINATE_SYSTEM_NAME = "PLANETOGRAPHIC"
COORDINATE_SYSTEM_TYPE = "BODY-FIXED ROTATING"
END_OBJECT = IMAGE_MAP_PROJECTION
END
```

Note: This example is not based on actual flyby geometries for a particular Titan pass.